UNIVERSITÁ DEGLI STUDI DI TRIESTE

FACOLTÁ DI SCIENZE MATEMATICHE FISICHE E NATURALI

CORSO DI LAUREA SPECIALISTICA IN FISICA

MEASUREMENT OF THE POLARIZATION AMPLITUDES OF THE $B_s \to \phi\phi$ DECAY AT CDFII

MISURA DELLE AMPIEZZE DI POLARIZZAZIONE DEL DECADIMENTO $B_s \to \phi\phi$ A CDFII

Laureando:
Mirco Dorigo

Relatrice:
Dott.ssa Anna Maria Zanetti
Correlatore:
Dott. Marco Rescigno

ANNO ACCADEMICO 2008/2009

"Haud igitur redit ad nilum res ulla, sed omnes
discidio redeunt in corpora materiai"

E dunque nessuna sostanza ritorna nel nulla, ma tutte dissolte ritornano alle particelle elementari della materia.

Lucrezio, *De Rerum Natura*

ABSTRACT

In this thesis we present the first measurement of the polarization amplitudes for the charmless $B_s \to \phi\phi \to [K^+K^-][K^+K^-]$ decay of the B_s meson. The result is achieved using an unbinned Maximum Likelihood fit to the data collected by the Collider Detector at Fermilab (CDF) in Run II (CDFII), in a period starting from March 2001 till April 2008, which corresponds to an integrated luminosity of 2.9 fb^{-1}. The resulting yield consists of 300 signal events selected by the Two Track Trigger (TTT).

The three estimated polarization amplitudes are:

$\lvert A_0\rvert^2$	$\lvert A_\parallel\rvert^2$	$\lvert A_\perp\rvert^2$
0.388 ± 0.042	0.257 ± 0.041	0.355 ± 0.044

and the resulting polarization fractions are:

longitudinal	transverse
0.388 ± 0.042	0.612 ± 0.060

Furthermore, our work puts in evidence an original topic, that was never observed until now: an unexpected dependence of the signal acceptance on the proper decay time (t) of the B_s mesons. This specific issue, which is most likely a general feature induced by any signal selection based on the lifetime information, is supposed to be related to the on-line TTT and off-line selections based on the impact parameter. The involved fit, indeed, reproduces the biases observed in large statistics Monte Carlo (MC) samples.

The thesis presents the same analysis performed for the $B_s^0 \to J\psi\phi$ decay as well, which is used as a control sample. The polarizations amplitudes we find are consistent with the published ones [1]; this result contributes to enforce the reliability of the analysis.

This work is considered ready to begin the procedure for official approval by the CDF collaboration pending the finalization of the systematic uncertainty which has not yet been fully completed.

SOMMARIO

In questa tesi viene presentata la misura delle ampiezze di polarizzazione del decadimento $B_s \to \phi\phi \to [K^+K^-][K^+K^-]$. Essa è la prima effettuata per questo tipo di decadimento ed è stata ottenuta dal un fit di tipo *unbinned Maximum Likelihood* a un campione di dati raccolti dal Collider Detector at Fermilab (CDF), a partire da marzo del 2001 fino ad aprile del 2008, e correspondenti a una luminosità integrata di 2.9 fb^{-1}. In questo campione sono stati selezionati 300 eventi di segnale nei dati acquisiti con l'utilizzo del Two Track Trigger (TTT).

Le tre ampiezze di polarizzazione misurate sono:

$\lvert A_0\rvert^2$	$\lvert A_\parallel\rvert^2$	$\lvert A_\perp\rvert^2$
0.388 ± 0.042	0.257 ± 0.041	0.355 ± 0.044

dalle quali si ottengono le seguenti frazioni di polarizzazione:

longitudinale	trasversa
0.388 ± 0.042	0.612 ± 0.060

Inoltre nel lavoro di tesi si è messo in luce un inastteso aspetto: la dipendenza dell'accettanza del segnale dal tempo proprio di decadimento del mesone B_s. Questo effetto, mai osservato nelle precedenti analisi di questo genere svolte a CDF, si presume essere dovuto alle selezioni sulla base del parametro d'impatto, effettuate sia on-line dal TTT sia a livello off-line. L' interesse sucitato da questo effetto è di carattere generale, in quanto può riguardare qualsiasi analisi che basi la propria selezione degli eventi sulle peculiarità della lunga vita media del mesone B_s. Nel fit finale si è pertanto sviluppato un metodo che consideri la nuova dipendenza osservata.

La tesi presenta la stessa analisi svolta anche per il decadimento $B_s^0 \to J\psi\phi$: esso è utilizzato come campione di test. I valori di polarizzazione trovati per questo decadimento sono consistenti con i risultati noti in letteratura [1]; questo convalida la consistenza e la correttezza dell'analisi sviluppata per il decadimento $B_s \to \phi\phi$.

In questa tesi si riporta infine il metodo per la valutazione delle incertezze sistematiche, ultimo tassello mancante per poter sottoporre l'analisi all'approvazione ufficiale da parte della collaborazione di CDF.

CONTENTS

LIST OF FIGURES

LIST OF TABLES

1 INTRODUCTION AND MOTIVATIONS

The Standard Model (SM) is the theoretical framework that describes the known elementary particles and their interactions. Over the past decades it has been greatly tested experimentally, proving itself very successful. Its predictions involving the fundamental building blocks of matter, the quarks, the leptons and the vector bosons, have been confirmed. In this picture, the physics of the b quark represents one of the most active research areas in high energy physics to challenge the SM predictions. In particular, the rich phenomenology of non-leptonic b-meson decays offers a great opportunity to search for CP violations, both direct and mixing-induced, and to explore the phase structure of the Cabibbo-Kobayashi-Maskawa (CKM) matrix [2].

Charmless hadronic b-meson decays proceed through an unique interplay of electroweak and low-energy strong interactions. The latter represents also the most challenging issue in the theoretical description of a large part of b-meson decay rates, since the predicted amplitudes are affected by significant uncertainties coming from the presence of strong interactions in non-perturbative regime. Several phenomenological models have been built, none of them properly accounting for all observed decay-rates and their CP asymmetry. Thus, the interpretation of experimental observations becomes complicated: any discrepancy between predictions and measurements may be ascribed either to improper treatment of hadronic uncertainties, or to contributions not expected in the SM. Accumulating further experimental information (for example in the B_s^0 field) is important in order to verify the theoretical calculations and arrive at more precise predictions.

One class of B decays which is particularly intriguing involves processes whose principal contribution comes from $\bar{b} \to \bar{s}$ penguin amplitudes. The reason is that there are already several results in these processes conflicting with the current SM expectations. These effects, conversely, could be taken into account by the presence of new physics. First, the CP asymmetry in $B_d^0 \to J/\psi K_S$ should be approximately equal to that in penguin-dominated $\bar{b} \to \bar{s}q\bar{q}$ transitions ($q = u, d, s$) within the SM; however, on average, these latter measurements yield a smaller value [3, 4, 5, 6]. Second, within the SM, one expects no triple-product asymmetries in $B \to \phi K^\star$ [7].[1] Nonetheless, both BaBar and Belle have measured such effects, albeit at low statistical significance [8, 9]. Third, the data on $B \to \pi K$ branching ratios and CP asymmetries [10, 11, 12, 13, 14] appear to be inconsistent with a SM fit [15, 16].

In the same scenario, another powerful challenge occurs in $B \to V_1 V_2$ decays, where the V_i are light vector mesons. Such systems have the peculiar nature that the decay rate can be explained by the definition of three specific decay amplitudes: these correspond to the three possible relative angular momenta L between the vector mesons. In fact, for two spin 1 particles, L can be equal to 0, 1, or 2 to obtain the spin 0 initial state. Different formalisms could be involved in this description; the most suitable one makes use of three *polarization* amplitudes (one longitudinal and two transverse). Since these are observable quantities, they can be measured from an angular analysis of the decay products: the emission angles of the final states particles (*i. e.*, the products from the V_i mesons decays) have to be studied in a proper reference frame to

1 The triple-product for a B meson decay to two vector mesons takes the form $\vec{q} \cdot (\vec{\epsilon_1} \times \vec{\epsilon_2})$, where $\vec{q}$ is the momentum of one of the vector mesons; $\vec{\epsilon_1}$ and $\vec{\epsilon_2}$ are the polarizations of the two vector mesons.

separate the three decay amplitudes.[2] If the final-state is a CP-eigenstate, this disentanglement allows one to investigate the B system CP-properties.

Within the SM, the expectation is that these amplitudes result in a dominant longitudinal polarization, with the transversely-polarized amplitudes suppressed by a factor m_V/m_B. While this is experimentally confirmed for $B \to \rho\rho$ decays, which receive $\bar{b} \to \bar{d}$ penguin contributions, in $B \to \phi K^\star$, a $\bar{b} \to \bar{s}$ penguin decay, it has been measured that the transverse polarization is about equal to the longitudinal one [17, 18, 19]. This surprising result is known as "Polarization Puzzle". This phenomenon could be more evident in the B meson decays involving penguin diagram, like the $B_s^0 \to \phi\phi$. New physics [20, 21], and SM [22, 23] explanations have been proposed.

The work presented here draws motivation from the above intriguing puzzles related to $\bar{b} \to \bar{s}$ penguin processes. The thesis describes the study of $B_s^0 \to \phi\phi$ decay. This is governed by the $\bar{b} \to \bar{s}$ transition and it is a pseudoscalar to vector-vector decay: it includes all the characteristics described above. Thus, it is an appealing candidates whose experimental analysis could bring more comprehension in the polarization puzzle as well as a better understanding of the low-energy strong interactions. Moreover, since each ϕ decay into two charged K mesons, the final state is a CP-eigenstate: this also offers the possibility to look for CP violations. Actually, this is an attractive topic because the first measurements of CP violation made at Tevatron for the B_s^0 mesons (in the $B_s^0 \to J/\psi\phi$ decay) seems not to be in agreement with the SM predictions [24, 25].

In addition, in the SM, the mixing-induced CP asymmetries in the dominant B_s^0 decay modes practically vanish: new physics is needed to change this prediction.While such new contributions are likely to affect also B_d^0–$\bar{B}_d^0$ mixing, they appear in the B_d^0 system as a correction to a non-zero SM prediction for the mixing-induced CP asymmetry. In the B_s^0 system, however, the new physics contribution is a correction to essentially zero [26]. Thus, they could be easily tested: a non-zero measured asymmetry is an unequivocal new physics proof. Obviously, measurements of both direct and mixing-induced CP asymmetries require high statistics data sample. Indeed, these represent a very prominent goal of the b-physics program at the forthcoming experiments [27]. The polarization analysis, discussed in this thesis, is an intermediate and obliged step toward the achievement of that goal and can potentially already reveal the presence of new physics.

The aim of the analysis presented here is the first measurement of $B_s^0 \to \phi\phi$ polarization amplitudes. It is the natural evolution of the first branching ratio measurement of this decay in 2005, with $180\,\text{pb}^{-1}$ of data collected by the CDF experiment at the Tevatron $p\bar{p}$ collider [28]. The latter was recently updated [29] with $2.9\,\text{fb}^{-1}$ of data: this update represents the starting point of the present analysis. This work has been presented regularly at the CDF B-physics group meetings at various stages of its development. It is considered ready to begin the procedure for official approval by the CDF collaboration pending the finalization of the systematic uncertainty which has not yet been fully completed.

The thesis is organized as follows:

CHAPTER 2 provides a concise description of the theoretical background needed to interpret the measurements. It is a non-exhaustive discussion, aiming at the introduction of the necessary tools and definitions, in particular, the differential decay rates as function of time and final state emission angles. The first chapter contains also the description of the analysis strategy.

CHAPTER 3 describes the experimental apparatus. It contains a general description of the accelerator and of the CDFII detector. The sub-detectors that reconstruct

2 This quantities are complex number. Then, experimentally on can extract their moduli and relative phases. The three amplitudes satisfy a unitarity relation: the sum of the three squared moduli is equal to 1. Thus, they are usual expressed as percentages or fractions of total polarization.

charged-particle trajectories and the trigger are described in greater detail, being the aspects of the detector more specific to the present analysis.

CHAPTER 4 explains the data samples collected with the detector. The TTT data-set is described in detail along with the different trigger paths (on-line selections) it is composed. The off-line selections for $B_s^0 \to \phi\phi$ and $B_s^0 \to J/\psi\phi$ events are also discussed, and comparison of significant distributions between data and MC simulations are presented. Finally the $B_s^0 \to \phi\phi$ and $B_s^0 \to J/\psi\phi$ event yields are shown and the main sources of background are discussed.

CHAPTER 5 contains the first step of our work: the time-integrated analysis. The fitting technique is introduced and it consists in an unbinned maximum likelihood fit of the reconstructed B candidates mass and the three helicity angles distributions of the B decay products. It is designed for the estimation of the polarization amplitudes. At this stage, the angular acceptance of the detector is assumed unrelated to the proper decay time of the B meson. It is determined with the MC described in the previous chapter. The fitter framework is checked by three tests: the pseudo-experiments pulls distributions, the fit of $B_s^0 \to J/\psi\phi$ decay as a control sample, and the fit on realistic MC data. The latter one reveals the correlation of the angular acceptance with the B meson proper decay time. Because of this complication, the analysis must switch to the next stage, which is the argument of the next chapter.

CHAPTER 6 details the time-dependent analysis. Here the general problem of dealing with a time-dependent angular acceptance is worked out. A solution is proposed and the new likelihood, which contains also the B proper decay time as input variable, is then built on this basis. This new fitter is subject to the pulls distributions test. Then, the improvements achieved is shown, looking at the fit on the realistic MC. Finally, the fit projections on real data distribution are shown, and a list of the main systematic uncertainties is also reported.

CHAPTER 7 provides the conclusions and the future perspectives.

As mentioned before, the thesis presents the same analysis performed for the $B_s^0 \to J\psi\phi$ as well: because its properties are well known, this decay is a powerful control sample. Since, it represents one of the fitter tests, the details of this analysis is reported in the Appendix B.

2 THE $B_s \to \phi\phi$ DECAY: THEORETICAL CONSIDERATIONS

This chapter provides some of the theoretical background needed to understand and to interpret the measurements studied in this thesis. This deals with the decay of B_s^0, a b-flavored meson. The theory of this decay requires some informations on how the b quark is bound into hadrons, some elementary concepts on symmetries and mixing, and some knowledge of the standard electroweak theory. They are briefly reminded here, but a background of the SM and of the Quantum Fields Theory (QFT) is assumed.

2.1 THEORETICAL TOOLS: INTRODUCTION

The main aim of B physics is to learn about the short distance dynamics of nature. Short distance physics couples to b quarks, while experiments detect b-flavored hadrons. One therefore needs to connect the properties of these hadrons in terms of the underlying b quark dynamics. Except for a few special cases, this requires an understanding of the long distance, non-perturbative properties of QCD. It is then useful to separate long distance physics from short distance using an Operator Product Expansion (OPE) or an effective field theory [30]. The basic idea is that interactions at higher scales give rise to local operators at lower scales. This allows us to think about the short distance phenomena responsible for the flavor structure in nature independent of the complications due to hadronic physics, which can then be attacked separately. This strategy can lead to very practical results: the hadronic part of an interesting process may be related by exact or approximate symmetries to the hadronic part of a measured process.

In the description of B decays several short distances arise. Charge-Parity (CP) and flavor violation stem from the weak scale and, probably, even shorter distances. The processes at these scales are separated from the ones at B mass scale with an OPE, leading to an effective Hamiltonian for flavor changing processes. This is what happens in the description of a penguin dominated decay, like the $B_s \to \phi\phi$.

Some useful definitions are:

- $\alpha_s(\mu^2)$ is the coupling constant of the strong interactions at the scale μ^2;
- G_F is the coupling constant of the Fermi theory of electro-weak interactions. It's value is[1] $G_F/(\hbar c)^3 = 1.166\,37(1) \times 10^{-5}\,\mathrm{GeV}^{-2}$.
- P is the operator that produces the spatial inversion of coordinates (*i. e.*, the discrete parity transformation):

$$\mathsf{P}\psi(\vec{r}) = \psi(\vec{-r}) \tag{2.1}$$

  P is hermitian ($\mathsf{P} = \mathsf{P}^\dagger$) and idempotent ($\mathsf{P}^2 = 1$). The only two eigenvalues of P are ± 1. If $\mathsf{P}\psi(\vec{r}) = \psi(\vec{-r}) = \psi(\vec{r})$, ψ is called a symmetric state; if $\mathsf{P}\psi(\vec{r}) =$

1 $\hbar$ is the reduced Planck constant $h/2\pi$, c is the speed of light

$\psi(-\vec{r}) = -\psi(\vec{r})$, ψ is an antisymmetric state. The intrinsic parity of a system of two particles α and β is

$$\mathsf{P}\,|\alpha\beta\rangle = \xi_\alpha \xi_\beta (-1)^L\,|\alpha\beta\rangle \tag{2.2}$$

where ξ_α and ξ_β are the intrinsic parity quantum numbers of the two particles, and L is the relative angular momentum between them.

- C is the operator of the charge conjugation that transforms all particles internal quantum numbers in those of the corresponding antiparticles, leaving all other coordinates unchanged. For example, $\mathsf{C}\,|e^-\rangle = |e^+\rangle$. C is hermitian ($\mathsf{C} = \mathsf{C}^\dagger$) and idempotent ($\mathsf{C}^2 = 1$).
- V is the CKM matrix which relates the mass quarks eigenstates d, s, and b, to the flavor eigenstates, d', s', and b':

$$\begin{pmatrix} d' \\ s' \\ b' \end{pmatrix} = \begin{pmatrix} V_{ud} & V_{us} & V_{ub} \\ V_{cd} & V_{cs} & V_{cb} \\ V_{td} & V_{ts} & V_{tb} \end{pmatrix} \begin{pmatrix} d \\ s \\ b \end{pmatrix}; \tag{2.3}$$

In the SM, the unitarity of the CKM matrix must hold:

$$\sum_{i=1}^{3} V_{ij} V_{ik}^\star = \sum_{i=1}^{3} V_{ji} V_{ki}^\star = \delta_{ij} \tag{2.4}$$

Expanding this equation for any j, k yields nine equations, of which the six equations involving the off-diagonal elements of δ_{ij} describe triangles in the complex plane. These six triangles fall into two groups of three, differing only by their orientation in the complex plane: these are the so-called unitarity triangles. The angles of the first triangle (see fig. 2.1) are given by

$$\begin{aligned} \alpha &= \arg\left(-\frac{V_{td}V_{tb}^\star}{V_{ud}V_{ub}^\star}\right) \\ \beta &= \arg\left(-\frac{V_{cd}V_{cb}^\star}{V_{td}V_{tb}^\star}\right) \\ \gamma &= \arg\left(-\frac{V_{ud}V_{ub}^\star}{V_{cd}V_{cb}^\star}\right) \end{aligned} \tag{2.5}$$

All unitarity triangles have the same area, commonly denoted by $J/2$. If CP is violated, J is different from zero.

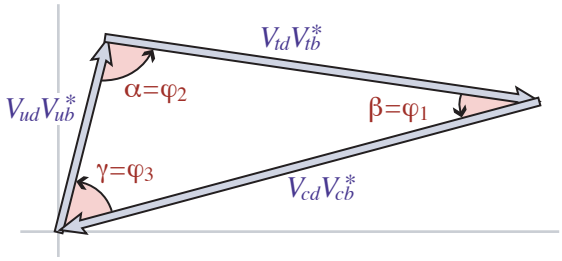

Figure 2.1: Graphical representation of the unitarity constraint as a triangle in the complex plane.

2.2 THE B MESONS

B mesons are composed of a bottom antiquark and either an up (B^+), down (B^0), strange (B_s^0) or charm (B_c^+) quark.[2] Obviously, each B meson has a corresponding antiparticle, that is composed of a bottom quark and an up (B^-), down ($\bar{B}^0$), strange ($\bar{B}_s^0$) or charm (B_c^-) antiquark respectively. Table 1 presents the main characteristics of the B mesons.

Particle	Quark content	Isospin	Mass (MeV/c^2)	Mean Lifetime (ps)
B^+	$u\bar{b}$	1/2	5279.15 ± 0.31	1.638 ± 0.011
B^0	$d\bar{b}$	1/2	5279.53 ± 0.33	1.530 ± 0.009
B_s^0	$s\bar{b}$	0	5366.3 ± 0.6	$1.470^{+0.026}_{-0.027}$
B_c^+	$c\bar{b}$	0	6276 ± 4	0.46 ± 0.07

Table 1: Main characteristics of B mesons. All B mesons have the same spin and parity $J^P = 0^-$.

As we can see, the constituents of the B_s mesons is one heavy quark (the b) and one light quark (the s). Remind that, in the static quark model, the rest mass of the b is $4.20^{+0.17}_{-0.07}\,\mathrm{GeV}/c^2$; whereas the one of s quark is only $104^{+26}_{-34}\,\mathrm{MeV}/c^2$. Mesons consisting of one heavy (mass M) and one light (mass m) quark have some aspects in common with a hydrogen atom, where the most of the mass is in the nucleus, *i. e.*, the proton (the analogue of the heavy quark) to which is bound the much lighter electron (the analogue of the light quark) [31]. Quantitatively, the atomic wave-function is, to first order, independent of the nuclear mass; correction are of order (electron mass)/(nucleus mass) or (atomic binding energy)/(nucleus mass). Similarly, in a heavy-light quarks system, the effect of the heavy quark on the energy levels is of the order Λ_{QCD}/M, where $\Lambda_{\mathrm{QCD}} \simeq 0.2\,\mathrm{GeV}$ is the strong-interaction scale parameter, representing the light quark mass and the gluon binding potential.

Consequently, in the limit $M \gg \Lambda_{\mathrm{QCD}}$, the heavy quark acts approximately as a static color-triplet source, and its spin and flavor do not affect the light degrees of freedom. This is analogous to atomic physics, where isotopes with different nuclei have nearly the same properties. Thus, the properties of heavy-light hadrons are related by a symmetry, called heavy quark symmetry (HQS) [30].[3]

2.2.1 Production

The production of a b-meson requires the presence of a b quark, so two different processes have to take place: the first one is the *production* of the b quark, and the second one is its *fragmentation* into the meson.

Quarks Production

There are two main ways for the b-quark production, which are different for the kind of accelerator involved: the first method makes use of e^+e^- collider (*e. g.*, the B factories at SLAC and KEK); in the second one, hadron collider are used (like the Tevatron, where p and $\bar{\mathrm{p}}$ collide). In both cases, the origin is a point-like interaction that results

2 The combination of a bottom antiquark and a top quark is not possible because of the top quark's short lifetime. The combination of a bottom antiquark and a bottom quark is not a B meson, but rather "bottomonium". In this document the notation B_s has the same meaning of B_s^0, and B_d has the same meaning of B^0.

3 The heavy quark spin-flavor symmetries are helpful for understanding many aspects of the spectroscopy and decays of heavy hadrons from first principles. For example, in the infinite mass limit, mass splittings between b-flavored hadrons can be related to those between charmed hadrons.

in a b-$\bar{b}$ pair. The main difference of the two types of production is that in the e^+e^- machines the energy of the b quark generated is well known and it is the same for each event. In fact, since e^+ and e^- are elementary particles, the beam energy is very close to the energy of b quarks produced. Instead, in hadron colliders the point-like interaction occurs between quarks and gluons, *i. e.*, the elementary constituents of the hadrons: their energies span a continuum spectrum, because they are fractions of the energy of the colliding particles.

In this case, the cross section for the production of a b quark is calculable in perturbative QCD as much as the heavy quark mass, m, is larger than Λ_{QCD} [32]. The cross section in the QCD improved parton model as a function of the center of mass energy squared s is

$$\sigma(s) = \sum_{i,j} \int \frac{dx_1}{x_1} \frac{dx_2}{x_2} \hat{\sigma}_{ij}(\hat{s}, m^2, \mu^2) F_i(x_1, \mu^2) F_j(x_2, \mu^2) \,, \tag{2.6}$$

where the F_i are the momentum densities of the partons in the incoming hadrons, and $\hat{s} = x_1 x_2 s$ is the parton total center-of-mass energy squared (x_i are the partons momentum fractions)[30]. The quantity $\hat{\sigma}_{ij}$ is the short distance cross section

$$\hat{\sigma}_{ij}(\hat{s}, m^2, \mu^2) = \sigma_0 c_{ij}(\hat{\rho}, \mu^2) \,, \tag{2.7}$$

where $\sigma_0 = \alpha_s^2(\mu^2)/m^2$ and $\hat{\rho} = 4m^2/\hat{s}$. The function c_{ij} has a perturbative expansion, which terms are known, either analytically or as a numerical fit. The lowest order short distance cross section is calculated from the diagrams in fig. 2.2. The top graphs

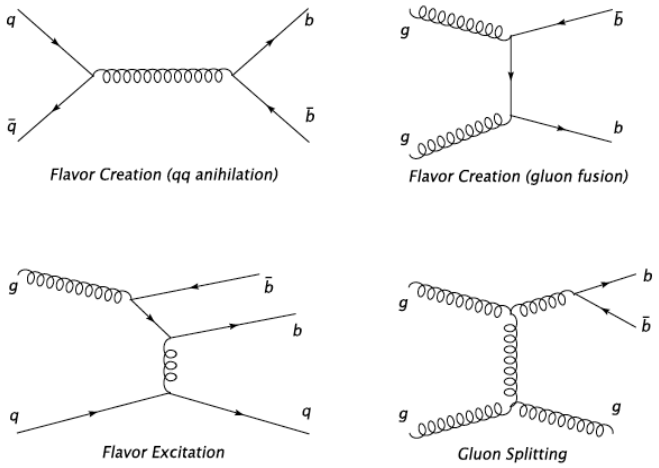

Figure 2.2: Diagrams for b quark production at lowest order.

are the lowest order contributions of the so called "flavor creation", where only a quarks and an antiquark or two gluons interact. Other two processes allow for the creation of a b-$\bar{b}$ pair: the "flavor excitation" and the "gluon splitting". Their lowest order diagrams are represented in fig. 2.2. In the flavor excitation a b from the sea quark of one of the interacting particles is scattered out in the strong interaction with a parton of the other hadron. The gluon splitting takes place when a gluon produced

in the hadron collision results in a b-$\bar{b}$ pair in the fragmentation process. All the three mechanisms of productions end in b-$\bar{b}$ pairs which differ for their resulting angular distribution in the laboratory frame: in the flavor creation the two particle is back-to-back; in the gluon splitting the azimuthal angles of the two particles are very close, and the flavor excitation presents the intermediate configurations between the two previous situations.

The cross section of $p\bar{p} \to \bar{b}X$ at the Tevatron, where $\sqrt{s} = 1.96\,\text{TeV}$, is

$$\sigma(p\bar{p} \to \bar{b}X,\ \sqrt{s} = 1.96\,\text{TeV},\ |Y_b| < 1) = 29.4^{+6.2}_{-5.4}\,\mu\text{b} \tag{2.8}$$

where Y_b is the b quark rapidity (see Sect. 3.2.1) [30]. In spite of the high b-$\bar{b}$ cross section, about a hundred times greater than the e^+e^- collider one, in hadron colliders it is a small percentage of the total cross section, which is of the order $\sigma_T \simeq 70\,\text{mb}$. This implies the need of an appropriate trigger selection to discriminate b-flavored events from the huge background. Typical trigger selection requires a lepton from semileptonic b-decays, a dimuon signal from $b \to J/\psi$ decays, and a signature based on the long lifetime of b-hadrons as in the case discussed in this thesis.

Fragmentation

Once the b ($\bar{b}$) is produced, the scale μ drops: at this point starts the fragmentation process. In fact, the fragmentation of quarks and gluons into hadrons involves confinement dynamics, and occurs at time scales that are long compared to those of the hard scattering that produced the quarks and gluons.

In single-particle inclusive hard-scattering processes, the fragmentation is factorized in perturbative QCD (see [33] and references therein) from the hard interaction and summarized in a non-perturbative fragmentation function (FF) $D_i^H(x, \mu)$. $D_i^H(x, \mu)$ is the probability density of a hadron H to form from parton i with momentum fraction x at factorization scale μ. Though non-perturbative, these FFs are universal and so, they may be determined for each hadron H in a few calibration experiments at some fixed scale μ_0, for subsequent use in other experiments and at other values of μ (see for example [34, 35]).

The fragmentation of heavy quarks is somewhat different.[4] When the heavy quark is produced with an energy not much larger than its mass, the fragmentation process consists mainly of the non-perturbative transition of the heavy quark to the hadron H, which one assumes can be described by a non-perturbative FF. One may make a general ansatz for the functional form of this FF, whose parameters are to be fixed by fitting to experimental data. A heavy flavored meson should retain a large fraction of the momentum of the primordial heavy quark, and therefore its FF should be much harder than that of a light hadron. In the limit of a very heavy quark, one expects the FF for a heavy quark to go into any heavy hadron to be peaked near 1. This effect can be seen in fig. 2.3 for the FF of a b quark in a B meson and it is used in the experimental identification of the heavy-flavored hadron.

The results of the fragmentation is to bind the quarks and gluons in colorless clusters of low relative momenta. They group in jets of hadrons, which flight in approximately the same directions of the quarks produced in the hard scattering. If one of the original quarks is a b, at least one of the jet's particles is a B meson or a b-flavored barion (*e. g.*, Λ_b). This is the main difference between the heavy and light quarks fragmentation: a b-flavored hadron can be experimentally identified under certain conditions.

4 By heavy quarks we mean charm and bottom quarks. Remember that the top quark decays by the weak interaction before it has time to hadronize.

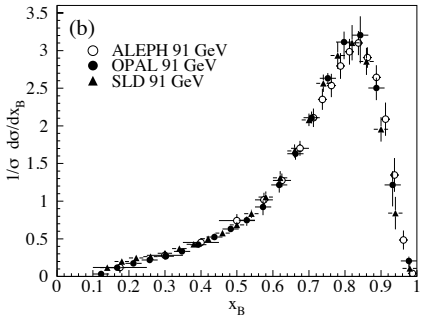

Figure 2.3: Measured e^+e^- fragmentation function of b quarks into B hadrons at $\sqrt{s} \simeq 91\,\text{GeV}$ [36].

The most part of b-hadrons produced in the hadronization are excited states (*e. g.*, $B^\star$ and $B^{\star\star}$): they decay by electromagnetic and strong interactions into other b-mesons (or barions), and pions, kaons and photons. The time scale of these processes are so short that is not possible to distinguish them from the primary interaction. In fig. 2.4 a sketch of the entire process is represented.

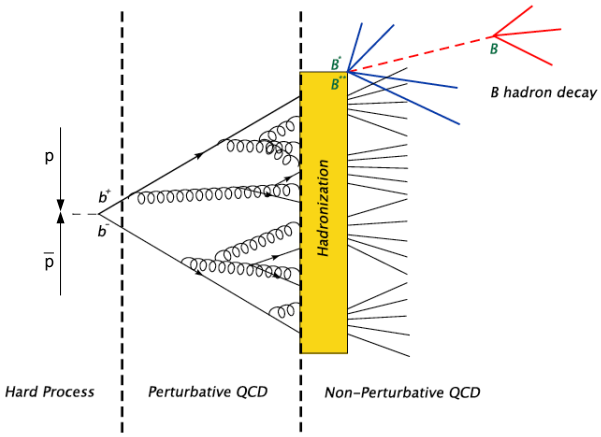

Figure 2.4: Sketch of fragmentation process.

2.2.2 Electro-Weak Decay: Effective Hamiltonian

To predict the decay rate of a B meson into some final state f, one must calculate the transition amplitude $\mathcal{M}$ for $B \to \text{f}$. In general there are many contributions to $\mathcal{M}$, each of which is, at the quark level, pictorially represented by Feynman diagrams such as those in fig. 2.5.

Quark diagrams are a poor description for the decay amplitude of a B meson. The quarks feel the strong interaction, whose nature changes drastically over the distances at which it is probed: at short distances, much smaller than $1/\Lambda_{\text{QCD}}$, the strong in-

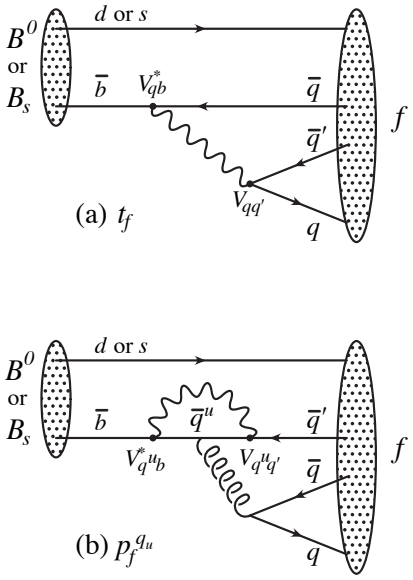

Figure 2.5: Tree exchange diagram, t_f (a), and penguin diagram, p_f (b).

teraction can be described perturbatively by dressing the lowest order diagrams in fig. 2.5 with gluons.

When traveling over a distance of order $1/\Lambda_{\text{QCD}}$, however, quarks and gluons hadronize and QCD becomes non-perturbative. Therefore the physics from different length scales, or, equivalently, from different energy scales must be treated differently. One theoretical tool for this is the OPE [30]. Schematically the decay amplitude $\mathcal{M}$ is expressed as

$$\mathcal{M} = -\frac{4G_{\text{F}}}{\sqrt{2}} V \sum_j C_j(\mu) \langle \text{f}| O_j(\mu) |B\rangle \left[1 + \mathcal{O}\left(\frac{m_b^2}{M_W^2}\right)\right], \tag{2.9}$$

where μ is a renormalization scale. Physics from distances shorter than μ^{-1} is contained in the Wilson coefficients C_j , and physics from distances longer than μ^{-1} is accounted for by the hadronic matrix elements $\langle \text{f}| O_j(\mu) |B\rangle$ of the local operators O_j. In principle, there are infinitely many terms in the OPE, but higher dimension operators yield contributions suppressed by powers of m_b^2/M_W^2.

All dependence on heavy masses $M \gg \mu$ such as m_t, M_W or the masses of new undiscovered heavy particles is contained in C_j . By convention one factors out $4G_{\text{F}}/\sqrt{2}$ and the CKM factors, which are denoted by V in eq. 2.9. On the other hand, the matrix element $\langle \text{f}| O_j(\mu) |B\rangle$ contains information from scales, such as Λ_{QCD}, that are below μ. Therefore, they can only be evaluated using non-perturbative methods such as lattice calculations, QCD sum rules, or by using related processes to obtain them from experimental data.

An important feature of the OPE in eq. 2.9 is the universality of the coefficients C_j; they are independent of the external states, *i. e.*, their numerical value is the same for all final states f. Therefore one can view the C_j 's as effective coupling constants and

the O_j 's as the corresponding interaction vertexes. Thus one can introduce the *effective Hamiltonian* that changes the bottom quantum number B by one unit:

$$\mathcal{H}^{|\Delta B|=1} = \frac{4G_F}{\sqrt{2}} V \sum_j C_j O_j + \text{h.c.} \tag{2.10}$$

An amplitude calculated from $\mathcal{H}^{|\Delta B|=1}$ defined at a scale of order m_b, reproduces the corresponding SM result up to corrections of order m_b^2/M_W^2 as indicated in eq. 2.9. Hard QCD effects can be included perturbatively in the Wilson coefficients, *i. e.*, by calculating Feynman diagrams with quarks and gluons.

The set of operators O_j needed in eq. 2.10 depends on the flavor structure of the physical process under consideration. Pictorially the operators are obtained by contracting the lines corresponding to heavy particles in the Feynman diagrams to a point. *E. g.*, the tree level diagram involving the W boson in fig. 2.5 generates the operator O_2^c shown in fig. 2.6. The Hamiltonian for $\Delta B = 1$ and $\Delta C = \Delta S = 0$ transitions

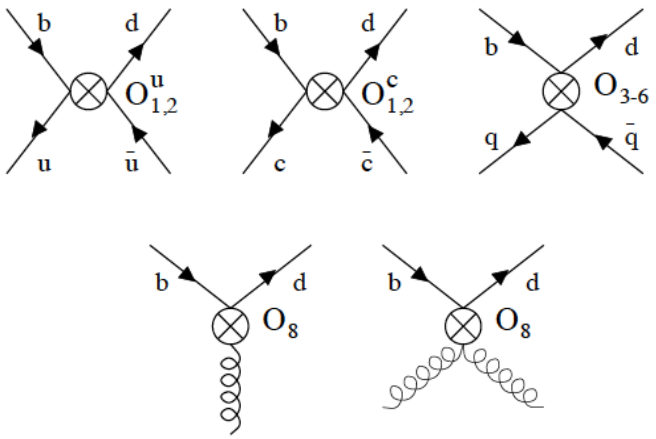

Figure 2.6: Effective operators of eq. 2.11. There are two types of fermion-gluon couplings associated with the chromomagnetic operator O_8.

must also accommodate for the so-called penguin diagram, shown in fig. 2.5.[5] The corresponding operator basis for a B_s decay reads:

$$\begin{aligned}
O_1^u &= \bar{s}_L^\alpha \gamma_\mu u_L^\beta \bar{u}_L^\beta \gamma^\mu b_L^\alpha, \\
O_2^u &= \bar{s}_L^\alpha \gamma_\mu u_L^\alpha \bar{u}_L^\beta \gamma^\mu b_L^\beta, \\
O_1^c &= \bar{s}_L^\alpha \gamma_\mu c_L^\beta \bar{c}_L^\beta \gamma^\mu b_L^\alpha, \\
O_2^c &= \bar{s}_L^\alpha \gamma_\mu c_L^\alpha \bar{c}_L^\beta \gamma^\mu b_L^\beta, \\
O_3 &= \sum_{q=u,d,s,c,b} \bar{s}_L^\alpha \gamma_\mu b_L^\alpha \bar{q}_L^\beta \gamma^\mu q_L^\beta, \\
O_4 &= \sum_{q=u,d,s,c,b} \bar{s}_L^\alpha \gamma_\mu b_L^\beta \bar{q}_L^\beta \gamma^\mu q_L^\alpha, \\
O_5 &= \sum_{q=u,d,s,c,b} \bar{s}_L^\alpha \gamma_\mu b_L^\alpha \bar{q}_R^\beta \gamma^\mu q_R^\beta, \\
O_6 &= \sum_{q=u,d,s,c,b} \bar{s}_L^\alpha \gamma_\mu b_L^\beta \bar{q}_R^\beta \gamma^\mu q_R^\alpha, \\
O_8 &= -\frac{g}{16\pi^2} m_b \bar{s}_L^\alpha \sigma^{\mu\nu} G_{\mu\nu}^a T^a b_R,
\end{aligned} \tag{2.11}$$

These operators are also depicted in fig. 2.6. In O_8, $G_{\mu\nu}^a$ is the chromomagnetic field strength tensor. The operators are grouped into classes, based on their origin: O_1 and O_2 are called *current-current operators*, O_3 through O_6 are called *four-quark penguin operators*, and O_8 is called the *chromomagnetic penguin operator*.

The operators in eq. 2.11 arise from the lowest order in the electroweak interaction, *i. e.*, diagrams involving a single W bosons plus QCD corrections to it. In some cases, especially when isospin breaking plays a role, one also needs to consider penguin diagrams which are of higher order in the electroweak fine structure constant α_{ew}. They give rise to the electroweak penguin operators:

$$\begin{aligned}
O_7 &= -\frac{e}{16\pi^2} m_b \bar{s}_L^\alpha \sigma^{\mu\nu} F_{\mu\nu} b_R^\alpha, \\
O_7^{\text{ew}} &= \frac{3}{2} \sum_{q=u,d,s,c,b} e_q \bar{s}_L^\alpha \gamma_\mu b_L^\alpha \bar{q}_R^\beta \gamma^\mu q_R^\beta, \\
O_8^{\text{ew}} &= \frac{3}{2} \sum_{q=u,d,s,c,b} e_q \bar{s}_L^\alpha \gamma_\mu b_L^\beta \bar{q}_R^\beta \gamma^\mu q_R^\alpha, \\
O_9^{\text{ew}} &= \frac{3}{2} \sum_{q=u,d,s,c,b} e_q \bar{s}_L^\alpha \gamma_\mu b_L^\alpha \bar{q}_L^\beta \gamma^\mu q_L^\beta, \\
O_{10}^{\text{ew}} &= \frac{3}{2} \sum_{q=u,d,s,c,b} e_q \bar{s}_L^\alpha \gamma_\mu b_L^\beta \bar{q}_L^\beta \gamma^\mu q_L^\alpha,
\end{aligned} \tag{2.12}$$

Here $F^{\mu\nu}$ is the electromagnetic field strength tensor, and e_q denotes the charge of quark q.

Hence the $\Delta B = 1$ and $\Delta C = \Delta S = 0$ Hamiltonian reads:

$$\mathcal{H}^{|\Delta B|=1} = \frac{4G_F}{\sqrt{2}} \left[\sum_{j=1}^{2} C_j \left(\xi_u O_j^u + \xi_c O_j^c \right) - \xi_t \sum_{j=3}^{8} C_j O_j - \xi_t \sum_{j=7}^{10} C_j^{\text{ew}} O_j \right] + \text{h.c.}, \tag{2.13}$$

where

$$\xi_q = V_{qb}^\star V_{qs} \tag{2.14}$$

5 C and S are the charmness and the strangeness quantum number, respectively.

Note that $\xi_u + \xi_c + \xi_t = 0$ by unitarity of the CKM matrix.

The operators introduced above are sufficient to describe non-leptonic transitions in the SM to order G_F. In extensions of the SM, on the other hand, the short distance structure can be very different. Additional operators with new Dirac structures, whose standard Wilson coefficients vanish, could enter the effective Hamiltonian. A list of these operators can be found in [37].

2.3 MIXING AND CP VIOLATION IN NEUTRAL B MESONS

The neutral B mesons, B_d and B_s, spontaneously transform into their own antiparticles and back. This phenomenon is called mixing (or flavor oscillation). The oscillation frequency has been measured in the B^0-$\bar{B}^0$ system to be about $0.507(5)\,\mathrm{ps}^{-1}$ [36] and in the B_s-$\bar{B}_s$ system to be $17.77(10)_{\mathrm{stat}}(07)_{\mathrm{syst}}\,\mathrm{ps}^{-1}$ [38]. The formalism that we are going to present for the mixing description can be applied both to the B_d-$\bar{B}_d$ and to the B_s-$\bar{B}_s$ system. Thus, first, we choose to use the notation B_q, where $q = d$ or s, properly pointing out the differences of the parameters, where necessary.

In the SM B_q-$\bar{B}_q$ mixing is caused by the fourth order flavor-changing weak interaction described by the box diagrams in fig. 2.7. Such transitions are called $|\Delta B| = 2$ transitions, because they change the bottom quantum number B by two units. In the SM $|\Delta B| = 2$ transition amplitudes are small, so measurements involving B_q-$\bar{B}_q$ mixing could easily be sensitive to new physics.

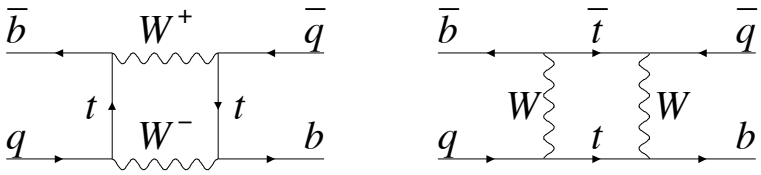

Figure 2.7: Dominant box diagrams for the $B_q^0 \to \bar{B}_q^0$ transitions ($q = d$ or s). Similar diagrams exist where one or both t quarks are replaced with c or u quarks.

An initially produced B_q (or $\bar{B}_q$) evolves in time into a superposition of B_q and $\bar{B}_q$. Let $|B_q(t)\rangle$ denote the state of a meson produced as a B_q at time $t = 0$, with an analogous definition for $|\bar{B}_q(t)\rangle$. The time evolution of these states is governed by the Schrödinger equation:

$$i\frac{d}{dt}\begin{pmatrix}|B_q(t)\rangle\\ |\bar{B}_q(t)\rangle\end{pmatrix} = \left(M - i\frac{\Gamma}{2}\right)\begin{pmatrix}|B_q(t)\rangle\\ |\bar{B}_q(t)\rangle\end{pmatrix} \tag{2.15}$$

with the mass matrix $M = M^\dagger$ and the decay matrix $\Gamma = \Gamma^\dagger$. [6] They are 2×2 time-independent matrices, whose off-diagonal elements, $M_{12} = M_{21}^\star$ and $\Gamma_{12} = \Gamma_{21}^\star$, correspond to B_q-$\bar{B}_q$ mixing. CPT invariance implies that $M_{11} = M_{22}$ and $\Gamma_{11} = \Gamma_{22}$.

The mass eigenstates at time $t = 0$, $|B_L\rangle$ and $|B_H\rangle$, are linear combinations of $|B_q\rangle$ and $|\bar{B}_q\rangle$:

$$\text{lighter eigenstate:} \qquad |B_L\rangle = p\,|B_q\rangle + q\,|\bar{B}_q\rangle\,, \tag{2.16a}$$

$$\text{heavier eigenstate:} \qquad |B_H\rangle = p\,|B_q\rangle - q\,|\bar{B}_q\rangle\,, \tag{2.16b}$$

6 The Schrödinger equation is not exactly valid, but the result of the so-called Wigner-Weisskopf approximation to the decay problem. In general, there are tiny corrections to the exponential decay laws at very short and very large times. These corrections are irrelevant for the mixing and CP studies at Run II, but they must be taken into account in high precision searches for CPT violation [30].

with $|p|^2 + |q|^2 = 1$. We denote the masses and widths of the two eigenstates with $M_{\mathrm{H,L}}$ and $\Gamma_{\mathrm{H,L}}$ and define

$$\Delta m = M_{\mathrm{H}} - M_{\mathrm{L}}\,, \tag{2.17a}$$

$$\Gamma = \frac{1}{\tau_B} = \frac{\Gamma_{\mathrm{L}} + \Gamma_{\mathrm{H}}}{2}\,, \tag{2.17b}$$

$$\Delta\Gamma = \Gamma_{\mathrm{L}} - \Gamma_{\mathrm{H}}. \tag{2.17c}$$

While $\Delta m > 0$ by definition, $\Delta\Gamma$ can have either sign. Our sign convention is such that $\Delta\Gamma > 0$ in the SM.

The SM predicts that for the B_d-$\bar{B}_d$ system $\Delta\Gamma_d/\Gamma_d$ is very small (below 1%), and for the B_s-$\bar{B}_s$ system $\Delta\Gamma_s/\Gamma_s$ is considerably larger (order of 10%). These width differences are caused by the existence of final states to which both the B_q^0 and $\bar{B}_q^0$ mesons can decay. Such decays involve $b \to c\bar{c}q$ quark-level transitions, which are Cabibbo suppressed if $q = d$ and Cabibbo-allowed if $q = s$. Direct time-dependent studies published by Delphi [39] and BaBar [40] can be combined to yield $|\Delta\Gamma_d/\Gamma_d| = 0.010 \pm 0.037$ [36]. Thus, in all formulae, terms containing $\Delta\Gamma_d$ can be neglected for the B_d-$\bar{B}_d$ system, but not for the B_s-$\bar{B}_s$. For these reason, in the following we prefer to refer to B_s mesons only, putting $q = s$ everywhere.

The last update results [36] for B_s meson are:

$$\Delta\Gamma_s = 0.062^{+0.034}_{-0.037}\,\mathrm{ps}^{-1} \tag{2.18a}$$

$$\frac{\Delta\Gamma_s}{\Gamma_s} = 0.092^{+0.051}_{-0.054} \tag{2.18b}$$

$$\tau_{\mathrm{L}} = \frac{1}{\Gamma_{\mathrm{L}}} = 1.408^{+0.033}_{-0.030}\,\mathrm{ps} \tag{2.18c}$$

$$\tau_{\mathrm{H}} = \frac{1}{\Gamma_{\mathrm{H}}} = 1.543^{+0.058}_{-0.060}\,\mathrm{ps} \tag{2.18d}$$

The time evolution of the mass eigenstates is governed by the two eigenvalues $M_{\mathrm{L,H}} - i\Gamma_{\mathrm{L,H}}$, *i. e.*,

$$|B_{\mathrm{L,H}}(t)\rangle = e^{-(iM_{\mathrm{L,H}} - \Gamma_{\mathrm{L,H}}/2)t}\,|B_{\mathrm{L,H}}\rangle \tag{2.19}$$

where $|B_{\mathrm{L,H}}\rangle = |B_{\mathrm{L,H}}(t=0)\rangle$. Now we can easily find the time evolution of $|B_s(t)\rangle$ and $|\bar{B}_s(t)\rangle$, using eq. 2.16 and eq. 2.19:

$$|B_s(t)\rangle = g_+(t)\,|B_s\rangle + \frac{q}{p} g_-(t)\,|\bar{B}_s\rangle \tag{2.20a}$$

$$|\bar{B}_s(t)\rangle = \frac{p}{q} g_-(t)\,|B_s\rangle + g_+(t)\,|\bar{B}_s\rangle\,, \tag{2.20b}$$

where

$$g_+(t) = e^{-imt}e^{-\Gamma t/2}\left[\cosh\frac{\Delta\Gamma t}{4}\cos\frac{\Delta m t}{2} - i\sinh\frac{\Delta\Gamma t}{4}\sin\frac{\Delta m t}{2}\right] \tag{2.21a}$$

$$g_-(t) = e^{-imt}e^{-\Gamma t/2}\left[-\sinh\frac{\Delta\Gamma t}{4}\cos\frac{\Delta m t}{2} + i\cosh\frac{\Delta\Gamma t}{4}\sin\frac{\Delta m t}{2}\right]. \tag{2.21b}$$

Note that the coefficient $g_+(t)$ has no zeros, and $g_-(t)$ vanishes only at $t = 0$. Hence an initially produced B_s will never turn into a pure $\bar{B}_s$ or back into a pure B_s. The

coefficients in eq. 2.21 will enter the formulae for the decay asymmetries in the combinations

$$|g_{\pm}(t)|^2 = \frac{e^{-\Gamma t}}{2}\left[\cosh\frac{\Delta\Gamma t}{2} \pm \cos\Delta m t\right] \tag{2.22a}$$

$$g_{+}^{\star}(t)g_{-}(t) = \frac{e^{-\Gamma t}}{2}\left[-\sinh\frac{\Delta\Gamma t}{2} + i\sin\Delta m t\right] \tag{2.22b}$$

By examining the eigenvalue problem of eq. 2.15 one finds that the experimental information model-independently implies $|\Gamma_{12}| \ll |M_{12}|$. By expanding the eigenvalues and q/p in Γ_{12}/M_{12}, one finds

$$\Delta m = 2|M_{12}|\,, \tag{2.23}$$

$$\Delta\Gamma = 2|\Gamma_{12}|\cos\phi_{\mathrm{V}}\,, \tag{2.24}$$

$$\frac{q}{p} = -e^{-i\phi_{\mathrm{M}}}\left[1 - \frac{a}{2}\right]. \tag{2.25}$$

Here the phase ϕ_{V} is defined as

$$\frac{M_{12}}{\Gamma_{12}} = -\left|\frac{M_{12}}{\Gamma_{12}}\right| e^{i\phi_{\mathrm{V}}} \tag{2.26}$$

and the mixing phase ϕ_{M} is

$$\phi_{\mathrm{M}} = \arg M_{12} \tag{2.27}$$

In eq. 2.25 we have kept a correction in the small parameter

$$a = \left|\frac{\Gamma_{12}}{M_{12}}\right| \sin\phi_{\mathrm{V}} \tag{2.28}$$

but neglected all terms of order Γ_{12}^2/M_{12}^2. The phase ϕ_{V} is physical and convention-independent; if $\phi_{\mathrm{V}} = 0$, CP violation in mixing vanishes. Γ_{12} is dominated by the real $b \to c\bar{c}s$ transition, which is a CKM-favoured tree-level decays: it is practically insensitive to new physics. On the other hand, M_{12} is almost completely induced by short-distance physics. Within the SM the top quarks give the dominant contribution to B_s-$\bar{B}_s$ mixing. This contribution is suppressed by four powers of the weak coupling constant and two powers of $|V_{ts}| \simeq 0.04$. Hence new physics can easily compete with the SM and possibly even dominate M_{12}. If the non-standard contributions to M_{12} are unrelated to the CKM mechanism of the three-generation SM, they will affect the mixing phase ϕ_{M}.

The SM prediction is $\phi_{\mathrm{M}} = \arg(V_{tb}V_{ts}^{\star})^2$ [41]. For the B_d-$\bar{B}_d$ system the large value of $\phi_{\mathrm{M}} = \arg(V_{tb}V_{td}^{\star})^2$ allows for the observation of the indirect CP-violation, with the measurement of the quantity $\sin 2\beta = 0.681 \pm 0.025$ [36].

Decay Rate

The time-dependent decay rate of an initially tagged B_s into some final state f is defined as

$$\Lambda(B_s(t) \to \mathrm{f}) = \frac{1}{N_B}\frac{dN(B_s(t) \to \mathrm{f})}{dt} \tag{2.29}$$

where $dN(B_s(t) \to \mathrm{f})$ denotes the number of decays of a B_s meson at time t into the final state f occurring within the time interval between t and $t + dt$. N_B is the

total number of B_s's produced at time $t = 0$. An analogous definition holds for $dN(\bar{B}_s(t) \to \mathrm{f})$ of an initially tagged $\bar{B}_s$ into the same previous final state f. One has

$$\Lambda(B_s(t) \to \mathrm{f}) = \mathcal{N}_\mathrm{f} \left| \langle \mathrm{f}|B_s(t)\rangle \right|^2 \text{ and } \Lambda(\bar{B}_s(t) \to \mathrm{f}) = \mathcal{N}_\mathrm{f} \left| \langle \mathrm{f}|\bar{B}_s(t)\rangle \right|^2 \tag{2.30}$$

Here $\mathcal{N}_\mathrm{f}$ is a time-independent normalization factor. To calculate $dN(B_s(t) \to \mathrm{f})$ we introduce the two decay amplitudes

$$A_\mathrm{f} = \langle \mathrm{f}|B_s\rangle \text{ and } \bar{A}_\mathrm{f} = \langle \mathrm{f}|\bar{B}_s\rangle \tag{2.31}$$

and the key quantity for CP violation

$$\lambda_\mathrm{f} = \frac{q}{p}\frac{\bar{A}_\mathrm{f}}{A_\mathrm{f}} \simeq -e^{-i\phi_\mathrm{M}}\frac{\bar{A}_\mathrm{f}}{A_\mathrm{f}}\left[1 - \frac{a}{2}\right] \tag{2.32}$$

We will see in the following sections that λ_f plays the pivotal role in CP asymmetries and other observables in B mixing. Finally with eq. 2.20, eq. 2.22 and $|p/q|^2 = (1+a)$ we find the desired formulae for the decay rates:

$$\begin{aligned}
\Lambda(B_s(t) \to \mathrm{f}) =& \mathcal{N}_\mathrm{f}|A_\mathrm{f}|^2 e^{-\Gamma t} \\
& \left[\frac{1+|\lambda_\mathrm{f}|^2}{2}\cosh\frac{\Delta\Gamma t}{2} + \frac{1-|\lambda_\mathrm{f}|^2}{2}\cos(\Delta m t) - \right. \\
& \left. - \Re\lambda_\mathrm{f}\sinh\frac{\Delta\Gamma t}{2} - \Im\lambda_\mathrm{f}\sin(\Delta m t)\right] \\
\Lambda(\bar{B}_s(t) \to \mathrm{f}) =& \mathcal{N}_\mathrm{f}|A_\mathrm{f}|^2 e^{-\Gamma t}(1+a) \\
& \left[\frac{1+|\lambda_\mathrm{f}|^2}{2}\cosh\frac{\Delta\Gamma t}{2} - \frac{1-|\lambda_\mathrm{f}|^2}{2}\cos(\Delta m t) - \right. \\
& \left. - \Re\lambda_\mathrm{f}\sinh\frac{\Delta\Gamma t}{2} + \Im\lambda_\mathrm{f}\sin(\Delta m t)\right].
\end{aligned} \tag{2.33}$$

Since B_s's and $\bar{B}_s$'s are produced in equal numbers at the Tevatron, the untagged decay rate for the decay $B \to \mathrm{f}$ reads

$$\begin{aligned}
\Lambda[\mathrm{f}, t] &= \Lambda(B_s(t) \to \mathrm{f}) + \Lambda(\bar{B}_s(t) \to \mathrm{f}) = \\
&= \mathcal{N}_\mathrm{f}|A_\mathrm{f}|^2(1+|\lambda_\mathrm{f}|^2)e^{-\Gamma t}\left[\cosh\frac{\Delta\Gamma t}{2} + A_{\Delta\Gamma}\sinh\frac{\Delta\Gamma t}{2}\right] + \mathcal{O}(a)
\end{aligned} \tag{2.34}$$

with

$$A_{\Delta\Gamma} = -\frac{2\Re\lambda_\mathrm{f}}{1+|\lambda_\mathrm{f}|^2} \tag{2.35}$$

From this equation one can see that untagged samples are interesting for the determination of $|\Delta\Gamma|$. Once $|\Delta\Gamma|$ is known, eq. 2.34 allows for the measurement of $\Re\lambda_\mathrm{f}$. Moreover, for decays whose final states are two vector mesons (see next section), eq. 2.34 provides $\Im\lambda_\mathrm{f}$ from the interference of CP-even and CP-odd terms. Finally we write down a more intuitive expression for $\Lambda[\mathrm{f}, t]$. From eq. 2.30 and eq. 2.20 one immediately finds

$$\Lambda[\mathrm{f}, t] = \mathcal{N}_\mathrm{f}\left[e^{-\Gamma_\mathrm{L} t}\left|\langle \mathrm{f}|B_\mathrm{L}\rangle\right|^2 + e^{-\Gamma_\mathrm{H} t}\left|\langle \mathrm{f}|B_\mathrm{H}\rangle\right|^2\right] + \mathcal{O}(a) \tag{2.36}$$

With eq. 2.16 one recovers eq. 2.36 from eq. 2.34. Now eq. 2.36 nicely shows that the decay of the untagged sample into some final state f is governed by two exponentials. If B_s mixing is correctly described by the SM, the mass eigenstates are to a high precision also CP eigenstates and eq. 2.36 proves useful for the description of decays into CP eigenstates.

CP *Violation*

For decays of B_s to a CP eigenstate, new physics can manifest itself in CP violation arising from the interference between decay amplitudes with and without mixing, which can be probed by measuring the time-dependent CP asymmetry

$$a_{\mathsf{CP}}(t) = \frac{\Lambda(B_s(t) \to \mathrm{f}) - \Lambda(\bar{B}_s(t) \to \mathrm{f})}{\Lambda(B_s(t) \to \mathrm{f}) + \Lambda(\bar{B}_s(t) \to \mathrm{f})} = \frac{A^{\mathrm{dir}} \cos(\Delta m t) + A^{\mathrm{mix}} \sin(\Delta m t)}{\cosh \frac{\Delta\Gamma t}{2} - A_{\Delta\Gamma} \sinh \frac{\Delta\Gamma t}{2}} \tag{2.37}$$

The CP asymmetries are:

$$A_{\mathsf{CP}}^{\mathrm{dir}} = \frac{1 - |\lambda_{\mathrm{f}}|^2}{1 + |\lambda_{\mathrm{f}}|^2} \tag{2.38a}$$

$$A_{\mathsf{CP}}^{\mathrm{mix}} = -\frac{2\Im\lambda_{\mathrm{f}}}{1 + |\lambda_{\mathrm{f}}|^2} \tag{2.38b}$$

$$A_{\Delta\Gamma} \text{ defined in eq. 2.35} \tag{2.38c}$$

which obey the relation

$$|A_{\mathsf{CP}}^{\mathrm{dir}}|^2 + |A_{\mathsf{CP}}^{\mathrm{mix}}|^2 + |A_{\Delta\Gamma}|^2 = 1. \tag{2.39}$$

If f is a CP eigenstate, $\mathsf{CP}\,|\mathrm{f}\rangle = \pm\,|\mathrm{f}\rangle$, then $A_{\mathsf{CP}}^{\mathrm{dir}} \neq 0$ or $A_{\mathsf{CP}}^{\mathrm{mix}} \neq 0$ signals CP violation:

- a non-vanishing $A_{\mathsf{CP}}^{\mathrm{dir}}$ implies $A_{\mathrm{f}} \neq \bar{A}_{\mathrm{f}}$, meaning direct CP violation;
- $A_{\mathsf{CP}}^{\mathrm{mix}}$ measures mixing-induced CP violation in the interference of $B_s \to \mathrm{f}$ and $\bar{B}_s \to \mathrm{f}$;
- $A_{\Delta\Gamma}$ plays a role, if $\Delta\Gamma$ is sizable, as we saw in eq. 2.34.

The interesting quantity is the a_{CP} of eq. 2.37. However, in practical terms experiments are always limited by statistics for the study of intrinsically rare processes. A pragmatic estimate of CP violation is actually the "number of B mesons needed", $\mathcal{N}_B$, to measure a particular CP-violating rate asymmetry. Given the branching ratio (R) for the process of interest, the number of events N is clearly $N = \mathcal{N}_B R$.[7] To discern an asymmetry a_{CP} at the σ significance level with only statistical errors, one defines that the number of B mesons needed to demonstrate the asymmetry is [42]

$$\mathcal{N}_B \simeq \frac{\sigma^2}{R\epsilon a_{\mathsf{CP}}^2} \tag{2.40}$$

where ϵ is the experimental efficiency (of the trigger and the reconstruction). In the ideal situation of $\epsilon = 1$, with $R \lesssim 10^{-5}$ for B_s, if you want a_{CP} with a relative errors of about 1%, you need $\mathcal{N}_B \gtrsim 10^4$ recontructed mesons. Note that if one goes to larger asymmetries, one usually suffers a loss in R (rarer modes) and vice versa.

7 R is the branching ratio of the entire decay chain; for example for the decay $B_s \to J/\psi\phi \to [\mu^+\mu^-][K^+K^-]$ one have to consider $R = R(B_s \to J/\psi\phi)R(J/\psi\phi \to \mu^+\mu^-)R(\phi \to K^+K^-)$.

SM Expectation and New Physics

In the SM, the phase can be expressed in terms of the CKM matrix elements that contribute to the respective mixing and decay diagrams:

$$\begin{aligned}\phi_V &= \phi_M - \phi_\Gamma = \\ &= \arg(V_{tb}V_{ts}^\star)^2 - \arg(-\Gamma_{12}) \simeq \arg(V_{tb}V_{ts}^\star)^2 - \arg(V_{cb}V_{cs}^\star)^2\end{aligned} \tag{2.41}$$

Because $\arg(V_{tb}V_{ts}^\star) \simeq \arg(V_{cb}V_{cs}^\star)$ and the remaining corrections to $\arg(-\Gamma_{12})$ involving $V_{ub}V_{us}^\star$ are small because suppressed by a factor m_c^2/m_b^2, ϕ_V^{SM} is predicted to be very small [8]:

$$\phi_V^{SM} = 0.0041 \pm 0.0008. \tag{2.42}$$

Traditionally, the phase β_s, defined as the phase of λ_f in the $b \to c\bar{c}s$ transition,is associated with CP violation in the B_s system, as it is the angle $\arg(-V_{cd}V_{cb}^\star/V_{tb}^\star V_{ts})$ of the B_s unitarity triangle. The phase β_s is predicted by the SM to be equal to $\beta_s^{SM} = 0.04 \pm 0.01$ [43]. In the hypothesis of the presence of new physics we can relate β_s and ϕ_V in the following manner. First, we define SM and new physics (NP) contributions to ϕ_V. With the phase conventions we have chosen, the NP contribution to ϕ_V and β_s is:

$$\phi_V = \phi_V^{SM} + \phi_V^{NP} \text{ and } 2\beta_s = 2\beta_s^{SM} - \phi_V^{NP} \tag{2.43}$$

Since both β_s^{SM} and ϕ_V^{SM} are expected to be negligibly small, in the presence of new physics, we neglect the SM contribution, and use the shorthand

$$2\beta_s \simeq -\phi_V^{NP}, \quad \phi_V \simeq \phi_V^{NP} \tag{2.44}$$

2.4 THE $P \to VV$ DECAY: ANGULAR DISTRIBUTIONS

The nomenclature $P \to VV$ stands for the class of the decays of a Pseudoscalar meson (with $J^P = 0^-$), like the B, into two Vector mesons ($J \neq 0$). The angular distribution of the B meson decay to two mesons with non-zero spin is of special interest because it is sensitive to quark-spin alignment in decay transition, and reflects both weak- and strong-interaction dynamics.

Most B-decay polarization analyses are limited to the case when the spin of the B-meson daughters is 1. In that case, there are only three independent amplitudes a, b and c, corresponding to the probability that the B_s meson decays in a state with one of the three possible relative angular momenta: if L is the relative angular momentum of the two vector mesons, with two spin 1 particles one can have $L = 0$, 1, 2 to obtain the spin 0 of the initial state.

The overall decay amplitude would involve three complex terms proportional to the above amplitude. The exact angular dependence would depend on the quantum numbers of the B-meson daughters and of their decay products. The most general covariant amplitude for a B meson with four-momentum p decaying into a pair of vector mesons V_1 and V_2 (with four-momentum k and q respectively) takes the form

$$\Lambda(B_s \to V_1(k)V_2(q)) = \lambda_1^{\star\mu}\lambda_2^{\star\nu}\left(ag_{\mu\nu} + \frac{b}{m_1 m_2}p_\mu p_\nu + i\frac{c}{m_1 m_2}\varepsilon^{\mu\nu\alpha\beta}k_\alpha q_\beta\right) \tag{2.45}$$

where, λ_1, λ_2 and m_1, m_2 represent the polarization vectors and masses of the vector mesons, respectively. Now we have to understand how these invariant amplitudes a, b, and c are related with the observables that we can measure. Some calculations are necessary: they are described in the following.

The starting point to obtain our observables is the definition of an appropriate reference frame. In this frame the variables necessary to the description of the process are identified as the kinematics degrees of freedom of the system. Let's refer to the B meson as the parent (or as the initial state) and to the two vector mesons as daughter particles (V_1 and V_2), and to their decay products as final state particles (P_1, P_2 from V_1, and P_3, P_4 from V_2).[8]

Each of the four final state particles has four kinematic degrees of freedom (the four components of the particle four-momentum). There are seven particles of well defined mass in the decay, which provide seven constraints from the relation between the four momentum and the invariant mass. In addition, since the entire system is translation and rotation invariant, the vector momentum of the parent B meson is irrelevant to the decay process, as well as the orientation of the decay with respect to the laboratory frame is. The former removes three degrees of freedom in the form of the vector momentum components of the B meson, while the latter removes three more in the form of Euler rotation angles of the decay frame with respect to the laboratory one. This leaves us with $16 - 7 - 3 - 3 = 3$ degrees of freedom in the decay. These remaining degrees of freedom are the angles at which the final state particles are produced. There are two standard choices we can make to define the three decay angles we wish to measure: the helicity and the transversity formalisms.[9] They are described in the following subsections.

2.4.1 Helicity Basis

In the helicity basis, the three decay angles form the vector [10]

$$\vec{\omega} = (\vartheta_1, \vartheta_2, \Phi). \tag{2.46}$$

We define ϑ_1 (ϑ_2) and Φ_1 (Φ_2) as the polar and azimuthal angles of the $P_1(P_3)$ three-momentum vector defined in the rest frame of their mother $V_1(V_2)$; the $z'(z'')$ axis is defined as the direction of the $V_1(V_2)$ momentum in the rest frame of the B_s; the $x'(x'')$ axis is an arbitrarily chosen direction in the plane normal to the $z'(z'')$ axis and the and $x'(x'')$ axes are defined to be opposite in direction to each other; then the y' and y'' axes are fixed uniquely. The Φ angle is the angle between the decay planes of the two daughter particles, given by $\Phi = \Phi_1 + \Phi_2$. These angles are shown in fig. 2.8.

With these definitions, it is customary to express the angular distributions in terms of the *helicity amplitudes*

$$H_\lambda = \langle V_1(\lambda) V_2(\lambda) | \, \mathcal{H}^{\text{eff}} \, | B_s \rangle \tag{2.47}$$

for $\lambda = 0, \pm 1$ (in the B rest frame $\lambda_1 = \lambda_2 = \lambda$). Note that $|H_0|^2 + |H_+|^2 + |H_-|^2 = 1$. The relations between the helicity and the invariant amplitudes are

$$H_0 = -au - b(u^2 - 1) \tag{2.48a}$$

$$H_\pm = -a \pm \sqrt{u^2 - 1}c \tag{2.48b}$$

where $u = p_1 p_2 / m_1 m_2$.

8 Fix the following convention: if the final states are charged particles, P_1 and P_3 are the positive charged ones.

9 There is also a third formalism, using partial wave definition as in the atomic spectroscopy; it is not presented here because we don't use it.

10 ω is not a vector in the proper sense: it is a convenient shorthand for an object with three components.

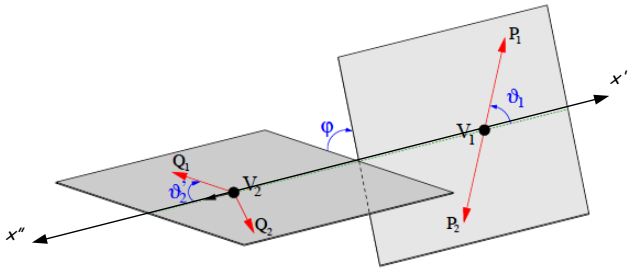

Figure 2.8: Definitions of the helicity angles $\vec{\omega} = (\vartheta_1, \vartheta_2, \Phi)$ for a general $P \to V_1 V_2$ decay. We identify $B_s \to \phi\phi \to [K^+K^-][K^+K^-]$ with $P \to V_1 V_2 \to [P_1 P_2][Q_1 Q_2]$.

In general, the explicit form of the angular distribution depends on the spin of the decay products of the two vector mesons. If the decay has pseudoscalar mesons in the final state, the normalized angular distribution is:

$$\begin{aligned}\frac{1}{\Gamma}\frac{d^3\Lambda}{d\vec{\omega}} = \frac{9}{8\pi}\Bigg[&\frac{1}{4}\frac{\Gamma_T}{\Gamma}\sin^2\vartheta_1\sin^2\vartheta_2 + \frac{\Gamma_L}{\Gamma}\cos^2\vartheta_1\cos^2\vartheta_2 + \\ &+ \frac{1}{4}\sin 2\vartheta_1 \sin 2\vartheta_2(\alpha_1\cos\Phi - \beta_1\sin\Phi) + \\ &+ \frac{1}{2}\sin^2\vartheta_1\sin^2\vartheta_2(\alpha_2\cos 2\Phi - \beta_2\sin 2\Phi)\Bigg]\end{aligned} \tag{2.49}$$

where

$$\begin{aligned}\frac{\Gamma_T}{\Gamma} &= \frac{|H_+|^2 + |H_-|^2}{|H_0|^2 + |H_+|^2 + |H_-|^2} \\ \frac{\Gamma_L}{\Gamma} &= \frac{|H_0|^2}{|H_0|^2 + |H_+|^2 + |H_-|^2} \\ \alpha_1 &= \frac{\Re(H_+ H_o^\star + H_- H_0^\star)}{|H_0|^2 + |H_+|^2 + |H_-|^2} \\ \beta_1 &= \frac{\Im(H_+ H_o^\star + H_- H_0^\star)}{|H_0|^2 + |H_+|^2 + |H_-|^2} \\ \alpha_2 &= \frac{\Re(H_+ H_-^\star)}{|H_0|^2 + |H_+|^2 + |H_-|^2} \\ \beta_2 &= \frac{\Im(H_+ H_-^\star)}{|H_0|^2 + |H_+|^2 + |H_-|^2}\end{aligned} \tag{2.50}$$

2.4.2 Transversity Basis

To obtain the advantage of more easily extracting the CP-odd and CP-even components, the angular distribution is often written in the *linear polarization* basis, which is defined in the following form

$$\Lambda(B_s \to V_1 V_2) = A_0 \frac{\lambda_1^{\star L}\lambda_2^{\star L}}{u} - A_{\parallel}\frac{\lambda_1^{\star T}\cdot\lambda_2^{\star T}}{\sqrt{2}} - iA_{\perp}\frac{(\lambda_1^{\star}\times\lambda_2^{\star})\cdot\hat{p}_2}{\sqrt{2}} \tag{2.51}$$

where u has been previously defined and $\hat{p}_2$ is the unit vector along the V_2 motion direction in the V_1 rest frame. The symbols λ_i^L represent the longitudinal components of the polarization vectors ($\lambda_1^L = \lambda_1 \cdot \vec{k}/|\vec{k}|$, $\lambda_2^L = \lambda_2 \cdot \vec{q}/|\vec{q}|$), while λ_i^T are the transverse component, $\lambda_i^T = \lambda_i - \lambda_i^L$. The transversity amplitudes A_0, $A_{\parallel}$ and $A_{\perp}$ are related to the helicity ones by

$$A_0 = H_0, \tag{2.52a}$$

$$A_{\parallel} = \frac{H_+ + H_-}{\sqrt{2}} \tag{2.52b}$$

$$A_{\perp} = \frac{H_+ - H_-}{\sqrt{2}} \tag{2.52c}$$

and the unitarity relation $|A_0|^2 + |A_{\parallel}|^2 + |A_{\perp}|^2 = 1$ is still valid. These amplitudes are often referred to as *polarization amplitudes*.

In the rest frame of V_1, V_2 moves in the x direction, and the z axis is perpendicular to the decay plane of $V_2 \to P_3P_4$ and we assume that the y-component of the P_3 three-momentum is non-negative. (Θ, Φ) are the angular coordinates of P_1 and Ψ is that of P_2, both in the rest frame of V_1 (see fig. 2.9). Then, the three transversity angles form the angles vector:

$$\vec{\Omega} = (\Theta, \Psi, \Phi). \tag{2.53}$$

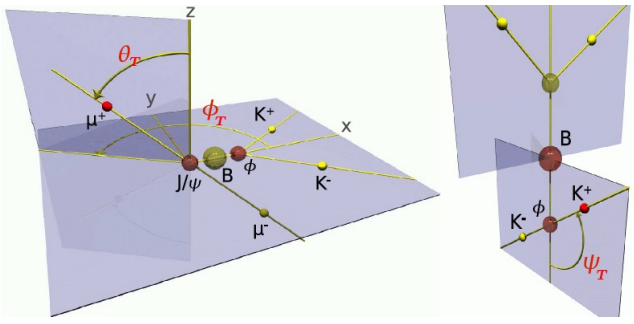

Figure 2.9: Definitions of the transversity angles.

The normalized differential decay rate in terms of the transversity amplitudes is given by

$$\begin{aligned}\frac{1}{\Gamma}\frac{d^3\Lambda}{d\vec{\Omega}} = \frac{9}{8\pi}\Bigg[&\frac{\Gamma_L}{\Gamma}\cos^2\Psi\sin^2\Theta\cos^2\Phi + \frac{\Gamma_\perp}{2\Gamma}\sin^2\Psi\sin^2\Theta\sin^2\Phi + \\ &+ \frac{\Gamma_\parallel}{2\Gamma}\sin^2\Psi\sin^2\Theta - \frac{\zeta}{2\sqrt{2}}\sin 2\Psi\sin^2\Theta\sin 2\Phi - \\ &- \frac{\xi_1}{2}\sin^2\Psi\sin 2\Theta\sin\Phi + \frac{\xi_2}{2\sqrt{2}}\sin 2\Psi\sin 2\Theta\cos\Phi\Bigg],\end{aligned} \tag{2.54}$$

where

$$\begin{aligned}\frac{\Gamma_L}{\Gamma} &= \frac{|A_0|^2}{|A_0|^2+|A_\parallel|^2+|A_\perp|^2} \\ \frac{\Gamma_\perp}{\Gamma} &= \frac{|A_\perp|^2}{|A_0|^2+|A_\parallel|^2+|A_\perp|^2} \\ \frac{\Gamma_\parallel}{\Gamma} &= \frac{|A_\parallel|^2}{|A_0|^2+|A_\parallel|^2+|A_\perp|^2} \\ \zeta &= \frac{\Re(A_\parallel A_0^\star)}{|A_0|^2+|A_\parallel|^2+|A_\perp|^2} \\ \xi_1 &= \frac{\Im(A_\perp A_\parallel^\star)}{|A_0|^2+|A_\parallel|^2+|A_\perp|^2} \\ \xi_2 &= \frac{\Im(A_\perp A_0^\star)}{|A_0|^2+|A_\parallel|^2+|A_\perp|^2}\end{aligned} \tag{2.55}$$

2.4.3 $B_s \to \phi\phi$

We are ready to give the differential angular decay rate in a proper basis for the two specific decays that we are going to study, $B_s \to \phi\phi$ and $B_s \to J/\psi\phi$. Both are $P \to VV$ decays: remind that

$$J^P[B_s] = 0^- \quad , \quad J^{PC}[\phi] = 1^{--} \text{ and } J^{PC}[J/\psi] = 1^{--} \tag{2.56}$$

Let start with the main one: $B_s \to \phi\phi$. The daughters state is made of two particles that are identical bosons: we need to choose a basis in which the two K^+K^- pairs from the two ϕ's are treated symmetrically, in order to obey Bose statistics. The natural basis that satisfy this requirement comes from the helicity formalism. Then, we treat the $B_s \to \phi\phi$ decay using the three angles defined in eq. 2.46, $\vec{\omega} = (\vartheta_1, \vartheta_2, \Phi)$.

We mentioned before that the transversity basis has the advantage of a more easily treatment of the system CP properties. Since the final state in $B_s \to \phi\phi$ is an admixture of CP-even and CP-odd eigenstates, we can use eq. 2.52a to obtain the polarization amplitudes. The resulting differential angular decay rate can be written as

$$\frac{d^4\Lambda(\vec{\omega},t)}{dtd\vec{\omega}} = \frac{9}{32\pi}\sum_{i=1}^{6} K_i(t) f_i(\vec{\omega}) \tag{2.57}$$

where the angular functions $f_i(\vec{\omega})$ are given by

$$\begin{aligned} f_1(\vec{\omega}) &= 4\cos^2\vartheta_1\cos^2\vartheta_2 \\ f_2(\vec{\omega}) &= \sin^2\vartheta_1\sin^2\vartheta_2(1+\cos 2\Phi) \\ f_3(\vec{\omega}) &= \sin^2\vartheta_1\sin^2\vartheta_2(1-\cos 2\Phi) \\ f_4(\vec{\omega}) &= -2\sin^2\vartheta_1\sin^2\vartheta_2\sin 2\Phi \\ f_5(\vec{\omega}) &= \sqrt{2}\sin 2\vartheta_1\sin 2\vartheta_2\cos\Phi \\ f_6(\vec{\omega}) &= -\sqrt{2}\sin 2\vartheta_1\sin 2\vartheta_2\sin\Phi \end{aligned} \tag{2.58}$$

while the time-dependent functions $K_i(t)$ are defined as

$$\begin{aligned} K_1(t) =& \frac{1}{2}|A_0|^2\left[(1+cos\phi_V)e^{-\Gamma_L t}+(1-cos\phi_V)e^{-\Gamma_H t}+2e^{-\Gamma t}\sin(\Delta m t)\sin\phi_V\right] \\ K_2(t) =& \frac{1}{2}|A_\parallel|^2\left[(1+cos\phi_V)e^{-\Gamma_L t}+(1-cos\phi_V)e^{-\Gamma_H t}+2e^{-\Gamma t}\sin(\Delta m t)\sin\phi_V\right] \\ K_3(t) =& \frac{1}{2}|A_\perp|^2\left[(1-cos\phi_V)e^{-\Gamma_L t}+(1+cos\phi_V)e^{-\Gamma_H t}-2e^{-\Gamma t}\sin(\Delta m t)\sin\phi_V\right] \\ K_4(t) =& |A_\parallel||A_\perp|\left[e^{-\Gamma t}\Big(\sin\delta_1\cos(\Delta m t)-\cos\delta_1\sin(\Delta m t)\cos\phi_V\Big)-\right. \\ & \left.-\frac{1}{2}\left(e^{-\Gamma_H t}-e^{-\Gamma_L t}\right)\cos\delta_1\sin\phi_V\right] \\ K_5(t) =& \frac{1}{2}|A_0||A_\parallel|\cos(\delta_2-\delta_1) \\ & \left[(1+cos\phi_V)e^{-\Gamma_L t}+(1-cos\phi_V)e^{-\Gamma_H t}+2e^{-\Gamma t}\sin(\Delta m t)\sin\phi_V\right] \\ K_6(t) =& |A_0||A_\parallel|\left[e^{-\Gamma t}\Big(\sin\delta_2\cos(\Delta m t)-\cos\delta_2\sin(\Delta m t)\cos\phi_V\Big)-\right. \\ & \left.-\frac{1}{2}\left(e^{-\Gamma_H t}-e^{-\Gamma_L t}\right)\cos\delta_2\sin\phi_V\right] \end{aligned} \tag{2.59}$$

The time-dependent angular distribution for a $\bar{B}_s$ meson can be obtained by reversing the sign of the terms proportional to $\sin(\Delta m t)$ or $\cos(\Delta m t)$ in the $K_i(t)$ functions.

Assuming that:

- we are not able to distinguish a B_s meson from a $\bar{B}_s$ meson and thus we have to sum over the B_s and $\bar{B}_s$ terms of distribution[11];
- we are not interested in measuring ϕ_V and we assume its value in the SM. We then fix $\phi_V = 0$ in the $K_i(t)$ functions;

then the differential angular decay rate of eq. 2.57 becomes

$$\frac{d^4\Lambda(\vec{\omega},t)}{dtd\vec{\omega}} = \frac{9}{32\pi}\left[\mathcal{F}_e(\vec{\omega})\mathcal{K}_L(t)+\mathcal{F}_o(\vec{\omega})\mathcal{K}_H(t)\right] \tag{2.60}$$

11 We are supposing that B_s and $\bar{B}_s$ are produced in equal numbers at the Tevatron.

where we distinct two time-dependent and two angular-dependent terms:

$$\mathcal{F}_e(\vec{\omega}) = |A_0|^2 f_1(\vec{\omega}) + |A_\parallel|^2 f_2(\vec{\omega}) + |A_0||A_\parallel| \cos\delta f_5(\vec{\omega}) \tag{2.61a}$$

$$\mathcal{F}_o(\vec{\omega}) = |A_\perp|^2 f_3(\vec{\omega}) \tag{2.61b}$$

$$\mathcal{K}_L(t) = 2e^{-\Gamma_L t} \tag{2.61c}$$

$$\mathcal{K}_H(t) = 2e^{-\Gamma_H t} \tag{2.61d}$$

A nice comment on eq. 2.60: if you compare this expression with eq. 2.36, you can find that

- $\mathcal{F}_e(\vec{\omega}) \sim |\langle f|B_L\rangle|^2$ represents the probability to find the $|\phi\phi\rangle$ state with $L = 0$ or $L = 2$ (S- or D-wave): $\mathsf{CP}\,|\phi\phi\rangle = (-1)^L\,|\phi\phi\rangle = |\phi\phi\rangle$, then $\mathsf{CP}\,|B_L\rangle = |B_L\rangle$; the light mass (short-lived) eigenstate is also a CP-even eigenstate.
- $\mathcal{F}_o(\vec{\omega}) \sim |\langle f|B_H\rangle|^2$ represents the probability to find the $|\phi\phi\rangle$ state with $L = 1$: $\mathsf{CP}\,|\phi\phi\rangle = (-1)^L\,|\phi\phi\rangle = -\,|\phi\phi\rangle$, then $\mathsf{CP}\,|B_H\rangle = -\,|B_H\rangle$; the heavy mass (long-lived) eigenstate is also a CP-odd eigenstate.

2.4.4 $B_s \to J/\psi\phi$

The customary choice for the $B_s \to J/\psi\phi$ angular analysis is the transversity basis. The differential angular decay rate has the same form of eq. 2.57, with the $f_i(\vec{\Omega})$ functions defined by:

$$\begin{aligned}
f_1(\vec{\Omega}) &= 4\cos^2\Psi(1-\sin^2\Theta\cos^2\Phi)\\
f_2(\vec{\Omega}) &= \sin^2\Psi(1-\sin^2\Theta\sin^2\Phi)\\
f_3(\vec{\Omega}) &= \sin^2\Psi\sin^2\Theta\\
f_4(\vec{\Omega}) &= \sin^2\Psi\sin 2\Theta\sin\Phi\\
f_5(\vec{\Omega}) &= -\frac{1}{\sqrt{2}}\sin 2\Psi\sin^2\Theta\sin 2\Phi\\
f_6(\vec{\Omega}) &= \frac{1}{\sqrt{2}}\sin 2\Psi\sin 2\Theta\cos\Phi
\end{aligned} \tag{2.62}$$

and replacing ϕ_V with $2\beta_s$ in the $K_i(t)$ terms.

As for $B_s \to \phi\phi$, if we sum over B_s and $\bar{B}_s$ terms and assume for β_s the SM value ($\beta_s \simeq 0$), we get the analogous distribution for $B_s \to J/\psi\phi$ as the one described by eq. 2.60.

2.5 ANALYSIS PURPOSE AND STRATEGY

2.5.1 Purpose and Current Experimental Status

The purpose of this thesis is the first measurements of the polarization amplitudes $|A_0|^2$, $|A_\parallel|^2$ and $|A_\perp|^2$ for the $B_s \to \phi\phi$ decay. Their theoretical predictions, coming from the explicit calculation of the operators in eq. 2.12, can be done only with approximate methods: there are different approaches, all affected by large uncertainties. We summarize the predicted values in tab. 2.

These polarization measurements are of particular interest because they can help to understand the so-called "polarization puzzles", described below, related to $\bar{b} \to \bar{s}$

	Γ_L/Γ [%]	$(\Gamma_\perp + \Gamma_\parallel)/\Gamma$ [%]	Comments
QCD factorization 1.a	43^{+0+61}_{-0-34}	57^{+0+61}_{-0-34}	
QCD factorization 1.b	48^{+0+26}_{-0-27}	52^{+0+26}_{-0-27}	WA from data
QCD factorization 2	86.6	13.4	see erratum
Naive factorization	88.3	11.7	see erratum
NLO EWP 1	86.3	13.7	T and P
NLO EWP 2	86.3	13.7	T, P and EWP
perturbative QCD	$61.9^{+3.6+2.5+0.0}_{-3.2-3.3-0.0}$	$38.1^{+3.6+2.5+0.0}_{-3.2-3.3-0.0}$	

Table 2: $B_s \to \phi\phi$ polarization amplitudes: theoretical predictions. Γ_L/Γ and $(\Gamma_\perp + \Gamma_\parallel)/\Gamma$ are the fraction of longitudinal and transverse polarisation, respectively. WA stands for "Weak Annihilation"; T, P and EWP stand for "Tree", "Penguin" and "Electroweak Penguin", respectively. The references are: [22] for QCD factorization 1.a and 1.b, [44] for QCD factorization 2 and Naive factorization, [45] for NLO EWP 1 and 2, [46] for perturbative QCD.

penguin processes. The interest in the polarization and CP-asymmetry measurements in penguin transition, such as $b \to s$ decays $B \to \phi K^\star$, $\rho K^\star$, $\omega K^\star$, and $b \to d$ decay $B \to K^\star \bar{K}^\star$, is mainly motivated by their potential sensitivity to physics beyond the SM.

The amplitude hierarchy $|H_0| \gg |H_\parallel| \gg |H_\perp|$ was expected in the B decays to light vector particles in both the penguin transition [47] and the tree-level transition [48]. There is confirmation by BaBar and Belle experiments of predominantly longitudinal polarization in the tree-level $b \to u$ transition, such as $B^0 \to \rho^+\rho^-$ [49, 50], $B^+ \to \rho^0\rho^+$ [51], and $B^+ \to \omega\rho^+$ [52], which is consistent with the analysis of the quark helicity conservation [48]. Because the longitudinal amplitude dominates the decay, a detailed amplitude analysis is not possible with current B samples, and limits on the transverse amplitude fraction are obtained. Only limits have been set on the $B^0 \to \omega\rho^0$, $\omega\omega$ [52] and evidence found for $B^0 \to \rho^0\rho^0$ [53] decays, still indicating that $b \to d$ penguin pollution is small in the charmless, strangeless vector-vector B decays.

On the other hand, the decay amplitudes for $B \to \phi K^\star$ have been measured by the BaBar and Belle experiments [17, 54, 55] and the fractions of longitudinal polarization $f_L = 0.50 \pm 0.05$ for the $B^+ \to \phi K^{\star+}$ decay, and $f_L = 0.484 \pm 0.033$ for the $B^0 \to \phi K^{\star 0}$ decay, indicate significant departure from the naive expectation of predominant longitudinal polarization. These suggest other contributions to the decay amplitude, previously neglected, either within the SM, such as penguin annihilation [56] or QCD rescattering [57], or from physics beyond the SM [58].

The search for vector-tensor $B \to \phi K^\star_J$ decays with $J = 2, 3, 4$ revealed a large fraction of longitudinal polarization in the decay $B \to \phi K^\star_2(1430)$ with $f_L = 0.85 \pm 0.08$ [17, 59]. Like $B \to \phi K^\star$, the decays $B \to \rho K^\star$ and $B \to \omega K^\star$ may be sensitive to new physics. Measurements of the longitudinal polarization fraction in $B^+ \to \rho^0 K^{\star 0}$ and $B^+ \to \rho^+ K^{\star 0}$ [60, 18] reveal a polarization anomaly similar to $B \to \phi K^\star$. At the same time, first measurement of the polarization in the $b \to d$ penguin decay $B^0 \to K^{\star 0}\bar{K}^{\star 0}$ indicates a large fraction of longitudinal polarization $f_L = 0.81^{+0.12}_{-0.13}$ [61].

The measurement of polarization in the penguin dominated B_s decay could challenge the SM explanation of the polarization puzzle or at least can offer the opportunity to further constrain theoretical parameters thus improving the predictive power of current theoretical tools.

2.5.2 Strategy

From March 2001 till April 2008, we have selected a sample of about 300 $B_s \to \phi\phi$ events in about 2.9 fb^{-1} of data collected with CDFII [29]. Comparing with the angular analysis of the topological similar decay $B_d \to \phi K^{0\star}$ performed at CDFII [62], we can estimate the statistical precision that we should get from our data sample. In tab. 3 the $B_d \to \phi K^{0\star}$ decay results are summarized: we have an yield of 60 events and the statistical uncertainty on the polarization amplitudes is of the order of 10%. In our $B_s \to \phi\phi$ samples we have about a factor 4 in the events number, then we expect a factor $1/2$ in the amplitude statistical uncertainties: they should be about 5%. The precision is thus sufficient to discriminate between various QCD predictions, provided the systematic uncertainty is kept at the same level.

	$B_d \to \phi K^{0\star}$
Yield	59 ± 9
$\lvert A_0 \rvert^2$	$0.571 \pm 0.097 \pm 0.050$
$\lvert A_\perp \rvert^2$	$0.206 \pm 0.089 \pm 0.045$
$\lvert A_\parallel \rvert^2$	$0.223 \pm 0.077 \pm 0.054$

Table 3: $B_d \to \phi K^{0\star}$ polarization amplitudes measured at CDFII with 360 pb^{-1} [62].

We proceed in two steps to reach our purpose:

TIME-INTEGRATED ANALYSIS We perform an unbinned Maximum Likelihood fit, using as probability density function (pdf) the distribution of eq. 2.60 integrated in time. Since eq. 2.60 doesn't present a function whose the time and the angular terms factorize, the time integration introduces a bias in the estimating parameters. Our hypothesis is that the statistics uncertainty is bigger than the systematic induced by the time integration. The latter should not be greater than $\Delta\Gamma/\Gamma \sim 10\%$. This analysis is described in Chapter 5.

TIME-DEPENDENT ANALYSIS This must be done if our hypothesis is not correct, or if non-trivial complications due to the time evolutions are found. In this case, eq. 2.60 is used, and the proper time of the particles enters the fit as input variable, like the basis angles. This is described in Chapter 6.

When performing any analysis, procedure and samples for the validation of the analysis itself is an important component. While studying the unknown properties of a specific decay mode, a general way to achieve such validation is to apply the developed framework on a kinematically equivalent decay mode, which properties are, on the other hand, very well known. Thus, an experimentalist can compare the results of what it is called *control sample* with the ones obtained independently from other experiments, which may have even a better statistical accuracy. Therefore, the control sample serves the purpose of improving the reliability of the main analysis. In this analysis, the $B_s \to J\psi\phi$ serves as control sample. For its intrinsic nature of control sample, many of the technical aspects are in common with the main analysis (*e. g.*, the same trigger selection) and, whenever possible, useless repetitions will be avoided.

3 THE UPGRADED COLLIDER DETECTOR AT THE FERMILAB TEVATRON

THE B MESON studied in this thesis are produced as a result of the head-on proton-antiproton collisions at a center of mass energy of 1.96 TeV. The resulting products and their properties are inferred from the kinematics of the "stable" particles that at the end interact with the detector instrumentation.[1]

This chapter provides a concise description of the complex infrastructure, accelerator and detector, involved in producing our data sample. A more detailed description of the tracking and the trigger systems is given, for the crucial role they have in the present analysis.

3.1 THE FERMILAB TEVATRON COLLIDER

The Tevatron collider is an accelerator that provides collisions of antiprotons with protons at a center-of-mass energy of 1.96 TeV. The Tevatron is an underground circular proton synchrotron, 1 km in radius, the last stage of a system of accelerators, storage rings, and transfer lines located at the Fermi National Accelerator Laboratory (FNAL), or Fermilab, about 50 km west from Chicago, Illinois, United States. While the machine operates in collider mode, "bunches" of protons, circulating clockwise as seen from above and spaced by 396 ns, collide against a similar beam of antiprotons accelerated counter-clockwise, both at energies of 980 GeV. A bunch is a collection of particles contained within one radio-frequency "bucket" (defined below).

The Tevatron was commissioned in 1983 as the first large-scale superconducting synchrotron in the world and, since then, various periods of operations occurred. Each period of Tevatron collider operations is conventionally identified as a Run.[2] Table 4 contains a summary of the Tevatron operations and performance since its construction. The present analysis uses the data collected in Run II.

The performance of the Tevatron collider is evaluated in terms of two key parameters: the available center-of-mass energy, $\sqrt{s}$, and the instantaneous luminosity, $\mathscr{L}$. The former defines the accessible phase-space for the production of resonances in the final states. The latter is the coefficient of proportionality between the rate of a given process and its cross-section σ:

$$\text{rate}\,[\text{events}\,\text{s}^{-1}] = \mathscr{L}\,[\text{cm}^{-2}\,\text{s}^{-1}] \times \sigma\,[\text{cm}^{2}]\,. \tag{3.1}$$

The time-integral of the eq. (3.1) is therefore a measure of the expected number of events n, produced in a finite time T:

$$n(T) = \int_0^T \mathscr{L}\sigma\, dt\,, \tag{3.2}$$

1 Stable in this context is relative to the size of the detector and the energy of the interactions. Muons, kaons and pions are not stable: they decay with mean life-times of the order of 10^{-6} s to 10^{-8} s. However, at energies of a few GeV and above, they are nearly stable as observed in the detector.

2 The Run is not to be confused with the *run*, defined in CDF as a continuous period of data-taking in approximately constant detector and beam conditions.

Date		$\sqrt{s}$ [TeV]	$\mathscr{L}$ [$\mathrm{cm^{-2}\,s^{-1}}$]	$\int \mathscr{L}\,dt$ [$\mathrm{pb^{-1}}$]
Mar 1983	End of the construction	–	–	–
Jul 1983	Proton energy: 512 GeV	–	–	–
Oct 1983	Fixed-target program	–	–	–
Feb 1984	Proton energy: 800 GeV	–	–	–
Oct 1985	First $\mathrm{p\bar{p}}$ collisions	1.6	10^{24}	–
Oct 1986	Proton energy 900 GeV	–	–	–
Jun 1988–May 1989	Run 0	1.8	2×10^{30}	$\simeq 4.5$
Aug 1992–Feb 1996	Run I	1.8/0.63	28×10^{30}	$\simeq 180$
Aug 2000	Beam energy: 980 GeV	–	–	–
Mar 2001	Run II start	1.96	5×10^{30}	–
Sep 2009	Best performances	1.96	3.6×10^{32}	$\simeq 6.9$

Table 4: Chronological overview of the Tevatron operation and performance. The fourth column reports the peak luminosity. The fifth column reports the delivered integrated luminosity. The last row shows the best performances as of this writing.

while the time-integral of the luminosity is the integrated luminosity:

$$\mathscr{L}_{\mathrm{int}} = \int_0^T \mathscr{L}\,dt\,. \tag{3.3}$$

Assuming an ideal head-on $\mathrm{p\bar{p}}$ collision with no crossing angle between the beams, the instantaneous luminosity is defined as

$$\mathscr{L} = 10^{-5}\frac{N_{\mathrm{p}}N_{\bar{\mathrm{p}}}Bf\beta\gamma}{2\pi\beta^{\star}\sqrt{(\epsilon_p+\epsilon_{\bar{p}})_x(\epsilon_p+\epsilon_{\bar{p}})_y}}\mathcal{H}(\sigma/\beta^{\star}) \qquad [10^{30}\,\mathrm{cm^{-2}\,s^{-1}}]\,. \tag{3.4}$$

It depends on the following Tevatron parameters: the number of circulating bunches in the ring ($B = 36$), the revolution frequency ($f = 47.713\,\mathrm{kHz}$), the Lorentz relativistic factor (boost, $\beta\gamma = 1045.8$ at 980 GeV), the average numbers of protons ($N_{\mathrm{p}} \approx 250 \times 10^9$) and antiprotons ($N_{\bar{\mathrm{p}}} \approx 10^9$) in a bunch, an empiric "hourglass" factor ($\mathcal{H} = 0.6$-–0.7), which is a function of the ratio between the longitudinal r.m.s. width of the bunch ($\sigma_z \approx 60\,\mathrm{cm}$) and the "beta function" calculated at the interaction point ($\beta^{\star} \approx 31\,\mathrm{cm}$), and the 95% normalized emittances of the beams ($\epsilon_{\mathrm{p}} \approx 18\pi\,\mathrm{mm\,mrad}$ and $\epsilon_{\bar{\mathrm{p}}} \approx 13\pi\,\mathrm{mm\,mrad}$ after injection).[3] The dominant limiting factor of the luminosity is the availability of monochromatic antiprotons that can be efficiently transferred through the accelerator chain for final collisions.

The Tevatron is an approximately circular synchrotron employing 772 dipole, 2 half-dipole, and 204 quadrupole superconducting magnets. Each is approximately 6 m long, 4 tons in mass, and is made of NbTi alloy filaments embedded in copper, kept at 4.3 K temperature by a large cryogenic system. A 4400 A current flows through each magnet to produce the 4.2 T magnetic field necessary to keep the particles on their orbit, while they are accelerated by eight radio-frequency (RF) cavities driven at approximately 53.105 Hz. Motions or friction by the approximately $4000\,\mathrm{N\,cm^{-1}}$ of outward pressure are avoided by epoxy-covered steel collars bound around the magnets.

3 The hourglass factor is a parameterization of the longitudinal profile of the beams in the collision region, which assumes the shape of an horizontal hourglass centered in the interaction region. The beta function is a parameter convenient for solving the equation of motion of a particle through an arbitrary beam transport system. The emittance ϵ measures the phase-space occupied by the particles of the beam. Three independent two-dimensional emittances are defined. The quantity $\sqrt{\beta\epsilon}$ is proportional to the r.m.s. width of the beam in the corresponding phase plane.

The particles are accelerated through the RF buckets. A bucket is one interval of the longitudinal restoring force provided by the RF cavities that results in a stable phase-space where a bunch may be captured and accelerated. In the following, we describe the procedure for obtaining a continuous period of collider operation using the same collection of protons and antiprotons, called a store. Further details can be found in [63].

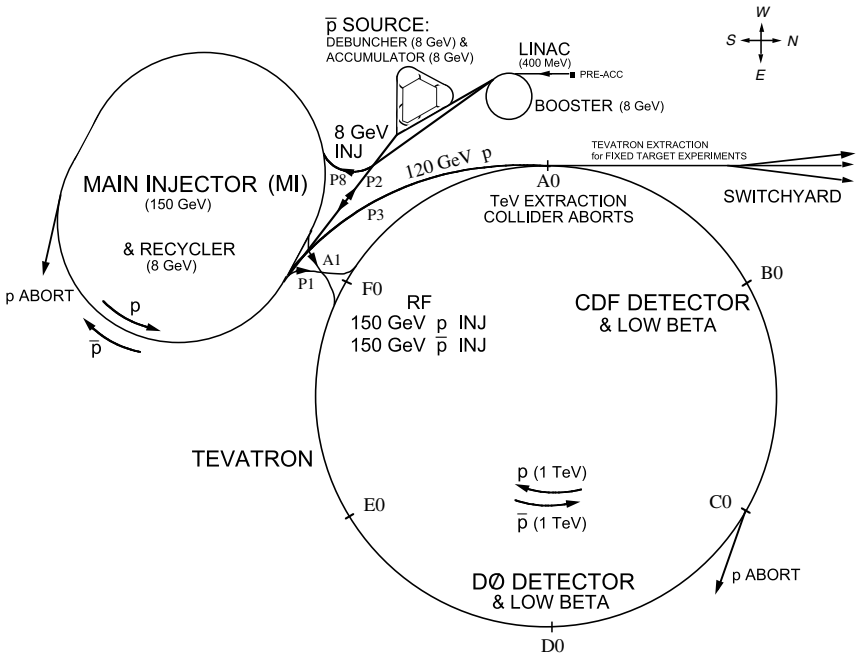

Figure 3.1: Illustration of the Fermilab Tevatron collider.

3.1.1 Proton production

Hot hydrogen gas is passed through a magnetron, which extracts a 50-55 mA current of 15–22 keV H^- ions, subsequently accelerated every 66 ms to 750 keV by a three-staged diode-capacitor voltage multiplier (Cockroft-Walton) accelerator. The proton beam, segmented into bunches, is then injected into a two-staged 150 m long linear accelerator (Linac, see fig. 3.1). First, a drift tube accelerator resonating at 201.249 MHz accelerates bunches of protons up to 116 MeV; then, a side-coupled cavity accelerator at 804.996 MHz increases their energy to 401.5 MeV before injection into the Booster.

The Booster (see fig. 3.1) is an alternating gradient synchrotron (orbit radius of 75.5 m) that accelerates protons to 8 GeV in 33 ms, sweeping from 38 to 53.105 MHz. At injection, a thin carbon foil is used to strip the electrons from the H^- ions to obtain protons. Injecting H^- ions rather than protons into the Booster allows the injection to proceed over multiple revolutions of the beam around the Booster Ring (usually 10–12).[4] There are two basic modes during collider operations: antiproton accumulation and injection.

4 If protons were instead injected, the magnetic field used to inject new protons onto orbit in the Booster would also deflect the already revolving protons out of orbit.

3.1.2 Antiproton production and accumulation

In accumulation mode, one set of 84 proton bunches (approximately 8×10^{12} p in total) is extracted from the Booster at 8 GeV and injected into the Main Injector every 2.2 s. The Main Injector (see fig. 3.1) is a 53.105 MHz circular synchrotron (528.5 m in radius), with 18 accelerating cavities and conventional magnets. The protons are accelerated to 120 GeV, and then extracted and directed to the antiproton production station, a rotating 7 cm-thick target made of nickel alloys containing chromium, iron and other metals.

The particles produced in the interaction are spatially wide-spread. They are collected and focused with a cylindrical lithium lens (760 T m^{-1}).[5] Eight GeV/c negatively-charged secondaries are momentum-selected by a 1.5 T pulsed dipole magnet. Typically, 21 antiprotons are collected for each 106 protons on target, resulting in a stacking rate of approximately 10–20 mA h^{-1}. The emerging antiprotons have a bunch structure similar to the one of the incident protons and are delivered to the Debuncher storage ring (see fig. 3.1).

This rounded triangular synchrotron, 90 m of mean radius, transforms the antiproton pulses in a continuous beam of monochromatic antiprotons. Stochastic cooling and bunch rotation are applied during many cycles.[6] From the Debuncher, 8.000 ± 0018) GeV antiprotons are transferred with 60%–70% efficiency into the Accumulator, a concentric storage ring 75 m in mean radius (see fig. 3.1), where they are stacked and cooled with a variety of systems until the maximum antiproton intensity is reached. Since 2004, optimized antiproton accumulation is achieved using the Recycler Ring (see fig. 3.1). This is a constant 8 GeV energy storage-ring placed in the Main Injector enclosure, that uses permanent magnets. It is used to gather antiprotons that are periodically transferred from the Accumulator (95% transfer efficiency) thus maintaining it at its optimum intensity regime. Recently, relativistic electron cooling was successfully implemented in the Recycler, further enhancing the Tevatron performance [65].[7]

3.1.3 Injection and collisions

Every 10–20 h, antiproton accumulation is stopped in preparation for injection. A set of seven proton bunches is extracted from the Booster, injected into the Main Injector, accelerated to 150 GeV, coalesced with $\approx$ 90% efficiency into a single bunch of $\approx 300 \times 10^9$ p, and then injected into the Tevatron.[8] This process is repeated every 12.5 s, until 36 proton bunches, separated by 396 ns, are loaded into the Tevatron central orbit. Typically, 65% of the protons in the Main Injector are successfully transferred to the Tevatron. The electrostatics separators (about 30 pairs of metal plates) are then activated in the Tevatron, in preparation for antiproton injection.

Four sets of 7–11 $\bar{p}$ bunches are extracted from the Accumulator (or from the Recycler) to the Main Injector, accelerated to 150 GeV, coalesced with $\approx$ 80% efficiency into four $\approx 30 \times 10^9$ $\bar{p}$ bunches separated by 396 ns, and then injected into the Tevatron, where protons are counter-rotating. Protons and antiprotons circulate in the same

5 Lithium is used to minimize beam loss from multiple-scattering.

6 *Stochastic cooling* is a technique used to reduce the transverse and energy spread of a particle beam without any accompanying beam-loss. This is achieved by applying iteratively a feedback mechanism that senses with extreme sensitivity the beam deviation from the ideal orbit with electrostatic plates, processes and amplifies it, and transmits an adequately-sized synchronized correction pulse to another set of plates downstream [64]. Bunch rotation is an RF manipulation technique that, using adequate phasing, transforms a beam with a large time spread and a small energy spread in a beam with a large energy spread and a small time spread, or vice versa.

7 Electron cooling is a method of damping through the interaction between the antiproton beam and an electron beam propagating together at the same average velocity.

8 Coalescing is the process of compacting into one dense bunch many smaller bunches.

enclosure, sharing magnet and vacuum systems. The separators minimize the beam-beam interactions, by keeping the proton and the antiproton beams, each about half a millimeter thick, into two non-intersecting closed helical orbits separated by approximately five millimeters (3σ–5σ) as they revolve in opposite directions. This allows controlling each beam nearly independently. The injection process is repeated nine times until 36 antiproton bunches circulate in the Tevatron.

Sweeping the Tevatron RF by $\approx$ 1 kHz, the beam is then accelerated in about a minute from 150 to 980 GeV, at which energy one particle completes the full revolution of the Tevatron circumference in 21 µs at 0.999 999 6 c. The beams are finally brought into collision at the two instrumented interaction-points located along two straight sections of the Tevatron: DØ and BØ, where the DØ and CDFII detectors, respectively, are located. Although the power produced in the collision is only 1–2 W, the stored energy of the beam is about 1.7 MJ, corresponding, approximately, to the kinetic energy of a 4.5 t truck moving at 100 km h^{-1}.

Special high-power quadrupole magnets ("low-β squeezers"), installed on the beam pipe at either side of the detectors, reduce the transverse spatial spread of the beams to maximize the collision rate in the interaction regions. The resulting transverse spatial distribution of the luminous region is approximately a two-dimensional Gaussian, with $\sigma_T \approx 30\,\mu m$. The typical longitudinal dimension of a bunch is 60–70 cm. The interaction regions have a roughly Gaussian distribution along the beam direction, with r.m.s. width $\sigma_z \approx 28$ cm. The center of the luminous region is shifted toward the nominal interaction point by fine tuning of the squeezers. The 36 bunches of protons (antiprotons) are distributed among the 1113 buckets in three equispaced "trains" of 12 bunches each. The inter-bunch spacing is 396 ns (21 buckets) within a train, while a 2.6 µs spacing (139 buckets, "abort gap") is kept between trains. The need for the abort gap is two-fold: it allows antiprotons injection (in coincidence with the proton abort gap) without perturbing the already revolving protons with the injecting magnet. Furthermore, when beam abortion is needed, the abort gap allows ramping-up the deflecting magnets without interfering with the beam during the transient, possibly damaging the detectors. As a consequence of this bunch distribution, the average bunch-crossing rate is 1.7 MHz, resulting from a 2.53 MHz rate, when the proton and antiproton trains are crossing, and zero rate in correspondence of the abort gaps.

The transverse profile of the beam is shaped to its optimized configuration to avoid detector damage from the tails of the p ($\bar{p}$) distributions interacting with the beam pipe: retractable collimators (iron plates) are moved perpendicularly toward the beam and trim-off the residual halo. When the beam profile is narrow enough and the conditions are safely stable, the detector is powered and the data-taking starts.

The number of overlapping inelastic interactions N for each bunch crossing is a Poisson-distributed variable that depends on the instantaneous luminosity. The observed distribution of the multiplicity of interaction vertexes yields $\bar{N} \approx 0.2$, 1.0, 2.0, and 6.0 for respectively, $\mathscr{L} \approx 1 \times 10^{31}$, 5×10^{31}, 10×10^{31}, and 30×10^{31} luminosities [66]. The luminosity decreases as a function of time during the store because of the interactions of the beam with residual molecules of gas that escaped the vacuum of the beam pipe, beam-halo interactions, and $\bar{p}$ depletion due to the collisions. During the 10–20 h of a store, the luminosity decreases by a factor of 2.5–5, the majority of data being collected at $\mathscr{L} \approx \mathscr{L}_0/2$. Just after the final injection, a new antiproton accumulation cycle is started. When the antiproton stack is sufficiently large and the colliding beams are degraded, the detector high-voltages are switched-off and the store is dumped. The beam is extracted via a switch-yard and sent to an absorption zone.

Beam abortion can occur also accidentally when a superconducting magnet rises its temperature above the critical value (*i. e.*, the magnet "quenches"), destroying the orbit of the beams. The time between the end of a store and the beginning of collisions of

the next one is typically 2 h, during which time calibrations of the sub-detectors and cosmic rays tests are usually performed.

3.1.4 Tevatron performance

Since the beginning of Run II the Tevatron performance has been steadily increasing. Currently (as of 2009), the Tevatron is running at a center-of-mass energy of 1.96 TeV with an inter bunch-crossing time of 396 ns.

The Tevatron set the world record of highest peak luminosity for a hadron collider of $3.6 \times 10^{32}\,\mathrm{cm}^{-2}/\mathrm{s}$. As of October 2009, physics quality data corresponding to $6.9\,\mathrm{fb}^{-1}$ are stored. The plot in fig. 3.2 shows the integrated luminosity since the beginning of run II.

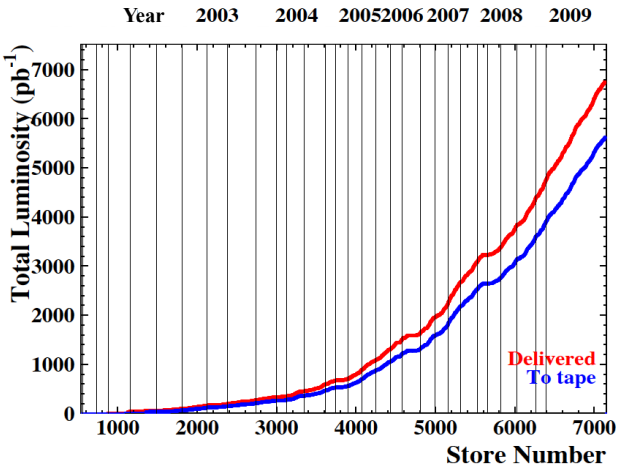

Figure 3.2: Integrated Luminosity since the beginning of run II.

3.2 THE CDF II DETECTOR

The CDFII detector is a large multi-purpose solenoidal magnetic spectrometer surrounded by 4π fast, projective calorimeters and fine-grained muon detectors. It is installed at the BØ interaction point of the Tevatron (see fig. 3.3) to determine energy, momentum and, whenever possible, the identity of a broad range of particles produced in 1.96 TeV $\mathrm{p\bar{p}}$ collisions. It was designed, built, and operated by a team of physicists, technicians, and engineers that, as of this writing, spans 60 institutions of 13 countries. Several upgrades modified the design of the original facility commissioned in 1985.[9] The most extensive upgrade started in 1995 and led to the current detector whose operation is generally referred to as CDFII.

3.2.1 Coordinates and notation

CDFII employs a right-handed Cartesian coordinate system with origin in the BØ interaction point, assumed coincident with the center of the drift chamber (see sec. 3.3.5).

9 Originally, the CDF acronym was meant for Collider Detector Facility.

The positive z-axis lies along the nominal beam-line pointing toward the proton direction (east). The (x, y) plane is therefore perpendicular to either beams, with positive y-axis pointing vertically upward and positive x-axis in the horizontal plane of the Tevatron, pointing radially outward with respect to the center of the ring.

Since the colliding beams of the Tevatron are unpolarized, the resulting physical observations are invariant under rotations around the beam line axis. Thus, a cylindrical (r, φ, z) coordinate system is particularly convenient to describe the detector geometry. Throughout this , *longitudinal* means parallel to the proton beam direction (*i. e.*, to the z-axis), and *transverse* means perpendicular to the proton beam direction, *i. e.*, in the $(x, y) \equiv (r, \varphi)$ plane.

In hadron-collisions environments, it is customary to use a variable invariant under $\hat{z}$ boosts as an unit of relativistic phase-space, instead of the polar angle θ. This variable is the *rapidity* defined as

$$Y = \frac{1}{2} \ln \left[\frac{E + p\cos(\theta)}{E - p\cos(\theta)} \right], \tag{3.5}$$

where $(E, \vec{p})$ is the energy-momentum four-vector of the particle. However, a measurement of rapidity still requires a detector with accurate particle identification capabilities because of the mass term entering E. Thus, for practical reasons, it is often preferred to substitute Y with its approximate expression η in the ultra-relativistic limit, usually valid for products of high-energy collisions:

$$Y \overset{p \gg m}{\longrightarrow} \eta + \mathcal{O}(m^2/p^2), \tag{3.6}$$

where the *pseudo-rapidity* $\eta \equiv -\ln[\tan(\theta/2)]$ is only function of the momenta. As the event-by-event longitudinal position of the actual interaction is distributed around the nominal interaction point with 30 cm r.m.s. width, it is useful to distinguish *detector pseudo-rapidity*, η_{det}, measured with respect to the $(0, 0, 0)$ nominal interaction point, from *particle pseudo-rapidity*, η, which is measured with respect to the z_0 position of the real vertex where the particle originated.[10]

Mapping the solid angle in terms of (pseudo)-rapidity and azimuthal angle is also convenient because the density of final-state particles in energetic hadronic collisions is approximately flat in the (Y, φ) space. The (pseudo)-rapidity dependence was observed experimentally, the azimuthal dependence derives from the fact that beams are unpolarized. Other convenient variables are the transverse component of the momentum with respect to the beam axis (p_{T}), the "transverse energy" (E_{T}), and the approximately Lorentz-invariant angular distance ΔR, defined as

$$\vec{p}_{\text{T}} \equiv (p_x, p_y) \rightarrow p_{\text{T}} \equiv p\sin(\theta), \quad E_{\text{T}} \equiv E\sin(\theta), \quad \text{and} \quad \Delta R \equiv \sqrt{\eta^2 + \phi^2}. \tag{3.7}$$

Throughout this , the magnitude of the vector $\vec{p}_{\text{T}}$ (and of any vector $\vec{v}$) is indicated as p_{T} (v) , instead of $|\vec{p}_{\text{T}}|$ ($|\vec{v}|$), for a simpler notation.

3.2.2 Overview

CDFII (see fig. 3.3) is a 5000 t assembly of sub-detectors, $\approx$ 16 m in length by $\approx$ 12 m in diameter, which can be moved from its garaged position, in the CDF assembly building, to its operation position on the Tevatron beam line. The 31.4 m move takes one day. The CDFII detector was designed and constructed with an approximately cylindrically symmetric layout both in the azimuthal plane and in the "forward" ($z > 0$, east) "backward" ($z < 0$, west) directions with spatial segmentation of its sub-components

10 An idea of the difference is given by considering that $\eta_{\text{det}} \approx \eta \pm 0.2$ if the particle was produced at $z = 60$ cm from the nominal interaction point.

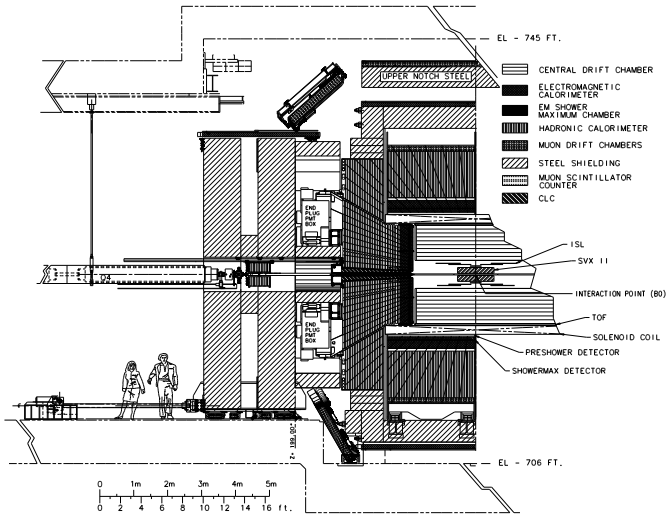

Figure 3.3: Elevation view of one half of the CDFII detector.

roughly uniform in pseudo-rapidity and azimuth. CDFII is composed of several specialized subsystems, each one designed to perform a different task, arranged in a standard layout for multipurpose detectors; starting from the interaction point, particles emitted within the acceptance region encounter in sequence: a thin wall beryllium vacuum pipe, a high-precision tracking system composed by an inner silicon system and an outer drift-chamber, a time-of-flight detector, a solenoidal magnet and its return steel yoke, finely segmented sampling calorimeters, and muon detectors.

Its main features are an excellent tracking performance, which provides high mass resolution and precisely reconstructed decay-vertexes, good electron and muon identification capabilities combined with charged-hadron identification, and an advanced trigger system that fully exploits the high event-rates. A detailed description of the CDFII detector can be found elsewhere [67] and in specific references cited for each sub-detector. In the following, we emphasize the tracking and the trigger systems, which are the aspects of the detector more specific to this analysis.

3.3 THE TRACKING SYSTEM

Three-dimensional charged particle tracking is achieved through an integrated system consisting of three silicon inner sub-detectors and a large outer drift-chamber, all contained in a superconducting solenoid (see fig. 3.4). The 1.41 T magnetic field and the 130 cm total lever arm provide excellent tracking performances.

In the central region ($|\eta_{\text{det}}| \lesssim 1$), 7 silicon samplings (one in the (r,φ) view plus six in the (r,φ,z) view), and 96 chamber samplings (48 (r,φ) plus 48 (r,z)) are available between 1.6 and 132 cm. In the forward and backward regions ($1 \lesssim |\eta_{\text{det}}| \lesssim 2$), 8 silicon samplings (one in the (r,ϕ) view plus seven in the (r,ϕ,z) view) are available between 1.6 and 29 cm, along with partial information from the chamber.

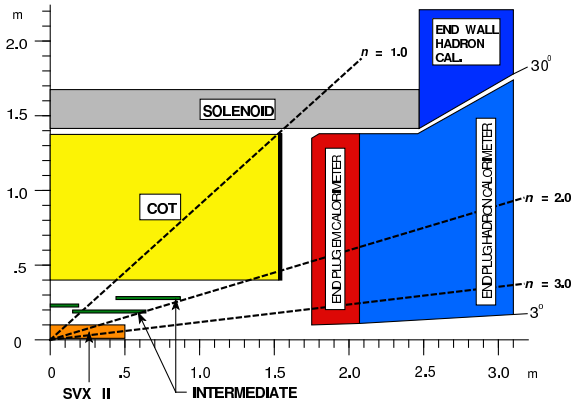

Figure 3.4: Elevation view of one quadrant of the inner portion of the CDFII detector showing the tracking volume surrounded by the solenoid and the forward calorimeters.

The high number of samplings over the 88 cm lever arm of the chamber ensure precise determination of curvature, azimuth, and pseudo-rapidity of the tracks in the central region. The chamber provides also track seeds for pattern-recognition in silicon.

The core of the silicon detector is the Silicon VerteX (SVXII) detector. It provides five three-dimensional measurements that extend the lever arm by 41.5 cm toward the beam thus allowing more precise determination of the trajectories and identification of decay-vertexes displaced from the beam-line. The SVXII has an outer and an inner extension. The outer extension, *i. e.*, the Intermediate Silicon Layers (ISL), provides a single (double) three-dimensional silicon measurement in the central (forward-backward) region, at intermediate radial distance from the chamber. The ISL allows efficient linking between tracks reconstructed in the chamber and hits detected in the SVXII, and extends the track finding at pseudo-rapidities $1 \lesssim |\eta_{\text{det}}| \lesssim 2$, where the chamber coverage is marginal. The inner extension, the Layer 00 (L00), is a light-weight silicon layer placed on the beam-pipe. It recovers the degradation in resolution of the reconstructed vertex position due to multiple scattering on the SVXII read-out electronics and cooling system, installed within the tracking volume. In addition, the L00, being made of state-of-the-art radiation-tolerant sensors, will extend the lifetime of the whole system when the effects of radiation damage will degrade the performance of the inner SVXII layers. The integrated design of the tracking system allowed commonality of components among sub-detectors (read-out chip, support structures, etc.) thus simplifying the construction and the operation.

All 722 432 channels from the $\approx 7.0\,\text{m}^2$ silicon active-surface employ 5644 radiation-tolerant, custom integrated read-out chips of the same type. This chip allows independent cycles of digitization of data and analog processing of subsequent data. The discriminated differential pulse from each channel is preamplified, digitized and propagated to the downstream data-acquisition. The ISL and the SVXII, whose mass is approximately 128 kg, share the carbon-fiber supporting structure.

The total amount of material in the silicon system, averaged over φ and z, varies roughly as $\frac{0.1X_0}{\sin(\theta)}$ in the $|\eta_{\text{det}}| \lesssim 1$ region, and roughly doubles in $1 \lesssim |\eta_{\text{det}}| \lesssim 2$ because of the presence of cables, cooling bulk-heads, and portions of the support frame.[11] The average amount of energy loss for a charged particle is roughly 9 MeV.

11 The symbol X_0 indicates the radiation length.

The total heat load of the silicon system is approximately 4 kW. To prevent thermal expansion, relative detector motion, increased leakage-current, and chip failure due to thermal heating, the silicon detectors and the associated front-end electronics are held at roughly constant temperature ranging from $-6\,^{\circ}\mathrm{C}$ to $-10\,^{\circ}\mathrm{C}$ for L00 and SVXII, and around $10\,^{\circ}\mathrm{C}$ for ISL, by an under-pressurized water and ethylene-glycol coolant flowing in aluminum pipes integrated in the supporting structures.

3.3.1 The magnet

A 1.4116 T solenoidal magnetic field is maintained in the region $r \lesssim 150\,\mathrm{cm}$ $|z| \lesssim 250\,\mathrm{cm}$ by circulating a 4650 A current (current density $1150\,\mathrm{A\,m^{-1}}$) through 1164 turns of an aluminum-stabilized NbTi/Cu super-conducting coil. The field is oriented along the positive $\hat{z}$ (proton) direction and is uniform to within 0.1% in the $|z| \lesssim 150\,\mathrm{cm}$ volume, where tracking measurements are made (see fig. 3.4). The tiny non-uniformities, mapped out during detector construction, are treated as small perturbations in the track-fitting algorithms. During data-taking, the field is continuously monitored by nuclear magnetic resonance probes with 0.01% accuracy. Any deviation from the mapped values is applied as a correction to the measured track parameters. The threshold to radially escape the magnetic field for a particle is $p_{\mathrm{T}} \gtrsim 0.3\,\mathrm{GeV}/c$ while the trajectory of a particle with $p_{\mathrm{T}} = 30\,\mathrm{GeV}/c$ deviates only 1.6 cm from a straight path of 150 cm. The solenoid is 4.8 m in length, 1.5 m in radius, $0.85 X_0$ in radial thickness (for normally incident particles.), and is cooled by forced flow of two-phase helium. Outside the coil, the return of the field flux is a box-shaped steel yoke, 9.4 m high by 7.6 m wide by 7.3 m long. It avoids interference between the field and the proper operations of the photo-multiplier tubes (PMT) used in the calorimeters.

3.3.2 Layer 00

The L00 is the innermost layer of the silicon detector [**?**]. It consist of a single, castellated layer of single-sided, AC-coupled silicon sensors mounted directly on the beam pipe at radii, alternating in φ, of 1.35 or 1.62 cm from the beam. It provides full azimuthal and $|z| \lesssim 47\,\mathrm{cm}$ longitudinal coverage. Longitudinally adjacent sensors $(0.84\ (\text{or } 1.46)\ \mathrm{cm} \times 7.84\,\mathrm{cm})$ are ganged in modules of 15.7 cm active-length arranged into twelve partially-overlapping φ sectors, and six longitudinal barrels. These radiation-tolerant sensors are biased to $\mathcal{O}(500\,\mathrm{V})$, which allows full depletion after $\mathcal{O}(5\,\mathrm{Mrad})$ integrated radiation doses. The strips are parallel to the beam axis allowing sampling of tracks in the (r, φ) plane. The inter-strip implant pitch of 25 µm with floating alternate strips results in 50 µm read-out pitch. The analog signals of the 13 824 channels are fed via fine-pitch cables, up $\approx 50\,\mathrm{cm}$ long, to the front-end electronics outside the tracking volume.

3.3.3 Silicon VerteX detector II

The SVXII is a fine resolution silicon micro-strip vertex detector which provides five three-dimensional samplings of tracks at 2.45 (3.0), 4.1 (4.6), 6.5 (7.0), 8.2 (8.7), and 10.1 (10.6) cm of radial distance from the beam with full pseudo-rapidity coverage in the $|\eta_{\mathrm{det}}| \lesssim 2$ region (see fig. 3.4 and fig. 3.5(a)) [68]. This corresponds to a length of $|z| \lesssim 96\,\mathrm{cm}$ along the beam-line, sufficient to cover the $\sigma_z \approx 28\,\mathrm{cm}$ longitudinal spread of the luminous region. The SVXII has a cylindrical geometry coaxial with the beam, and its mechanical layout is segmented in three 32 cm axial sections ("barrels") times twelve 30° azimuthal sectors ("wedges") times five equally-spaced radial layers. A

small overlap between the edges of adjacent azimuthal sectors helps wedge-to-wedge alignment (see fig. 3.5(b)).

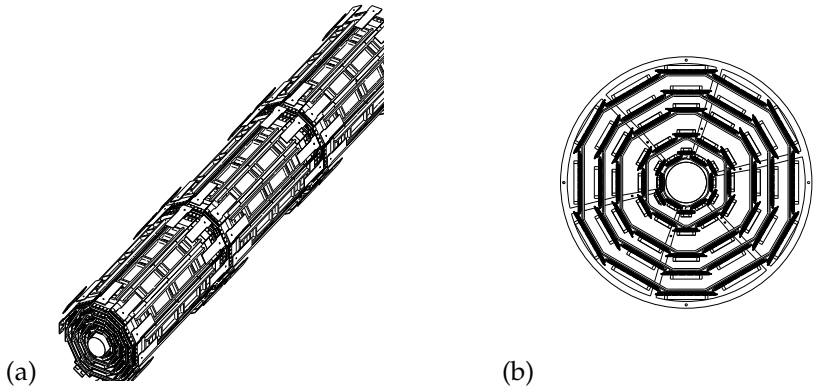

(a) (b)

Figure 3.5: Schematic illustration of the three instrumented mechanical barrels of SVXII (a) and of the cross-section of a SVXII barrel in the (r, φ) plane (b).

Sensors in a single layer are arranged into independent longitudinal read-out units, called "ladders". Each ladder comprises two, double-sided sensors and a multi-layer electronic board, all glued on a carbon-fiber support. Front-end electronics, biasing circuits, and fan-out are located on the board that serves the pair of sensors whose strips are wire-bonded together resulting in a 15 cm active length. At a given radial layer and azimuth, each barrel contains pairs of ladders stacked length-wise head-to-head to keep the read-out electronic at the two outside extremities of the barrel (see fig. 3.5(a)). The active surface consists of double-sided, AC-coupled, 7.5 cm $\times$ 1.5–5.8 cm silicon sensors with micro-strips implanted on a 300 µm thick, high resistivity bulk. Bias is applied through integrated poly-silicon resistors. On one side, all sensors have axial strips (*i. e.*, parallel to the beam direction) spaced by approximately 60–65 µm, for a precise reconstruction of the φ coordinate. On the reverse side, the following combination of read-out pitch (strip orientations with respect to the beam) is used: 141 µm (90°), 125.5 µm (90°), 60 µm (−1.2°), 141 µm (90°), 65 µm (1.2°), from the innermost to the outermost layer for reconstructing the z coordinate. A total of 405 504 electronics channels are used for SVXII.

3.3.4 Intermediate Silicon Layers

The ISL is a silicon tracker placed at intermediate radial distance between the SVXII and the drift chamber (see fig. 3.4), and covering the $|\eta_{\text{det}}| \lesssim 2$ pseudo-rapidity range for a total length of 174 cm along z [69]. At $|\eta_{\text{det}}| \lesssim 1$ a single layer of silicon sensors is mounted on a cylindrical barrel at radius of 22.6 (or 23.1 cm). At $1 \lesssim |\eta_{\text{det}}| \lesssim 2$ two layers of silicon sensors are arranged into two pairs of concentric barrels (inner and outer). In the inner (outer) barrel, staggered ladders alternate at radii of 19.7 and 20.2 cm (28.6 and 29.0 cm). One pair of barrels is installed in the forward region, the other one in the backward region. Each barrel is azimuthally divided into a 30° structure matching the SVXII segmentation. The basic read-out unit consists of an electronic board and three sensors ganged together resulting in a total active length of 25 cm. ISL employs 888 5.7 cm $\times$ 7.5 (6.7) cm double-sided, AC-coupled, 300 µm-thick sensors. Each sensor has axial strips spaced by 112 µm on one side, and 1.2°-angled strips spaced 112–146 µm on the reverse, for 303 104 total channels.

3.3.5 Central Outer Tracker

A multi-wire, open-cell drift chamber provides charged particle tracking at large radii in the central pseudo-rapidity region ($|\eta_{\text{det}}| \lesssim 1$, see fig. 3.4) [70]. The Central Outer Tracker (COT) has an hollow-cylindrical geometry, its active volume spans from 43.4 to 132.3 cm in radius and $|z| \lesssim 155$ cm in the axial direction. Arranged radially into eight "super-layers", it contains 96 planes of wires that run the length of the chamber between two end-plates (see fig. 3.6(a)). Each super-layer is divided into φ cells; within a cell, the trajectory of a charged particle is sampled at 12 radii (spaced 0.583 cm apart) where sense wires (anodes) are strung. Four super-layers employ sense-wires parallel to the beam axis, for the measurement of the hit coordinates in the (r, φ) plane. These are radially interleaved with four stereo super-layers whose wires are alternately canted at angles of $+2^\circ$ and -2° with respect to the beam-line. Combined read-out of stereo and axial super-layers allows the measurement of the (r, z) hit coordinates. Each super-layer is azimuthally segmented into open drift-cells. The drift cell layout (see fig. 3.6(b)) consists of a wire plane closed azimuthally by cathode sheets spaced approximately 2 cm apart. The wire plane contains sense wires alternating with field-shaping wires, which control the gain on the sense wires optimizing the electric field intensity. The cathode is a 6.35 µm-thick Mylar sheet with vapor-deposited gold shared with the neighboring cell.[12] Innermost and outermost radial extremities of a cell (*i. e.*, the boundaries between super-layers) are closed both mechanically and electrostatically by Mylar strips with an additional field-shaping wire attached, the shaper wire.

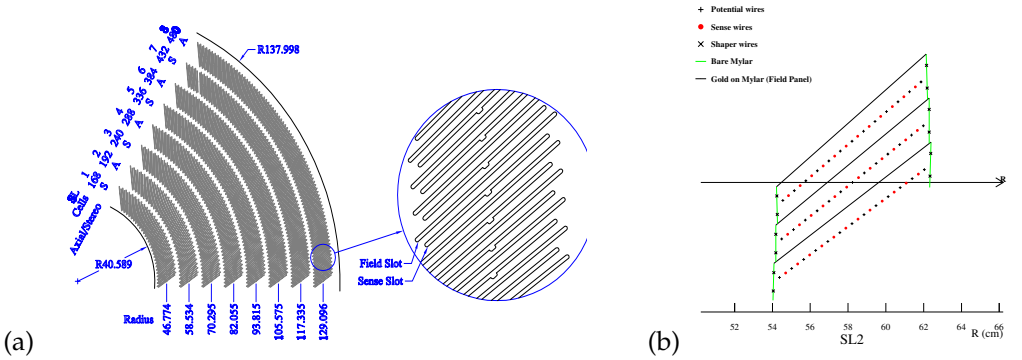

(a) (b)

Figure 3.6: A 1/6 section of the COT end-plate (a). For each super-layer the total number of cells, the wire orientation (axial or stereo), and the average radius [cm] are given. The enlargement shows in details the slot were wire planes (sense) and field sheet (field) are installed. Sketch of an axial cross-section of three cells in super-layer 2, (b). The arrow shows the radial direction.

Both the field sheet and wire plane have a center ($z \approx 0.0$ cm) support rod that limits motion due to electrostatic forces. Each wire plane contains 12 sense, 13 field-shaping, and 4 shaper wires, all made of 40 µm-diameter gold-plated tungsten. Wire planes are not aligned with the chamber radius: a $\zeta = 35^\circ$ azimuthal tilt (see fig. 3.6(b)) partially compensates for the Lorentz angle of the drifting electrons in the magnetic field.[13] The tilted-cell geometry helps in the drift-velocity calibration, since every high-p_{T}

12 Gold, used also for the wires, was chosen because of its good conductivity, high work function, resistance to etching by positive ions, and low chemical reactivity.

13 In the presence of crossed electric ($\vec{E}$) and magnetic ($\vec{B}$) fields, electrons drifting in a gas move at an angle ζ with respect to the electric field direction, given by $\zeta \approx \arctan\left(\frac{v(E,B=0)B}{kE}\right)$, where $v(E, B = 0)$ is the drift velocity without a magnetic field, and k is a $\mathcal{O}(1)$ empirical parameter that depends on the gas and on the

(radial) track samples the full range of drift distances within each super-layer. Further benefit of the tilt is that the left-right ambiguity is resolved for particles coming from the z-axis since the ghost track in each super-layer appears azimuthally rotated by $\arctan[2\tan(\zeta)] \approx 54°$, simplifying the pattern recognition problem.

A 50 : 50 gas admixture of argon and ethane bubbled through isopropyl alcohol (1.7%) flows at $9.45\,\mathrm{L\,min^{-1}}$ in the active volume of the chamber with its pressure being continuously monitored by four probes. Since 2003, the flux has been increased by a factor of ten to contrast the adverse effect of wire aging. High voltage is applied to the sense and field-shaping wires to generate a $1.9\,\mathrm{kV\,cm^{-1}}$ drift electric-field. This value, combined with the drift gas, results in a maximum drift-time of about 177 ns along a maximum drift-distance of 0.88 cm, allowing for read-out and processing of the COT data between two consecutive bunch-crossings. The average $180\,\mathrm{kV\,cm^{-1}}$ field present at the surface of the sense wire produces typical gains of 2×10^4. The 30 240 sense wires are read-out by the front-end chip, which provides input protection, amplification, shaping, baseline restoration, discrimination, and charge measurement. The input-charge information is encoded (logarithmically) in the signal width for dE/dx sampling, and is fed to a time-to-digital converter that records leading and trailing-edge times of signal in 1 ns bins. Hit times are later processed by the pattern recognition software to reconstruct trajectories. The material of the COT corresponds to an average $0.017X_0$ for tracks at normal incidence.

3.3.6 Tracking performance

Within an uniform axial magnetic field in vacuum, the trajectory of a charged particle produced with non-zero initial velocity in the bending plane of the magnet is described by an helix. The arc of an helix described by a particle of charge q in the magnetic volume of CDF is parameterized using three transverse, and two longitudinal parameters:

- $\boldsymbol{C}$ – signed helix (half)-curvature, defined as $C \equiv \frac{q}{2R}$, where R is the radius of the helix. This is directly related to the transverse momentum: $p_\mathrm{T} = \frac{cB}{2|C|}$;
- $\boldsymbol{\varphi_0}$ – φ direction of the particle at the point of closest approach to the z-axis;
- $\boldsymbol{d_0}$ – signed impact parameter, *i. e.*, the distance of closest approach to the z-axis, defined as $d_0 \equiv q(\sqrt{x_c^2 + y_c^2} - R)$, where (x_c, y_c) are the coordinates of the center-guide;
- $\boldsymbol{\lambda}$ – the helix pitch, *i. e.*, $\cot(\theta)$, where θ is the polar direction of the particle at the point of its closest approach to the z-axis. This is directly related to the longitudinal component of the momentum: $p_z = p_\mathrm{T}\cot(\theta)$;
- $\boldsymbol{z_0}$ – the z coordinate of the point of closest approach to the z-axis.

The trajectory of a charged particle satisfies the following equations [71]:

$$x = r\sin(\varphi) - (r + d_0)\sin(\varphi_0) \tag{3.8a}$$
$$y = -r\cos(\varphi) + (r + d_0)\cos(\varphi_0) \tag{3.8b}$$
$$z = z_0 + s\lambda, \tag{3.8c}$$

where s is the projected length along the track, $r = 1/2C$, and $\varphi = 2Cs + \varphi_0$. The reconstruction of a charged-particle trajectory consists in determining the above parameters through an helical fit of a set of spatial measurements ("hits") reconstructed

electric field. A common solution for this problem consists in using tilted cells (*i. e.*, tilted drift electric field) that compensate the Lorentz angle linearizing the time-to-distance relation.

in the tracking detectors by clustering and pattern-recognition algorithms. The helical fit takes into account field non-uniformities and scattering in the detector material. A concise overview of the tracking algorithms is given in the following, see [72, 73] for more details.

Tracking in the COT

The COT efficiency for tracks is typically 99%. The single-hit resolution is 140 μm, including a 75 μm contribution from the ≈ 0.5 ns spread in the measurement of the time of the interaction. Internal alignments of the COT cells are maintained within 10 μm using cosmic rays. Curvatures effects from gravitational and electrostatic sagging are under control within 0.5% by equalizing the difference of E/p between electrons and positrons as a function of $\cot(\theta)$. The typical resolutions on track parameters are the following: $\sigma_{p_T}/p_T^2 \approx 0.0015\,(\mathrm{GeV}/c)^{-1}$, $\sigma_{\varphi_0} \approx 0.035^\circ$, $\sigma_{d_0} \approx 250\,\mu\mathrm{m}$, $\sigma_\theta \approx 0.17^\circ$, and $\sigma_{z_0} \approx 0.3\,\mathrm{cm}$ for tracks fit with no silicon information or beam constraint.

Tracking in the silicon detector

Two unexpected phenomena, occurred at the beginning of Run II, were the dominant causes of the current inefficiency [74]. The first contribution is related to two beam incidents: in March 2002, the failure of multiple Tevatron RF cavities debunched the beam, causing high losses and consequent quenching of the magnets. The beam was aborted with an uncontrolled deflection that exposed the CDFII detector to a flux of more than 10^7 minimum ionizing particles per cm^2 in less than 150 ns; in November 2002, a failure on the deflecting magnets induced an incidental Tevatron abort in which some bunches were deflected into CDFII. Addition of faster interlock systems and more collimators prevented further occurrence of such incidents.

The second phenomenon was the break-up of wire-bonds oriented orthogonally to the magnetic field, due to resonant Lorentz forces occurring in read-out tests at 16 kHz frequency. A temporary inefficiency was induced by 35% of ISL cooling-lines being blocked by epoxy, after installation. This prevented a large portion of ISL from being active, until all the lines were cleared with a laser (in January 2003).

The signal-to-noise ratio ranges from 14 : 1 for the (r, φ) layers of the SVXII to 10 : 1 for the L00. The best (r, φ) position resolution achieved is 9 μm, using two-strip clusters in SVXII. The z_0 resolution is typically 70 μm. An active real-time optical survey keeps the SVXII axis parallel to the beam within 20 μm along the SVXII length. Tight assembling tolerances (10 μm in φ and 40 μm in r) combined with a set of off-line algorithms provide internal and global L00, SVXII, and ISL alignment accurate within 20 μm, and constantly monitored in time. The excellent overall accuracy of the silicon alignment is confirmed by the fluctuations of the measured impact parameters of prompt particles as a function of z and φ, which do not exceed 2 μm. This can be compared with a typical impact parameter resolution of a few tenths of microns. The average offline tracking efficiency is 94%. In the $1 \lesssim |\eta| \lesssim 2$ region, where no COT coverage is present, seeding the silicon-only track with calorimeter information provides efficiencies over 70%, with minimal fake rates.

The silicon information improves the impact parameter resolution of tracks which, depending on the number (and radial distance) of the silicon hits, may reach $\sigma_{d_0} \approx 20\,\mu\mathrm{m}$ (not including the transverse beam size). This value, combined with the $\sigma_T \approx 30\,\mu\mathrm{m}$ transverse beam size, is sufficiently small with respect to the typical transverse decay-lengths of heavy flavors (a few hundred microns) to allow separation of their decay-vertexes from production vertexes. The silicon tracker improves also the stereo resolutions up to $\sigma_\theta \approx 0.06^\circ$, and $\sigma_{z_0} \approx 70\,\mu\mathrm{m}$, while the transverse momentum and the azimuthal resolutions remain approximately the same of COT-only tracks.

3.4 OTHER DETECTORS

In this we briefly describe the sub-detectors not used in this analysis.

3.4.1 Time of Flight detector

The Time Of Flight detector (TOF) is a cylindrical array made of 216 scintillating bars [75] and it is located between the external surface of the COT and the cryostat containing the superconducting solenoid. Bars are 280 cm long and oriented along the beam axis all around the inner cryostat surface at an average radial distance of 138 cm. Both longitudinal sides of the bars collect the light pulse into photomultiplier and measure accurately the timing of the two pulses. The time between the bunch crossing and the scintillation signal in these bars defines the β of the charged particle while the momentum is provided by the tracking system. Particle Identification (PID) information is available through the combination of TOF information and tracking measurements. The measured mean time resolution is now 110 ps. This guarantees a separation between charged pions and kaons with $p_T \lesssim 1.6\,\mathrm{GeV}/c$ equivalent to 2σ, assuming Gaussian distributions. Unfortunately, in high luminosity conditions ($\mathscr{L} \gtrsim 5 \times 10^{31}\,\mathrm{cm}^{-2}\,\mathrm{s}^{-1}$) the occupancy of the single bars determines a degradation in efficiency, which is about 60% per track.

3.4.2 Calorimeters

Outside the solenoid, scintillator-based calorimetry covers the region $\eta_{\mathrm{det}} \leq 3.6$, and is devoted to the measurement of the energy deposition of photons, electrons and hadrons using the shower sampling technique.

The basic structure consists of alternating layers of passive absorber and plastic scintillator. Neutral particles and charged particles with a transverse momentum greater than about 350 MeV/c are likely to escape the solenoid's magnetic field and penetrate into the CDFII calorimeters.These are finely segmented in solid angle around the nominal collision point, and coarsely segmented radially outward from the collision point (in-depth segmentation.) Angular segmentation is organized in projective towers. Each tower has a truncated-pyramidal architecture having the imaginary vertex pointing to the nominal interaction point and the base is a rectangular cell in the $(\eta_{\mathrm{det}}, \varphi)$ space. Radial segmentation of each tower instead consists of two compartments, the inner (closer to the beam) devoted to the measure of the electromagnetic component of the shower, and the outer devoted to the measure of the hadronic fraction of energy. These two compartments are read independently through separated electronics channels.

A different fraction of energy release in the two compartments distinguishes photons and electrons from hadronic particles. CDFII calorimetry is divided in several independent subsystems presented in the following subsections.

Central region: CEM, CHA, WHA

The radial extension of the calorimeters in the central region is $1.73\,\mathrm{m} < r < 3.5\,\mathrm{m}$. The Central ElectroMagnetic Calorimeter (CEM) [76, 77] is constructed as four azimuthal arches (NE, NW, SE, SW) each of which subtends 180° and is divided into twelve 15° wedges. A wedge consists of 31 layers of 5 mm thick polystyrene scintillator interleaved with 30 aluminum-clad lead 3.2 mm thick sheets, divided along η_{det} into ten towers ($\delta\eta_{\mathrm{det}} \approx 0.11$ per tower). To maintain a constant thickness in X_0, compensating the $\sin(\theta)$ variation between towers, some lead layers are replaced with

increasing amounts of acrylic as a function of η_{det}[14]. Light from each tower is collected by sheets of acrylic wavelength shifter at both azimuthal tower boundaries and guided to two phototubes per tower. The spatial resolution of the CEM is about 2 mm. The outer two towers in one wedge (known as chimney towers) are missing to allow solenoid access, for a resulting total number of 478 instrumented towers. At a radial depth of $5.9X_0$, which is approximately the depth corresponding to the peak of shower development, the CEntral Strip multi-wire proportional chambers (CES) measure the transverse shower shape with ≈1.5 cm segmentation. A further set of multi-wire proportional chambers, the Central Pre-Radiator (CPR) [78] is located in the gap between the outer surface of the solenoid and the CEM. It monitors photon conversions started before the first CEM layer. Phototube gains are calibrated once per store using an automated system of Xenon or LED light flashers.

The hadronic compartment is the combination of two sub-systems: the Central HAdronic (CHA) and Wall HAdronic (WHA) [79] calorimeters. Analogously as in the CEM, in both systems four "C"-shaped arches contain 48 wedges. Each CHA wedge is segmented into 9 η_{det} towers matching in size and position the CEM towers. The WHA wedge instead consists of 6 towers of which three are matching CHA towers. Radially a CHA tower is constructed of 32 layers of 2.5 thick steel absorber alternating with 1.0 cm thick acrylic scintillator. WHA towers structure is similar but there are only 15 layers of 5.1 cm thick absorber.

The total thickness of the electromagnetic section corresponds to approximately $19X_0$ ($1\lambda_{\text{int}}$, where λ_{int} is the pion nuclear absorption length in units of $\text{g}\,\text{cm}^{-2}$), for a relative energy resolution $\sigma_E/E = 13.5\%/\sqrt{E\sin(\theta)} \oplus 2\%$.[15] The total thickness of the hadronic section corresponds to approximately $4.5\lambda_{\text{int}}$, for an energy resolution of $\sigma_E/E = 50\%/\sqrt{E\sin(\theta)} \oplus 3\%$ for the central, and $\sigma_E/E = 75\%/\sqrt{E\sin(\theta)} \oplus 4\%$ for the end-wall.

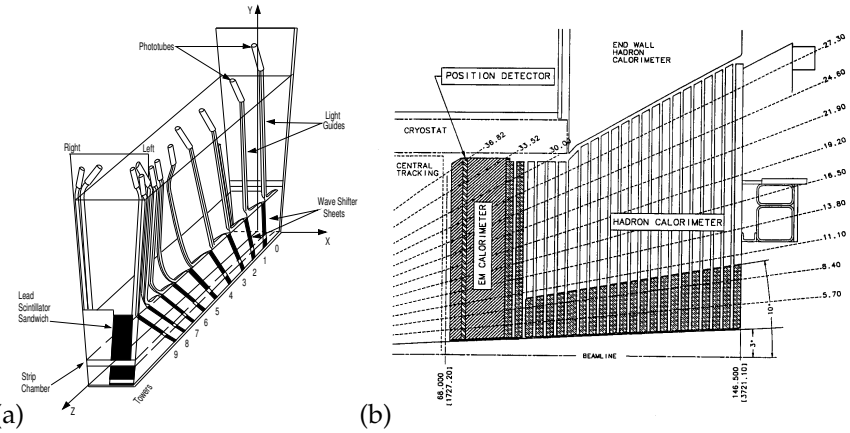

Figure 3.7: Schematic illustration of an azimuthal sector of the central electromagnetic calorimeter (a). Elevation view of one quarter of the plug calorimeter (b).

Forward region: PEM, PHA

The coverage of the $1.1 \leq |\eta_{\text{det}}| \leq 3.6$ region relies on the scintillating tile Plug calorimeter [80, 81, 82] which is composed of two identical devices, one installed

14 The number of lead layers varies from 30 in the innermost ($|\eta_{\text{det}}| \approx 0.06$) tower to 20 in the outermost ($|\eta_{\text{det}}| \approx 1.0$).

15 The first term is called the "stochastic" term and derives from the intrinsic fluctuations of the shower sampling process and of the PMT photo-electron yield. The second term, added in quadrature, depends on the calorimeter non-uniformities and on the uncertainty on the calibrations. All energies are in GeV.

in $\eta_{\text{det}} > 0$ region and the other in the $\eta_{\text{det}} < 0$. Each of these two halves has electromagnetic and hadronic compartments (see fig. 3.7(b)).

In each half, the absorber of the Plug ElectroMagnetic calorimeter (PEM) consists of 23 "doughnuts"- shaped lead plates, 2.77 m in outer diameter, which have a central hole where the beam pipe is located. Each plate is made out of 4.5 mm thick calcium-tin-lead sandwiched between two 0.5 mm thick stainless-steel sheets. Between the absorber plates are inserted the 4 mm thick scintillator tiles organized azimuthally in 15° triangularly-shaped wedges. The signal of each tile is collected independently by embedded wavelength-shifter fibers which guide it to the photomultipliers. A preshower detector consist of a thicker (10 mm) amount of scintillator installed in the first layer of PEM, while shower maximum sampling is performed at radial depth of $\approx 6X_0$ by two tilted layers of scintillator strips (pitch 5 mm).

Each half of the hadronic compartment, Plug HAdronic calorimeter (PHA), is azimuthally subdivided in 12 wedge-shaped modules each subtending 30°. In depth each module consists of 23 layers of 5 cm thick iron absorber alternated with 6 mm scintillator layers. Within each sampling layer the scintillator is arranged in tiles similar to those used in the PEM.

The total thickness of the electromagnetic section corresponds to approximately $21X_0$ ($1\lambda_{\text{int}}$), for an energy resolution of $\sigma_E/E = 16\%/\sqrt{E\sin(\theta)} \oplus 1\%$. The total thickness of the hadronic section corresponds to approximately $7\lambda_{\text{int}}$, for an energy resolution of $\sigma_E/E = 74\%/\sqrt{E\sin(\theta)} \oplus 4\%$.

3.4.3 Muon systems

CDFII is equipped with scintillating counters and drift tubes [83, 84] installed at various radial distances from the beam to detect muons and shielded by the iron structure of the inner detector. Scintillators serve as trigger and vetoes while the drift chambers measure the φ coordinate using the absolute difference of drift electrons arrival time between two cells, and the z coordinate by charge division. These systems cover the whole range of pseudorapidity $|\eta_{\text{det}}| < 2$ and are used only to identify the penetrating muon reconstructing a small segment of their path (stub) sampled by the chambers. The momentum measurement is performed by pointing back the stub to the corresponding track in the COT. The shield is constituted by the iron of the calorimeter, the return yoke and further steel walls intended to filter out the punch-through of hadrons. Different muon sub-systems cover different geometrical regions. In the $|\eta_{\text{det}}| < 0.6$ region moving outward from the beam we encounter the inner Central MUon detector (CMU) chambers at radial distance of 3.5 m. Approximately $5.4\lambda_{\text{int}}(\pi)$ of material separate the luminous region from the CMU resulting in about 1/220 high energy hadrons traversing the calorimeter and reaching the muon detectors.[16] In order to recognize and discard them, the Central Muon uPgrade (CMP) chambers lie in the same η_{det} region separated radially from the CMU by a 60 cm thick wall of steel achieving a rejection of 95% of the fake muons.

The muon coverage in the $0.6 < |\eta_{\text{det}}| < 1.0$ volume is ensured by the Central Muon eXtension (CMX) chambers, embedded in scintillator counters and placed at radius of 3.5 m. The Intermediate MUon detectors (IMU) are instead drift tubes covering the pseudorapidity range of $1.0 < |\eta_{\text{det}}| < 2.0$. CDFII triggers on muons only emerging at $|\eta_{\text{det}}| < 1.5$ where the muon coverage is segmented with sufficient granularity to survive high occupancies. The granularity of muon devices in the forward regions is less fine and not adequate for triggering, but sufficient for offline muon assignment to high p_{T} tracks going through that region.

16 This defines also a p_{T}threshold for muons reaching the CMU which is approximately 1.4 GeV/c.

3.4.4 Cherenkov Luminosity Counters

The luminosity ($\mathscr{L}$) is inferred from the average number of inelastic interactions per bunch crossing ($\overline{N}$) according to $\overline{N} \times f_{\text{b.c.}} = \sigma_{\text{p}\bar{\text{p}}-\text{in.}} \times \varepsilon \times \mathscr{L}$, where the bunch-crossing frequency ($f_{\text{b.c.}}$) is precisely known from the Tevatron RF, $\sigma_{\text{p}\bar{\text{p}}-\text{in.}} = 59.3 \pm 2.3\,\text{mb}$ is the inelastic $\text{p}\bar{\text{p}}$ cross-section resulting from the averaged CDF and E811 luminosity-independent measurements at $\sqrt{s} = 1.8\,\text{TeV}$ [85], and extrapolated to $\sqrt{s} = 1.96\,\text{TeV}$, and ε is the efficiency for detecting an inelastic scattering.

The Cherenkov Luminosity Counters (CLC) are two separate modules, covering the $3.7 \lesssim |\eta_{\text{det}}| \lesssim 4.7$ range symmetrically in the forward and backward regions [86]. Each module consists of 48 thin, 110–180 cm long, conical, isobutane-filled Cherenkov counters. They are arranged around the beam-pipe in three concentric layers and point to the nominal interaction region. The base of each cone, 6–8 cm in diameter and located at the furthest extremity from the interaction region, contains a conical mirror that collects the light into a PMT, partially shielded from the solenoidal magnetic field. Isobutane guarantees high refraction index and good transparency for ultraviolet photons. With a Cherenkov angle $\theta_C = 3.4°$, the momentum thresholds for light emission are $9.3\,\text{MeV}/c$ for electrons and $2.6\,\text{GeV}/c$ for charged pions. Prompt charged particles from the $\text{p}\bar{\text{p}}$ interaction are likely to traverse the full counter length, thus generating large signals and allowing discrimination from the smaller signals of angled particles due to the beam halo or to secondary interactions. In addition, the signal amplitude distribution shows distinct peaks for different particle multiplicities entering the counters. This allow a measurement of $\overline{N}$ with 4.4% relative uncertainty in the luminosity range $10^{31} \lesssim \mathscr{L} \lesssim 10^{32}\,\text{cm}^{-2}\,\text{s}^{-1}$. This accuracy, combined with the 4% relative uncertainty on the inelastic $\text{p}\bar{\text{p}}$ cross-section, results in an instantaneous luminosity measured with 5.9% relative uncertainty.

3.5 TRIGGER AND DATA ACQUISITION SYSTEM

From the rule of thumb $1\,\mu\text{b} = 1\,\text{Hz}$ at $\mathscr{L} = 10^{30}\,\text{cm}^{-2}\,\text{s}^{-1}$, we obtain that, at a typical Tevatron instantaneous luminosity $\mathscr{L} \approx 4 \times 10^{32}\,\text{cm}^{-2}\,\text{s}^{-1}$, and with an inelastic $\text{p}\bar{\text{p}}$ cross-section of $\sigma_{\text{p}\bar{\text{p}}-\text{in.}} \approx 60\,\text{mb}$, approximately 2.5×10^7 inelastic collisions per second occur, corresponding to one inelastic $\text{p}\bar{\text{p}}$ interaction per bunch crossing on average.[17] Since the read-out of the entire detector needs about 2 ms on average, after the acquisition of one event, another approximately 5000 interactions would occur and remain unrecorded. The percentage of events which are rejected because the trigger is busy processing previous events is referred to as trigger *deadtime*.

On the other hand, the average size of the information associated to each event from the $\mathcal{O}(10^6)$ total CDFII channels is 140 kB. Even in case of deadtime-less read-out of the detector, in order to record all events, an approximate throughput and storage rate of $350\,\text{GB}\,\text{s}^{-1}$ would be needed, largely beyond the possibilities of currently available technology.

Since the cross-sections of most interesting processes are 10^3–10^{12} times smaller than the inelastic $\text{p}\bar{\text{p}}$ cross-section, the above problems may be overcome with an on-line preselection of the most interesting events. This is the task of the trigger system, which evaluates the partial information provided by the detector and discards the uninteresting events on-line.

The CDFII trigger is a three-level system that selectively reduces the acquisition rate, with virtually no deadtime, *i. e.*, keeping each event in the trigger memory a time sufficient to allow for a trigger decision without inhibiting acquisition of the following

17 Abort gaps can be neglected for this estimate.

events (see fig. 3.8). Each level receives the accepted event from the previous one and, provided with detector information of increasing complexity and with more time for processing, applies a logical "OR" of several set of programmable selection criteria to make its decision.

Prior to any trigger level, the bunched structure of the beams is exploited to reject cosmic-ray events by gating the front-end electronics of all sub-detectors in correspondence of the bunch crossing. The front-end electronics of each sub-detector, packaged in Versa Module Eurocard modules hosted in about 120 crates, has a 42-cells deep pipeline synchronized with the Tevatron clock-cycle (*i. e.*, 132 ns).

The Tevatron clock picks-up a timing marker from the synchrotron RF and forwards this bunch-crossing signal to the trigger and to the front-end electronics. Since the inter-bunch time is 396 ns, the pipeline collects data corresponding to a maximum of $42 \times 132/396 = 14$ bunch crossings, automatically rejecting 2/3 of cycles corresponding to the crossing of empty buckets. For each crossing, data enter the pipeline for read-out and eventual use at Level-2, and a Level-1 decision on a preceding crossing is made before the corresponding data reach the end of the pipeline. The Level-1 has $132\,\text{ns} \times 42 \simeq 5.5\,\mu\text{s}$ to make its decision before the contents of the buffer is deleted. On a Level-1 accept, the data from the Level-1 buffer are passed to the four-cell Level-2 buffer integrated in the front-end electronics of each sub-detector, and the event is queued for a Level-2 decision. While data in a Level-2 buffer are being processed, they cannot be overwritten by incoming data corresponding to a subsequent Level-1 accept. If a Level-1 accept occurs while all four Level-2 buffers are occupied, trigger deadtime is incurred. The $5.5\,\mu\text{s} \times 4 \simeq 20\,\mu\text{s}$ latency of the Level-2 decision is less than approximately 80% of the average time between Level-1 accepts, to minimize deadtime. On a Level-2 accept, the entire detector is read-out, thereby emptying a cell in all detector buffers for the next event; the event is queued for read-out in Level-3 and for eventual storage to permanent memory.

The following description emphasizes the aspects of the trigger specific to this analysis: particular detail is devoted to the devices dedicated to the identification of tracks produced in decays displaced from the hard $p\bar{p}$ interaction vertex. These tracks populate events enriched in long-lived heavy-flavor decays, including the $B_s \to \phi\phi$ decays we wish to reconstruct.

3.5.1 Level-1

At Level-1, a synchronous system of custom-designed hardware processes a simplified subset of data in three parallel streams to reconstruct coarse information from the calorimeters (total energy and presence of single towers over threshold), the COT (two-dimensional tracks in the transverse plane), and the muon system (muon stubs in the CMU, CMX, and CMP chambers). A decision stage combines the information from these low-resolution physics objects, called "primitives", into more sophisticated objects, *e. g.*, track primitives are matched with muon stubs, or tower primitives, to form muon, electron, or jet objects, which then undergo some basic selections.[18]

Drift chamber track-processor

The eXtremely Fast Tracker (XFT) is a custom processor that identifies two-dimensional tracks in the (r, φ) view of the COT (transverse plane) in time with the Level-1 decision. It uses pattern matching to first identify short segments of tracks and then to link them into full-length tracks [87]. After classifying the hits of the four axial COT super-layers

18 A particle jet is a flow of observable secondary particles produced in a spatially collimated form, as a consequence of the hadronization of partons produced in the hard collision.

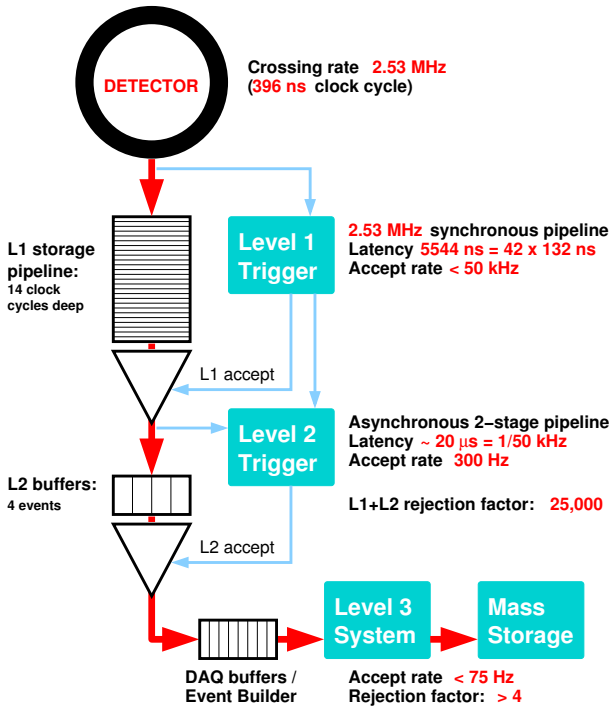

Figure 3.8: Functional block diagram of the CDFII trigger and data acquisition system.

in "prompt" (0–66 ns) or "delayed" hits (67–220 ns), depending upon the observed drift-time within the cell, track segments are reconstructed in each axial super-layer. A pattern-matching algorithm searches for coincidences between the observed combinations of hits in each super-layer — a minimum of 11 (out of 12) hits is required — and a set of predetermined patterns. If a coincidence between segments crossing four super-layers is found, two-dimensional XFT-tracks are reconstructed by linking the segments. The segments are compared with a set of about 2400 predetermined patterns corresponding to all tracks with $p_T \gtrsim 1.5\,\mathrm{GeV}/c$ originating from the beam line. The comparison proceeds in parallel in each of the 288 azimuthal 1.25°-sectors in which XFT logically divides the chamber. If no track is found using all four super-layers, then the best track found in the innermost three super-layers is output. The track-finding efficiency and the fake-rate with respect to the off-line tracks depend on the instantaneous luminosity, and were measured to be $\varepsilon \approx 96\%$, and 3%, respectively, for tracks with $p_T \gtrsim 1.5\,\mathrm{GeV}/c$ at $\mathscr{L} \simeq 10^{31}\,\mathrm{cm}^{-2}\,\mathrm{s}^{-1}$. The observed momentum resolution is $\sigma_{p_T}/p_T^2 \approx 0.017\,(\mathrm{GeV}/c)^{-1}$, and the azimuthal resolution is $\sigma_{\varphi_6} \approx 0.3°$, where φ_6 is the azimuthal angle of the track measured at the sixth COT super-layer, located at 106 cm radius from the beam line.

3.5.2 Level-2

At Level-2, an asynchronous system of custom-designed hardware processes the time-ordered events accepted by the Level-1. Additional information from the shower-maximum strip chambers in the central calorimeter and the axial hits in the SVXII is combined with Level-1 primitives to produce Level-2 primitives. A crude energy-clustering is done in the calorimeters by merging the energies in adjacent towers to the

energy of a seed tower above threshold. Level-1 track primitives matched with consistent shower-maximum clusters provide refined electron candidates whose azimuthal position is known with 2° accuracy. Information from the (r, φ) sides of the SVXII is combined with Level-1 tracks primitives to form two-dimensional tracks with resolution similar to the off-line one. Finally, an array of programmable processors makes the trigger decision, while the Level-2 objects relative to the following event accepted at Level-1 are already being reconstructed.

Silicon Vertex Trigger

Reconstructing decay vertexes on-line is technically challenging and requires constrained geometrical fitting of (previously reconstructed) high-resolution tracks at high event-rates. The Silicon Vertex Trigger (SVT) computes instead the impact parameters of the charged particles, which is faster than fully reconstructing their decay vertexes, but still provides information on the lifetime of the decaying particle [88, 89]. The full spatial resolution of silicon detectors is needed to discriminate $\mathcal{O}(100\,\mu\text{m})$ impact parameters from the $\mathcal{O}(10\,\mu\text{m})$ beam spot. Thus the SVT requires the coincidence of hits in four axial SVXII layers with a XFT track. Since the silicon signals are digitized only after the Level-1 accept decision, the SVT is used at Level-2, whose average latency is around 20 µs. Within this time, the SVT reconstructs two-dimensional tracks in the bending plane of the spectrometer with off-line resolution, a task that typically needs thousands of milliseconds to be accomplished by the off-line CPUs. SVT speed is largely due to a highly-parallelized structure and to the implementation of novel techniques both in pattern recognition and in track fitting.

The SVT receives in input the XFT tracks and the digitized pulse-heights from the SVXII layers. It first finds charge clusters in silicon, by converting a list of channel numbers and pulse heights into charge-weighed hit centroids. At this point the pattern recognition is separated in two stages. First, a low-resolution stage is implemented by grouping together adjacent detector channels into "super-bins". Their width in the azimuthal direction is programmable, with 250–700 µm typical values. A set containing about 95% of all super-bin combinations compatible with the trajectory of a charged particle with $p_T \gtrsim 2\,\text{GeV}/c$ originated from the beam line ("patterns") is calculated in advance from simulation and stored in a special design memories (Associative Memories [88, 89]) . For each azimuthal sector, the 32 768 most probable patterns are stored. On-line, an algorithm detects low-resolution candidate tracks called "roads" by matching super-bins containing hits with the stored patterns. A road is a combination four excited super-bins in different SVXII layers plus the XFT track parameters, which are logically treated as additional hits (see fig. 3.9(a)). In the Associative Memories system, maximum parallelism is exploited to speed-up the processing, using a working principle similar to the one of the bingo game: while the silicon hits are being read out, each "player" marks the matching super-bins on his "score-card"; each "bingo" corresponds to a road and is retained for further processing. A maximum of 64 roads per event, each one having a maximum of 8 hits per super-bin, is output. At this stage, pattern recognition is done during detector read-out with no additional processing time. The resolution is coarse enough to reduce the fraction of accidental combinations, but fine enough to separate most tracks. Once a track is confined to a road, most of the pattern recognition is done, leaving the remaining ambiguities, as multiple hits in the same super-bin, to the stage of track fitting.

In principle, no exact linear relation exists between the transverse parameters C, φ_0, and d_0 of a track in a solenoidal field, and the coordinates at which the track intersects a radial set of flat detector planes. But for $p_T \gtrsim 2\,\text{GeV}/c$, $|d_0| \lesssim 1\,\text{mm}$ and $|\Delta\varphi_0| \lesssim 15°$, a linear fit biases the reconstructed d_0 by at most a few percent. The track-fitting process exploits this feature by expanding the non-linear constraints

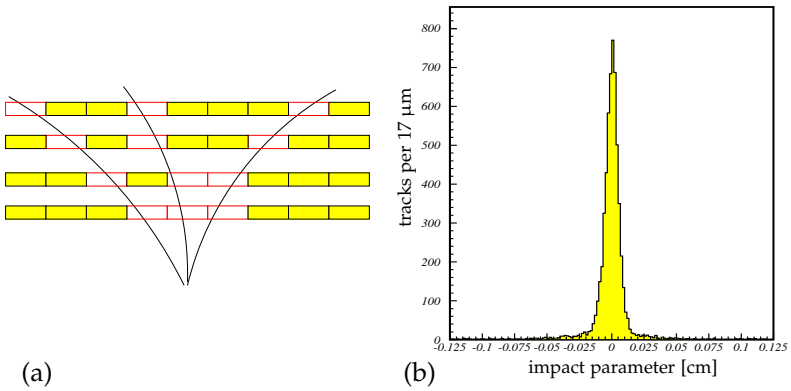

Figure 3.9: Schematic illustration of combinations of super-bins (in the transverse plane) corresponding to the passage of charged particles in four radial silicon layers (a). Impact parameter distribution as measured by the SVT (b).

and the parameters of the real track to first order with respect to the reference track associated to each road. A linear expansion in the hit positions of both the track parameters and the χ^2 is used. The fit process is thus reduced to computing a few scalar products, which is done within 250 ns per track. The needed constants, which depend on detector geometry and alignments, are evaluated in advance and stored in an internal memory. The output of the SVT are the reconstructed parameters of the two-dimensional track in the transverse plane: φ_0, p_T, and the impact parameter, d_0. The list of parameters for all found tracks is sent to Level-2 for trigger decision.

The SVT measures the impact parameter with a r.m.s. width $\sigma_{d_0,\mathrm{SVT}} \approx 35\,\mu\mathrm{m}$, with an average latency of 24 μs, 9 μs of which being spent waiting for the start of the read-out of silicon data. This resolution is comparable with the off-line one for tracks not using L00 hits, and yields a distribution of impact parameter of prompt tracks with respect to the z axis with $\sigma_{d_0} \approx 47\,\mu\mathrm{m}$ (see fig. 3.9(b)) when combined with the transverse beam-spot size.[19] The SVT efficiency is higher than 85%. This efficiency is defined as the ratio between the number of tracks reconstructed by SVT and all XFT-matched off-line silicon tracks that are of physics analysis quality.

The impact parameter is a quantity measured with respect to the beam. If the actual beam position in the transverse plane is shifted by an amount d_{beam} with respect to the origin of the SVT reference frame, all prompt tracks appear to SVT as having $\mathcal{O}(d_{\mathrm{beam}})$ impact parameters. This is relevant since the beam is usually displaced from its nominal $(0, 0, z)$ position. Between Tevatron stores, $\mathcal{O}(500\,\mu\mathrm{m})$ displacements in the transverse plane and $\mathcal{O}(100\,\mu\mathrm{rad})$ slopes with respect to the detector axis may occur. In addition, the beam can drift by $\mathcal{O}(10\,\mu\mathrm{m})$ in the transverse plane even during a single store. However, a simple geometric relation prescribes that the impact parameter of a track (d_0), calculated with respect to a point displaced from its production vertex, is a sinusoidal function of its azimuthal coordinate (φ_0):

$$d_0 = y_v \cos(\varphi_0) - x_v \sin(\varphi_0), \tag{3.9}$$

where $\vec{x}_v = (x_v, y_v)$ are the coordinates of the production vertex.

Using eq. (3.9), the SVT measures the actual coordinates of the beam position with respect to the detector system and subtracts them from the measured impact parameters, in order to provide physical impact parameters. Using about 10^5 tracks every 30

19 Prompt tracks are those associated to particles produced in the hard $p\bar{p}$ interaction.

seconds, six transverse beam positions (one for each SVXII semi-barrel) are determined on-line. The six samplings (one for each SVXII barrel) along the $\hat{z}$ direction provide a measurement of the slope of the beam with respect to the nominal z-axis.

For the proper measurement of impact parameters, the beam slope is more harmful than the transverse drift, because it breaks the cylindrical symmetry of the system. The SVT does not have access to the z_0 coordinate of tracks. For each track, only the longitudinal coordinate of the SVXII half-barrel that detected the track is known. But half-barrels are too long (16 cm) to allow for a reliable correction of the beam slope. When significant slopes are observed, the Tevatron beam division is alerted, and they apply a corrective action on the magnets.

Beam mis-alignments affect also the SVT efficiency. Owing to its modular structure and to the limited size of the pattern bank, the SVT can not identify charged particles that cross adjacent SVXII wedges. In normal conditions, these are only a small fraction of $p_T > 2\,\mathrm{GeV}/c$ particles, typically due to the bending trajectory and of the finite beam-spot size. However, in presence of beam offset from the nominal position, this fraction significantly increases, thus inducing SVT inefficiency.

3.5.3 Level-3

The digitized output relative to the Level-2-accepted event reaches Level-3 via optical fibers and it is fragmented in all sub-detectors. It is collected by a custom hardware switch that arranges it in the proper order and transfers it to commercial computers, running LINUX and organized in a modular and parallelized structure of 16 subsystems [90]. The ordered fragments are assembled in the *event record*, a block of data that univocally corresponds to a bunch crossing and is ready for the analysis of the Level-3 software. The event reconstruction benefits from full detector information and improved resolution with respect to the preceding trigger levels, including three-dimensional track reconstruction, tight matching between tracks and calorimeter or muon information, and calibration information. If an event satisfies the Level-3 requirements, the corresponding event record is transferred to mass storage at a maximum rate of $20\,\mathrm{MB\,s^{-1}}$. A fraction of the output is monitored in real time to search for detector malfunctions, to derive calibrations constants and to graphically display events. The Level-3 decision is made after the full reconstruction of the event is completed and the integrity of its data is checked, a process that takes a few milliseconds.

3.6 OPERATIONS AND DATA QUALITY

The proper operation of the detector and the quality of the on-line data-taking is continuously ensured by "crews" of five collaborators plus one technician which alternate on duty with eight-hours shifts, plus several sub-detector experts available on request. The on-line crew, in communication with the Tevatron crew, ensures smooth data-acquisition, monitors the crucial parameters of all sub-detectors, and intervenes in case of malfunctions. The average data-taking efficiency is 85%. The inefficiency is approximately equally shared in a 5% arising at the beginning of the store, when the detector is not powered while waiting for stable beam conditions, a 5% due to trigger deadtime, and a 5% due to unexpected detector or Data AcQuisition (DAQ) problems. When no beam is present, cosmic-rays runs are taken, or calibrations of the sub-detector are done. During the Tevatron shut-down periods, the crew coordinates and helps the work of experts that directly access the detector.

Each time that at least one of the trigger paths fires, an "event" is labeled with a progressive number. Events are grouped into runs, *i. e.*, periods of continuous data-

taking in constant configurations of trigger table, set of active sub-detectors and so forth.[20] Several parameters of the operations (*e. g.*, beam-line position and slope, set of calibrations, etc.) are stored in the database on a run-averaged format.

All data manipulations occurring some time after the data are written to permanent memories are referred to as *off-line* processes, as opposed to the on-line operations that take place in real time, during the data-taking. The most important off-line operation is the processing with a centralized *production* analysis that generates collections of high-level physics objects suitable for analysis, such as tracks, vertexes, muons, electrons, jets, etc. from low-level information such as hits in the tracking sub-detectors, muon stubs, fired calorimeter towers, etc. [91]. During the production, more precise information about the detector conditions (*e. g.*, calibrations, beam-line positions, alignment constants, masks of malfunctioning detector-channels, etc.) and more sophisticated algorithms are used than those ones available at the Level-3 of the trigger. The production may be repeated when improved detector information or reconstruction algorithms become available: this typically occurs once or twice every year. The reprocessing uses large farms of commercial processors that reconstruct approximately 10^7 events per day employing approximately 2–5 s per event with 1 GHz CPU.[21] The added information increases the event size by typically 20% after production.

To ensure homogeneous data-taking conditions, each run undergoes a quality inspection. On-line shift operators, off-line production operators, and sub-detector experts certify in what fraction of data the running conditions for all relevant sub-detectors are compliant to physics-quality standards.

When detectable problems of the detector occur, the data-taking is quickly stopped, so very short runs are likely to contain corrupted data. Runs with fewer than 10^8 live Tevatron clock-cycles, or fewer than 10^4 (10^3) Level-1 (Level-2) accepts, or containing data corresponding to an integrated luminosity $\int \mathscr{L}\, dt < 1\,\mathrm{nb}^{-1}$ are excluded from physics analysis. On-line shift operators further exclude the runs in which temporary or test trigger tables were used.[22] Runs whose data underwent problems or software crashes during the production are excluded off-line.

Accurate integrated luminosity measurements are ensured in physics-quality data by requiring the CLC to be operative during the data-taking and by verifying that a set of luminosity and beam-monitor probe quantities are within the expected ranges. Shift operators ensure that Level-1 and Level-2 trigger operate correctly and that the rate of SVXII data corruption errors is smaller than 1%.[23] SVT experts verify that the on-line fit and subtraction of the beam position is done correctly and that the SVT occupancy is within the expected limits. In addition, higher level quantities, such as event yields of $J/\psi \to \mu^+\mu^-$, $D^0 \to K^-\pi^+$, and $D^{\star +} \to D^0\pi^+$ decays are monitored on-line and are required to be within the expected ranges. For analyses that use COT information, the minimum integrated luminosity required is $10\,\mathrm{nb}^{-1}$ and the fraction of noisy COT channels is required to be smaller than 1%.

20 The data acquisition might need to be interrupted and recovered for several motivations, including the need for enabling or disabling a sub-detector, the need for a change in the trigger table, a problem in the DAQ chain and so forth.

21 The event size, and the processing-time increase roughly linearly with the instantaneous luminosity.

22 It is sometimes necessary to test new configurations of the trigger selections in a real data-taking condition to monitor trigger rates, performance and so on.

23 The read-out of the silicon detector and the proper integration of the information in the on-line infrastructure is a complex operation which, occasionally, leads to a certain fraction of data to be improperly processed.

3.7 MONTE CARLO SIMULATION OF DETECTOR AND TRIGGER

Estimation of the fraction of events of a certain type that escape the detector acceptance, or detailed studies of the expected response of the detector to the passage of particles is a common need in many analyses. Usually, complex detector geometries and the numerous effects that need to be accounted for in predicting their response make it the analytical derivation of the relevant distributions impractical or impossible. MC techniques are an useful and widely-used tool to solve this problem. We provide here a short overview of the standard CDFII simulation. Further details can be found in [92].

In the standard CDFII simulation, the detector geometry and material are modelled using the version 3 of the GEANT package [93] tuned to test-beam and collision data. GEANT receives in input the positions, the four-momenta, and the identities of all particles produced by the simulated collisions that have long enough lifetimes to exit the beam pipe. It simulates their paths in the detector, modelling their interactions (*bremsstrahlung*, multiple scattering, nuclear interactions, photon conversions, etc.) and the consequent generation of signals on a single channel basis. Specific packages substitute GEANT for some sub-detectors: the calorimeter response is simulated with GFLASH, a faster parametric shower-simulator [94] tuned for single-particle response and shower-shape using test-beam data (8–230 GeV electrons and charged pions) and collision data (0.5–40 GeV/c single isolated tracks); the drift-time within the COT is simulated using the GARFIELD standard package [95] further tuned on data; the charge-deposition model in the silicon uses a parametric model, tuned on data, which accounts for restricted Landau distributions, production of δ-rays, capacitive charge-sharing between neighboring strips, and noise [96].[24] Furthermore, the actual trigger logic is simulated. The output of the simulated data mimics the structure of collision data, allowing their analysis with the same reconstruction programs used for collision data.

The detector and trigger configuration undergo variations during data-taking. Minor variations may occur between runs, while larger variations occur, for instance, after major hardware improvements, or Tevatron shut-down periods. For a more detailed simulation of the actual experimental conditions, the simulation has been interfaced with the on-line database that reports, on a run-by-run basis, all known changes in configuration (position and slope of the beam line, relative mis-alignments between sub-detectors, trigger-table used, set of SVT parameters) and local or temporary inefficiencies in the silicon tracker (active coverage, noisy channels, etc.). This allows us to simulate the detailed configuration of any set of real runs and to use it, after proper luminosity reweighing, for modeling the realistic detector response in any given subset of data.

24 The δ-rays are knock-on electrons emitted from atoms when the passage of charged particles through matter results in transmitted energies of more than a few keV in a single collision.

4 DATA SET AND RECONSTRUCTION

CONTENTS

THE RESULT of any measurement is based on the amount and quality of the data collected: this chapter describes the samples of data used to perform the analyses reported. These data was recorded by the CDFII detector from a period starting from March 2001 till April 2008. The sample used corresponds to an integrated luminosity of 2.9 fb^{-1}.

In order to get the desired information, the events of interest (referred to as "signal") need to be extracted from the multitude of other uninteresting events ("background"). Since the signal selection was performed in the $B_s \to \phi\phi$ branching ratio analysis [29], the purpose here is to briefly summarize the two main stages of this process. The first step is the on-line trigger selection, which collects events most likely containing B decays. The off-line selection is the second step: it is aimed at obtaining the data sample such that the statistical uncertainties on the quantities one wishes to measure are minimized.

4.1 USEFUL VARIABLES

Before discussing the details of trigger and off-line selection, it is useful to define some relevant quantities used in the analysis. All quantities are calculated in the laboratory frame and are illustrated in fig. 4.1. All of them can be defined for each particles of the two decays of interest ($B_s \to \phi\phi \to [K^+K^-][K^+K^-]$ and $B_s \to J/\psi\phi \to [K^+K^-][\mu^+\mu^-]$). They are:

TRANSVERSE MOMENTUM ($\vec{p}_T$): the projection of the momentum vector onto the transverse plane.[1] Another useful quantity used in the selection is the scalar sum of the transverse momenta of the two decay particles, $\sum p_T = p_T^{(1)} + p_T^{(2)}$.

1 The plane perpendicular to the proton beam direction, in which the profile of the interaction region is approximately Gaussian with width $\sigma \simeq 30\,\mu\text{m}$.

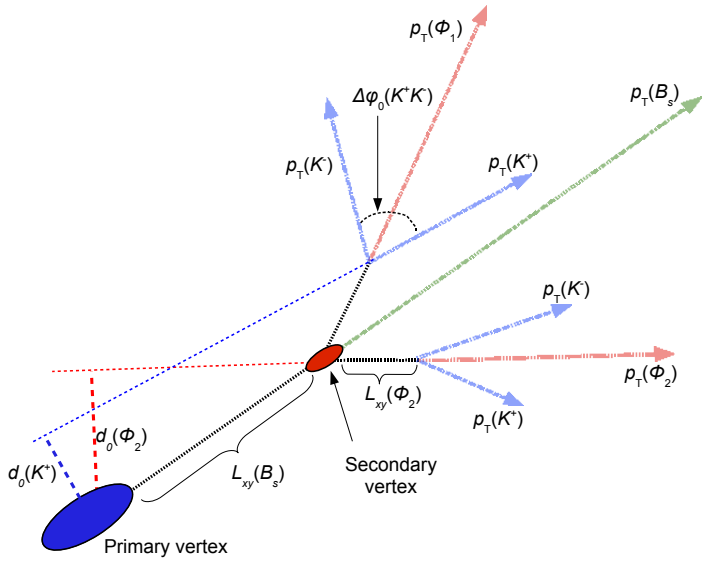

Figure 4.1: Illustration of a $p\bar{p}$ event containing a $B_s \to \phi\phi \to [K^+K^-][K^+K^-]$ projected into the transverse plane. Ellipses indicate vertexes, arrows indicate the transverse momenta (*i. e.*, the direction) of charged particles. Nothing is to scale.

PRIMARY VERTEX: the space-point of the reconstructed primary $p\bar{p}$ interaction, where a b-quark pair, once produced, quickly hadronizes to a b-hadron pair. An event may contain multiple primary vertexes due to multiple hard $p\bar{p}$ collisions occurring in the same bunch-crossing ("pile-up" event[2]).

SECONDARY VERTEX: the space-point in which the decay of a long-lived particle occurs. Its displacement with respect to the primary vertex in the transverse plane are indicated by the vector

$$\vec{x}_v = \vec{\beta}_T \gamma c t = (\vec{p}_T/m)ct, \tag{4.1}$$

for a particle of mass m and momentum p that decays at a time t after its production. Multiple secondary vertexes may be present in the same event. They can be due to the intersection of tracks from various sources, including the decay of the other heavy-flavor produced in the event, the decay of additional heavy-flavors produced in a pile-up event, fake (*i. e.*, due to accidental combinations of noise hits) or mis-measured (*i. e.*, partially contaminated by noise hits) tracks.

TRANSVERSE DECAY-LENGTH (L_T or L_{xy}): the displacement of the secondary vertex with respect to the primary one, projected onto the transverse momentum vector of the decaying particle:

$$L_{xy} = \frac{\vec{p}_T \cdot \vec{x}_v}{p_T} \tag{4.2}$$

2 When a beam of protons crosses a beam of antiprotons, multiple hard interactions may occur between different proton-antiproton pairs. Each hard interaction contribute with an associated fragmentation process and underlying event.

IMPACT PARAMETER (d_0): the component in the transverse plane of the distance of closest approach between a track and the primary vertex. This is a signed quantity defined as

$$d_0 = \frac{\hat{z} \cdot (\vec{p}_T \times \vec{x}_v)}{p_T}. \tag{4.3}$$

The impact parameter is typically different from zero for the decay products of long-lived particles, while it is comparable with the convolution of its resolution and the transverse size of the beam for particles produced in the proximity of the primary vertex (prompt background).

AZIMUTHAL OPENING ANGLE ($\Delta\varphi$): the opening angle between the two outgoing decay particles projected on the transverse plane.

PSEUDORAPIDITY OPENING "ANGLE" ($\Delta\eta$): the difference of the pseudorapidities of the two outgoing decay particles.

Some variables distributions of the particles of the decays under study are shown throughout this chapter.

4.2 ON-LINE SELECTION: THE TWO TRACK TRIGGER

Different analyses require different selection criteria. A trigger system is used to identify interesting events for a specific analysis, within the large rate of $p\bar{p}$ collisions. Over the course of a Tevatron store the luminosity decreases. In order to fully use the available bandwidth, the trigger criteria have to vary accordingly to the luminosity. Higher trigger rates at high luminosity arise from both an increase in the real physics rate as well as an increase in fake triggers due to multiple interactions. As the luminosity falls, the trigger bandwidth becomes under-utilized and lower purity triggers are thus enabled through a system that is used to automatically increase their prescale level and to prioritize the various triggers paths.

For both $B_s \to \phi\phi$ and $B_s \to J/\psi\phi$ decays we used the Two Track Trigger (TTT) selection. With TTT it is intended a peculiar trigger system made of a collection of trigger paths, called "scenarios", which aim at identifying heavy flavor decays based upon kinematics, topology and decay time information. They are all characterized by the presence of at least a pair of displaced tracks to reconstruct a vertex.

B mesons have a relatively long lifetime because their decays are governed by weak interactions. In fact they fly on average 0.5 mm before decaying, which is a larger distance than the intrinsic beam size. Thus their decay products are characterized by a non-zero impact parameter. This turns out to be very convenient for their identification. The TTT paths use the precise information on the track hits from the silicon vertex detector with the SVT system that looks for displaced tracks at on-line level. The TTT is thus able to trigger on long-lived particles, collecting data samples enriched in events containing bottom and charm hadrons: it is extremely powerful in rejecting light flavor (u, d, s) backgrounds.

The main TTT characteristics are:

LEVEL-1 selection: a pair of XFT tracks with a lower cut on the p_T of the tracks, on the $\sum p_T$ of the tracks, and an upper cut on $\Delta\varphi_6$, the opening angle between the two tracks, as measured at COT super-layer 6.

LEVEL-2 selection: the XFT tracks are matched with the SVXII by SVT, which computes track parameters: they must satisfy the criteria from Level-1 in addition to cuts

on d_0 and L_{xy}. These last two cuts are very efficient at rejecting the light quarks background.

LEVEL-3 selection: approximately same cuts of Level-2 using the fit based on the full detector information COT+SVXII. At this stage three dimensional fits are available and it is possible to apply a cut on the distance between the closest approach to the z axis of the tracks, Δz_0.

Our analysis uses the data sample collected with three TTT trigger paths:

- B_CHARM_HIGHPT,
- B_CHARM_L1
- B_CHARM_LOWPT.

Their selections are reported in tab. 5. The B_CHARM_HIGHPT trigger provides a sample with higher purity (defined as signal-to-background ratio) and lower trigger rate compared to the B_CHARM_L1 and B_CHARM_LOWPT. At moderate instantaneous luminosity, bandwidth becomes available and B_CHARM_L1 is enabled with a dynamic prescale. Finally B_CHARM_LOWPT is active at low luminosity.

	Level-1	Level-2	Level-3
	XFT tracks	SVT tracks	COT+SVXII tracks
B_CHARM_HIGHPT	opposite charge $p_T > 2.5\,\text{GeV}/c$ $\Delta\varphi_6 < 135°$ $\sum p_T > 6.5\,\text{GeV}/c$	opposite charge $p_T > 2.5\,\text{GeV}/c$ $2° < \Delta\varphi_0 < 90°$ $\sum p_T > 6.5\,\text{GeV}/c$ $120\,\mu\text{m} < d_0 < 1000\,\mu\text{m}$ $L_{xy} > 200\,\mu\text{m}$	opposite charge $p_T > 2.5\,\text{GeV}/c$ $2° < \Delta\varphi_0 < 90°$ $\sum p_T > 6.5\,\text{GeV}/c$ $80\,\mu\text{m} < d_0 < 1000\,\mu\text{m}$ $L_{xy} > 200\,\mu\text{m}$ $\lvert\Delta z_0\rvert < 5\,\text{cm}$
B_CHARM_L1	opposite charge $p_T > 2.0\,\text{GeV}/c$ $\Delta\varphi_6 < 135°$ $\sum p_T > 5.5\,\text{GeV}/c$	opposite charge $p_T > 2.0\,\text{GeV}/c$ $2° < \Delta\varphi_0 < 90°$ $\sum p_T > 5.5\,\text{GeV}/c$ $120\,\mu\text{m} < d_0 < 1000\,\mu\text{m}$ $L_{xy} > 200\,\mu\text{m}$	opposite charge $p_T > 2.0\,\text{GeV}/c$ $2° < \Delta\varphi_0 < 90°$ $\sum p_T > 5.5\,\text{GeV}/c$ $120\,\mu\text{m} < d_0 < 1000\,\mu\text{m}$ $L_{xy} > 200\,\mu\text{m}$ $\lvert\Delta z_0\rvert < 5\,\text{cm}$
B_CHARM_LOWPT	$p_T > 2.0\,\text{GeV}/c$ $\Delta\varphi_6 < 90°$	$p_T > 2.0\,\text{GeV}/c$ $\Delta\varphi_0 < 90°$ $120\,\mu\text{m} < d_0 < 1000\,\mu\text{m}$ $L_{xy} > 200\,\mu\text{m}$	$p_T > 2.0\,\text{GeV}/c$ $2° < \Delta\varphi_0 < 90°$ $120\,\mu\text{m} < d_0 < 1000\,\mu\text{m}$ $L_{xy} > 200\,\mu\text{m}$ $\lvert\Delta z_0\rvert < 5\,\text{cm}$

Table 5: B_CHARM_HIGHPT, B_CHARM_L1 and B_CHARM_LOWPT trigger paths selections.

In this work, we refer to exclusive trigger configurations. These are defined as follow:

- HIGHPT: only B_CHARM_HIGHPT;
- ScA (Scenario A) : events selected by B_CHARM_L1 and not by B_CHARM_HIGHPT;
- LOWPT: events selected by B_CHARM_LOWPT but not by both B_CHARM_L1 and B_CHARM_HIGHPT.

Their percentages on the total sample are listed in tab. 6 for both decays. We request the matching between at least two reconstructed tracks and the SVT tracks. The confirmation of the B_CHARM_LOWPT trigger selections is imposed.

4.3 OFF-LINE SELECTION

In fig. 4.2 the distribution of the $K^+K^-K^+K^-$ invariant mass after only trigger selection is shown: no evident mass signal is recognizable in the B mass window. Indeed, the on-line selection is not sufficient: a further selection is needed to minimize the background fraction and extract the signal from the data stored. This is performed by the off-line selection.

Trigger Paths	Fractions	
	$B_s \to \phi\phi$	$B_s \to J/\psi\phi$
HIGHPT	0.39 ± 0.05	0.42 ± 0.02
ScA	0.38 ± 0.05	0.33 ± 0.02
LOWPT	0.22 ± 0.04	0.26 ± 0.02

Table 6: Trigger paths fractions (exclusive selection).

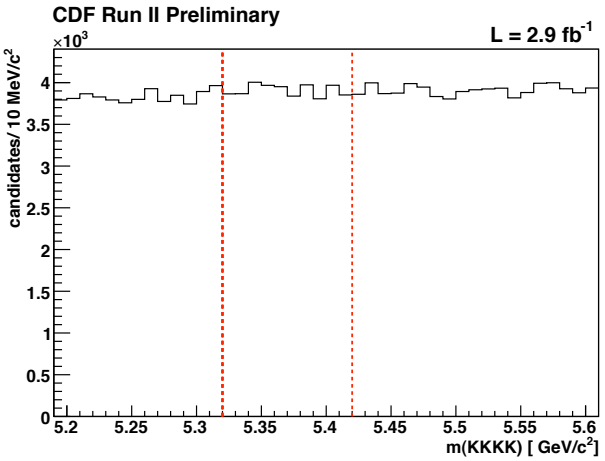

Figure 4.2: Four kaons invariant mass after on-line selections. The two red dotted line represent the region around the B_s mass.

4.3.1 Data Format

We use the `BStntuple` framework [97], which is an extension of the `Stntuple` [98] framework developed in CDF to minimize the computation time and storage space. The `BStntuple` contains structures that hold the reconstructed candidates informations, the stable and decaying objects. The format allows several potential decay candidates in the same event to share links to common data blocks.

In order to obtain a smaller size `BStntuple`, a skimming procedure was performed on the $B_s \to \phi\phi$ block mainly aimed to reduce the background by applying only a loose selection criteria on the B candidates. We choose to cut on variables which have very similar behaviour for $B_s \to \phi\phi$ and $B_s \to J/\psi\phi$ decays introducing little or no inefficiency for $B_s \to \phi\phi$; they are:

- $L^B_{xy} > 200\,\mu\text{m}$ for the transverse decay-length of the reconstructed B;
- $p^B_T > 5.0\,\text{GeV}/c$ for its transverse momentum.

For the $B_s \to J/\psi\phi$ reconstruction, in the `BStntuple` the constraint that the $\mu^+\mu^-$ invariant mass is equal to the $J\psi\phi$ mass value reported in the Particle Data Group (PDG) is required.

4.3.2 Selection Optimization

In the off-line selection, one has to choose the relevant variables which are able to discriminate between the signal and the background. Then, a cut on each of this variables must be applied. In the past [28] the cut selection was decided with the

aim to maximize the chance of either observing for the first time the $B_s \to \phi\phi$ or setting a limit. In the present circumstances we are instead interested in minimizing the statistical uncertainty in our measurements.

For any given sample, an optimization of the selection is a procedure that selects a sub-sample that provides the smallest (expected) statistical uncertainty on the quantity one wishes to measure. In principle, to define a correct optimization, one should try all possible configurations of selection requirements, repeat the measurement in each of the resulting sub-samples, and then apply the optimal selection. In practice, the number of the possible selections is often so large that repeating the full measurement many times may become difficult. However, a fast and reliable method to evaluate the resolution expected from a measurement is provided by the Minimum Variance Bound (MVB) [99, 100]. Given the data, the MVB provides an upper bound to the precision that can be achieved on a parameter, whatever the estimation procedure used.

In the simplified case of a counting experiment to determine the number S of signal events within a total number of $S + B$ events (where B is the number of background events), the expected statistical resolution σ on the signal yield, estimated with the MVB, obeys the following expression:

$$\frac{1}{\sigma} \propto \frac{S}{\sqrt{S+B}} \tag{4.4}$$

The optimal selection would be one that maximizes eq. (4.4): this expression, which is rigorously valid for a counting experiment, is still sufficiently accurate in the case of a likelihood fit of a continuous distribution.

This is what was performed in the branching ratio analysis for the selection optimization, both of $B_s \to \phi\phi$ and $B_s \to J/\psi\phi$ decays. In this particular case only kinematic variables are used, since these where the most reliable ones. These variables are:

- for the $B_s \to \phi\phi$ decay:
  - L^B_{xy}: transverse decay length of the reconstructed B;
  - d^B_0: impact parameter of the reconstructed B;
  - $d^\phi_{0\,\mathrm{max}}$: impact parameter of the ϕ with higher momentum;
  - $p^{\mathrm{min}}_{\mathrm{T}}$: transverse momentum of the softer kaon;
  - χ^2_{xy}: χ^2 of the fit used in the reconstruction of the secondary vertex;
- for the $B_s \to J/\psi\phi$ decay:
  - L^B_{xy}: transverse decay length of the reconstructed B;
  - d^B_0: impact parameter of the reconstructed B;
  - $p^\phi_{\mathrm{T}\,\mathrm{min}}$: transverse momentum of the ϕ;
  - $p^{J/\psi}_{\mathrm{T}\,\mathrm{min}}$: transverse momentum of the J/ψ;
  - χ^2_{xy}: χ^2 of the fit used in the reconstruction of the secondary vertex;

The distributions of these variables are shown in fig. 4.3. Since we are using the same data sample selected of that measurement, we address to [29] for optimization's details and we report here only the results. The optimized cuts for the two signals are summarized in tab. 7.

Variables		Requirements	
		$B_s \to \phi\phi$	$B_s \to J/\psi\phi$
L^B_{xy}	[μm]	> 330	> 290
$p^K_{\mathrm{T}\,\mathrm{min}}$	[GeV/c]	> 0.7	
$p^\phi_{\mathrm{T}\,\mathrm{min}}$	[GeV/c]		> 1.4
χ^2_{xy}		< 17	< 15
d^B_0	[μm]	< 65	< 80
$d^\phi_{0\,\mathrm{max}}$	[μm]	> 85	
$p^{J/\psi}_{\mathrm{T}\ \mathrm{min}}$	[GeV/c]		> 2.0

Table 7: Optimized selections found in [29] following MVB.

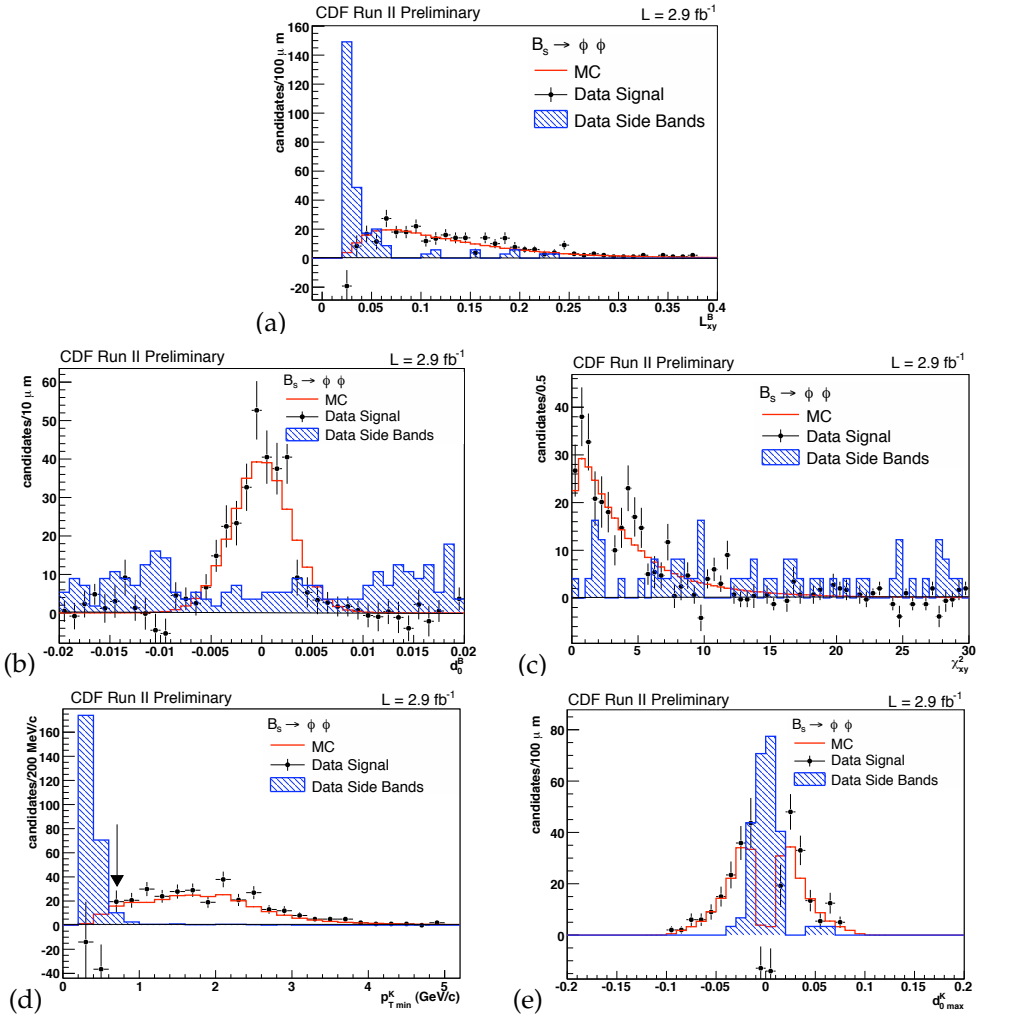

Figure 4.3: Variables used in the $B_s \to \phi\phi$ selection: L^B_{xy} (a), d^B_0 (b), χ^2_{xy} (c), $p^K_{\mathrm{T}\,\mathrm{min}}$ (d) and $d^\phi_{0\,\mathrm{max}}$ (e). The black points are side-bands subtracted data (see Sect. 4.5); the red line is the reweighted MC; the blue histogram is the sidebands data distribution.

4.4 THE FINAL DATA SAMPLE

Applying the optimized cuts the invariant mass distributions, $m_{K^+K^-K^+K^-}$ for the $B_s \to \phi\phi$ and $m_{K^+K^-\mu^+\mu^-}$ for the $B_s \to J/\psi\phi$, are obtained (fig. 4.4 and fig. 4.5). These provides us with a first insight on the background and signal composition. In these distributions at least three components can be identified:

THE SIGNAL: from the branching ratio analysis, we have the following number of signal events:

	$B_s \to \phi\phi$	$B_s \to J/\psi\phi$
Yield	295 ± 20	1766 ± 48

These yields are extract from a binned fit [29]: the fit function used is the sum of two gaussians (having the same mean value but different resolutions) and a decreasing exponential. They are described in the next chapter.

COMBINATORICS BACKGROUND: these are random combinations of charged tracks accidentally satisfying the selection requirements. They produce a continuous invariant B_s mass distribution and we expect a smooth slowing decreasing distribution in the signal region. It is the more important source of background in our analysis.

PHYSICS BACKGROUND: it is due to partially reconstructed heavy flavor decays or to an incorrect mass assignment to the tracks of other B meson decays (they are often referred to as *reflections*). We expect a distribution with a peak under the signal:

- for the $B_s \to \phi\phi$: the decays that could produce reflections in the B_s mass window are: $B_d \to \phi K^\star \to [K^+K^-][K^{+(-)}\pi^{-(+)}]$ and $B_s \to \bar{K}^\star K^\star \to [K^{+(-)}\pi^{-(+)}][K^{+(-)}\pi^{-(+)}]$; these reflections occur when the $K^\star$ is incorrectly reconstructed as a ϕ. The estimated number of reflection events is [29]:

	$B_s \to \bar{K}^\star K^\star$	$B_s \to \phi K^\star$
Events	0	8 ± 3
Fraction respect to signal events [%]	10^{-6}	3 ± 1

  Since its tiny percentage respect to the signal events, the $B_d \to \bar{K}^\star K^\star$ reflection is neglected.

- for the $B_s \to J/\psi\phi$: the more frequent decay is the $B_d \to J/\psi K^\star \to [\mu^+\mu^-][K^{+(-)}\pi^{-(+)}]$ decay; it occurs when in the reconstruction the daughter tracks of the $K^\star$ are assumed to be two kaons and an incorrect invariant mass is computed. The estimated number of reflection events is [29]:

	$B_d \to J/\psi K^\star$
Events	70 ± 20
Fraction respect to signal events [%]	4 ± 1

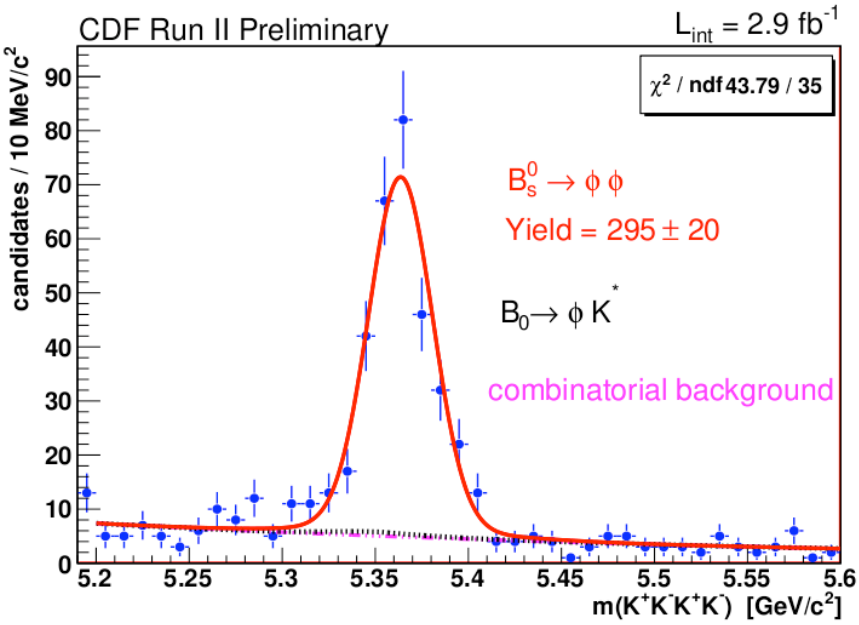

Figure 4.4: Background and signal composition in the $B_s \to \phi\phi$ decay. The blue points represent data after the optimized selection; the red line is the total fit distribution; in black the reflection component; in purple the combinatorial background.

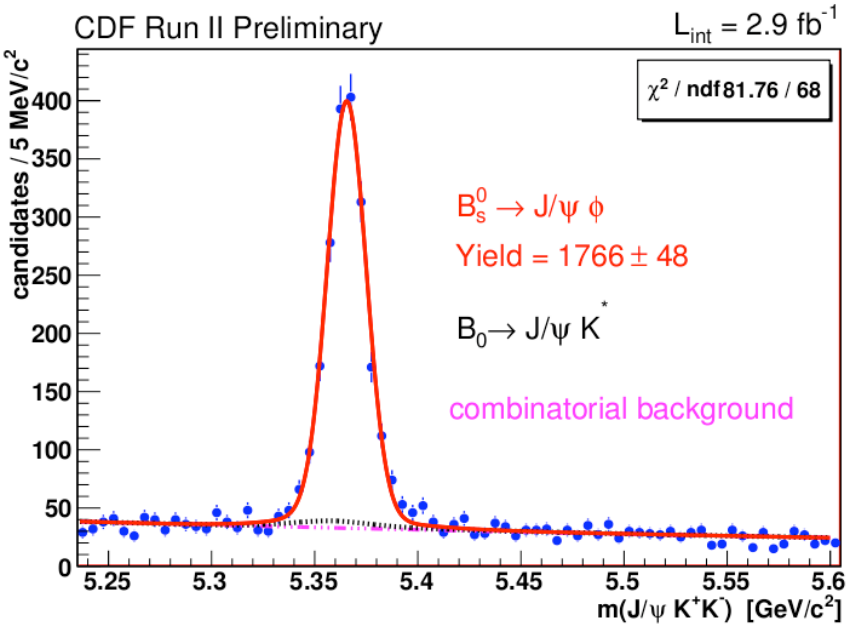

Figure 4.5: Background and signal composition in the $B_s \to J/\psi\phi$ decay. The blue points represent the data satisfying the off-line selection; the red line is the total fit distribution; in black the reflection component; in purple the combinatorial background.

4.5 MONTE CARLO DATA

In this analysis, simulation of B production and decay processes and of the subsequent detector response is used for several reasons:

- to model physics background;
- to model the acceptance of the combined detector and trigger system in the space of helicity (transversity) angular variables;
- to get distribution of B decay time;
- to test the fitter framework.

An analytical treatment of all the interactions involved from the $p\bar{p}$ collisions to B production, decay, and the interactions with matter in the detector is simply impossible. Such a treatment in any case would be unnecessarily detailed for the tasks described above. The alternative method is to use numerical simulation to carry out these tasks. The algorithms used all involve some type of random sampling to simulate processes, and are collectively called Monte Carlo (MC) simulation. The simulation is divided into several steps, which reproduce in order the main physical processes and processing steps involved in collecting data from real $p\bar{p}$ interactions.

The first step in simulation is the treatment of the $p\bar{p}$ hard scattering, and the outgoing quark and gluon collision products, followed by simulation of the fragmentation and hadronization processes which yield hadrons and associated jets. We used the BGENERATOR package [101]: it concentrates on producing only one B meson per event, which yields a great advantage in computational speed. On the other hand, by design it does not mimic the full collision environment, as the PYTHIA package could perform. For our purposes, BGENERATOR is sufficient since we wish to model single B decay samples.

The second step is the simulation of the full decay chain of the B mesons under study. For this task, we use the EVTGEN package [102]. EVTGEN is specialized for heavy flavor decays and accounts correctly for quantum mechanical interference effects. In order to model the detector angular acceptance for both $B_s \to \phi\phi$ and $B_s \to J/\psi\phi$, we use the phase-space decay model of EVTGEN. Phase-space means that all spins of the particles in the final state are averaged. This yields flat distributions in the angular variables whose acceptance we wish to study.

The third step in simulation incorporates the interaction of the decay products (K^+K^- and $\mu^+\mu^-$) with the detector material. For this task we use the CDFSIM package [103], which is a CDFII-specific full detector simulation based on the GEANT simulator [104]. The final step is the simulation of the triggering and event reconstruction that data events pass through. CDFSIM outputs simulated events with the same data banks as the raw real data events.

The detector and trigger configurations have undergone several variations during Run II. The simulation can access the databases and thus allows us to simulate the detailed configuration of any set of real data-taking runs for modeling the realistic detector response in any given subset of data. On the other hand, the MC is not able to reproduce exactly the trigger behavior of the trigger-paths which have a built-in dependence on the instantaneous luminosity, because this information is not fully stored in the database. In order to use all the trigger paths, in [29] it was checked that, once we reweight MC events in a way suitable to reproduce the different trigger mixture observed in data, a sufficiently good agreement is observed in all relevant variables.

The output of the MC simulation is then processed with the software package which reconstructs B decays and writes the output events in the `BStntuple` format, allowing

us an easier comparison between MC and data. Some plots of these comparisons are shown in the following figs. 4.6 – 4.7, and in the previous fig. 4.3. For other distributions we point to [29]. In the comparison, we adopt the following nomenclature: the *side-band subtraction* is the operation performed on the real data subtracting from the events, in a window around the signal region in the invariant mass histogram of the B_s candidate, $[5.32; 5.42]\,\mathrm{GeV}/c^2$, those events which are located in the sidebands. The two sidebands are: the left one from 5.244 to 5.294 GeV/c^2 and the right one from 5.444 to 5.494 GeV/c^2. The side-band subtraction is needed in the comparison, because the MC data reproduce only the signal events.

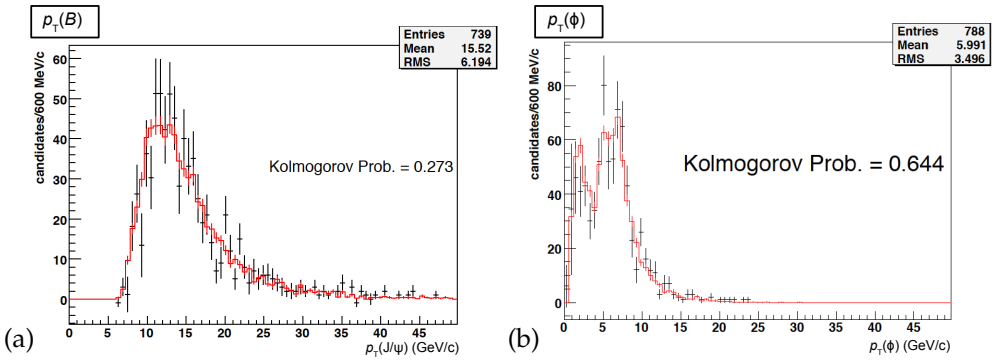

Figure 4.6: Comparison of data and MC in the $B_s \to \phi\phi$: p_T of the reconstructed B_s meson (a), p_T of the reconstructed ϕ meson (b). The plot shows the comparison between MC data (red line) and side-bands subtracted data (black points), used in the MC validation.

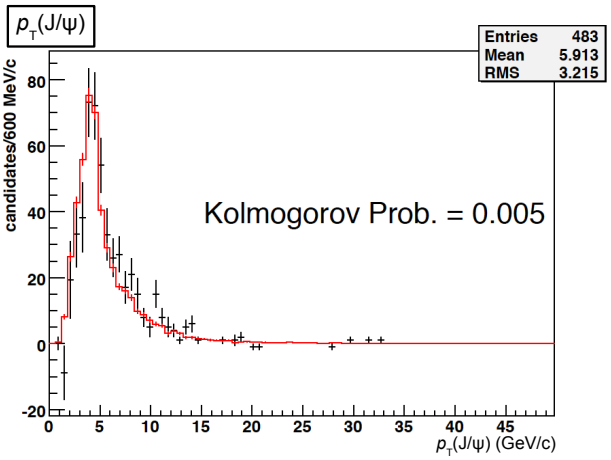

Figure 4.7: p_T of the reconstructed J/ψ meson in the $B_s \to J/\psi\phi$ decay. The plot shows the comparison between MC data (red line) and side-bands subtracted data (black points), used in the MC validation.

4.6 SIGNAL CHARACTERIZATION AND ANGULAR DISTRIBUTION

We are interested to obtain the largest available data sample. Therefore, in the analysis we would like to use the reconstructed B candidates coming from the union of the three exclusive trigger selections, `HIGHPT`, `ScA` and `LOWPT`. Since the different trigger requirements may introduce some large discrepancies from one trigger selection to another, we look for these differences in the variables distributions. In particular, we check the consistencies of the angular variables, which are the most significant for our analysis. The comparison of the three trigger selections are shown in figs. 4.8 – 4.10. For other distributions we point to [29]. A good agreement is seen: the Kolmogorov test performed returns probabilities which are

- about 5% for distributions (a) and (b) in fig 4.8;
- greater than 30% for distributions (c) and (d) in fig 4.8;
- greater than 10% for distributions in figs. 4.9 and 4.10.

This allow us to easily use all the three exclusive subsamples together in a single fit.

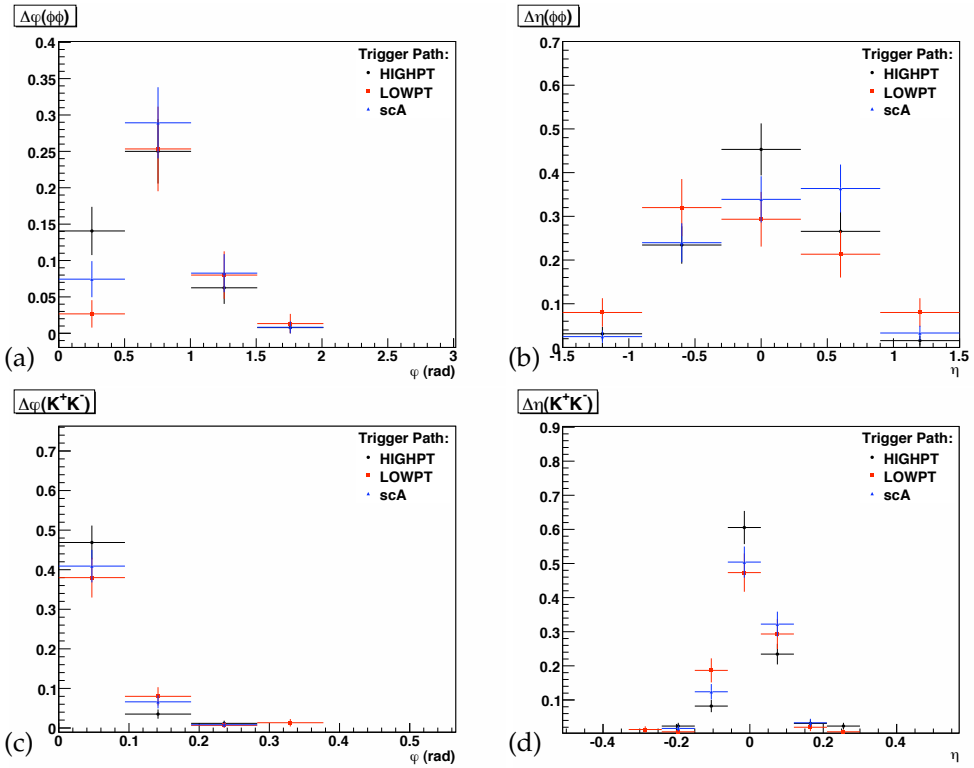

Figure 4.8: Comparison of trigger paths for the $B_s \to \phi\phi$ decay: $\Delta\varphi$ (a) and $\Delta\eta$ (b) between the ϕ, $\Delta\varphi$ (c) and $\Delta\eta$ (d) between the K^+K^-. The black points are `HIGHPT`, the blue points are `LOWPT` and the red ones are `ScA`.

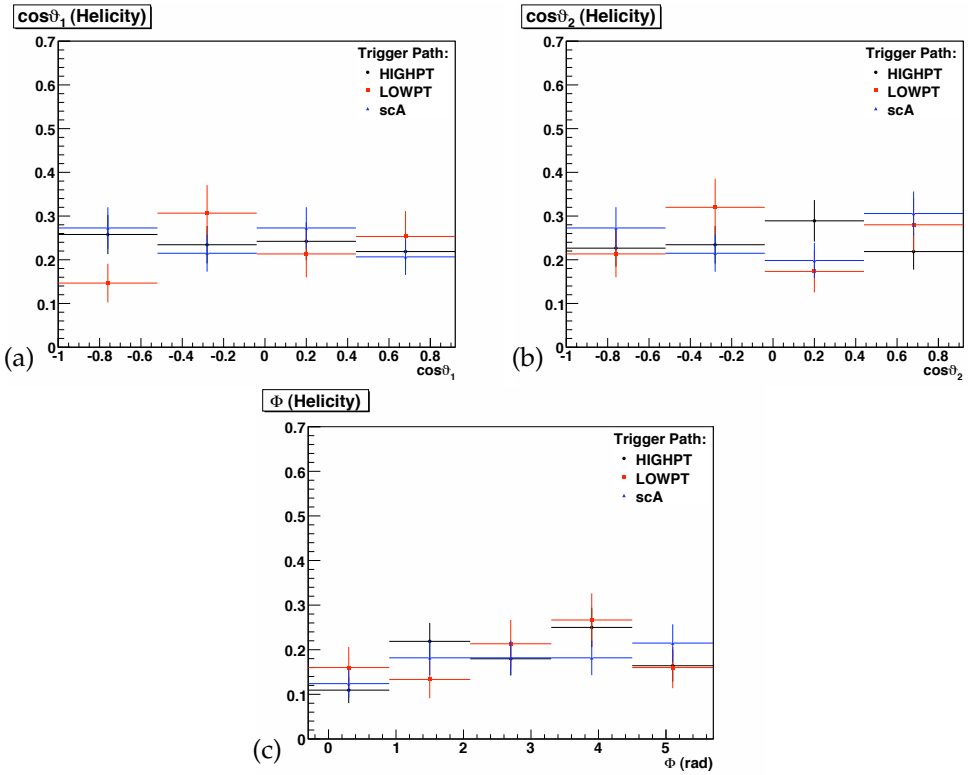

Figure 4.9: Helicity angles of the $B_s \to \phi\phi$ for the different trigger paths: $\cos\vartheta_1$ (a), $\cos\vartheta_2$ (b) and Φ (c) . The black points are `HIGHPT`, the blue points are `LOWPT` and the red ones are `ScA`.

Another check performed is the comparison between the distributions for the high-luminosity runs and the low-luminosity ones. We split the events into two sets:

- events for run numbers $> 228\,596$, which correspond to high-luminosity data sample,
- events for run numbers $\leq 228\,596$, which correspond to low-luminosity data sample,

and we look for discrepancies in the distributions shapes. These comparisons are reported in fig. 4.11. Again, a good agreement is seen, since the Kolmogorov test performed returns probabilities greater than 85%.

Finally, we present in fig. 4.12 the mass distribution of the reconstructed ϕ meson after the off-line selection. A fit is performed with the convolution of a Breit-Wigner function (resonance) and a Gaussian function (experimental resolution). The width of the Breit-Wigner function is fixed from the PDG value ($4.26 \pm 4\,\mathrm{MeV}/c^2$). From this fit we deduce that there are no evident non-resonant (scalar) components under the ϕ peak signal.

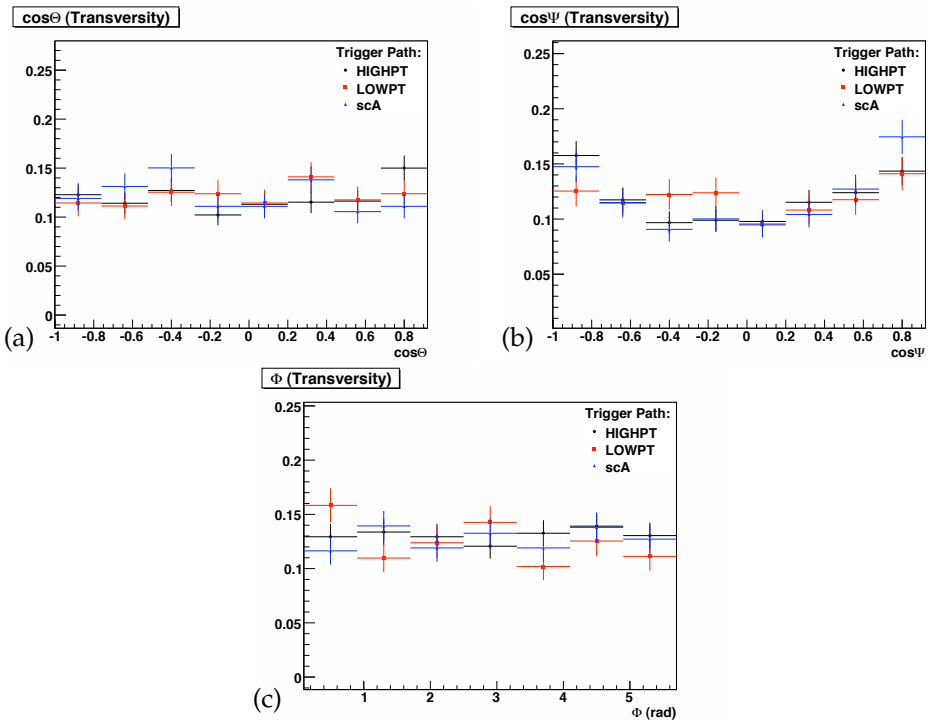

Figure 4.10: Transversity angles of the $B_s \to J/\psi\phi$ for the different trigger paths: $\cos\Theta$ (a), $\cos\Psi$ (b) and Φ (c) . The black points are `HIGHPT`, the blue points are `LOWPT` and the red ones are `ScA`.

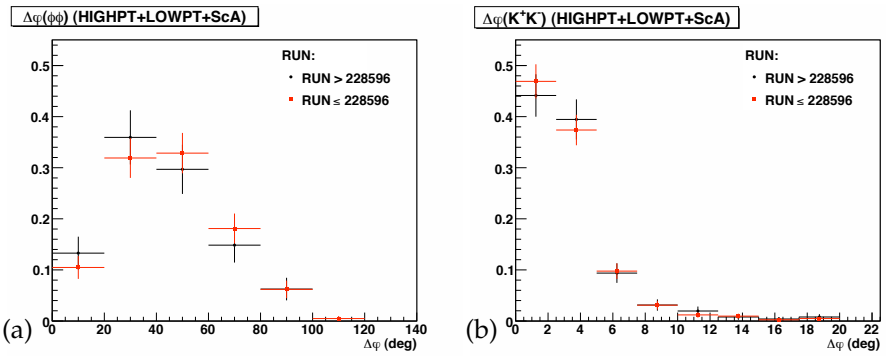

Figure 4.11: Comparison of high-luminosity and low-luminosity runs for the $B_s \to \phi\phi$ decay: $\Delta\varphi$ between the ϕ (b), $\Delta\varphi$ between the K^+K^- (b). The black points are high-luminosity runs, the red points are low-luminosity ones.

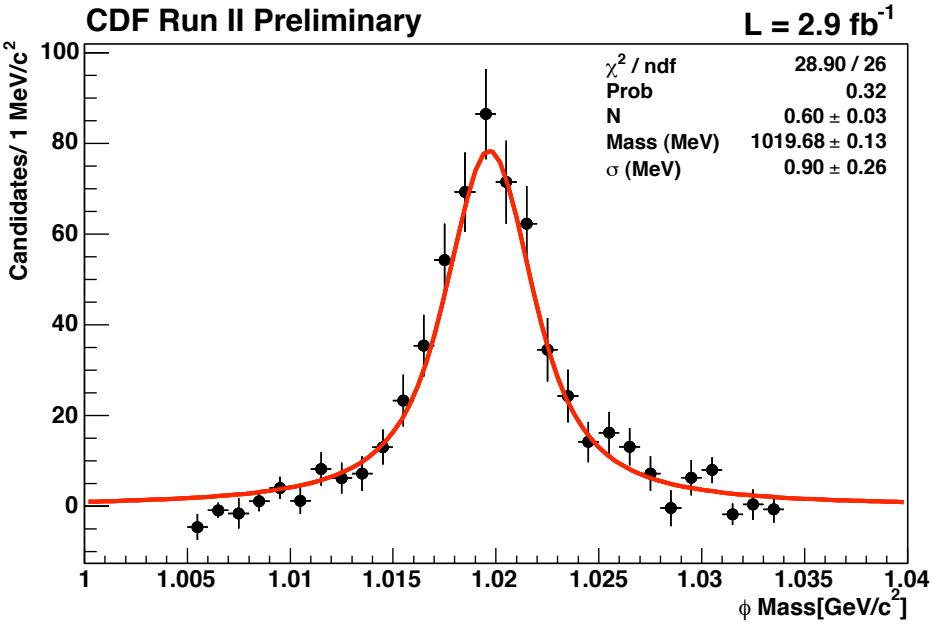

Figure 4.12: Reconstructed ϕ mass after off-line selection. The black points are side-bands subtracted data; the red line is the fit performed with the convolution of a Breit-Wigner function (resonance) and a Gaussian function (experimental resolution). The σ parameter is the Gaussian resolution width. M is is the central mass value; N is a normalization factor.

5 TIME-INTEGRATED ANALYSIS

CONTENTS

In this chapter we present the first attempt to measure the $B_s \to \phi\phi$ polarization amplitudes: the time-integrated analysis. As a first step in this approach a fit to the reconstructed mass and angular variables is developed and tested on simulated- experiments, real data and high statistics realistic MC. The latter test revealed a possible shortfall of this first approach due to an expected dependence of the signal acceptance on the proper decay time of the B_s mesons. Investigations on this specific issue, which is most likely a general feature induced by any signal selection based on the lifetime information, and, as such, something that should be thoroughly examined also in the future experiments, are reported in this Chapter while an attempt to solve this problem is proposed in the next Chapter. In the present Chapter we present several components of the fitter and the related study on the data that will remain unchanged in the final fit described later.

5.1 STRATEGY

The aim of the analysis is the estimation of the two polarization amplitudes, $|A_0|^2$ and $|A_\parallel|^2$ and the relative phase between them, using as probability density function the

angular decay rate distribution of eq. 2.60 integrated in time. We want to perform an unbinned Maximum Likelihood (ML) fit to the mass and the three helicity angles distributions of the reconstructed B candidates. The mass distribution is used in the fit to discriminate the signal yield with respect to the background. Since in eq. 2.60 the time and the angular terms do not factorize, the time integration introduces a bias in the estimated parameters. In fact, the time evolution in eq. 2.60 is represented by two expressions having different live times: $\tau_L = 1/\Gamma_L$ and $\tau_H = 1/\Gamma_H$. Our hypothesis is that the statistical uncertainty of our measurement is bigger than the systematic one induced by the time integration. The latter should not be greater than $\Delta\Gamma/\Gamma \sim 10\%$.

In eq. 2.60 we fix Γ_L and Γ_H to the latest PDG values. Moreover, the CP-violation's phase ϕ_V is set equal to zero, as its value in the SM prediction is very small. In the analysis we don't distinguish between B_s and $\bar{B}_s$ at the production time (*untagged* analysis). At this stage, the detector acceptance in the angular variables defined in Sec. 2.4.1 is assumed unrelated to the B meson proper decay time. This acceptance is determined with the MC program described in the previous chapter.

The fitter framework will be checked by three tests: the pseudo-experiments pulls distributions, the fit of the $B_s \to J/\psi\phi$ decays as a control sample, and the fit on realistic MC data. The latter one actually reveals the correlation of the angular acceptance with the B meson proper decay time. Because of this complication, a time-dependent analysis has been performed as well and it is the subject of the next Chapter.

5.2 FITTING TECHNIQUE

5.2.1 Unbinned Maximum Likelihood Fit

The parameters estimation is obtained through the construction of the likelihood function of the data sample under study. Suppose we have a set of n measured quantities $\vec{x} = (x_1, \ldots, x_n)$ described by a joint probability density function (pdf) $g(\vec{x}; \vec{\xi})$, where $\vec{\xi} = (\xi_1, \ldots, \xi_k)$ is a set of k parameters whose values are unknown. The likelihood function is given by the pdf evaluated with $\vec{x}$, but expressed as a function of the parameters, *i. e.*, $\mathcal{L}(\vec{\xi}) = g(\vec{x}; \vec{\xi})$. If the measurements x_i are statistically independent and each follow the pdf $g(\vec{x}; \vec{\xi})$, then the joint pdf for $\vec{x}$ factorizes and the likelihood function is

$$\mathcal{L}(\vec{\xi}) = \prod_{i=1}^{n} g(x_i; \vec{\xi}). \tag{5.1}$$

The method of ML takes the estimators $\hat{\xi}$ to be those values of $\vec{\xi}$ that maximize $\mathcal{L}(\vec{\xi})$. It is usually easier to work with $\ln \mathcal{L}$, and since both $\mathcal{L}$ and $\ln \mathcal{L}$ are maximized for the same parameter values $\vec{\xi}$, the ML estimators can be found by solving the likelihood equations:

$$\frac{\partial \ln \mathcal{L}}{\partial \xi_i} = 0, \quad i = 1, \ldots, k. \tag{5.2}$$

ML estimators are approximately unbiased and efficient for large data samples [36], under quite general conditions, and the method has a wide range of applicability. The inverse V^{-1} of the covariance matrix $V_{ij} = \mathrm{cov}[\hat{\xi}_i, \hat{\xi}_j]$ for a set of ML estimators can be estimated by using

$$\hat{V}^{-1}_{ij} = -\left.\frac{\partial^2 \ln \mathcal{L}}{\partial \xi_i \partial \xi_j}\right|_{\hat{\xi}}. \tag{5.3}$$

5.2.2 Numerical Maximization

For most of the fits the solution of eq. (5.2) is analytically impossible to find. Thus, a numerical method must be used. Here, this is achieved by minimizing the value $-2\log\mathcal{L}$ using the software package MINUIT [105]. MINUIT is conceived as a tool to find the minimum value of a multi-parameter function and analyze the shape of the function around the minimum. The main application is foreseen for statistical analysis, working on χ^2 or log-likelihood functions, to compute the best-fit parameter values and uncertainties, including correlations between the parameters. It is especially suited to handle complex problems.

The MINUIT package works on the multi-parameter function $F = -2\log\mathcal{L}$. The value of F depends on the parameters to be estimated. The user can request MINUIT to minimize F with respect to the parameters, that is, to find those values of the parameters which give the lowest value of F.

The width of the function around the minimum, or more generally, the shape of the function in some neighbourhood of the minimum, gives information about the uncertainty on the parameters values, often called the parameter error.

The MINUIT processors MIGRAD and HESSE produce an error matrix. This matrix is the inverse of the matrix of the second derivatives of F (eq. (5.3)). Therefore, errors based on the MINUIT error matrix take into account of all the parameter correlations. When the error matrix has been calculated then the parameter errors printed by MINUIT are the square roots of the diagonal elements of this matrix.

5.2.3 Note on the Test of Goodness of Fit

Once a fit is performed, one would estimate the goodness of the results obtained. There is no direct method for testing the goodness-of-fit of an unbinned ML fit. Different approaches have been proposed in literature for this purpose, but none is rigorously correct [**?**]. In order to have a feasible estimation of the goodness of our fit, we compare the distributions of data with the joint pdf corresponding to the Likelihood function evaluated with the set of parameters $\vec{\xi} = \hat{\xi}$. We can define the *fit projection* onto the observable x_i as the following one-dimensional function:

$$\mathscr{P}(x_i, \hat{\xi}) = \int g(\vec{x}, \hat{\xi})\, dx_1 \dots dx_{i-1} dx_{i+1} \dots dx_n \tag{5.4}$$

which is the predicted distribution for x_i under the assumed values for the fit parameters, and it can be overlaid to the experimental data. This allows us to detect possible discrepancies between the observed distributions and our model.

Then, we perform the comparison of the fit projection onto x_i with its data distribution making a χ^2 test. To simplify the notation, x_i is called z. Then:

- we construct the z distribution, filling an histogram of M bins of (constant) width Δ. Each bin is identified by the point (z_j, w_j), where z_j and w_j are the central value and the content of the j-th bin, respectively;
- we build an equivalent M-bins-histogram, evaluating the expected content $w_j^{(e)}$ of each bin with the projection $\mathscr{P}(z, \hat{\xi})$. This is defined by:

$$w_j^{(e)} = \big(\mathscr{P}(z_j, \hat{\xi})\Delta\big) N; \tag{5.5}$$

  where N is the total number of events.[1]

1 If there is only one observable per event, then $N = n$. In general, for each event i corresponds a vector of observables $\vec{x}_i = (x_1^{(i)}, \dots, x_l^{(i)})$.

- the χ^2 is

$$\chi^2 = \sum_j^M \frac{\left(w_j - w_j^{(e)}\right)^2}{w_j}; \tag{5.6}$$

- we evaluate the probability of the given χ^2, whose degrees of freedom are $M-1$, since the normalization is fixed by the number of events N.

In the following, when a χ^2 probability for the unbinned ML fit is reported, it refers to the one computed with the above procedure. The test returns a rough evaluation of the goodness-of-fit, since it doesn't take into account for the correlations among the variables: it has to be considered only as a qualitative indicator.

5.2.4 The Probability Distribution Function

As mentioned before, one needs to known the pdf of the data sample to construct the likelihood function. In the following, the pdf functional form is presented for our cases, describing it component by component.

As an event is reconstructed, several are the measured quantities, called observables, which describe a decay mode and can be used as input variables to the fitter. For this B_s angular analysis, the reconstructed quantities are:

- the mass m;
- the angles
  - $\vec{\omega} = (\cos\vartheta_1, \cos\vartheta_2, \Phi)$, for the $B_s \to \phi\phi$ decay;
  - $\vec{\Omega} = (\cos\Theta, \cos\Psi, \Phi)$, for the $B_s \to J/\psi\phi$ decay;

Here, m is the reconstructed mass of the B candidate. For the $B_s \to \phi\phi$ decay, the angles forming the vector $\vec{\omega}$ are defined in the helicity basis chosen to treat symmetrically the two K^+K^- pairs decaying from the two ϕ in order to obey Bose statistics (see the theoretical section); the vector Ω is composed by angles defined in the customary transversity basis for the $B_s \to J/\psi\phi$ decay.

The identification of the two ϕ as ϕ_1 and ϕ_2 (and then of the two angles θ_1 and θ_2) is randomly implemented in the code to avoid any bias caused by the internal ordering (*e. g.*, in $p_T(\phi)$) of the particles in the `BStntuple`, in order to carry out the symmetry mentioned above. We proceed as follow: for each reconstructed B_s candidate,

- if the event number is even, we use the internal ordering of the `BStntuple`;
- if the event number is odd, the two indexes, 1 and 2, of the `BStntuple` order are exchanged among each other.

This simple algorithm assures the symmetry of the variables under indexes exchange $1 \leftrightarrow 2$. Since our main purpose is the $B_s \to \phi\phi$ angular analysis, in the following all the notations refer to its study. We leave the description of the $B_s \to J/\psi\phi$ analysis in a separate section (Sec. 5.6).

The observables m and $\vec{\omega}$ give rise to the vector

$$\vec{x}_i = (m_i, \vec{\omega}_i) \tag{5.7}$$

where i spans over the number of events in the data sample, so the above called measurement vector is $\vec{x} = (\vec{x}_1, \ldots, \vec{x}_N)$. As we saw in the previous chapter, all $\vec{x}_i$ can be divided into two sets: the events which come from the decay under study, the signal, and the events which are not related to it, the background. Accordingly,

the pdf is the sum of two components: g_s, representing the signal set, and g_b, for the background events, *i. e.*

$$g(\vec{x}_i, \vec{\xi}) = (1 - f_b) g_s(\vec{x}_i, \vec{\xi}_s) + f_b g_b(\vec{x}_i, \vec{\xi}_b), \tag{5.8}$$

where f_b is the fraction of background events ($0 \leq f_b \leq 1$). Since the mass and the angular variables are statistically independent, the pdf can be factorized in two corresponding terms:

$$g_s(\vec{x}_i, \vec{\xi}_s) = g_s^{(m)}(m_i, \vec{\xi}_s^m) g_s^{(\omega)}(\vec{\omega}_i, \vec{\xi}_s^\omega), \tag{5.9a}$$

$$g_b(\vec{x}_i, \vec{\xi}_b) = g_b^{(m)}(m_i, \vec{\xi}_b^m) g_b^{(\omega)}(\vec{\omega}_i, \vec{\xi}_b^\omega) \tag{5.9b}$$

$$\tag{5.9c}$$

The pdf must be normalized to one, thus the following relations hold:

$$\int g_{s/b}^{(m)} \, dm = 1, \tag{5.10a}$$

$$\int g_{s/b}^{(\omega)} \, d\vec{\omega} = 1. \tag{5.10b}$$

We evaluate the best parametrization of the pdf components, using also the MC simulation. They are presented in the following sections. This procedure allowed us to fix some parameters in the function parameterization and then to make a global fit with a limited number of free parameters.

At this stage of the work, we don't consider the reflection components in the background parametrization: since they are a tiny percentage of the total data sample, they can be neglected at first order. Thus, throughout this chapter, when we refer to the background, we mean only the dominant combinatorial component.

5.3 MASS MODEL

The signal distribution has a width of around 20 MeV for the $B_s \to \phi\phi$ (see fig. 4.4 in the previous chapter). It is parameterized with two gaussian functions having the same mean value M but different resolutions, σ and $k\sigma$. This choice is fairly standard and takes into account the detector effects that cause an additional spread in the tail distributions. The function used to parametrize the distributions is the following:

$$g_s^{(m)} = h \frac{1}{\sqrt{2\pi}\sigma} e^{-\frac{(m-M)^2}{2\sigma^2}} + (1-h) \frac{1}{\sqrt{2\pi}k\sigma} e^{-\frac{(m-M)^2}{2k^2\sigma^2}} \tag{5.11}$$

where h is the fraction of one gaussian component with respect to the other. Fitting the MC events of fig. 5.1, we obtained the parameters summarized in tab. 8 . In the final

Parameter	MC fit value
M [GeV/c^2]	5.36995 ± 0.00004
σ [GeV/c^2]	0.01577 ± 0.00004
k	2.87 ± 0.03
h	0.932 ± 0.002

Table 8: Parameters of MC data mass fit for $B_s \to \phi\phi$. All symbols are defined in the text.

fit the multiplicative factor k and the fraction h are fixed, while the other parameters are left free.

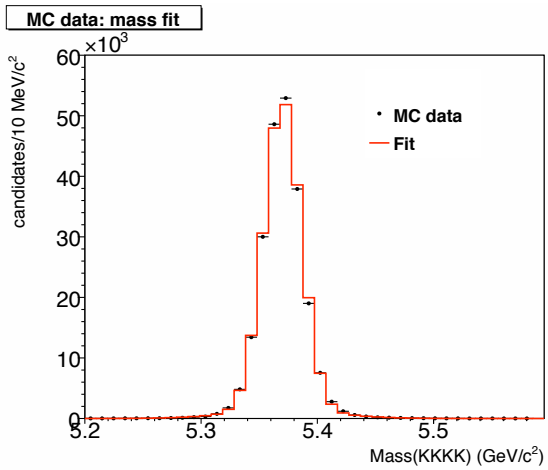

Figure 5.1: Mass fit of MC data for $B_s \to \phi\phi$. The black points are the MC data; the red line is the resulting fit distribution.

The mass background follows, with a good approximation, an exponentially decreasing behavior:

$$g_b^{(m)} = \frac{b}{e^{-bm_{\min}} - e^{-bm_{\max}}} e^{-bm} \tag{5.12}$$

where b is the slope of the exponential function, and m spans the interval $[m_{\min} = 5.2, m_{\max} = 5.6]$ GeV/c^2. In this case, we didn't perform a MC study and a simple parametrization has been used instead.

5.3.1 Comparison with Binned Likelihood Fit of the BR Analysis

We can compare the results of this unbinned ML fit of the reconstructed B mass with respect to the binned fit performed in the branching ratio analysis [29]. This allows us to check the tiny effects of the reflections in the background component, since the binned fit takes them into account and since the data sample is the same for the two fits. Table 9 reports the two fit's results and the mass distributions are shown in fig. 5.2. The χ^2 probability of the unbinned mass fit is 0.07. We obtain a very good agreement in the central values and in their uncertainties. This could be sufficient to justify the reflections' neglect at first order.

Parameter	Unbinned fit	Binned fit
M [GeV/c^2]	5.364 ± 0.001	5.364 ± 0.001
σ [GeV/c^2]	0.016 ± 0.001	0.017 ± 0.001
f_b	0.38 ± 0.03	0.39 ± 0.03
b	2.7 ± 0.7	2.5 ± 0.7

Table 9: Comparison of the mass fit results with the branching ratio analysis' ones [29].

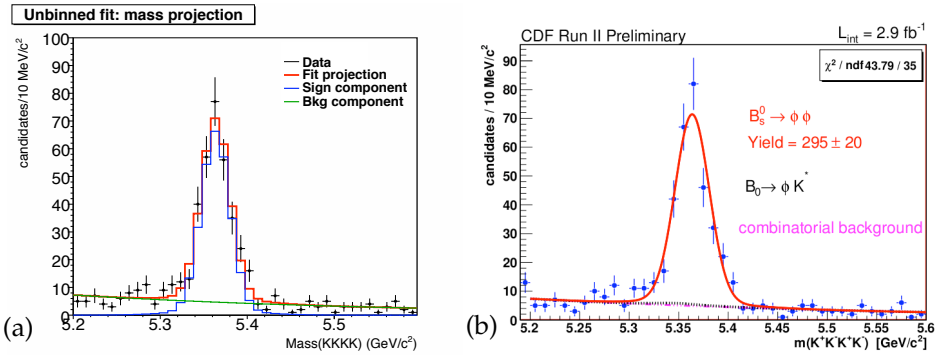

Figure 5.2: Comparison of our fit mass projection with the fit of the branching ratio analysis. (a) mass projection of the unbinned fit; (b) binned fit in [29]. The χ^2 probability of the unbinned mass fit is 0.07.

5.4 ANGULAR MODEL

The pdf used to describe the helicity angular distribution for the signal is obtained integrating in time the theoretical differential decay rate reported in eq. (2.60) of sec. 2.4.3. It is important to stress that this formula has been obtained summing over the initially produced B_s and $\bar{B}_s$, without attempting to tag the production flavor identification at the production time, and, assuming no CP violation, fixing $\phi_V = 0$ as in the SM. Thus, the resulting signal angular pdf is:

$$g_s^{(\omega)} = \frac{d^3\Lambda(\vec{\omega})}{d\vec{\omega}} = \frac{9}{32\pi}\frac{1}{\tilde{W}}\left[\tilde{\mathcal{F}}_e(\vec{\omega}) + \tilde{\mathcal{F}}_o(\vec{\omega})\right] \tag{5.13}$$

where

$$\tilde{\mathcal{F}}_e = \frac{2}{\Gamma_L}\left[|A_0|^2 f_1(\vec{\omega}) + |A_\parallel|^2 f_2(\vec{\omega}) + |A_0||A_\parallel|\cos\delta f_5(\vec{\omega})\right] \tag{5.14}$$

$$\tilde{\mathcal{F}}_o = \frac{2}{\Gamma_H}|A_\perp|^2 f_3(\vec{\omega}) \tag{5.15}$$

$$\tilde{W} = \frac{|A_0|^2 + |A_\parallel|^2}{\Gamma_L} + \frac{|A_\perp|^2}{\Gamma_H} \tag{5.16}$$

and the notation has been described in sec. 2.4.3. Since we want to measure only the polarization amplitudes, we fix Γ_L and Γ_H to the latest PDG values (see eq. (2.18a)) in the final fit.

5.4.1 Detector Angular Acceptance

In the case of an ideal detector we could assume an homogeneous acceptance distribution for the angles. Since CDF does not have uniform efficiency and performances in the three-dimensional space, we expect not to have a uniform acceptance in the helicity (transversity) angles. In principle, the trigger paths and the off-line selection, could modify the angular distribution as well. Another source of inefficiency is due to the p_T acceptance: the helicity variables are strictly related to the K p_T since, in practice, the computation of the angles is based on the reconstructed momenta. Thus, a part of the angular inefficiency comes from the events which have in the final state K with low p_T that are lost in the on-line selection. So it is crucial for the analysis to be able to unfold all these effects, which are usually referred to as "angular acceptance".

In order to study the detector impact on the angular distributions, we generate a "phase space MC" data sample with uniform distributions in all the angular variables (in the following we refer to it as "flat MC"). Phase space MC means that the MC simulates the decays considering only the phase space variables of the particles: particles spins in the final state are averaged.

The simulated events are passed through the full-fledged detector simulation. Then, they are selected with the same on-line and off-line requirements of the real data. Thus, we can obtain a three-dimensional acceptance curve $\mathcal{A}(\vec{\omega})$, which accounts for the detector acceptance in the angular variables. In practice, we construct $\mathcal{A}(\vec{\omega})$ as a three-dimensional histogram $H(\vec{\omega})$, and the acceptance is calculated as the ratio of accepted and generated events in each three-dimensional bin in ω divided by the total number of generated events such that the sum of the weights in all the bins in the histogram is 1. The three-dimensional histogram is made of 223 000 events, which fill $20 \times 20 \times 20$ bins. Thus, the acceptance function can be interpreted as the probability to find an event at each position in the $\vec{\omega}$ space. The projections of $H(\vec{\omega})$ onto the three axes of the helicity angles basis are shown in fig. 5.3. We note that the detector and the other selections don't change the Φ distribution, that is still flat.

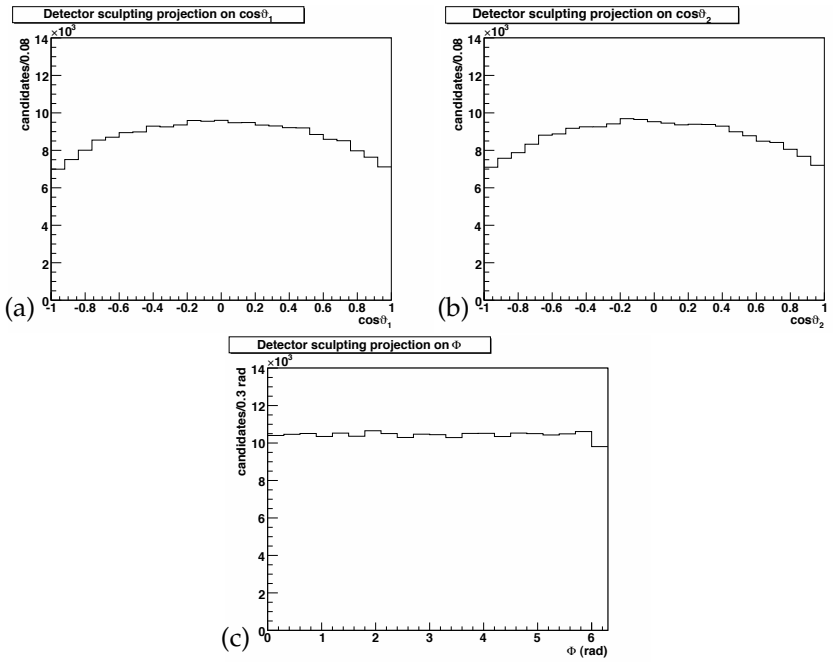

Figure 5.3: Detector angular acceptance projections: $\cos\vartheta_1$ (a), $\cos\vartheta_2$ (b) and Φ (c).

The angular acceptance effect is finally taken into account by the multiplicative term $\mathcal{A}(\vec{\omega})$ in the signal angular pdf:

$$g_s^{(\omega)} = \frac{d^3\Lambda(\vec{\omega})}{d\vec{\omega}} \rightarrow g_s^{(\omega)} = \frac{1}{\mathcal{N}} \frac{d^3\Lambda(\vec{\omega})}{d\vec{\omega}} \mathcal{A}(\vec{\omega}) \tag{5.17}$$

where $\mathcal{N}$ is a normalization term. The presence of $\mathcal{A}(\vec{\omega})$ bring some complication in the normalization process: both the angular distribution and the acceptance distribution are independently normalized, thus it is not assured that their product will be normalized as well. The normalization procedure for the calculation of $\mathcal{N}$ is described in Appendix A.

5.4.2 Effect of Different Trigger Path on the Detector Angular Acceptance

There is the possibility that the acceptance curve is different for the three trigger path selections. If this happens, more complications arise in the analysis of all exclusive trigger sets together. To check if this is the case, we look at the projections of $H(\vec{\omega})$ for the different trigger paths. They are shown in fig. 5.4: we can conclude that $H(\vec{\omega})$ is quite similar for each trigger selection. This test also guarantees no dependencies on the integrated luminosity collected with the three different trigger paths. These allows us to use in a straightforward way all the exclusive data set together, minimizing the statistical errors on ours measurements.

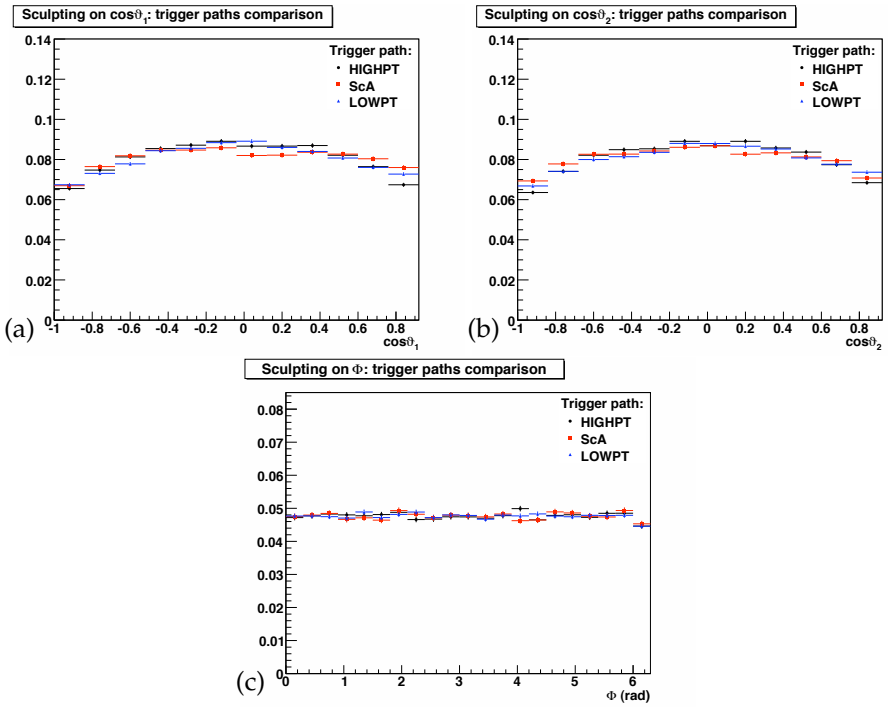

Figure 5.4: Effect of different trigger path on angular detector angular acceptance: $\cos\vartheta_1$ (a), $\cos\vartheta_2$ (b) and Φ (c).

5.4.3 Comparison with Previous Works

In some of the previous CDF angular analysis, another method has been adopted to treat the detector angular acceptance. Like the one presented above, it makes use of the flat MC, but in a different way.

In principle, the angular acceptance besides the angular variables is a function of kinematic variables as well as the detailed trigger criteria: we have $\mathcal{A}(\vec{\omega},\vec{k})$, where $\vec{k}$ is the vector of the kinematic variables. Thus, remembering the form of the differential decay rate of eq. (2.57), the signal pdf is

$$\frac{1}{\mathcal{N}}\frac{d^3\Lambda(\vec{\omega})}{d\vec{\omega}}V(\vec{k})\mathcal{A}(\vec{\omega},\vec{k}) = \frac{V(\vec{k})\mathcal{A}(\vec{\omega},\vec{k})}{\mathcal{N}}\sum_{i=1}^{6}K_i f_i(\vec{\omega}) \tag{5.18}$$

where $V(\vec{k})$ is the distribution of the candidates in the $\vec{k}$ space. $\mathcal{N}$ is the normalization factor:

$$\begin{aligned}\mathcal{N} &= \int\int d\vec{\omega} d\vec{k} \frac{d^3\Lambda(\vec{\omega})}{d\vec{\omega}} V(\vec{k}) \mathcal{A}(\vec{\omega}, \vec{k}) = \\ &= \sum_{i=1}^{6} K_i \left[\int\int d\vec{\omega} d\vec{k} f_i(\vec{\omega}) V(\vec{k}) \mathcal{A}(\vec{\omega}, \vec{k}) \right] \\ &= \sum_{i=1}^{6} K_i \zeta_i\end{aligned} \tag{5.19}$$

In the last line of eq. (5.19), the coefficients ζ_i are the result of the double integral in the second line: they can be computed once using the flat MC. In fact, in the limit of infinite number of reconstructed candidates, $N \to \infty$, the following relation holds:

$$\zeta_i = \frac{1}{N} \sum_{j}^{N} f_i(\omega_j), \text{ with } \omega_j \in \{\text{flat MC}\} \tag{5.20}$$

Then, the method of ML requires the maximization of the log $\mathcal{L}$:[2]

$$\begin{aligned}\log \mathcal{L} &= \sum_{j}^{N} \log \left[\frac{V(\vec{k_j}) \mathcal{A}(\vec{\omega_j}, \vec{k_j})}{\mathcal{N}} \sum_{i=1}^{6} K_i f_i(\vec{\omega_j}) \right] \\ &= \sum_{j}^{N} \log \left[\sum_{i=1}^{6} K_i f_i(\vec{\omega_j}) \right] - N \log \left[\sum_{i=1}^{6} K_i \zeta_i \right] + \sum_{j}^{N} \log \left[V(\vec{k_j}) \mathcal{A}(\vec{\omega_j}) \right]\end{aligned} \tag{5.21}$$

Since the last term of the second line of eq. (5.21) doesn't depend on the fit parameters, it can be removed from the likelihood function: it is a constant in the maximization procedure. Thus, the final fit doesn't depend on the knowledge of the analytic form of the detector angular acceptance: the entire information of its effect is contained in the ζ_i coefficients.

This method seems more convenient than ours, but, paying attention of some assumptions in this approach, we will realize that they are not so different. This method is based on the eq. (5.20). This formula is an approximation, because:

1. the identity is valid only in the limit of $N \to \infty$;
2. the equation represents a good description as well as the MC data can reproduce the real data.

The same considerations can be done for our method. First, the histogram takes automatically into account the $V(\vec{k})$ distribution. Second, if we model the acceptance curves $\mathcal{A}(\vec{\omega}, \vec{k})$ with a three-dimensional histogram $H(\vec{\omega}, \vec{k})$, coming from the flat MC, this is subjected to the same two issues presented above:

1. the histogram reproduces a continuum function only in the limit of an infinitesimal bin's volume, *i. e.*, an infinite number of bins, which requires an infinite number of events;
2. since the histogram comes from the MC simulation, its quality depends on the MC's ability to reproduce the real data.

2 For simplicity, here is considered only the angular part.

Finally, we don't find any reasons to prefer one of the two methods. Our choice comes only from a pragmatic motivation: the framework used to perform the analysis is a modification of an older one involving the histogram's method.

A further comparison with the previous works is to look at the angular acceptance projections. This is the first time that the $B_s \to \phi\phi$ decay is studied and its descriptions make use of the helicity angles. However, the other decays analyzed at CDF are all described in the transversity basis: they are $B_s \to J\psi\phi$ and $B_d \to J/\psi K^{0\star}$ in [1, 106], $B_d \to J/\psi K^{0\star}$ and $B_d \to \phi K^{0\star}$ in [62] . Anyway, ϑ_1 (of helicity basis) and Θ (of the transversity basis) are the same angles (see the definitions in sec. 2.4). Thus, it is correct to compare the $\cos\vartheta_1$ angular acceptance distribution with the one of $\cos\Theta$. Looking at the analysis listed above, we find that:

- the distributions' shape is the same of fig. 5.3;
- the difference between the maximum of the distribution at $\cos\Theta = 0$ and the minimum at $\cos\Theta = \pm 1$ is about 20% and it is of the same order of what we find in our distribution.

If one wants to look at the other angles, the control samples used here ($B_s \to J\psi\phi$), which is described with the transversity angles, must be considered. We only mention here that no discrepancies are found with respect to the analysis in [1, 106, 62], as can be seen from the plots in fig. B.3 of the Appendix B, which represent the transversity angular acceptance projections for the $B_s \to J\psi\phi$ decay.

The agreement with the angular acceptance projections of the previous work confirms that the main consequence of the angular acceptance on the angular distributions comes from the detector geometry; it is independent of certain trigger details.

5.4.4 Background Parameterization

It is reasonable to suppose that the helicity angles do not have any intrinsic meaning for the combinatorial background. To verify this hypothesis in fig. 5.5 we compare the side-bands angular distributions and those of the flat MC data. Thus, we use a purely empirical model derived by analysing the angular distributions in the mass sidebands to model the background. In order to increase the statistic of the side-bands region, we enlarge the side-bands width ranges with respect to the ones defined in Sect 4.5. 4.5, choosing the two intervals $[5.02; 5.22]$ GeV/c^2 and $[5.52; 5.72]$ GeV/c^2; then we also remove the $L_{xy} > 330\,\mu$m cut selection, which doesn't have any appreciable effects on the angular variables distributions, as one can see in fig. 5.6.

Looking at the scatter plots in fig. 5.7, we see that the angular variables are not correlated in the sideband regions; then the angular background pdf factorizes in the product of three terms:

$$g_b = g_b^{(\omega_1)} g_b^{(\omega_2)} g_b^{(\omega_3)} \tag{5.22}$$

where for the $B_s \to \phi\phi$ decay the parameterizations adopted are:

$$g_b^{(\omega_1)} = \frac{1}{2(1 + \frac{p_{\vartheta_1}}{3})} \left(1 + p_{\vartheta_1} \cos^2\vartheta_1\right), \tag{5.23a}$$

$$g_b^{(\omega_2)} = \frac{1}{2(1 + \frac{p_{\vartheta_2}}{3})} \left(1 + p_{\vartheta_2} \cos^2\vartheta_2\right), \tag{5.23b}$$

$$g_b^{(\omega_3)} = \frac{1}{2\pi(1 + p_\Phi \pi)} \left(1 + p_\Phi \cos\Phi\right), \tag{5.23c}$$

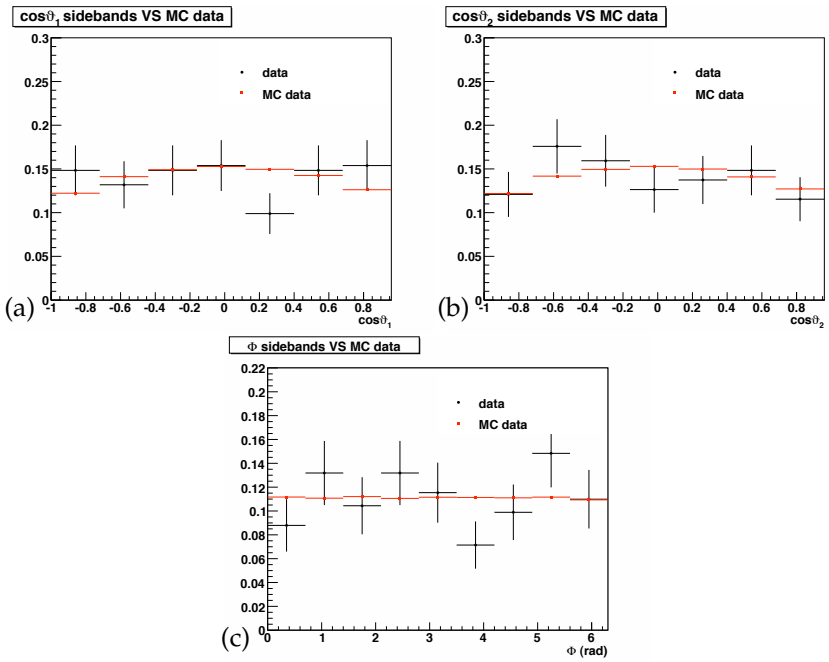

Figure 5.5: Comparison between side-bands and MC data angular distributions: $\cos\vartheta_1$ (a), $\cos\vartheta_2$ (b) and Φ (c). Black points are side-bands data; red points are MC data. All plots present a Kolmogorov test probability greater than 88%.

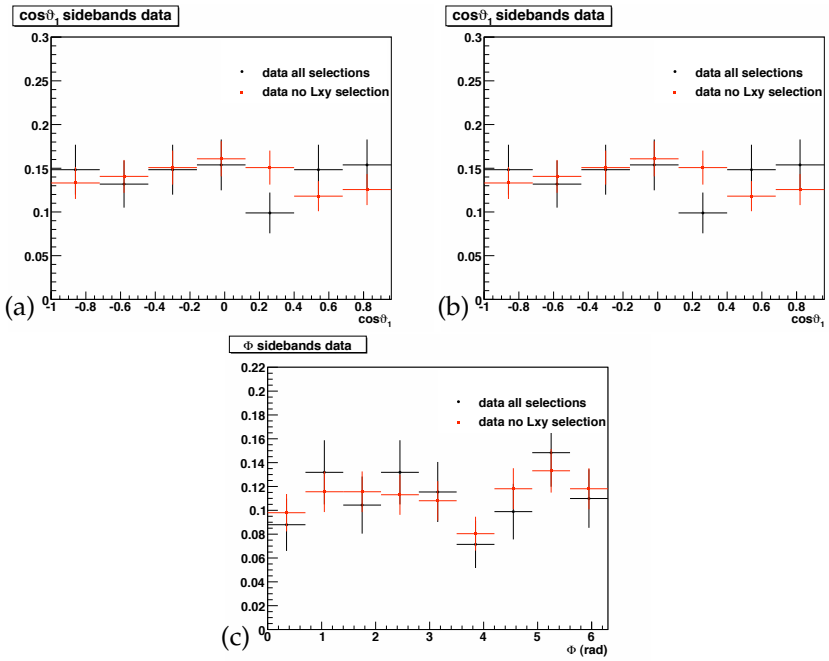

Figure 5.6: Comparison between side-bands data angular distributions with and without the L_{xy} selection: $\cos\vartheta_1$ (a), $\cos\vartheta_2$ (b) and Φ (c). Black points are side-bands data with all selections (see Sect. 4.3); red points are side-bands data removing the $L_{xy} > 330\,\mu\text{m}$ selection. All plots present a Kolmogorov test probability greater than 80%.

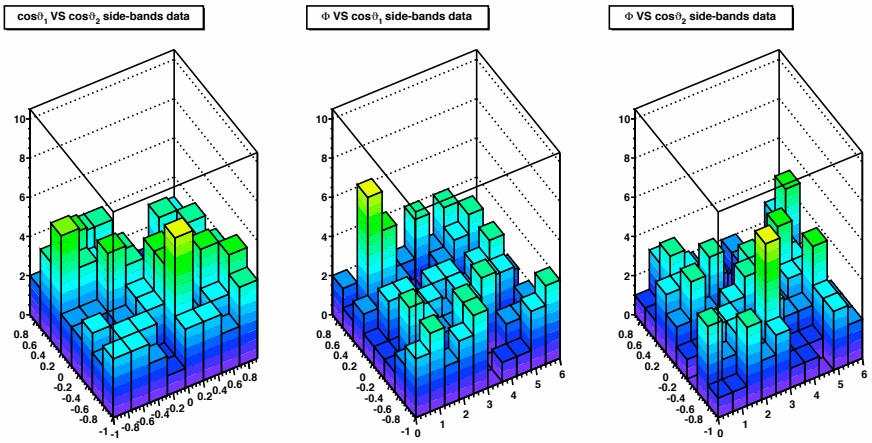

Figure 5.7: Scatter plots for test of angular variables correlation in the side-band regions. On the right, $\cos\vartheta_1$ versus $\cos\vartheta_2$. In the middle, $\cos\vartheta_1$ versus Φ. On the left, $\cos\vartheta_2$ versus Φ.

We perform a binned fit to the sideband angular distributions using the above equations and we determine the parameters p_j table 10. Though this is a simple description, we find that it is adequate to describe the angular distributions in the sidebands (see Figure 5.8).

Parameter	Binned fit value
p_{ϑ_1}	-14 ± 10
p_{ϑ_2}	-11 ± 10
p_Φ	0.02 ± 0.03

Table 10: Parameters of the binned sidebands fit for $B_s \to \phi\phi$ fit.

5.4.5 Parameters Summary

Let us summarize all the parameter that enter the complete Likelihood in the final fit. The input variables are the mass m and the helicity angles $\vec{\omega} = (\vartheta_1, \vartheta_2, \Phi)$ for each reconstructed candidate that passed the off-line selection. The ten fit parameters are reported in tab. 11.

	Signal	Background
Mass	M, σ	f_b, b
Angular	$\lvert A_0\rvert^2$, $\lvert A_\parallel\rvert^2$, δ	p_{ϑ_1}, p_{ϑ_2}, p_Φ

Table 11: Parameters summary of the time-integrated $B_s \to \phi\phi$ fit.

The following quantities are fixed in the final fit:

- k and h, from the MC fit;
- $\tau_L = \Gamma_L$ and $\tau_L = \Gamma_L$, the two mean life-time of the B_s mass eigenstates, are taken from the last PDG values;

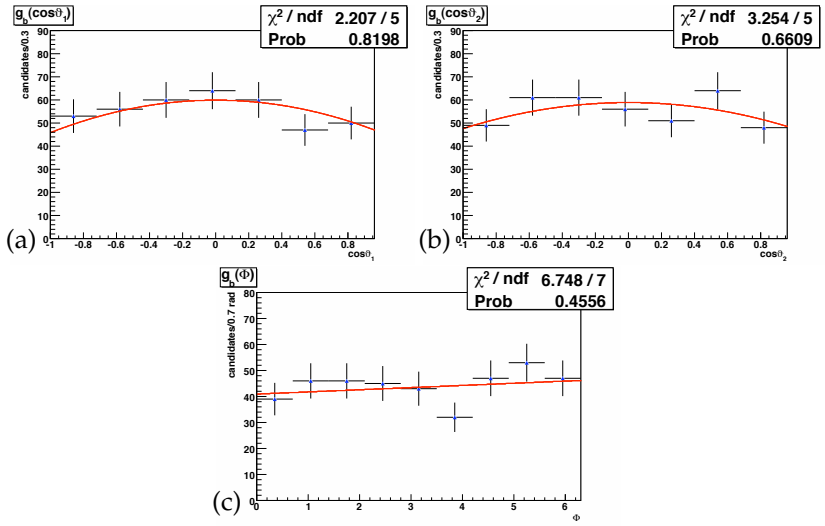

Figure 5.8: Side-bands data fit to determine the background parameterizations for the $B_s \to \phi\phi$ decay: $\cos\vartheta_1$ (a), $\cos\vartheta_2$ (b) and Φ (c). Black points are side-bands data; red lines are the fitting functions described in the text.

Before carrying out the fit over the data sample, we perform several tests. The aim is to validate the correctness of the implementation, to investigate the likelihood behavior as function of the parameters, to look at their resolutions and to detect any potential fit biases. The tests that we perform are:

1. the pulls distributions;
2. the fit of $B_s \to J/\psi\phi$, used as a control sample;
3. the fit of the realistic MC;

They are described in the following sections.

5.5 PULLS DISTRIBUTIONS

The study of pulls distributions are a commonly used method. The procedure is as follows: we generate a large set of pseudo-experiments (referred to as "toysMC"), randomly polling the probability density function in each variable subspace to assign a value to the event variables. As a consequence, each pseudo-experiment yields a different random sample of events. For each of these pseudo-experiments, we perform a fit in the same way we do on the data. For each parameter ξ_i on the fit, the corresponding pull $\mathcal{P}_i$ is defined as:

$$\mathcal{P}_i = \frac{\xi_i^{\text{fit}} - \xi_i^{\text{input}}}{\sigma_i} \tag{5.24}$$

where ξ_i^{input} is the parameter assigned in the random generation of the pseudo-experiment variables, ξ_i^{fit} is its value found by the fitter, and σ_i is its uncertainty. In our pull studies, we adopt the convention that the pull for a given pseudo-experiment is calculated using the positive (negative) error in the denominator if the fit value is lower (higher) than the input value.

In principle, the variables $\mathcal{P}_i$ are gaussian distributed, with mean and width equal to 0 and 1, respectively. Thus, if the fitter is correct, we expect to find this kind of pulls distributions. Naturally, several complications could arise. In some cases, there can be a hard physical limit on one or both sides of the allowed parameter range. In other cases, a degeneracy in the likelihood expression itself can lead to a fit value that is simply another equivalent minimum without being a physically different value (as far as the likelihood itself would be able to measure). These problems manifest themselves in a modification of the pull distributions, like a non zero mean, a width different from one, or a non gaussian shape. Thus, one has to understand if these complications are related to some errors in the fitter implementations, or to some intrinsic fitter limitations.

At first stage, we perform the fit on 1000 pseudo-experiments of 100 000 events each: it's more than 300 times of the events per experiment that we have in the actual $B_s \to \phi\phi$ data samples, so it is mostly a test of the fitter as a machinery to correctly extract the parameters given in input to generate the toyMC sample. In fact, first, it is preferable to work with large data sample in order to decrease the pulls parameters uncertainty and to have a better control on the result, since different complications can arise in presence of low statistics. Anyway, the fraction of signal to background is fixed to reproduce the real data sample. We generate the events using as input parameters the results of the final fit performed on the actual $B_s \to \phi\phi$ sample, which are described in the last section of this Chapter. The results of this test are very satisfactory; they are presented in tab. 12. The pull distributions are reported in fig. 5.9.

Parameter	Input value	Mean	Variance	Prob(χ^2) [%]
M	5.364 GeV/c^2	-0.01 ± 0.03	0.96 ± 0.02	34
σ	0.016 GeV/c^2	-0.06 ± 0.03	0.98 ± 0.02	28
f_b	0.38	0.03 ± 0.03	1.02 ± 0.02	31
b	2.7 c^2/GeV	-0.04 ± 0.03	1.03 ± 0.02	6
$\lvert A_0 \rvert^2$	0.35	0.02 ± 0.03	1.01 ± 0.02	98
$\lvert A_\parallel \rvert^2$	0.29	0.00 ± 0.03	1.00 ± 0.02	86
δ	0.4 rad	0.05 ± 0.03	1.02 ± 0.02	28
p_{ϑ_1}	0.3	0.04 ± 0.03	0.98 ± 0.02	68
p_{ϑ_2}	0.8	0.02 ± 0.03	1.00 ± 0.02	75
p_Φ	0.03	0.00 ± 0.03	1.05 ± 0.02	6

Table 12: Pulls mean and variance for $B_s \to \phi\phi$ (100 000 events per pseudo-experiment). The fifth column presents the χ^2 probability for a gaussian fit of the pulls distribution with mean and variance 0 and 1, respectively.

5.5.1 Expected Resolution on the Polarization Observables

We repeat the previous test fitting samples with 1000 events for each pseudo-experiments, which is of the same order of the statistics we have in 2.9 fb^{-1} of data. In this way, we can check if there is any significant change in the fitter behaviour that might be caused by the lower statistic of the actual B_s sample. Again, the generation of pseudo-experiments is done using as input parameters the results of the final fit performed on the actual $B_s \to \phi\phi$ sample. The results of this test are reported in tab. 13, and the pulls distributions are shown in fig. 5.10. The resolution (third column of the table) of the polarization amplitudes are consistent with the one expected in Sect. 2.5.2 (4%).

We find that the fitter returns unbiased estimates and consistent uncertainties for all parameters except for two of them: δ and p_Φ. The latter presents a shift of the

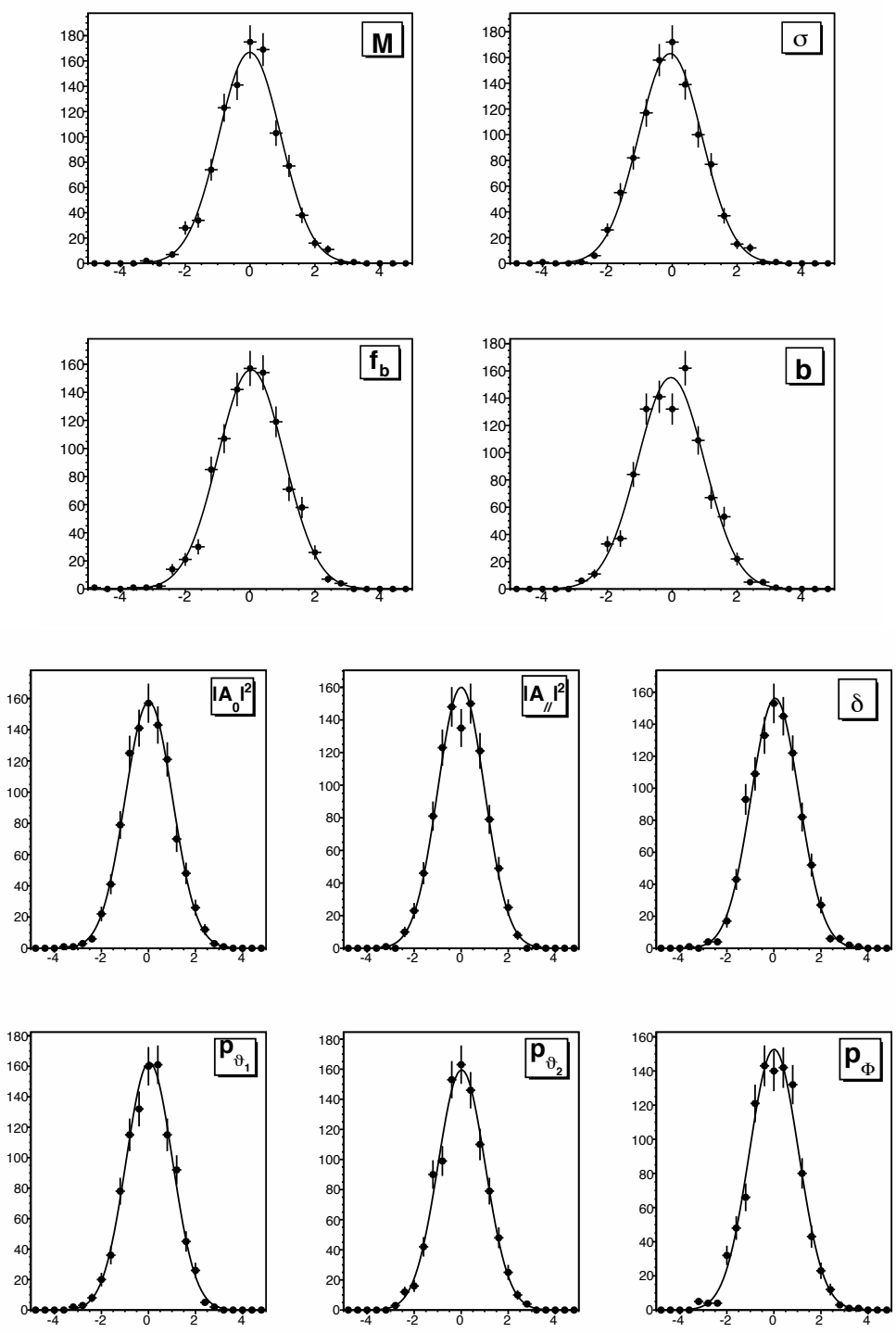

Figure 5.9: Pulls distributions of fit parameters for $B_s \to \phi\phi$ (100 000 events per pseudo-experiment).

Parameter	Input value	Average fit error	Mean	Variance	Prob(χ^2) [%]
M	5.364 GeV/c^2	0.0008 GeV/c^2	0.01 ± 0.03	1.01 ± 0.02	66
σ	0.016 GeV/c^2	0.0007 GeV/c^2	-0.08 ± 0.03	1.03 ± 0.02	43
f_b	0.38	0.02	-0.09 ± 0.03	1.00 ± 0.02	65
b	2.7 c^2/GeV	0.5 c^2/GeV	-0.04 ± 0.03	1.00 ± 0.02	98
$\|A_0\|^2$	0.35	0.03	0.03 ± 0.03	0.99 ± 0.02	65
$\|A_\parallel\|^2$	0.29	0.03	0.02 ± 0.03	1.02 ± 0.02	38
δ	0.4 rad	0.3 rad	0.13 ± 0.03	0.88 ± 0.02	0
p_{ϑ_1}	0.3	0.1	0.03 ± 0.03	0.99 ± 0.02	88
p_{ϑ_2}	0.8	0.1	0.00 ± 0.03	0.96 ± 0.02	75
p_Φ	0.03	0.04	0.11 ± 0.03	1.02 ± 0.02	0

Table 13: Pulls mean and variance for $B_s \to \phi\phi$ (1000 events per pseudo-experiment). In the second column the input parameters of the generation are listed. The third column reports the average error in the pseudo-experiments fit (resolution). The fourth and the fifth columns list the mean value and the variance of the pull distributions, respectively. The sixth column presents the χ^2 probability for a gaussian fit of the pulls distribution with mean and variance 0 and 1, respectively.

mean value of order of about 0.1 sigma, but its shape is almost gaussian. The strong phase δ instead seems to be affected by a different problem, since the distribution is not gaussian. Both these complications arise in presence of low statistic: the fit on the data sample might returns a biased estimates for this two parameters. The behaviour of the δ pull distribution requires further examination that it is performed in subsection 5.5.3.

5.5.2 Expected Resolution as a Function of Input Parameters

The fitter must estimate unbiased parameters independently of the specif value of the parameters. Naively, since in principle there is no criteria to prefer some values with respect to others, we don't want that the fitter results depend on the parameters value. Thus, in order to check if this condition is satisfied, we perform a pulls distributions test by changing one by one the input parameters for the generation of the pseudo-experiments variables.

In tab. 14, we report the result of the test; four different sets of input values are given. Since we are interest in the polarization amplitudes, we fixed the mass parameters and we vary the values of the signal angular parameters. Because of its problematic nature shown in the previous section, the strong phase δ is discussed separately.

On average we are satisfied with the results obtained. The resolution for each parameter doesn't appreciably change for each set and it is of the same order of the one obtained in the previous test. One could just argue about the result for $|A_0|^2$ pull mean in the first set of values in tab. 14. On the other hand, its distribution has a gaussian shape, as the χ^2 probability reveals. Thus, for the moment we disregard this issue and we'll check it better in the case the fit results on actual data presents a similar set of parameters. The other parameters pulls that are not shown in tab. 14 are all gaussian, with mean value and variance consistent with 0 and 1, respectively.

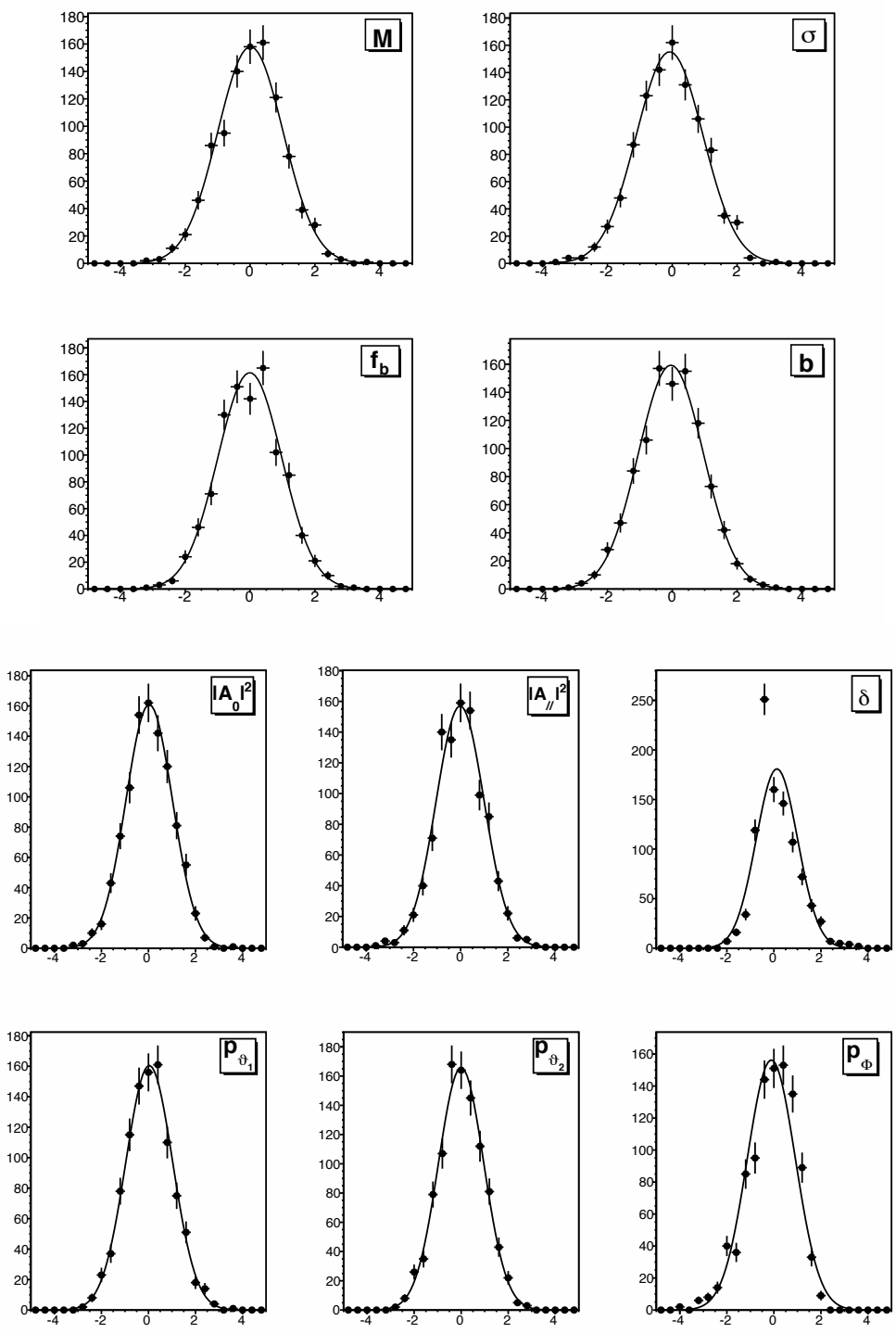

Figure 5.10: Pulls distributions of fit parameters for $B_s \to \phi\phi$ (1000 events per pseudo-experiment).

Parameter	Input value	Average fit error	Mean	Variance	Prob(χ^2) [%]
$\lvert A_0\rvert^2$	0.2	0.03	-0.12 ± 0.03	0.99 ± 0.02	20
$\lvert A_\parallel\rvert^2$	0.4	0.03	0.03 ± 0.03	1.03 ± 0.02	16
δ	1.57 rad	0.1 rad	0.05 ± 0.03	1.01 ± 0.02	26
$\lvert A_0\rvert^2$	0.7	0.02	0.03 ± 0.03	1.03 ± 0.02	2
$\lvert A_\parallel\rvert^2$	0.1	0.02	-0.04 ± 0.03	0.98 ± 0.02	61
δ	1.57 rad	0.1 rad	-0.01 ± 0.03	0.98 ± 0.02	47
$\lvert A_0\rvert^2$	0.2	0.02	-0.05 ± 0.05	1.02 ± 0.03	4
$\lvert A_\parallel\rvert^2$	0.7	0.02	0.06 ± 0.05	1.02 ± 0.03	8
δ	1.57 rad	0.1 rad	-0.04 ± 0.05	1.04 ± 0.03	65
$\lvert A_0\rvert^2$	0.1	0.03	-0.08 ± 0.05	1.03 ± 0.03	81
$\lvert A_\parallel\rvert^2$	0.2	0.03	0.04 ± 0.04	1.02 ± 0.03	2
δ	1.57 rad	0.2 rad	0.05 ± 0.04	0.94 ± 0.03	11

Table 14: Pulls test to check the resolution as a function of input parameters.

5.5.3 The Measurement of the Phase

We want to better understand the behaviour of the δ pulls distributions. First, from the previous tests, we learned that this complication:

- arises only in presence of low statistic;
- vanishes for $\delta \simeq \pi/2$ rad, as one can see in table 14.

We perform a set of pseudo-experiments changing the input value of the strong phase to span the interval $[0, 2\pi]$ rad. We fix all other parameters (also the polarization amplitudes, $|A_0|^2$ and $|A_\parallel|^2$). We report the results of the δ pulls distributions in tab. 15. This study puts in evidence a periodic behaviour of the pull distributions: if

δ Input value [rad]	Mean	Variance	Prob(χ^2) [%]
0.0	//	//	//
$\pi/16$	0.15 ± 0.06	0.84 ± 0.05	0
$\pi/8$	0.21 ± 0.04	0.93 ± 0.03	0
$\pi/4$	0.11 ± 0.04	0.92 ± 0.03	6
$\pi/2$	0.01 ± 0.05	1.04 ± 0.03	89
$3\pi/4$	0.05 ± 0.04	0.97 ± 0.03	0
$7\pi/8$	-0.12 ± 0.04	0.97 ± 0.03	0
π	//	//	//
$9\pi/8$	0.15 ± 0.06	0.89 ± 0.04	0
$3\pi/2$	-0.02 ± 0.05	1.04 ± 0.03	74
$15\pi/8$	-0.22 ± 0.04	0.93 ± 0.03	0

Table 15: Pulls test to study the behaviour of the strong phase pulls.

the input value is near either to $\delta \simeq 0$ rad or to $\delta \simeq \pi$ rad, the pulls are not gaussian and the fitter returns a biased estimate. The biases are greater as δ is closer to those two values, referred to as critic points. Although, when the input value is $\delta \simeq \pi/2$ rad or $\delta \simeq 3\pi/2$ rad the pulls are gaussian.

Furthermore, if we look to the distributions of the fitted value in the pseudo-experiments, we found a strange behaviour, that is the origin of the pulls distribution issue. When the input phase is close to the critic points, *e. g.*, $\pi/16$ rad ($9\pi/8$ rad), the fitter fails the parameter estimation and it often returns the value of the closest critic point, *i. e.*,

0 rad (π rad). The distribution presents a peak centered on the specific critic point value, as one can see in some representative distributions in fig. 5.11. Thus, the δ pulls issue is due to those pseudo-experiments in which the fit returns a certain critic point as parameter value. This is as less probable as farther to a critic points the input value is, or as larger the statistic is.

We have not already understood the cause in the fitter of this issue, but we can explain its periodic behaviour in the range $[0, 2\pi]$ rad: since the strong phase δ enters the fit as the argument of the cosine function, there is an ambiguity on its definition, because, naively speaking, $\cos(\delta) = \cos(-\delta)$. This implies that the likelihood function has two equivalent maxima in the δ space. They can be seen in fig. 5.19 of the Sect. 6.5. This ambiguity is well known from a previous similar angular analysis [106], which is actually affected by a similar problem.

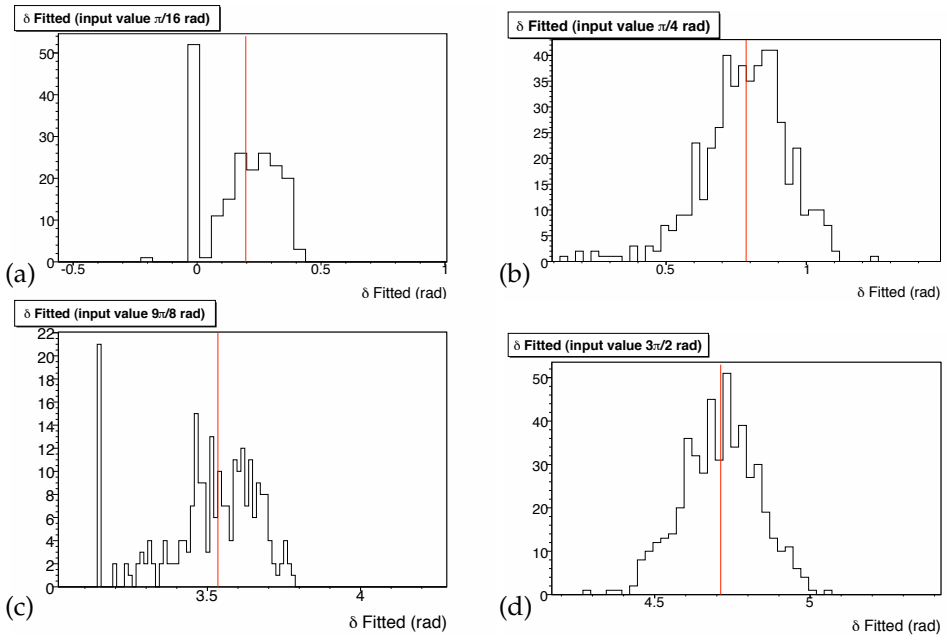

Figure 5.11: Distribution of the δ fitted values in the pseudo-experiments for four different input values: $\delta = \pi/16$ (a), $\delta = \pi/4$ (b), $\delta = 9\pi/8$ (c) and $\delta = 3\pi/2$ (d). The red lines represent the value of the input parameter.

5.6 FIT TO THE TTT $B_s \to J/\psi\phi$ SAMPLE

The second test is the implementation of the developed framework to fit the $B_s \to J/\psi\phi$ data sample collected with the same TTT selection of the $B_s \to \phi\phi$ decay (see previous Chapter). We use the $B_s \to J/\psi\phi$ decay mode as a control sample: we compare the results coming from our fit with the ones obtained in the different analysis published in [1], whose events was collected at CDFII by a different trigger selection, the Dimuon trigger (see later). Therefore, the control sample serves the purpose of improving the reliability of the main analysis. In this section, we summarize the procedure and we discuss the results for the $B_s \to J/\psi\phi$, leaving the analysis details in the Appendix B.

For its intrinsic nature of control sample, many of the technical aspects are in common with the $B_s \to \phi\phi$ analysis. The main difference is that the $B_s \to J/\psi\phi$ decay is described making use of the transversity angles $\vec{\Omega} = (\Theta, \Psi, \Phi)$ presented in Sect. 2.4.2.

First, we build the likelihood function for this case. The pdf structure is the same of eq. 5.8. In particular, the pdf components are described by:

- the equations 5.11 and 5.12 for the mass parameterization, since the distribution is similar to the $B_s \to \phi\phi$ one (compare fig. 4.5 and fig. 4.4). The parameters of the second gaussian is fixed from the fit to the MC data (see App. B).
- The equation 5.13 provides the signal angular parameterization, replacing the functions $f_i(\vec{\omega})$ and the phase ϕ_V by $f_i(\vec{\Omega})$ (eq. 2.62) and by $2\beta_s$, respectively. As in the main analysis:
  - we assume no CP-violation, fixing $\beta_s = 0$;
  - we set Γ_L and Γ_H to the latest PDG values;
  - the angular acceptance is taken from the three-dimensional histogram of the flatMC;
  - the angular background term comes from the parameterization of the sidebands events.

Then, the fitter is subjected to two tests: the pulls distributions and the fit to the real MC data sample. They are reported in the App. B. The pulls distribution test reveals unbiased estimate for all parameters, except for the strong phase δ, as in the $B_s \to \phi\phi$ case.

5.6.1 Fit Results and Projections

The results of the fit performed on 2.9 fb^{-1} of data for the $B_s \to J/\psi\phi$ are listed in the table 16. The fit projections onto the three transversity angles are shown in fig. 5.18

Parameter	Our fit value
$\lvert A_0\rvert^2$	0.539 ± 0.021
$\lvert A_\parallel\rvert^2$	0.246 ± 0.029
δ	0.0 ± 0.29

Table 16: Parameters of angular fit for $B_s \to J/\psi\phi$.

5.6.2 Comparison with the Dimuon Sample Results

We compare the results in tab. 16 with the ones obtained in the analysis published in [1], whose data were collected by the CDFII detector between February 2002 and January 2007, and correspond to an integrated luminosity of 1.7 fb^{-1}. First, we briefly summarize that analysis.

The events with $J/\psi \to \mu^+\mu^-$ decays were recorded using a different trigger selection. This is the Dimuon trigger, which requires two oppositely-charged COT tracks matched to muon chamber track segments with a dimuon mass between 2.7 and 4.0 GeV/c^2.

In the offline analysis, $B_0 \to J/\psi\phi$ decays are reconstructed making use of an artificial neural network (ANN). The ANN is trained to separate B_s decays from the

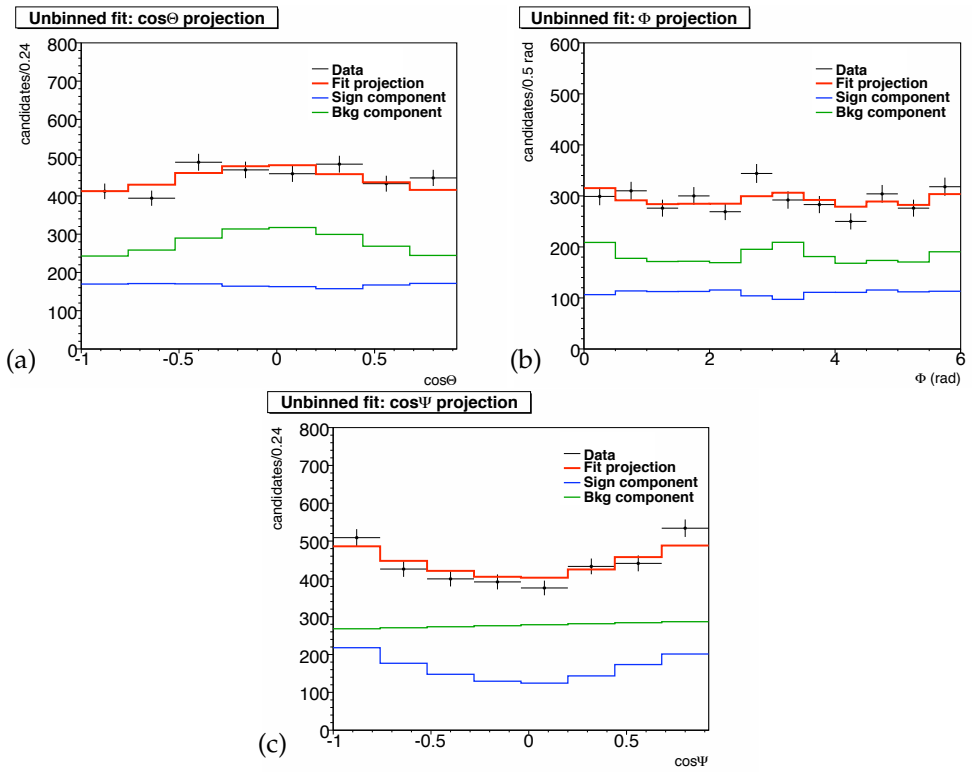

Figure 5.12: Angular fit projections for $B_s \to J/\psi\phi$: $\cos\Theta$ (a), $\cos\Psi$ (b) and Φ (c). The χ^2 probabilities of the fit projections are 0.21, 0.17 and 0.16 respectively.

combinatorial background, which is the dominant one. The signal is modelled with simulated events and data from B_s mass sidebands are used to model the combinatorial background. The input variables to the ANN are kinematic quantities, vertex fit quality parameters, and particle-identification information obtained from the muon system, the time-of-flight detector, and the dE/dx measurements. The requirement on the ANN output is selected by maximizing the significance $S/\sqrt{S+B}$ on data where S (B) is the number of signal (background) events in a $\pm 20\,\mathrm{MeV}/c^2$ window around the B_s mass peak position. The selected sample contains about 2500 $B_s \to J/\psi\phi$ decays. The ratio S/B is about 30%. In our TTT sample we have $S = 1766$ and $S/B \simeq 70\%$, thus, even if we collect a low statistic, we can reach the same resolution for the fitted parameters.

To extract the parameters, an unbinned ML fit is performed with pdf depending on mass, lifetime, and transversity angles. For the pdf of the background, empirical models are used with floating fit parameters determined from the data. Because correlations among the three angles are negligible, the angular pdf can be factorized as a product of polynomials in $\cos^2\Theta$, $\cos 2\Phi$ and $\cos\Psi$.

The lifetime-angular distribution without acceptance effects is given by eq. 2.57. The analysis is time dependent, since it is aimed at the estimation of $\Delta\Gamma_s$. The angular distribution of the B_s decays is modified by the detector acceptance as well as trigger and selection efficiencies. This effect is taken into account with an acceptance function, $\mathcal{A}(\vec{\Omega})$, derived from simulated $B_s \to J/\psi\phi$ decays. The factor $\mathcal{A}(\vec{\Omega})$ is described by a three-dimensional histogram with 20 bins in each of the angles, as we made in the $B_s \to \phi\phi$ analysis. The dominant source of systematic uncertainties on the amplitudes is the angular background model. Under the assumption of CP conservation ($\beta_s = 0$),

the result in tab. 17 are obtained. The first uncertainties are statistical, the second ones systematic. They do not quote an estimate of the strong phase because its likelihood profile is non-parabolic and this makes the uncertainty estimate unreliable. The fit projection are shown in fig. 5.13.

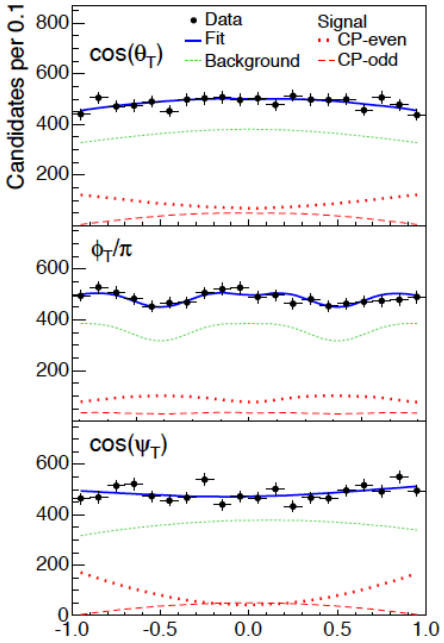

Figure 5.13: Angular projections for $B_s \to J/\psi\phi$ in [1].

The agreement of our results with the ones published in [1] is very satisfactory: the central values are consistent within the uncertainty ranges. For a better comparison, we report the two analysis results in the same table (17). In conclusion, the two experiments have compatible results among each other and provide us with an important successful check of our framework on the kinematically equivalent data sample $B_s \to J/\psi\phi$: this result contributes to enforce the reliability of our angular analysis implementation.

Parameter	Our fit result	Dimuon sample result
$\lvert A_0\rvert^2$	0.539 ± 0.021	$0.531 \pm 0.020 \pm 0.007$
$\lvert A_\parallel\rvert^2$	0.246 ± 0.029	$0.239 \pm 0.029 \pm 0.011$

Table 17: Comparison of our fit results and the ones in [1] for $B_s \to J/\psi\phi$.

5.7 FIT TO THE REALISTIC MC

The fit to the realistic MC data sample is the last test that we present. The MC is called "realistic" because it reproduces in order the main physical processes and the

processing steps involved in collecting data from real $p\bar{p}$ interactions, as described in Sect. 4.5.

The purpose of the test is to check if the fit is reliable. This means that the fit should return the same set of parameters adopted in the MC generation of the events. We fit the phase space MC used for the calculation of the detector angular acceptance. We expect to find no polarization, since the phase space MC has all the final state particles with averaged spins. This means that the polarization amplitudes are $|A_0|^2 \simeq |A_\parallel|^2 \simeq |A_\perp|^2 \simeq 0.33$ and that the strong phase is $\delta \simeq \pi/2$. In the realistic MC, the B_s are simulated to decay with a unique mean life. Thus, for this fit we put $\tau_L = \tau_H = \tau$.[3]

We find that the fit is not able to reproduce the expected values of the polarization amplitudes, although the strong phase is correctly estimated. The results are listed in table 18. The fit projections on the three helicity angles distributions are reported in fig. 5.14. The distributions are not well modelled by the fitting functions, except for the Φ projection.

Parameter	MC fit value
$\|A_0\|^2$	0.311 ± 0.001
$\|A_\parallel\|^2$	0.344 ± 0.001
δ [rad]	1.573 ± 0.005

Table 18: Parameters of the realistic MC angular fit for $B_s \to \phi\phi$

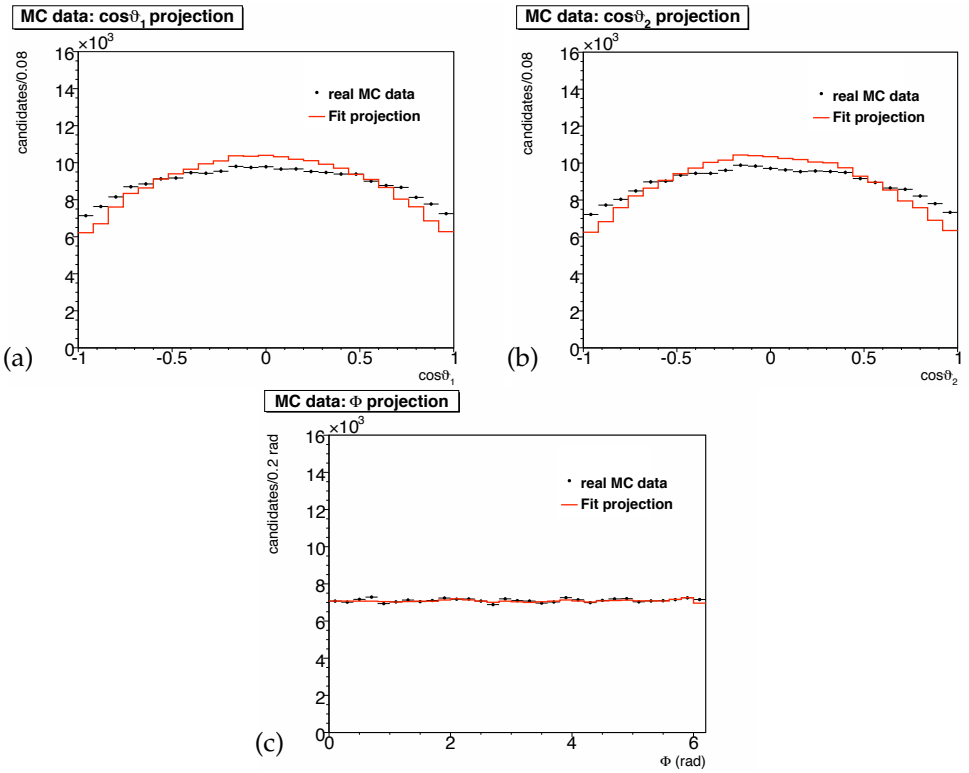

Figure 5.14: Angular fit projections of realistic MC for $B_s \to \phi\phi$: $\cos\vartheta_1$ (a), $\cos\vartheta_2$ (b) and Φ (c). The χ^2 probabilities of the fit projections are 0 for (a) and (b), and 0.44 for (c).

3 The value of τ is not important, since, putting $\tau_L = \tau_H$, it becomes a constant factor that multiply the likelihood (see eq. 5.13).

5.7.1 Dependence of the Angular Acceptance on the B Proper Decay Time

We want to understand the origin of the problem in the polarization amplitudes estimation on the real MC data sample, and, in particular, the unsatisfactory behavior of the $\cos\vartheta_{1(2)}$ fit projections. We can exclude that the origin is a intrinsic problem of the fitter framework, since the other two test (the pulls distributions and the control sample results) clearly reveal the correctness of the implementation and the reliability of the results.

We argue that the cause is the approximation adopted in the treatment of the detector angular acceptance: we have assumed that $\mathcal{A}(\vec{\omega})$ is not dependent on the reconstructed B_s proper decay time t. Thus, we check if this hypothesis is correct, by dividing the MC data sample in three sets (see fig. 5.15):

- set$_1$: events which have $ct \in [0.00; 0.05]$ cm;
- set$_2$: events which have $ct \in]0.05; 0.10]$ cm;
- set$_3$: events which have $ct \in]0.10; 0.50]$ cm.

For each set the three-dimensional histogram representing the angular acceptance, $H_i(\vec{\omega})$ ($i = 1, 2, 3$), is built, and then its projections on the three helicity angles are produced. We call this the operation of "binning the angular acceptance in slices of ct".[4] Thus, we compare the three different slices in ct for each $H_i(\vec{\omega})$ projection.

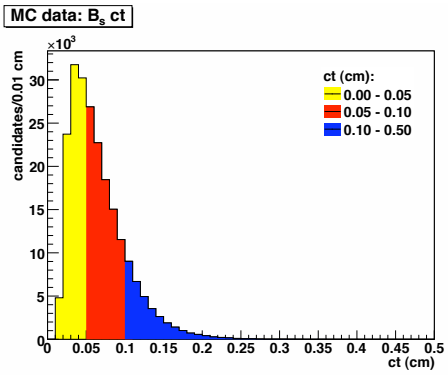

Figure 5.15: ct distribution of real MC data sample. The three ct slices are represented with different colors: in yellow $0.00\,\text{cm} < ct < 0.05\,\text{cm}$, in red $0.05\,\text{cm} \leq ct < 0.10\,\text{cm}$ and in blue $0.10\,\text{cm} < ct < 0.50\,\text{cm}$.

They are shown in fig. 5.16. From these plots the effect of the angular acceptance dependence on ct is evident in the $\cos\vartheta_1$ and $\cos\vartheta_2$ variables; the Φ projection, instead, is quite the same for each bin of ct. We perform a Kolmogorov test (tab. 19) on these projections, that confirms the changes of the $\cos\vartheta_{1(2)}$ projections with ct. Moreover, these changes with ct of the $\cos\vartheta_{1(2)}$ angular acceptance projections present the same shape's differences of the fit projections with respect to the data distribution. It is interesting that there is no dependence on ct for the Φ acceptance projection, and this is consistent with the fact that the fit projection correctly reproduces the realistic MC data distribution. We conclude that the assumption of no correlation with t of the detector acceptance is the origin of the problem in the polarization amplitudes estimation on the realistic MC data sample.

4 In the following, we often refer to the reconstructed B proper decay time t using the observable ct and vice versa, since they have equivalent meaning for us, being the speed of light c only a dimensional conversion factor.

Variable		Kolmogorov Probability
$\cos\vartheta_1$	set_1 Vs set_2	2×10^{-4}
	set_2 Vs set_3	9×10^{-4}
	set_1 Vs set_3	1×10^{-9}
$\cos\vartheta_2$	set_1 Vs set_2	5×10^{-5}
	set_2 Vs set_3	5×10^{-5}
	set_1 Vs set_3	1×10^{-12}
Φ	set_1 Vs set_2	0.36
	set_2 Vs set_3	0.57
	set_1 Vs set_3	0.65

Table 19: Comparison between three different slices of ct of the angular acceptance.

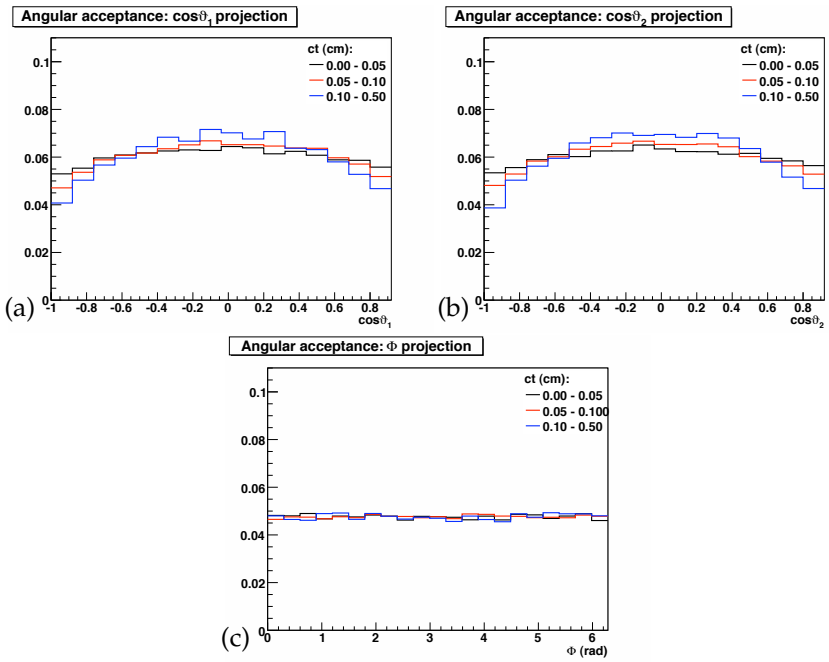

Figure 5.16: Dependence of detector angular acceptance projections on ct: $\cos\vartheta_1$ (a), $\cos\vartheta_2$ (b) and Φ (c).

5.7.2 Impact on the Measurement of $\mathcal{A}(\vec{\omega})$ dependence on ct

We want to estimate the impact on the fit to the real data sample of the detector angular acceptance dependence on ct. In fact, the MC data sample has around 223 000 events, which is above 600 times more events that we have in the actual $B_s \to \phi\phi$ data sample. Thus, this effect may have small observable consequences in the final fit compared to the statistical uncertainty. If this is the case, we can include it in the computation of final the systematic uncertainty; otherwise, we have to change the fit to consider the dependence of the angular acceptance on the B_s proper decay time.

We proceed as follow:

- we bin the three-dimensional histogram $H(\vec{\omega})$ with the three slices of ct above presented (see fig. 5.15); thus, we deal with three different acceptance curves, $H_i(\vec{\omega})$, one for each of the defined ct interval.

- using the toyMC tools, we generate a pseudo-experiment made of 50 000 events, in which we apply the original no-*ct*-binned angular acceptance;
- we fit the previous pseudo-experiment, using each of the $H_i(\vec{\omega})$ acceptance in the angular pdf separately.

This allow us to estimate the difference between the input polarization amplitudes, and the fitted ones, for each acceptance $H_i(\vec{\omega})$. We choose to generate the pseudo-experiments with $|A_0|^2 = |A_\parallel|^2 = 0.333$ and $\delta = \pi/2$, as in the flatMC. The results are reported in tab. 20 for $|A_0|^2$, and in tab. 21 for $|A_\parallel|^2$. In both tables, the third column reports the difference $\Delta_{\text{i-f}}$ between the input and the fitted central values. On average, $\Delta_{\text{i-f}}$ are of order of about 2-3%, with a peak of 6%. In the next section, we report the results of the fit performed on the actual data sample: we find that the statistical uncertainties of the polarization amplitudes are about 4%. Since they are of the same order of the differences $\Delta_{\text{i-f}}$, we choose to properly change the fit to consider also the detector angular acceptance dependence on the reconstructed B_s meson proper decay time. This is described in the next Chapter.

Acceptance	$\lvert A_0\rvert^2$	$\Delta_{\text{i-f}}$
$H_1(\omega)$	0.300 ± 0.003	0.033
$H_2(\omega)$	0.342 ± 0.003	0.009
$H_3(\omega)$	0.391 ± 0.003	0.058

Table 20: Differences between fitted and input values of $|A_0|^2$ for the three detector acceptances.

Fit acceptance	$\lvert A_\parallel\rvert^2$	$\Delta_{\text{i-f}}$
$H_1(\omega)$	0.348 ± 0.003	0.015
$H_2(\omega)$	0.328 ± 0.003	0.005
$H_3(\omega)$	0.301 ± 0.003	0.032

Table 21: Differences between fitted and input values of $|A_\parallel|^2$ for the three detector acceptances.

We make a further study, similar to the one above, on the changes of the angular acceptance with *ct*. The purpose is to try a smaller bin width of the *ct*-slices with respect to the three previous defined, to check if the differences $\Delta_{\text{i-f}}$ in the polarization amplitudes estimation can be minimized. This represents the first step to the handling of the time-dependent angular acceptance, that is discussed in the next Chapter. We proceed as follow:

- we bin the three-dimensional histogram $H(\vec{\omega})$ in five slices of *ct* (see fig. 5.17); thus, we deal with five different acceptance curves, $H_i(\vec{\omega})$, one for each of the following *ct* interval:
  1. $H_1(\vec{\omega})$ for events which have $ct \in [0.0000; 0.0375]$ cm;
  2. $H_2(\vec{\omega})$ for events which have $ct \in]0.0375; 0.0550]$ cm;
  3. $H_3(\vec{\omega})$ for events which have $ct \in]0.0550; 0.0750]$ cm;
  4. $H_4(\vec{\omega})$ for events which have $ct \in]0.0750; 0.0950]$ cm;
  5. $H_5(\vec{\omega})$ for events which have $ct \in]0.0950; 0.5000]$ cm.

  The *ct* segmentation is chosen in order to have, on average, about the same number of events per bin (≈ 26) in each of the $H_i(\vec{\omega})$ histogram, as in case of the initial no-*ct*-binned angular acceptance (≈ 28); for this reason, since the flat MC is made of 223 000 events, the three-dimensional histograms are built with $12 \times 12 \times 12$ bins.

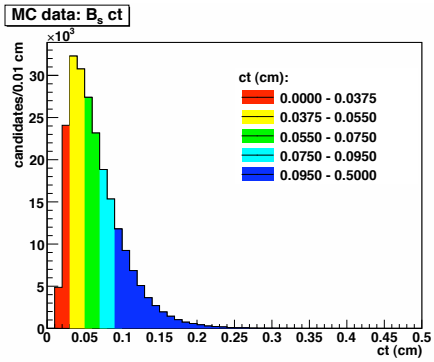

Figure 5.17: ct distribution of real MC data sample. The five ct slices are represented with different colors: in red $0.0\,\text{cm} \leq ct < 0.0375\,\text{cm}$, in yellow $0.0375\,\text{cm} < ct < 0.055\,\text{cm}$, in green $0.055\,\text{cm} \leq ct < 0.075\,\text{cm}$, in light blue $0.075\,\text{cm} \leq ct < 0.095\,\text{cm}$, and in blue $0.095\,\text{cm} < ct < 0.50\,\text{cm}$.

- using the toyMC tools, we generate a pseudo-experiment made of 1000 events (the same order of events that we have in the actual sample), in which we apply the $H_i(\vec{\omega})$ detector acceptance;
- we fit the previous pseudo-experiment, using the $H_{i+1}(\vec{\omega})$ acceptance in the angular pdf.

Thus we can compute the differences $\Delta_{\text{i-f}}$ between the input polarization amplitudes, generated with the $H_i(\omega)$ acceptance slice, and the fitted ones, using the $H_{i+1}(\omega)$ acceptance slice. This allow us to study:

1. the variation of $\Delta_{\text{i-f}}$ with the slices, and thus, with ct;
2. if we can reduce the differences between an acceptance slice and the next one with a smaller binning of ct.

Again, we generate the pseudo-experiments with $|A_0|^2 = |A_\parallel|^2 = 0.333$ and $\delta = \pi/2$. The results are reported in tab. 22 for $|A_0|^2$, and in tab. 23 for $|A_\parallel|^2$. We find that the values of $\Delta_{\text{i-f}}$ decrease with the smaller binning of ct, although, on average, the $\Delta_{\text{i-f}}$ are still of the order of 1-2%.

In principle, one can further reduce the ct bin width and make more slices than five; anyway there is a practical issue: a larger number of bins requires also a huge number of events generated in the flatMC, to maintain a certain number of events per bin to control the fluctuations of the three-dimensional acceptance histogram. We see that, both in the $|A_0|^2$ and in the $|A_\parallel|^2$ estimation, the largest $\Delta_{\text{i-f}}$ is for the case where the pseudo-experiment is generated using $H_4(\omega)$ and it is fitted with $H_5(\omega)$. Maybe, the cause of this is the large ct bin of the $H_5(\omega)$, that doesn't consider the variation of the acceptance in the tail of the ct distribution (see fig. 5.17).

5.8 TIME-INTEGRATED FIT TO REAL DATA

The results of the fit performed on $2.9\,\text{fb}^{-1}$ of data for the $B_s \to \phi\phi$ are finally listed in the table 24. We observe that the statistical uncertainties of the polarization amplitudes are of the same order of the ones that we have quoted in Sect. 2.5.2. The correlation coefficient between $|A_0|^2$ and $|A_\parallel|^2$ is $\rho = -0.447$.

Generation acceptance	Fit acceptance	fitted $\|A_0\|^2$	$\Delta_{\text{i-f}}$
$H_1(\omega)$	$H_2(\omega)$	0.35 ± 0.03	0.02
$H_2(\omega)$	$H_3(\omega)$	0.35 ± 0.03	0.02
$H_3(\omega)$	$H_4(\omega)$	0.36 ± 0.03	0.03
$H_4(\omega)$	$H_5(\omega)$	0.37 ± 0.03	0.04

Table 22: Differences between fitted and input values of $|A_0|^2$ for the five detector acceptances.

Generation acceptance	Fit acceptance	fitted $\|A_\parallel\|^2$	$\Delta_{\text{i-f}}$
$H_1(\omega)$	$H_2(\omega)$	0.33 ± 0.03	0.00
$H_2(\omega)$	$H_3(\omega)$	0.32 ± 0.03	0.01
$H_3(\omega)$	$H_4(\omega)$	0.32 ± 0.03	0.01
$H_4(\omega)$	$H_5(\omega)$	0.31 ± 0.03	0.02

Table 23: Differences between fitted and input values of $|A_\parallel|^2$ for the five detector acceptances.

Parameter	Fit value
M [GeV/c^2]	5.364 ± 0.001
σ [GeV/c^2]	0.016 ± 0.001
f_b	0.38 ± 0.03
b [c^2/GeV]	2.7 ± 0.7
$\|A_0\|^2$	0.351 ± 0.041
$\|A_\parallel\|^2$	0.286 ± 0.043
δ [rad]	0.4 ± 0.4
p_{ϑ_1}	0.3 ± 0.3
p_{ϑ_2}	0.8 ± 0.5
p_Φ	0.03 ± 0.06

Table 24: Results of the time-integrated fit for $B_s \to \phi\phi$.

The time-integrated fit projections onto the three helicity angles are shown in fig. 5.18: we see that the data distributions are very well reproduced by the fitting functions. The χ^2 probabilities of the fit projections are 0.46 for $\cos\vartheta_1$, 0.62 for $\cos\vartheta_2$ and 0.11 for Φ. The $\cos\vartheta_1$ and $\cos\vartheta_2$ projection present a very similar behaviour, both in the signal and in the background components, which is a confirmation of the symmetry of these two variables.

5.8.1 Likelihood scan

The results are given in terms of the ML estimates. Therefore the likelihood parabolic behaviour for the relevant parameters has to be checked. This can be achieved with the likelihood scans. In a scan, the value of the likelihood function is sampled by varying a certain parameter, leaving all other parameters fixed at the estimated value. The curve resulting from each scan is plotted in order to show the approximate behaviour of the likelihood. The procedure is not intended for minimization, thus the value of the minimum showed in the scan plot could be a little bit different with respect to the estimate point in the minimization procedure.

The likelihood scans for the polarization amplitudes and the strong phases are reported in fig. 5.19. The scans for the polarization amplitudes shows the expected parabolic behaviour mandatory to be able to have a reliable point estimate. This is not

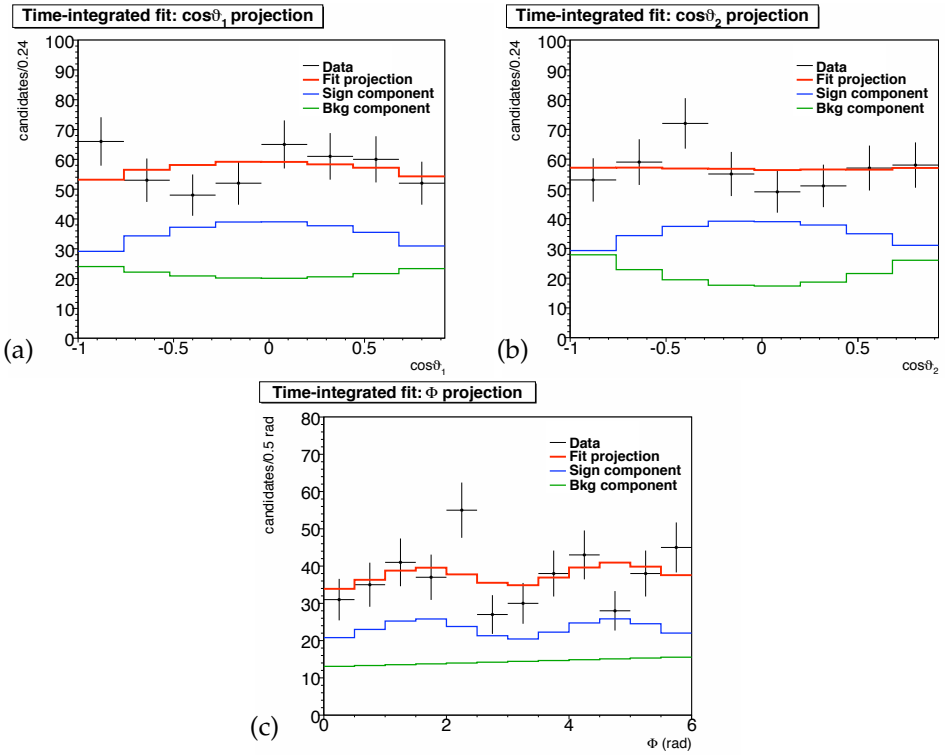

Figure 5.18: Angular projections of the time-integrated fit for $B_s \to \phi\phi$: $\cos\vartheta_1$ (a), $\cos\vartheta_2$ (b) and Φ (c). The χ^2 probabilities of the fit projections are 0.46, 0.62 and 0.11 respectively.

the case for the strong phase: the definition ambiguity can be seen in the likelihood profile, which has two minima. Since the likelihood scan for δ has a non-parabolic shape and because of its biases put in evidence in Sect. 5.5.3, we don't consider the point estimate for this quantity.

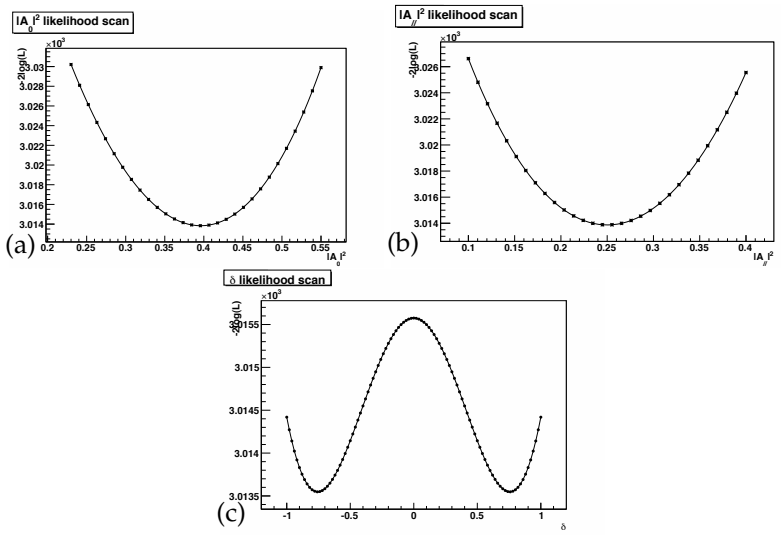

Figure 5.19: Likelihood scans of the time-integrated fit for $B_s \to \phi\phi$: $|A_0|^2$ (a), $|A_\parallel|^2$ (b) and δ (c).

6 TIME-DEPENDENT ANALYSIS

CONTENTS

THIS CHAPTER details the time-dependent analysis. The general problem of dealing with a time-dependent angular acceptance is worked out: a solution is proposed and the new likelihood, which contains also the reconstructed B_s proper decay time, t, as input variable, is then built on this basis. Thus, in this thesis, with "time-dependent" we mean that the fit takes into account the dependencies on t of the detector angular acceptance and the time evolution in the angular decay rate. In particular, this means that we use eq. 2.60 instead of eq. 5.13 as the signal angular pdf:

$$g_s(\vec{\omega}) = \frac{1}{\mathcal{N}}\mathcal{A}(\vec{\omega})\frac{d^3\Lambda}{d\vec{\omega}} \rightarrow g_s(\vec{\omega}, t) = \frac{1}{\mathcal{N}'}\mathcal{A}(\vec{\omega}, t)\frac{d^4\Lambda}{dtd\vec{\omega}}$$

The new fitter is tested by studying to the pull distributions. Then, the achieved improvements are shown, testing the framework with the fit to the realistic MC. Finally, we measure the polarization amplitudes of the $B_s \rightarrow \phi\phi$ decay, and the fit projections onto the data distributions are shown. A list of the sources of the systematic uncertainties is also reported.

6.1 HANDLING OF A TIME-DEPENDENT ANGULAR ACCEPTANCE

In the previous chapter, we demonstrate the dependence of the detector angular acceptance on the reconstructed B proper decay time. This is the first time that such an effect has been discovered in CDF analyses in the B sector. Actually, in the previous angular analyses, like in [1, 62], the constancy of the acceptance with respect to t was always naturally assumed.

One may ask himself why this doesn't happen in our case, or why the acceptance ct-dependence was not visible till now. While is quite simple to answer to the second question, the first one seems not to be so trivial. A hypothesis is that the origin of this surprising behaviour is due to the TTT and off-line cut selections on the impact parameter of the reconstructed K mesons, which is closely related to the helicity angles (for instance, $|\cos\vartheta_1| \approx 1$ corresponds to a $d_0(K_1) \approx 0$); the correlation of the $d_0(K)$ selection to the B_s proper time is not so obvious, because for each B_s meson there are four K particles that can trigger, and because the $d_0(K)$ may depend on the

corresponding $d_0(\phi)$. An exact answer needs a precise study. Anyway, we think that the effect was not observed before because:

- there was no other angular analysis that uses the TTT selection, except for the $B_d \to \phi K^{0\star}$ analysis in [62];
- the $B_d \to \phi K^{0\star}$ analysis has a lower statistics sample with respect to ours, thus, even if a similar effect was present, it could be neglected (see tab. 3);
- the off-line selection in [62] is not based on same particle impact parameter cut selection, as ours is;
- the topology of the $B_d \to \phi K^{0\star}$ is a little bit different with respect to the $B_s \to \phi\phi$, since the $K^{0\star}$ decay in a $K\pi$ pair.

While a detailed study to investigate the exact origin of this issue with the aim of reducing the impact of this on the analysis would be desirable in the future, in the following we detail a general solution that could be applied to the present problem as well as in other cases where such a time dependent angular acceptance is found. Thus, in the following we discuss a way to treat the "time-dependent" angular acceptance and to modify the time-integrated fit.

6.1.1 The New Detector Angular Acceptance

It is very difficult to find the analytical form of $\mathcal{A}(\vec{\omega})$ because of the correlations among the three helicity angles. Actually, we have used the three-dimensional histogram $H(\vec{\omega})$ to model empirically the detector angular acceptance, since the angles correlations don't allow us to simple write $\mathcal{A}(\vec{\omega})$ as the product of three terms $\mathcal{A}_{\vartheta_1}(\vartheta_1)\mathcal{A}_{\vartheta_2}(\vartheta_2)\mathcal{A}_{\Phi}(\Phi)$.

Now, the situation becomes more complicated, because we have to consider that $\mathcal{A}$ is also a function of t:

$$\mathcal{A}(\vec{\omega}) \to \mathcal{A}(\vec{\omega}, t) \tag{6.1}$$

By comparing the acceptance projected on helicity angle in different bins of ct we notice that a non trivial correlation exist between angle and time so that it is not possible to write a simple factorization of $\mathcal{A}(\vec{\omega}, t)$ in two terms, $\mathcal{A}(\vec{\omega})\mathcal{A}_t(t)$.

A feasible solution could be the generalization of the three-dimensional histogram $H(\vec{\omega})$: one may construct an object $H(\vec{\omega}, t)$, which is an extension of $H(\vec{\omega})$, adding to it another dimension, which account for the t variable. If $H(\vec{\omega})$ returns the probability to find an event at each position in the three-dimensional $\vec{\omega}$ space, $H(\vec{\omega}, t)$ accounts for this probability in the four-dimensional $\vec{\omega} \otimes t$ space. The construction of $H(\vec{\omega}, t)$ is simple: one divides the $\vec{\omega} \otimes t$ space in N four-dimensional cells,

$$v_i = [\cos\vartheta_1^{(i)}, \cos\vartheta_1^{(i+1)}] \times [\cos\vartheta_2^{(i)}, \cos\vartheta_2^{(i+1)}] \times [\Phi^{(i)}, \Phi^{(i+1)}] \times [t^{(i)}, t^{(i+1)}]. \tag{6.2}$$

Then each v_i cell is filled, counting how many events, generated with the flatMC, have the right value $(\cos\hat{\vartheta}_1, \cos\hat{\vartheta}_2, \hat{\Phi}, \hat{t}) \in v_i$. Thus, once $H(\vec{\omega}, t)$ is normalized to one dividing each cell content by the total number of event used, $H(\vec{\omega}, t)$ is an effective representation of the four-dimensional detector acceptance curve $\mathcal{A}(\vec{\omega}, t)$.

In practice, we compute $H(\vec{\omega}, t)$ by the procedure of binning the angular acceptance in slices of ct, adopted in the previous chapter to put in evidence the dependence of

$\mathcal{A}(\vec{\omega})$ on t: the binning of the t axis has an effect on $H(\vec{\omega}, t)$ that is represented by the various ct slices $H_i(\vec{\omega})$. Thus, the four-dimensional angular acceptance becomes:

$$H(\vec{\omega}, t) = \begin{cases} H_1(\vec{\omega}) \text{ if } t \in [t^{(0)}, t^{(1)}] \\ H_2(\vec{\omega}) \text{ if } t \in [t^{(1)}, t^{(2)}] \\ \dots \\ H_i(\vec{\omega}) \text{ if } t \in [t^{(i)}, t^{(i+1)}] \\ \dots \\ H_N(\vec{\omega}) \text{ if } t \in [t^{(N-1)}, t^{(N)}] \end{cases} \tag{6.3}$$

In principle, a large number of slices (*i. e.*, a small bin width) assures a better sampling of the variation in t, but a restriction is imposed by the total number of events generated in the flatMC, as mentioned in Sect 5.7.2, since a certain number of event per bin in the H_i histograms is necessary to control the fluctuations of each bin content. We can use the five slices defined in Sect. 5.7.2. The flatMC used is made of about 223 000 events, divided in $12 \times 12 \times 12$ bins in $\vec{\omega}$ and 5 slices in ct: on average, we have about 26 events per bin which corresponds to a mean fluctuation of order of 20%.

A new conceptual topic arises from the construction of the angular acceptance with the slices of ct. In fact, eq. 6.3 must be treat as a *conditional probability*, since the $H_i(\vec{\omega})$ returns the probability of an event to have a certain value $\hat{\omega}$, given $t \in [t^{(i)}, t^{(i+1)}]$. We use the following general notation:

- a conditional probability is written $\mathcal{P}(a|b)$ (the probability of some variable a, given the occurrence of some other variable b);
- a joint probability, *i. e.*, the probability of two variables in conjunction, is written $\mathcal{P}(a \cap b)$, or simply $\mathcal{P}(a, b)$.
- $\mathcal{P}(a)$ is the prior probability or marginal probability of a. It is prior in the sense that it does not take into account any information about b.

The following equation holds:

$$\mathcal{P}(a|b) = \frac{\mathcal{P}(a \cap b)}{\mathcal{P}(b)} \tag{6.4}$$

With the eq. 6.3 we pass to the use of a "conditional angular acceptance":

$$\mathcal{A}(\vec{\omega}, t) \to \mathcal{A}(\vec{\omega}|t) \tag{6.5}$$

6.2 THE NEW TIME-DEPENDENT LIKELIHOOD

To include the new effect in the fit, we have to consider the reconstructed B_s proper decay time in the set of the input variables as well, since for each event the likelihood function has to assign the correct angular acceptance slice. This means that the likelihood must account the time evolution. The mass pdf is independent on t, so it doesn't change. The time evolution enters in the angular component: we have to use as the signal angular pdf the decay rate as a function of both the proper decay time and the helicity angles, described by eq. 2.60, instead of its time integration (eq. 5.13):

$$\frac{d^3\Lambda}{d\vec{\omega}} \to \frac{d^4\Lambda}{dt d\vec{\omega}} = f(\vec{\omega}, t) \tag{6.6}$$

The new angular pdf is in practice a joint probability of $\vec{\omega}$ and t. This has to be combined with the angular acceptance, that in our representation, $H(\vec{\omega}|t)$, is a conditional probability.

We have two choices:

1. find a method to compute $H(\vec{\omega}, t)$, instead of $H(\vec{\omega}|t)$;
2. transform $f(\vec{\omega}, t)$ in $f(\vec{\omega}|t)$. This is possible using the definition 6.4:

$$f(\vec{\omega}|t) = \frac{f(\vec{\omega}, t)}{g(t)} \tag{6.7}$$

where $g(t) = \int f(\vec{\omega}, t) d\vec{\omega}$ is the prior probability of t.

The second option is the most feasible one, since the computation of $g(t)$ requires a simple integration.

We recall here eq. 2.60, *i. e.*,

$$f(\vec{\omega}, t) = \frac{9}{32\pi}\left[\mathcal{F}_{\mathrm{e}}(\vec{\omega})\mathcal{K}_{\mathrm{L}}(t) + \mathcal{F}_{\mathrm{o}}(\vec{\omega})\mathcal{K}_{\mathrm{H}}(t)\right] \tag{6.8}$$

where we have distinct two time-dependent and two angular-dependent terms:

$$\mathcal{F}_{\mathrm{e}}(\vec{\omega}) = |A_0|^2 f_1(\vec{\omega}) + |A_{\parallel}|^2 f_2(\vec{\omega}) + |A_0||A_{\parallel}| \cos\delta f_5(\vec{\omega}) \tag{6.9a}$$

$$\mathcal{F}_{\mathrm{o}}(\vec{\omega}) = |A_{\perp}|^2 f_3(\vec{\omega}) \tag{6.9b}$$

$$\mathcal{K}_{\mathrm{L}}(t) = 2e^{-\Gamma_{\mathrm{L}} t} \tag{6.9c}$$

$$\mathcal{K}_{\mathrm{H}}(t) = 2e^{-\Gamma_{\mathrm{H}} t} \tag{6.9d}$$

Then we observe that:

$$\begin{aligned} g(t) = \int f(\vec{\omega}, t) d\vec{\omega} = (|A_0|^2 + |A_{\parallel}|^2)\mathcal{K}_{\mathrm{L}}(t) + |A_{\perp}|^2 \mathcal{K}_{\mathrm{H}}(t) = \\ = a\mathcal{K}_{\mathrm{L}}(t) + b\mathcal{K}_{\mathrm{H}}(t) \end{aligned} \tag{6.10}$$

This equation nicely shows that the polarization amplitudes combines to give the fractions, $a = |A_0|^2 + |A_{\parallel}|^2$ and $b = |A_{\perp}|^2$, of the two time-evolution components. We can rewrite eq. 6.7 in the following form:

$$f(\vec{\omega}|t) = \frac{9}{32\pi}\left[\mathcal{F}_{\mathrm{e}}(\vec{\omega})\mathcal{U}(t) + \mathcal{F}_{\mathrm{o}}(\vec{\omega})\mathcal{V}(t)\right] \tag{6.11}$$

with the definition of:

$$\mathcal{U}(t) = \frac{\mathcal{K}_{\mathrm{L}}(t)}{g(t)} = \frac{\mathcal{K}_{\mathrm{L}}(t)}{a\mathcal{K}_{\mathrm{L}}(t) + b\mathcal{K}_{\mathrm{H}}(t)} \tag{6.12a}$$

$$\mathcal{V}(t) = \frac{\mathcal{K}_{\mathrm{H}}(t)}{g(t)} = \frac{\mathcal{K}_{\mathrm{H}}(t)}{a\mathcal{K}_{\mathrm{L}}(t) + b\mathcal{K}_{\mathrm{H}}(t)} \tag{6.12b}$$

Hence, the signal angular pdf becomes the following conditional probability

$$g_{\mathrm{s}}(\vec{\omega}|t) = \frac{1}{\mathcal{N}'}\frac{9}{32\pi}\left[\mathcal{F}_{\mathrm{e}}(\vec{\omega})\mathcal{U}(t) + \mathcal{F}_{\mathrm{o}}(\vec{\omega})\mathcal{V}(t)\right]\mathcal{A}(\vec{\omega}|t) \tag{6.13}$$

and the normalization factor $\mathcal{N}'$ is discussed in the Appendix A. We are not interested in the estimation of Γ_{L} and Γ_{H}, thus we fix them to the latest PDG value as we did in the time-integrated fit. Then, we can model the two time-evolution term, $\mathcal{U}(t)$ and $\mathcal{V}(t)$, using a realistic MC simulation: $\mathcal{K}_{\mathrm{L}}(t)$ and $\mathcal{K}_{\mathrm{H}}(t)$ are represented in practice by two histograms, $h_{\mathrm{L}}(t)$ and $h_{\mathrm{H}}(t)$, that are the ct distributions of the events generated with

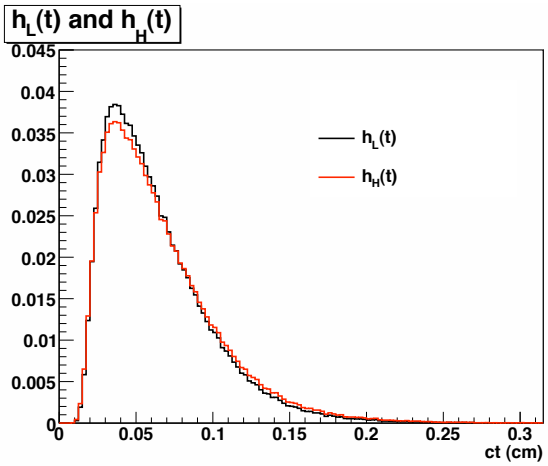

Figure 6.1: Plots of $h_{\mathrm{L}}(t)$ (in black) and $h_{\mathrm{H}}(t)$ (in red).

the mean time lives τ_{L} and τ_{H}, respectively. These histograms, properly normalized to one, are in fact the two components of the prior probability density $g(t)$. They are shown in fig. 6.1. The use of the MC histograms allows us to automatically take into account the detector and selection effects on the ct distribution, such as resolution in the ct measurement and the trigger ct-acceptance.

Finally, the representation of the resulting signal angular pdf is:

$$g_{\mathrm{s}}(\vec{\omega}|t) = \frac{1}{\mathcal{N}'}\frac{9}{32\pi}\left[\mathcal{F}_{\mathrm{e}}(\vec{\omega})\frac{h_{\mathrm{L}}(t)}{ah_{\mathrm{L}}(t)+bh_{\mathrm{H}}(t)} + \mathcal{F}_{\mathrm{o}}(\vec{\omega})\frac{h_{\mathrm{H}}(t)}{ah_{\mathrm{L}}(t)+bh_{\mathrm{H}}(t)}\right]H(\vec{\omega}|t) \quad (6.14)$$

6.2.1 Angular Background Parameterization

In the time-integrated fit, we verified that the three helicity angles are not correlated among each other, looking at their scatter plots in the side-bands events (fig. 5.7). This allow us to write the angular background pdf as the product of three functions, one for each helicity angles.

In the time-dependent fit, we would like to treat the angular background pdf in the same simple manner, although we know this is an approximation, since, in principle, the helicity angles could be correlated to t in the background events as well as they are in the signal samples. To check how good is this treatment of the background pdf, we divide the side-bands events in two sets, A and B:

- A events with $ct < 0.03\,\mathrm{cm}$;
- B events with $ct \geq 0.5\,\mathrm{cm}$.

Then we compare the shapes of the angular distributions of A and B. Their plots are shown in fig. 6.2. The Kolmogorov test returns probabilities (tab 25) which justify the use of the factorization of the angular background pdf in the following way:

$$g_{\mathrm{b}}(\vec{\omega},t) = g_{\mathrm{b}}^{(\omega_1)}g_{\mathrm{b}}^{(\omega_2)}g_{\mathrm{b}}^{(\omega_3)}g_{\mathrm{b}}^{(t)} \quad (6.15)$$

where the functions $g_{\mathrm{b}}^{(\omega_1)}$, $g_{\mathrm{b}}^{(\omega_2)}$ and $g^{(\omega_3)}$ are defined by the eq. 5.23.

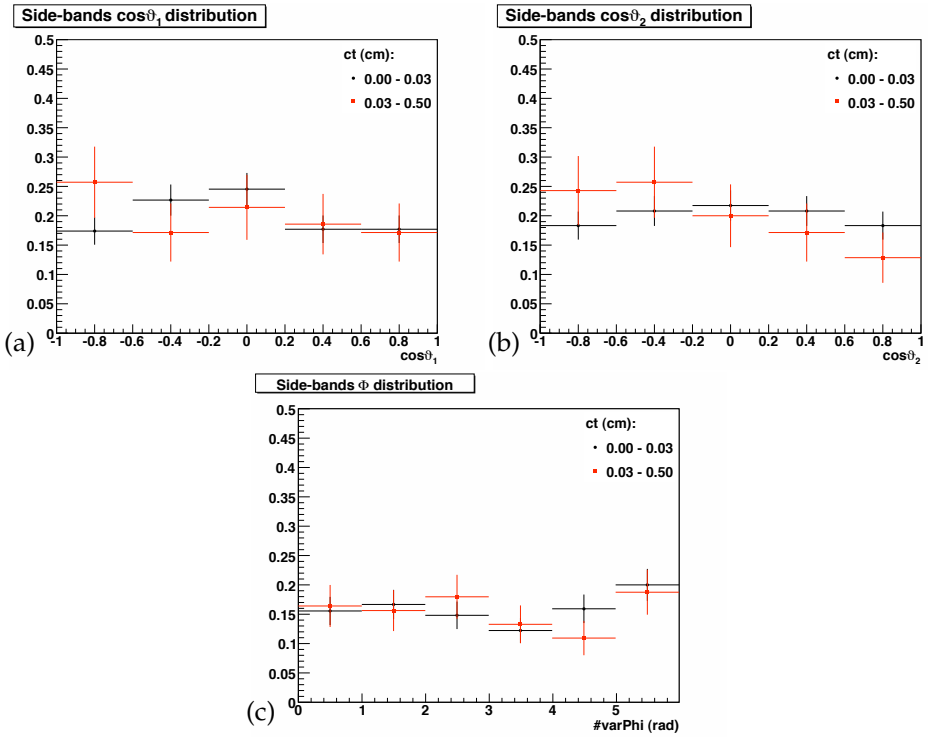

Figure 6.2: Comparisons of the angular distributions of the set A and the set B: $\cos\vartheta_1$ (a), $\cos\vartheta_2$ (b) and Φ (c). Black points are events with $ct < 0.03\,\text{cm}$; red points are events with $ct \geq 0.03\,\text{cm}$.

Variable	Kolmogorov test probability
$\cos\vartheta_1$	0.82
$\cos\vartheta_2$	0.51
Φ	0.95

Table 25: Kolmogorov test probabilities of angular side-bands distributions for the set A and the set B.

The pdf $g_b(\vec{\omega}, t)$ is a joint probability of $\vec{\omega}$ and t. We can transform it in a conditional probability as the angular signal pdf, using def. 6.4:

$$g_b(\vec{\omega}, t) \to g_b(\vec{\omega}|t) = \frac{g_b(\vec{\omega}, t)}{g_b^{(t)}} = \frac{g_b^{(\omega_1)} g_b^{(\omega_2)} g_b^{(\omega_3)} g_b^{(t)}}{g_b^{(t)}} = \\ = g_b^{(\omega_1)} g_b^{(\omega_2)} g^{(\omega_3)} \tag{6.16}$$

Hence, with the factorization of the variables terms we can use the background pdf adopted in the time-integrated fit, since the test in fig 6.2 allows us to assume that the background pdf is independent on the reconstructed B proper decay time.

6.3 NEW FIT SUMMARY

We now summarize the time-dependent fit features:

- the input variables are the reconstructed B_s mass m and proper decay time t, and the reconstructed K helicity angles $\vec{\omega} = (\vartheta_1, \vartheta_2, \Phi)$;
- the mass pdf is not changed with respect to the one of time-integrated analysis, both for the signal and the background components. They are described by eq. 5.11 and eq. 5.12, respectively.
- The angular background pdf is the same of the time-integrated fit as well.
- The angular signal pdf is represented by eq. 6.14, where:
  - the detector acceptance is given by the three-dimensional slices $H_i(\vec{\omega})$ for each ct-bins i ($i = 1, \ldots, 5$) identified in Sect 5.7.2;
  - the time evolution terms, $\mathcal{U}(t)$ and $\mathcal{V}(t)$, are modelled using the combination of the MC histograms $h_L(t)$ and $h_H(t)$ (eq. 6.12).
- We deal with the same ten fit parameters defined in the time-integrated fit, reported in tab. 26.

	Signal	Background
Mass	M, σ	f_b, b
Angular	$\lvert A_0\rvert^2$, $\lvert A_\parallel\rvert^2$, δ	p_{ϑ_1}, p_{ϑ_2}, p_Φ

Table 26: Parameters summary of the time-dependent $B_s \to \phi\phi$ fit.

- The following quantities are fixed in the final fit:
  - k and h, from the MC fit;
  - $\tau_L = \Gamma_L$ and $\tau_L = \Gamma_L$, the two mean life-time of the B_s mass eigenstates, are taken from the last PDG values and they are used in the generation of the $h_L(t)$ and $h_H(t)$ histograms.
  - $\phi_V = 0$, assuming no CP-violation;

6.4 FITTER TESTS

Before carrying out the fit over the data sample, we perform two tests: the pull distributions check and the fit to the realistic MC following the same approach we used for the time-integrated analysis. These test are described in the following sections.

6.4.1 Pulls Distributions

We perform the pulls distribution test, fitting samples with 1000 events for each pseudo-experiments, It is useful to check if there is any potential bias and any significant change in the fitter behaviour with respect to the time-integrated case. The pseudo-experiments are generated with the *bootstrap* of the real data sample. The bootstrap is a useful statistical technique described in [107].[1] The bootstrapped pseudo-experiment is obtained by random sampling the real data set, given at each event the

1 Bootstrapping is the practice of estimating properties of an estimator by measuring those properties when sampling from an approximating distribution. One standard choice for an approximating distribution is the empirical distribution of the observed data.

same probability to be chosen. The results of the test are reported in tab. 27, and the pulls distributions are shown in fig. 6.3. The resolution (third column of the table) of each parameter is consistent with the one found in the time-integrated fit (tab. 13).

Parameter	Input value	Average fit error	Mean	Variance	Prob(χ^2) [%]
M	5.364 GeV/c^2	0.0009 GeV/c^2	-0.02 ± 0.03	0.99 ± 0.02	93
σ	0.017 GeV/c^2	0.0008 GeV/c^2	-0.04 ± 0.04	1.16 ± 0.03	20
f_b	0.40	0.02	-0.09 ± 0.03	1.03 ± 0.02	21
b	2.6 c^2/GeV	0.5 c^2/GeV	0.00 ± 0.03	1.03 ± 0.02	14
$\lvert A_0 \rvert^2$	0.39	0.03	0.00 ± 0.03	1.03 ± 0.02	14
$\lvert A_\parallel \rvert^2$	0.26	0.03	-0.02 ± 0.03	1.03 ± 0.02	64
δ	0.4 rad	0.3 rad	0.13 ± 0.03	0.93 ± 0.02	0
p_{ϑ_1}	0.2	0.2	0.10 ± 0.03	1.02 ± 0.02	0
p_{ϑ_2}	0.5	0.3	-0.05 ± 0.03	1.05 ± 0.02	0
p_Φ	0.03	0.04	0.11 ± 0.03	1.02 ± 0.02	0

Table 27: Pulls mean and variance for time-dependent fit. In the second column the input parameters of the generation are listed. The third column reports the average error in the pseudo-experiments fit (resolution). The fourth and the fifth columns list the mean value and the variance of the pull distributions, respectively. The sixth column presents the χ^2 probability for a gaussian fit of the pulls distribution with mean and variance 0 and 1, respectively.

We find that the fitter returns unbiased estimates and consistent uncertainties for the polarization amplitudes. The strong phase δ presents the same problem of the time-integrated fit. The pulls of the other parameters are within 0.1 σ of their mean values.

6.4.2 Improvements of Realistic MC Fit

The fit to the realistic MC data sample is the second test of the time-dependent fit. The purpose of the test is to compare the results with the ones of the time-integrated fit to the same realistic MC data sample, in order to check if there are improvements with the new pdf definition. Thus, we fit the phase space MC used for the calculation of the detector angular acceptance as we discuss in Sect. 5.7. The results are listed in table 28. The fit projections onto the three helicity angles distributions are reported in figs. 6.4–6.6. The differences between the estimated values and the input ones are still of the order of 1-2%. Anyway, the improvements achieved by the new fit is evident in the fit projections onto the $\cos\vartheta_{1(2)}$ distributions, looking at the comparisons in figs. 6.4 and 6.5. The not complete agreement with the expected values could be due to the binning of the ct-slices: with this large statistic a smaller bin width is probably needed to account for the ct-variations of the angular acceptance. The shifts from the expected values could indeed represent an estimation of the systematic uncertainties of the measurements due to the ct-bin width.

Parameter	MC time-dependent fit value
$\lvert A_0 \rvert^2$	0.356 ± 0.001
$\lvert A_\parallel \rvert^2$	0.322 ± 0.001
δ [rad]	1.567 ± 0.005

Table 28: Parameters of the realistic MC angular fit for $B_s \to \phi\phi$

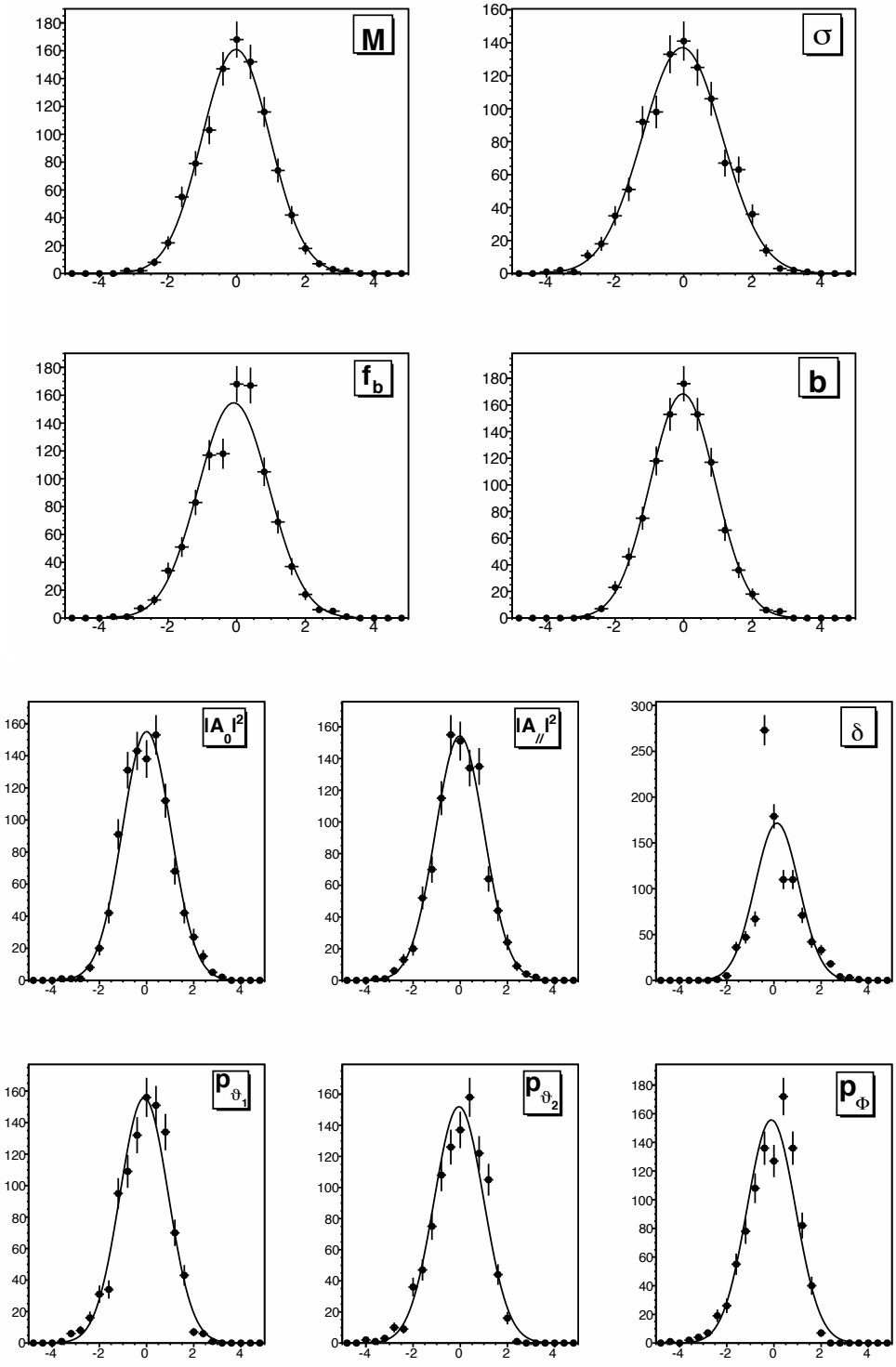

Figure 6.3: Pulls distributions for time-dependent fit

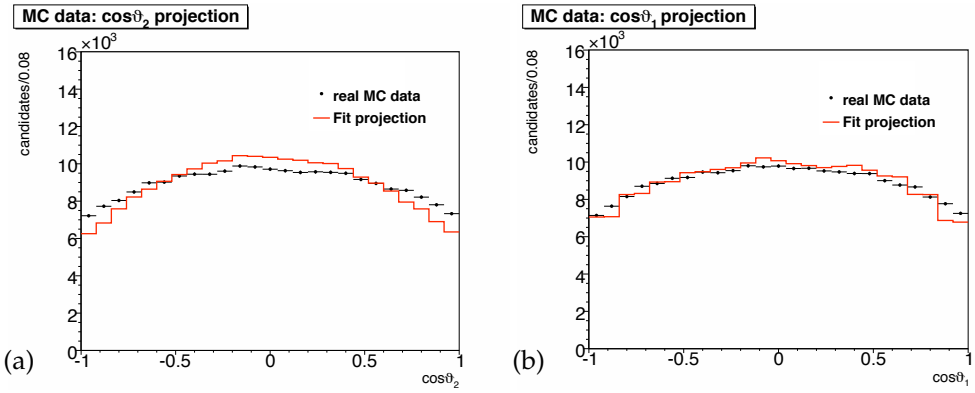

Figure 6.4: Comparison of the time-integrated and the time-dependent fit to the MC data: $\cos\vartheta_1$ projection. (a) time-integrated fit; (b) time-dependent fit. The black points are MC data, the red line is the fit projection.

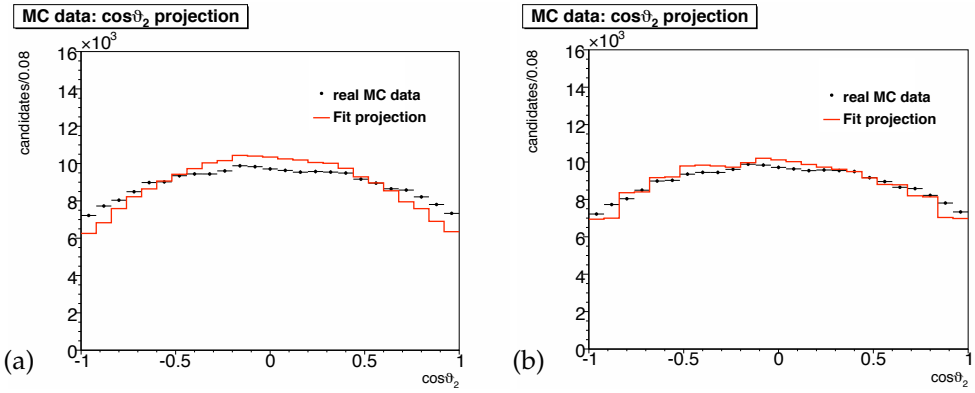

Figure 6.5: Comparison of the time-integrated and the time-dependent fit to the MC data: $\cos\vartheta_2$ projection. (a) time-integrated fit; (b) time-dependent fit. The black points are MC data, the red line is the fit projection.

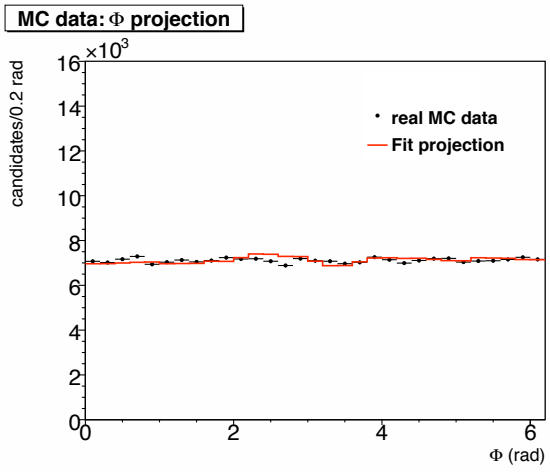

Figure 6.6: Time-dependent fit to the MC data: Φ projection. The black points are MC data, the red line is the fit projection.

6.5 TIME-DEPENDENT FIT TO REAL DATA

The results of the time-dependent fit performed on 2.9 fb^{-1} of data for the $B_s \to \phi\phi$ are finally listed in the table 29. Table 30 reports the correlation coefficients between the parameters. We observe that each parameter measurement is consistent with the corresponding time-integrated fit result within the uncertainties.

Parameter	Fit value
M [GeV/c^2]	5.364 ± 0.001
σ [GeV/c^2]	0.017 ± 0.001
f_b	0.40 ± 0.03
b [c^2/GeV]	2.6 ± 0.6
$\lvert A_0 \rvert^2$	0.388 ± 0.042
$\lvert A_\parallel \rvert^2$	0.257 ± 0.041
δ [rad]	0.4 ± 0.3
p_{ϑ_1}	0.1 ± 0.3
p_{ϑ_2}	0.5 ± 0.4
p_Φ	0.03 ± 0.05

Table 29: Results of the time-dependent fit for $B_s \to \phi\phi$.

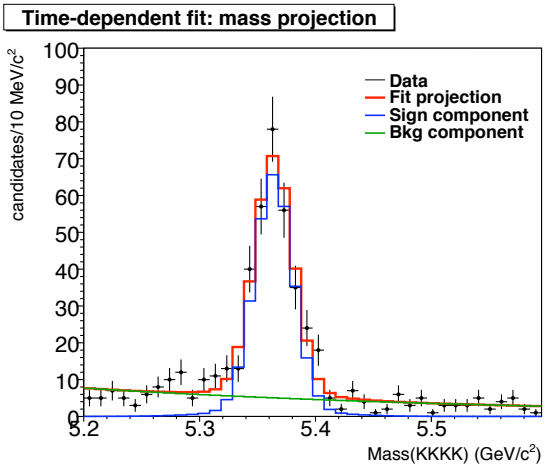

Figure 6.7: Time-dependent fit projection onto the mass distribution for $B_s \to \phi\phi$. The black points are the data; the red line is the resulting fit distribution. The blue line represents the signal component, the green line the background. The χ^2 probability of the fit projection is 0.02,

The time-dependent fit projections onto the three helicity angles are shown in fig. 6.8: we see that the data distributions are very well reproduced by the fitting functions. The χ^2 probabilities of the fit projections are 0.60 for $\cos\vartheta_1$, 0.38 for $\cos\vartheta_2$ and 0.12 for Φ. The time-dependent fit projections onto the mass distribution is shown in fig. 6.7. In fig. 6.9 we compare the ct distribution of the events in the mass signal peak side-bands subtracted with the histogram of $g(t)$ where the a and b fractions are calculated with the estimated polarization amplitudes. The χ^2 test on these two distributions returns a probability of 46%.

6.5.1 Likelihood Scan

The likelihood scans for the polarization amplitudes and the strong phases are reported in fig. 6.10. The scans for the polarization amplitudes shows the expected parabolic behaviour mandatory to be able to have a reliable point estimate. This is not the case for the strong phase: the definition ambiguity can be seen in the likelihood profile, which has two minima. Since the likelihood scan for δ has a non-parabolic shape and because of its biases put in evidence in Sect. 5.5.3, we don't consider acceptable the point estimate for this quantity.

6.5.2 Perspectives: Systematic Studies

The next natural step to complete the measurement is the computation of the systematic uncertainty. In the following we discuss a list of the main systematic sources, but we could not be achieved in the time frame of this thesis their estimation.

The systematic uncertainty for the ML fit is meant to cover the effects which may have not been properly incorporated in our model and could precisely lead to systematic biases on the estimates. These uncertainties are mostly evaluated using pseudo-experiments technique. For a parameter ξ, the magnitude of a systematics is evaluated from the difference of the mean ξ_{syst} from the toyMC with the systematic effect included and the mean ξ_{ref} of the toyMC when the effect is removed. Thus, we will evaluate the systematic effects by simulating experiments with a different parameterization while using the default model for fitting.

UNCERTAINTIES ON Γ VALUES. The uncertainties on the values of $\Gamma_{\text{L(H)}}$ have an impact on the estimates. To compute this effect we will fit some pseudo-experiments generated varying the value of $\Gamma_{\text{L(H)}}$ within one sigma of their uncertainties. Performing a fit to a pseudo-experiment sample generated with the central value of $\Gamma_{\text{L(H)}}$, one gets the systematic uncertainty, looking at the differences of the estimate values for two kind of pseudo-experiments.

ANGULAR BACKGROUND PARAMETERIZATION. We observe a good agreement between the data in the sideband mass regions and the angular background model, but we cannot exactly know if we used a too simple or too complex models. Thus, we will test it fitting some pseudo-experiments in which the angular background is generated using different models, as some linear functions for all angular variables or, alternatively, a similar functional form as the one of the signal component. Then we will performs a fit to a pseudo-experiment generated with the same model used in the fit to the real data. The difference between the obtained estimate in the various fits defines the systematic uncertainty related to the angular background parameterization.

Another potentially source of a systematic effect in the angular background component comes from the assumption of no-correlation of the angular variables with the proper decay time t. In order to estimate a systematic effect introduced by this assumption, we will proceed as in the previous case, using toyMC where the angular background component is generated with a certain reasonable function of both angles and time.

NON-RESONANT CONTRIBUTION. The fit of the reconstructed ϕ mass distribution shows that there are no evident non-resonant components under the ϕ peak signal (fig. 4.12). However, it is possible that there is a very small S-wave (scalar) contribution to the angular distribution, such as a f_0 state. To compute this effect, one has first to estimate the fraction of these events in our data sample. Then,

one can model with the MC technique the contribution of this scalar component into the angular distribution. Thus, the usually pseudo-experiments procedure allows one to compute the order of the systematic uncertainty of such an effect.

REFLECTIONS CONTRIBUTION. In our fit we do not include the $B_s \to \phi K^\star$ reflection component. Anyway, we already know its fraction in our data sample from the branching ratio analysis (see Sect. 4.4). To estimate the systematic effect introduced by not accounting for the reflections, we can proceed with the pseudo-experiments technique in a similar way of the case of the non-resonant contribution.

RESIDUAL DISCREPANCY BETWEEN DATA AND MC. In Sect. 4.5 we mention the MC validation performed in the branching ratio analysis [29]. A residual discrepancy between the MC and the actual data distributions could be present and a further investigate is desirable, because the MC simulation plays a pivotal role in the fitter framework, with the construction of the histograms that represents the angular acceptance and the time evolution terms in the signal pdf. Thus, we will proceed as follow:

- find the kinematic variables that present some discrepancy between the data and the MC;
- reweight the MC distributions in order to achieve a greater agreement in these distributions;
- use the reweighted MC to construct the needed histograms;
- fit the real data sample applying the reweighted MC histograms in the pdf;
- compare the estimates of that fit with the ones obtained by the not-reweighted MC.

The latter comparison (in particular the differences of the estimates in the two fits) gives the order of the systematic uncertainty due to the residual discrepancy between the actual data and the MC model.

BIN OF THE ct-SLICES. It is evident that the number of the ct-slice and thus their bin width have a consequence in the model of the acceptance variation with t for the angular acceptance. The sampling of this dependency improves as well as the number of the slices increase and their bin width becomes smaller. In particular, the latter condition is needed in the tail of the ct-distribution. In this case we can reduce this systematic effect. We will increase the statistic of the flatMC data sample in order to allow one to construct the $H(\vec{\omega}|t)$ with a greater number of slices than five.

We expect a small contribution to the total error by the systematic uncertainties, since the statistical uncertainties should be dominant. Actually, the time-dependent fit avoids the time integration of the differential decay rate, which was estimated to be the main systematic source of the analysis.

	M	σ	f_b	b	$\lvert A_0\rvert^2$	$\lvert A_\parallel\rvert^2$	δ	p_{ϑ_1}	p_{ϑ_2}	p_Φ
M	$+1.000$	-0.028	$+0.017$	$+0.070$	-0.006	-0.016	-0.002	$+0.011$	$+0.013$	$+0.004$
σ	-0.028	$+1.000$	-0.364	-0.020	$+0.051$	-0.030	$+0.100$	$+0.039$	-0.009	$+0.004$
f_b	$+0.017$	-0.364	$+1.000$	$+0.021$	-0.042	$+0.018$	-0.142	-0.035	-0.016	$+0.007$
b	$+0.070$	-0.020	$+0.021$	$+1.000$	-0.005	-0.004	-0.004	$+0.002$	$+0.005$	$+0.002$
$\lvert A_0\rvert^2$	-0.006	$+0.051$	-0.042	-0.005	$+1.000$	-0.433	$+0.137$	-0.146	-0.164	-0.024
$\lvert A_\parallel\rvert^2$	-0.016	-0.030	$+0.018$	-0.004	-0.433	$+1.000$	$+0.091$	$+0.066$	$+0.090$	$+0.005$
δ	-0.002	$+0.100$	-0.142	-0.004	$+0.137$	$+0.091$	$+1.000$	$+0.002$	-0.029	-0.006
p_{ϑ_1}	$+0.011$	$+0.039$	-0.035	$+0.002$	-0.146	$+0.066$	$+0.002$	$+1.000$	$+0.070$	$+0.040$
p_{ϑ_2}	$+0.013$	-0.009	-0.016	$+0.005$	-0.164	$+0.090$	-0.029	$+0.070$	$+1.000$	$+0.017$
p_Φ	$+0.004$	$+0.004$	$+0.007$	$+0.002$	-0.024	$+0.005$	-0.006	$+0.040$	$+0.017$	$+1.000$

Table 30: Correlation coefficients of the time-dependent fit for $B_s \to \phi\phi$.

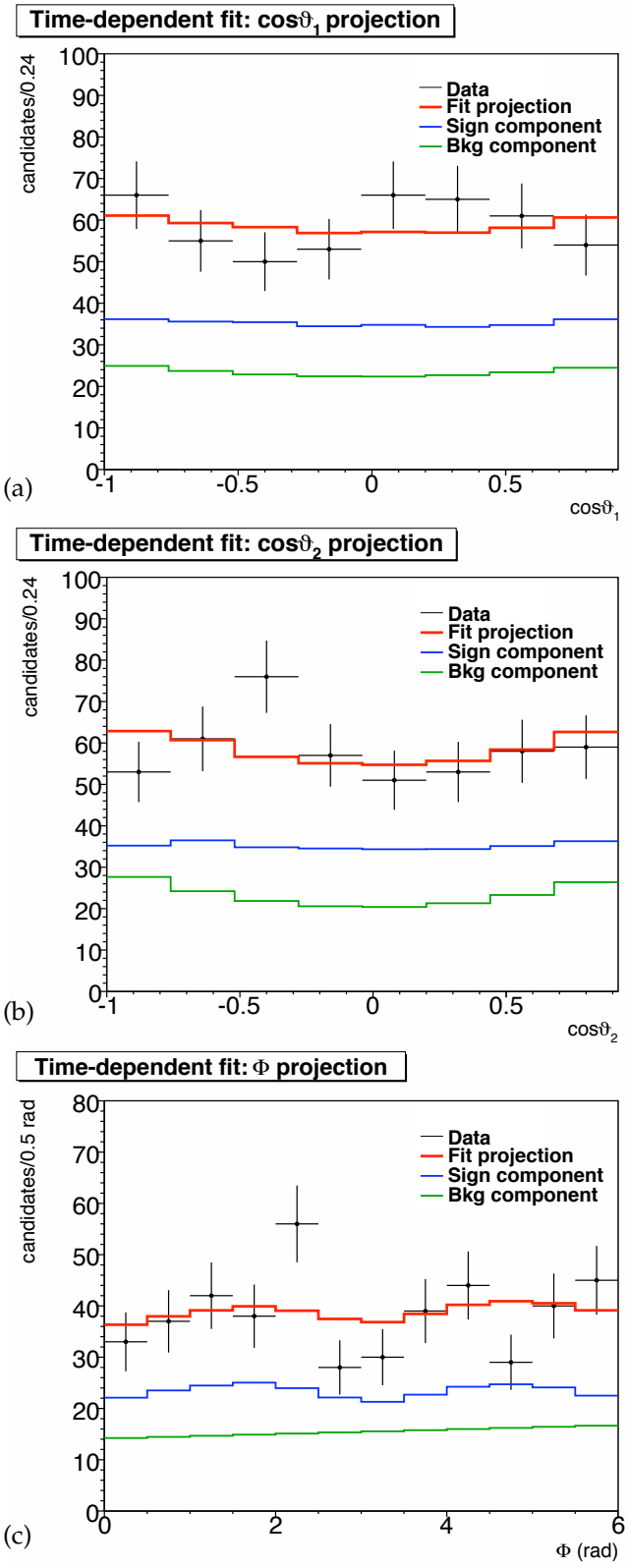

Figure 6.8: Angular projections of the time-dependent fit for $B_s \to \phi\phi$: $\cos\vartheta_1$ (a), $\cos\vartheta_2$ (b) and Φ (c). The χ^2 probabilities of the fit projections are 0.60, 0.38 and 0.12 respectively.

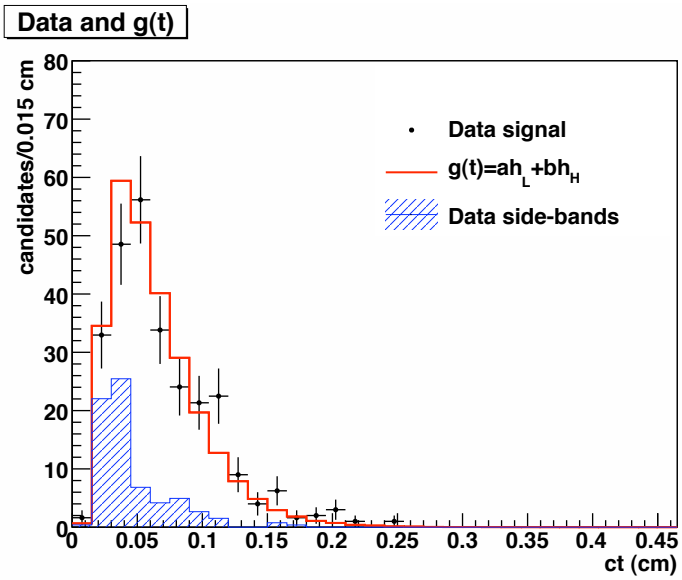

Figure 6.9: Comparison of ct data distribution and $g(t)$ for $B_s \to \phi\phi$. The black points are sidebands subtracted data (see Sect. 4.5); the red line is the histogram of $g(t)$ where the a and b fractions are calculated with the estimated polarization amplitudes; the blue histogram is the sidebands data distribution. The comparison of these distributions returns a χ^2 probability of 0.46.

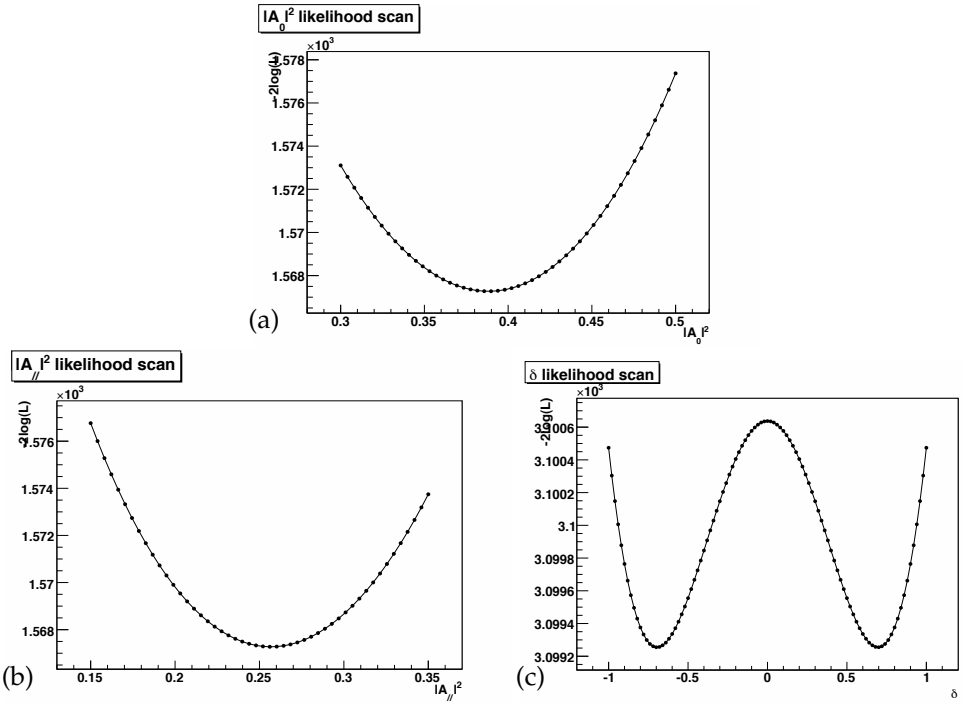

Figure 6.10: Likelihood scans of the time-dependent fit for $B_s \to \phi\phi$: $|A_0|^2$ (a), $|A_\parallel|^2$ (b) and δ (c).

7 CONCLUSIONS

In this thesis we have presented the first measurement of the polarization amplitudes for the charmless $B_s \to \phi\phi \to [K^+K^-][K^+K^-]$ decay of the B_s meson. The result is achieved using an unbinned Maximum Likelihood fit to the data collected by the CDFII detector, in a period starting from March 2001 till April 2008, which corresponds to an integrated luminosity of $2.9\,\text{fb}^{-1}$. This measurement represents the natural evolution of the branching ratio analysis [29], in which a yield of 300 signal events was selected using the data sample collected by the Two Track Trigger.

In the analysis we don't distinguish between B_s and $\bar{B}_s$ at the production time (*untagged* analysis) and we assume the B_s mixing phase $\phi_V = 0$ because in the SM its value is very small. The final fit takes into account the time evolution of the angular decay rate in terms of the B_s Light and Heavy mass eigenstates evolutions, but their two mean time lives, τ_L and τ_H, are taken as external parameters and they are fixed to the latest PDG values. The input fit variables are the reconstructed B_s mass and proper decay time, and the reconstructed K^+ helicity angles. The fitter framework is checked by different tests. First, the pull distributions, which shows that the estimates are unbiased; second, the fit of the realistic Monte Carlo data. Third, the fit of the $B_s \to J/\psi\phi$ decay selected by the TTT: the polarizations amplitudes we find are consistent with the ones reported in [1]; this result contributes to enforce the reliability of the analysis.

Furthermore, our work puts in evidence an original topic, that was never observed until now: an unexpected dependence of the signal acceptance on the proper decay time (t) of the B_s mesons. This specific issue, which is most likely a general feature induced by any signal selection based on the lifetime information, is supposed to be related to the on-line TTT and off-line selections based on the impact parameter.

This complication is handled by binning in slices of t the signal acceptance, which is modeled using the MC simulation. Such treatment involves the construction of the pdf that enters the Likelihood thought as a conditional probability of the mass and the helicity angles, given the t of the events. The final time-dependent fit, indeed, reproduces the biases observed in large statistics MC samples.

The three estimated polarization amplitudes are:

$\lvert A_0\rvert^2$	$\lvert A_\parallel\rvert^2$	$\lvert A_\perp\rvert^2$
0.388 ± 0.042	0.257 ± 0.041	0.355 ± 0.044

and the resulting polarization fractions are:

longitudinal (f_L)	transverse (f_T)
0.388 ± 0.042	0.612 ± 0.060

7.1 PERSPECTIVES

The systematic uncertainties listed at the end of the previous chapter have to be computed and this is the next foreseen step of this analysis. Anyway, we expect that the

statistical uncertainties give the dominant contribution to the total error. Actually, the final fit avoids the time integration of the differential decay rate, which was estimated to be the main source of the systematic uncertainty. An improvement of the used procedure, that minimizes the systematic uncertainty due to the binning in ct of the signal acceptance, could be achieved increasing the number of the MC simulated events: this allows one to use more ct-slices of a smaller bin width, and to better sample the variation with t of the signal acceptance. Besides, with a large number of events a direct implementation of the "four-dimensional histogram" described in Sect. 6.1.1 can be made.

The measurement is performed with $2.9\,\text{fb}^{-1}$ of data, achieved by CDFII in April of the last year. As of this writing, $6.9\,\text{fb}^{-1}$ of data is already delivered, and at the end of the next year an integrated luminosity of about $10\,\text{fb}^{-1}$ is expected. Thus, it is possible to extend the analysis to a greater data sample in order to minimize the statistical uncertainties. A rough calculation, which doesn't take into account the prescaling of the different triggers with the instantaneous luminosity, shows that the reachable resolutions σ on the polarization amplitudes is:

$$\sigma = 0.04\sqrt{\frac{2.9}{10}} \approx 0.02 \tag{7.1}$$

Hence, we could expect a factor $1/2$ of the current statistical uncertainty for the analysis in $10\,\text{fb}^{-1}$ of data.

Moreover, the extension of the analysis beyond $2.9\,\text{fb}^{-1}$ of data allows us to measure the two mean live times τ_L and τ_H. Actually, not much more statistics with respect to the ones in ours sample are needed to perform a time-dependent fit aimed at the Γ_L and Γ_H estimation; such an analysis, indeed, could just require only little modifications to the time-dependent fit described in this thesis.

7.2 THEORETICAL CONSIDERATIONS ON THE RESULTS

From our measurement we can draw the following considerations:

1. the amplitude hierarchy $|A_0| \gg |A_\parallel| \simeq |A_\perp|$ of the SM is not satisfied in the $B_s \to \phi\phi$ decay, being $|A_0| \simeq |A_\perp| \gtrsim |A_\parallel|$;
2. the longitudinal polarization fraction is less than the transverse one, in contrast with
   - the SM expectation, that predicts a dominant longitudinal fraction with the transversely-polarized amplitudes suppressed by a factor m_ϕ / m_{B_s};
   - the decay amplitudes for $B \to \phi K^\star$, a $\bar{b} \to \bar{s}$ penguin transition like the $B_s \to \phi\phi$, measured by the BaBar and the Belle experiments [17, 54, 55], which result in a transverse polarization about equal to the longitudinal one, being $f_L = 0.50 \pm 0.05$ for the $B^+ \to \phi K^{\star +}$ decay, and $f_L = 0.484 \pm 0.033$ for the $B^0 \to \phi K^{\star 0}$ decay.

We compare our results with the theoretical predictions of the various approaches adopted in the calculation of the polarization amplitudes. They are reported in tab. 31. We find that our central values are consistent within the uncertainty ranges with the expectations of the QCD factorization 1.a. and 1.b in [22], while they are not with the expectation of perturbative QCD [46]. The approach adopted in [22] justifies the violation of the amplitudes hierarchy and the large transverse polarization fraction with the penguin weak-annihilation effects (see eq. 2.12 of Sect. 2.2.2), because the penguin

	f_L [%]	f_T [%]
Our experimental result	38.8 ± 4.2	61.2 ± 6.0
QCD factorization 1.a	43^{+0+61}_{-0-34}	57^{+0+61}_{-0-34}
QCD factorization 1.b	48^{+0+26}_{-0-27}	52^{+0+26}_{-0-27}
QCD factorization 2	86.6	13.4
Naive factorization	88.3	11.7
NLO EWP 1	86.3	13.7
NLO EWP 2	86.3	13.7
perturbative QCD	$61.9^{+3.6+2.5+0.0}_{-3.2-3.3-0.0}$	$38.1^{+3.6+2.5+0.0}_{-3.2-3.3-0.0}$

Table 31: Comparison of our experimental results with the theoretical predictions. The references are: [22] for QCD factorization 1.a and 1.b, [44] for QCD factorization 2 and Naive factorization, [45] for NLO EWP 1 and 2, [46] for perturbative QCD.

annihilation plays a more significant role for the transverse polarization amplitudes than for the longitudinal polarization ones.

In fact, in this model the penguin weak annihilation:

- gives small contribution to the longitudinal penguin amplitude;
- can (but do not need to) give large contribution to the transverse polarisation in penguin-dominated decays;
- doesn't give such an enhancement to the tree amplitudes, hence tree-dominated decays should be predominantly longitudinally polarized, as it was observed for the tree-level $b \to u$ transition, such as $B^0 \to \rho^+\rho^-$ [49, 50], $B^+ \to \rho^0\rho^+$ [51], and $B^+ \to \omega\rho^+$ [52];

Anyway, the penguin annihilation amplitude is phenomenologically indistinguishable from the QCD penguin amplitude (O_8 of eq. 2.11). and no polarization observables can be calculated reliably from the theory alone, and this is the cause of the large uncertainties in the predictions.

Even thought the model in [22] seems to account for the experimental results obtained in this thesis, further theoretical investigations are needed. We can finally state that the measurement presented in this thesis gives important inputs to the theoretical frameworks of the penguin dominated B_s decay, which should help to improve the predictive power of the current theoretical tools and challenge the SM explanation of the polarization puzzle.

A NORMALIZATION OF THE ANGULAR DISTRIBUTIONS

In the final likelihood formulation, the signal angular pdf is expressed as the product of a function of the three helicity angles, $f(\vec{\omega}) = \sum_{i=1}^{6} K_i f_i(\vec{\omega})$, (eq. 5.13, for the time-integrated fit, and eq. 6.13 for the time-dependent one), and a three-dimensional histogram, $H(\vec{\omega})$, that models the detector angular acceptance $\mathcal{A}(\vec{\omega})$.[1]

In this appendix we are going to discuss the numerical technique used for the normalization $\mathcal{N}$ of such pdf:

$$g_s(\vec{\omega}) = \frac{1}{\mathcal{N}} H(\vec{\omega}) f(\vec{\omega}) \tag{A.1}$$

Naively, we have to evaluate the integral of a mathematical function multiplied by a function represented by a histogram. We cannot anymore compute it analytically, but we need a numerical computation. In order to simplify the problem, let's start with the one-dimensional case.

Given an integrable function $f(x)$ ($\int f(x)\,dx = F(x)$), a histogram $\gamma(x)$ normalized to one and a number of bins N along the x axis, the numerical computation of the normalization factor $\mathcal{N}$

$$\mathcal{N} = \int_{x_{\min}}^{x_{\max}} f(x)\gamma(x)\,dx \tag{A.2}$$

can be approximated by the following sum:

$$\mathcal{N} \simeq \sum_{j}^{N} \mathcal{I}_j^f \mathcal{I}_j^\gamma \tag{A.3}$$

where

$$\mathcal{I}_j^f = \int_{x_{\min}^j}^{x_{\max}^j} f(x)\,dx \tag{A.4a}$$

$$\mathcal{I}_j^\gamma = \gamma(x_j)\Delta_j \tag{A.4b}$$

and x_j is the central point of the j-th bin $\Delta_j = x_{\max}^j - x_{\min}^j$ (see fig. A.1). If the bin width is constant for each j ($\Delta_j = \Delta$), then we can write

$$\mathcal{N} = M\Delta \tag{A.5}$$

where

$$\begin{aligned} M &= \sum_{j}^{N} \mathcal{I}_j^f \gamma(x_j) = \\ &= \left[F(x_{\max}^1) - F(x_{\min}^1)\right]\gamma(x_1) + \cdots + \left[F(x_{\max}^N) - F(x_{\min}^N)\right]\gamma(x_N) \end{aligned} \tag{A.6}$$

1 For the moment, we can consider the pdf to be a function only of the angles without loss of generality, although the pdf of the time-dependent fit has also the B meson proper decay time. For the transversity variables, one has exactly the same situation, considering $\vec{\Omega}$ instead of $\vec{\omega}$.

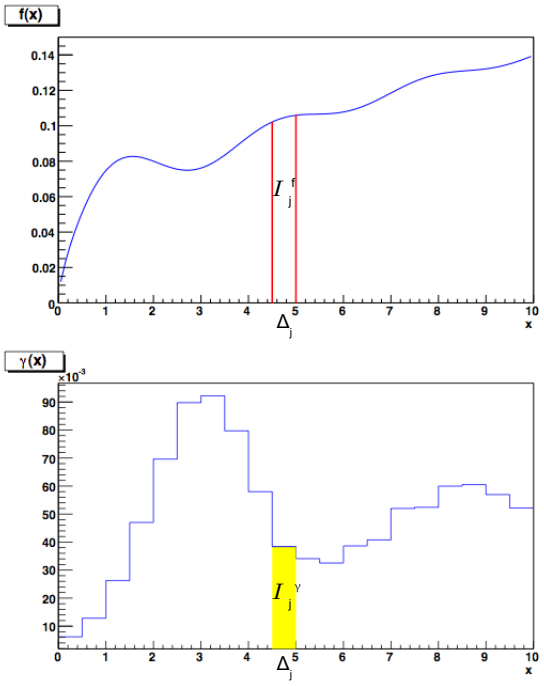

Figure A.1: Graphical example of the $\mathcal{I}_j^f$ and the $\mathcal{I}_j^\gamma$ terms.

If $F(x)$ is a linear combination of two (or more) functions of x, $F(x) = K_1F_1(x) + K_2F_2(x)$, M can be easily evaluated:

$$\begin{aligned} M &= \big(F(x^1_{\max}) - F(x^1_{\min})\big)\gamma(x_1) + \cdots + \big(F(x^N_{\max}) - F(x^N_{\min})\big)\gamma(x_N) = \\ &= K_1\Big[\big(F_1(x^1_{\max}) - F_1(x^1_{\min})\big)\gamma(x_1) + \cdots + \big(F_1(x^N_{\max}) - F_1(x^N_{\min})\big)\gamma(x_N)\Big] + \\ &+ K_2\Big[\big(F_2(x^1_{\max}) - F_2(x^1_{\min})\big)\gamma(x_1) + \cdots + \big(F_2(x^N_{\max}) - F_2(x^N_{\min})\big)\gamma(x_N)\Big] = \\ &= K_1w_1 + K_2w_2 \end{aligned} \tag{A.7}$$

where in the last line we define the weights $w_i = \big(F_i(x^1_{\max}) - F_i(x^1_{\min})\big)\gamma(x_1) + \cdots + \big(F_i(x^N_{\max}) - F_i(x^N_{\min})\big)\gamma(x_N)$.

The extension to our three-dimensional case is then straightforward, replacing:

$$\begin{aligned} f(x) &\to f(\vec{\omega}) = \sum_{i=1}^{6} K_i f_i(\vec{\omega}) \\ \int f(x)dx = F(x) &\to \int f(\vec{\omega})\, d\vec{\omega} = F(\vec{\omega}) = \sum_{i=1}^{6} K_i F_i(\vec{\omega}) \\ \gamma(x) &\to H(\vec{\omega}) \end{aligned} \tag{A.8}$$

and the bin width becomes a bin volume: $\Delta \to V$. The function $f(\omega)$ is normalized by the following integral over the total solid angle:

$$\int_{-1}^{1}\int_{-1}^{1}\int_{0}^{2\pi} f(\vec{\omega})\, d\cos\vartheta_1\, d\cos\vartheta_2\, d\Phi = \frac{32\pi}{9(K_1+K_2+K_3)} = \frac{1}{\eta(K_1,K_2,K_3)}. \tag{A.9}$$

Then, the normalized pdf is

$$g_s(\vec{\omega}) = \frac{\eta(K_1,K_2,K_3)\sum_{i=1}^{6} K_i f_i(\vec{\omega})}{\sum_{i=1}^{6} K_i w_i}\frac{H(\vec{\omega})}{\mathcal{V}} \tag{A.10}$$

The parameters we want to estimate within the fit are all contained in the K_i coefficients. Thus, the weights w_i can be computed once, before starting the maximization procedure, since they are constant and don't depend on the parameters. Moreover, assuming no CP-violation and summing over B_s and $\bar{B}_s$ terms, we have only K_1, K_2, K_3 and K_5, as we described in Sect. 2.4.3.

In the case of the time-integrated fit:

$$\begin{aligned} K_1 &= |A_0|^2/\Gamma_L \\ K_2 &= |A_\parallel|^2/\Gamma_L \\ K_3 &= |A_\perp|^2/\Gamma_H \\ K_5 &= |A_0||A_\parallel|\cos\delta/\Gamma_L \end{aligned} \tag{A.11}$$

then, the $\eta(K_1,K_2,K_3)$ becomes:

$$\eta(K_1,K_2,K_3) = \frac{9}{32\pi}\frac{1}{\frac{|A_0|^2+|A_\parallel|^2}{\Gamma_L}+\frac{|A_\perp|^2}{\Gamma_H}} \tag{A.12}$$

where one recognizes that the second fraction is the term $1/\tilde{W}$ of eq. 5.13 in the Sect. 5.4.

For the time dependent fit, the situation is a little bit different. The pdf, $f(\vec{\omega}|t)$ (eq. 6.13), is defined for each ct-bin Δt_i ($i = 1,\ldots,5$) of the angular acceptance histogram $H_i(\vec{\omega}|t)$ and must be integrated both in time and in the $\vec{\omega}$-space:

$$\begin{aligned} \mathcal{N} &= \sum_{i=1}^{5}\mathcal{N}_i = \\ &= \sum_{i=1}^{5}\left\{\int_{\Delta t_i}\int\left[\mathcal{F}_e(\vec{\omega})\mathcal{U}(t)+\mathcal{F}_o(\vec{\omega})\mathcal{V}(t)\right]H_i(\vec{\omega})\,dtd\vec{\omega}\right\} = \\ &= \sum_{i=1}^{5}\left\{\int\left[\mathcal{F}_e(\vec{\omega})\int_{\Delta t_i}\mathcal{U}(t)dt+\mathcal{F}_o(\vec{\omega})\int_{\Delta t_i}\mathcal{V}(t)dt\right]H_i(\vec{\omega})\,d\vec{\omega}\right\} = \\ &= \sum_{i=1}^{5}\left\{\int\left[\mathcal{F}_e(\vec{\omega})g_{\mathcal{U}i}+\mathcal{F}_o(\vec{\omega})g_{\mathcal{V}i}\right]H_i(\vec{\omega})\,d\vec{\omega}\right\} \end{aligned} \tag{A.13}$$

where in the last line we introduce the ten coefficients g_{ji} ($j = \mathcal{U},\mathcal{V}$):

$$g_{\mathcal{U}i} = \int_{\Delta t_i}\mathcal{U}(t)dt \tag{A.14a}$$

$$g_{\mathcal{V}i} = \int_{\Delta t_i}\mathcal{V}(t)dt. \tag{A.14b}$$

These coefficients depend on the parameters $a = |A_0|^2 + |A_\parallel|$ and $b = |A_\perp|^2$, contained in $\mathcal{U}(t)$ and $\mathcal{V}(t)$; thus, they must be calculated each time that the values a and b change in the numerical maximization. Anyway, they are easy to compute, because $\mathcal{U}(t)$ and $\mathcal{V}(t)$ are expressed in term of the two histograms $h_{\mathrm{L}}(t)$ and $h_{\mathrm{H}}(t)$; in practice, one has:

$$\begin{aligned}
\tilde{g}_{\mathcal{U}i} &= \sum_k \frac{n_{\mathrm{L}}(t_k)}{a n_{\mathrm{L}}(t_k) + b n_{\mathrm{H}}(t_k)} \quad \forall t_k \in \Delta t_i \\
\tilde{g}_{\mathcal{V}i} &= \sum_k \frac{n_{\mathrm{L}}(t_k)}{a n_{\mathrm{L}}(t_k) + b n_{\mathrm{H}}(t_k)} \quad \forall t_k \in \Delta t_i \\
g_{\mathcal{U}i} &= \frac{\tilde{g}_{\mathcal{U}i}}{\sum_l^5 \tilde{g}_{\mathcal{U}l}} \\
g_{\mathcal{V}i} &= \frac{\tilde{g}_{\mathcal{V}i}}{\sum_l^5 \tilde{g}_{\mathcal{V}l}}
\end{aligned} \tag{A.15}$$

where $n_{\mathrm{L(H)}}(t_k)$ is the content of the histogram $h_{\mathrm{L(H)}}(t)$ in its bin centered in t_k.[2]

Once the time-evolution is integrated, each factor $\mathcal{N}_i$ is obtained as in the time-integrated case:

$$\mathcal{N}_i = \int f_i(\vec{\omega})\, d\vec{\omega} = \left[K_1 w_{1i}(\vec{\omega}) + K_2 w_{2i}(\vec{\omega}) + K_5 w_{5i}(\vec{\omega})\right] g_{\mathcal{U}i} + K_3 w_{3i}(\vec{\omega}) g_{\mathcal{V}i} \tag{A.16}$$

and, finally,

$$\mathcal{N} = \sum_{i=5}^{5} \left\{ \left[K_1 w_{1i}(\vec{\omega}) + K_2 w_{2i}(\vec{\omega}) + K_5 w_{5i}(\vec{\omega})\right] g_{\mathcal{U}i} + K_3 w_{3i}(\vec{\omega}) g_{\mathcal{V}i} \right\} \tag{A.17}$$

In this case,

$$\begin{aligned}
K_1 &= |A_0|^2 \\
K_2 &= |A_\parallel|^2 \\
K_3 &= |A_\perp|^2 \\
K_5 &= |A_0||A_\parallel| \cos\delta
\end{aligned} \tag{A.18}$$

then, the $\eta(K_1, K_2, K_3)$ becomes simply the factor $9/(32\pi)$.

2 The ct-bin of the $h_{\mathrm{L(H)}}$ histogram is not a bin Δt_i of $H(\vec{\omega}|t)$.

B THE $B_s \to J/\psi\phi$ ANALYSIS DETAILS

In this appendix we report the analysis details of the $B_s \to J/\psi\phi$ data sample collected with the TTT. Since most of the technical details are in common with the main analysis, here the presentation is quite schematic, following the same scheme of the main text. The results are reported and commented in Sect. 5.6.

B.1 MASS MODEL

The signal function has a width of around 10 MeV (see fig. 4.5). It is parameterized with two gaussian functions having the same mean value M but different resolutions, σ and $k\sigma$:

$$g_s^{(m)} = h\frac{1}{\sqrt{2\pi}\sigma}e^{-\frac{(m-M)^2}{2\sigma^2}} + (1-h)\frac{1}{\sqrt{2\pi}k\sigma}e^{-\frac{(m-M)^2}{2k^2\sigma^2}} \tag{B.1}$$

where h is the fraction of one gaussian component with respect to the other. Fitting the MC events of fig. B.1 we obtained the parameters summarized in tab. 32 . In the final

Parameter	MC fit value
M [GeV/c^2]	5.36916 ± 0.00007
σ [GeV/c^2]	0.01577 ± 0.00004
k	2.9 ± 0.1
h	0.929 ± 0.005

Table 32: Parameters of MC data mass fit for $B_s \to J/\psi\phi$.

fit the multiplicative factor k and the fraction h are fixed, while the other parameters are left free.

The mass background follows an exponentially decreasing behavior:

$$g_b^{(m)} = \frac{b}{e^{-bm_{\min}} - e^{-bm_{\max}}}e^{-bm} \tag{B.2}$$

where b is the slope of the exponential function, and m spans the interval $[m_{\min} = 5.2, m_{\max} = 5.6]$ GeV/c.

We compare the results of this unbinned maximum likelihood fit of the reconstructed B mass to the others of the binned fit performed in the branching ratio analysis [29]. The data sample is the same for the two fits. Table 33 reports the two fit's results and the mass distributions with the fit function overlaid are shown in fig. B.2. The binned fit takes into account for the reflections. At variance with the $B_s \to \phi\phi$ decay, in this case the reflections impact can be seen by comparing the two background parameters, F_b and b, in the table 33. In fig. B.2, the height of the total fit projection at the value M is lower respect to the data distribution, because of the absence of the reflections component under the peak signal. So from the comparison we can check if there is a sizable effect due to the fact that we disregard the reflection in our fit. Anyway, we obtain a good agreement in the central values and in the uncertainties for the signal parameters.

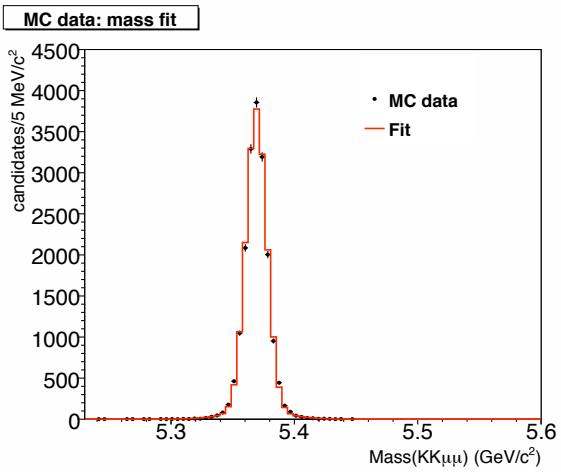

Figure B.1: Mass fit of MC data for $B_s \to J/\psi\phi$. The black points are the MC data; the red line is the resulting fit distribution. The χ^2 probability of the fit projection is 0.43.

Parameter	Unbinned fit	Binned fit
M [GeV/c^2]	5.3657 ± 0.0003	5.3660 ± 0.0003
σ [GeV/c^2]	0.0090 ± 0.0003	0.0094 ± 0.0003
f_b	0.63 ± 0.01	0.57 ± 0.01
b	-1.5 ± 0.2	-1.2 ± 0.2

Table 33: Comparison of the mass fit results with the branching ratio analysis' ones [29].

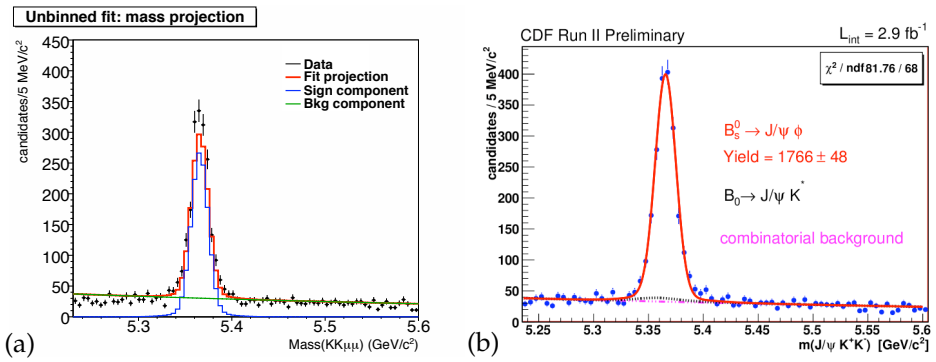

Figure B.2: Comparison of our fit result (a) with the one from the branching ratio analysis (b).

B.2 ANGULAR MODEL

The equation 5.13 provides the signal angular parameterization, replacing the functions $f_i(\vec{\omega})$ and the phase ϕ_V by $f_i(\vec{\Omega})$ (eq. 2.62) and by $2\beta_s$, respectively.

We evaluate the three-dimensional acceptance curve $\mathcal{A}(\vec{\omega})$, which accounts for the angular detector acceptance, constructing the three-dimensional histogram $H(\vec{\omega})$, as we do for the main analysis. The projections of $H(\vec{\omega})$ onto the three axes of the transversity angles basis are shown in fig. B.3.

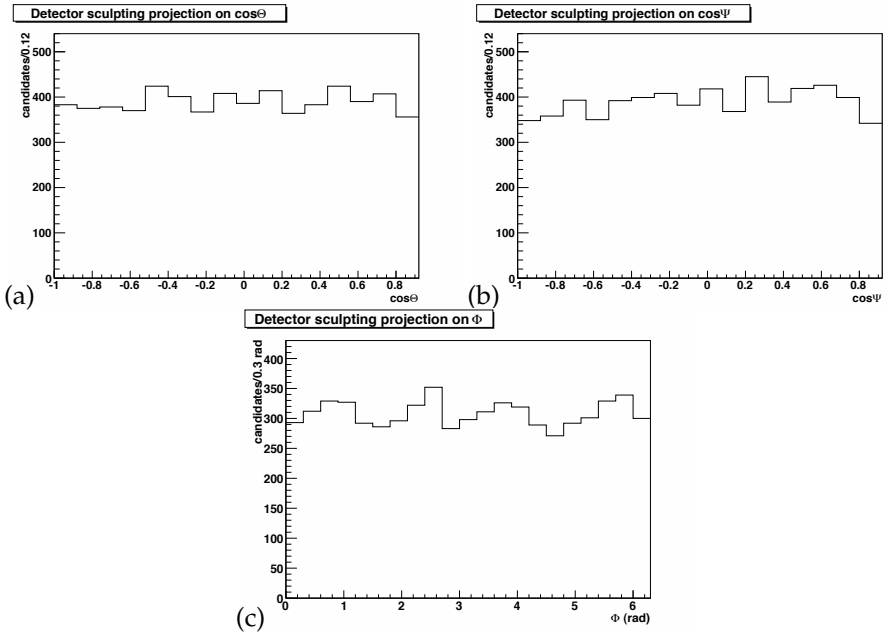

Figure B.3: Detector angular acceptance projections: $\cos\Theta$ (a), $\cos\Psi$ (b) and Φ (c).

B.2.1 Effect of different trigger path on angular detector angular acceptance

There is the possibility that the acceptance curve is different for the three trigger path selections. We want to check if this is the case: we look at the projections of $H(\vec{\omega})$ for the different trigger paths. They are shown in fig. B.4: we can conclude that $H(\vec{\omega})$ is similar for each trigger selections. This test also guarantees no dependencies on the integrated luminosity collected with the three different trigger paths. These allows us to easily combine of all exclusive data sets.

B.2.2 Angular Background parameterization

It is reasonable to suppose that the transversity angles do not have any intrinsic meaning for the combinatorial background. Thus, we use a purely empirical model derived by analysing the angular distributions in the mass sidebands to model the background. Looking at the scatter plots in fig. B.5, we see that the angular variables are not correlated in the sideband regions; then the angular part of the background pdf factorizes in the product of three terms:

$$g_b^{(\omega)} = g_b^{(\omega_1)} g_b^{(\omega_2)} g_b^{(\omega_3)} \tag{B.3}$$

where for the $B_s \to J/\psi\phi$ decay the parameterization adopted are:

$$g_b^{(\omega_1)} = \frac{1}{2(1+\frac{p_\Theta^{(1)}}{3}+\frac{p_\Theta^{(2)}}{5})}\left(1 + p_\Theta^{(1)}\cos^2\Theta + p_\Theta^{(2)}\cos^4\Theta\right), \tag{B.4a}$$

$$g_b^{(\omega_2)} = \frac{1}{2}\left(1 + p_\Psi \cos\Psi\right), \tag{B.4b}$$

$$g_b^{(\omega_3)} = \frac{1}{5\pi}\left(1 + \frac{1+p_\Phi^{(1)}\cos\Phi}{2} + \frac{1+p_\Phi^{(2)}\cos 2\Phi}{2} + \frac{1+p_\Phi^{(3)}\cos 4\Phi}{2}\right), \tag{B.4c}$$

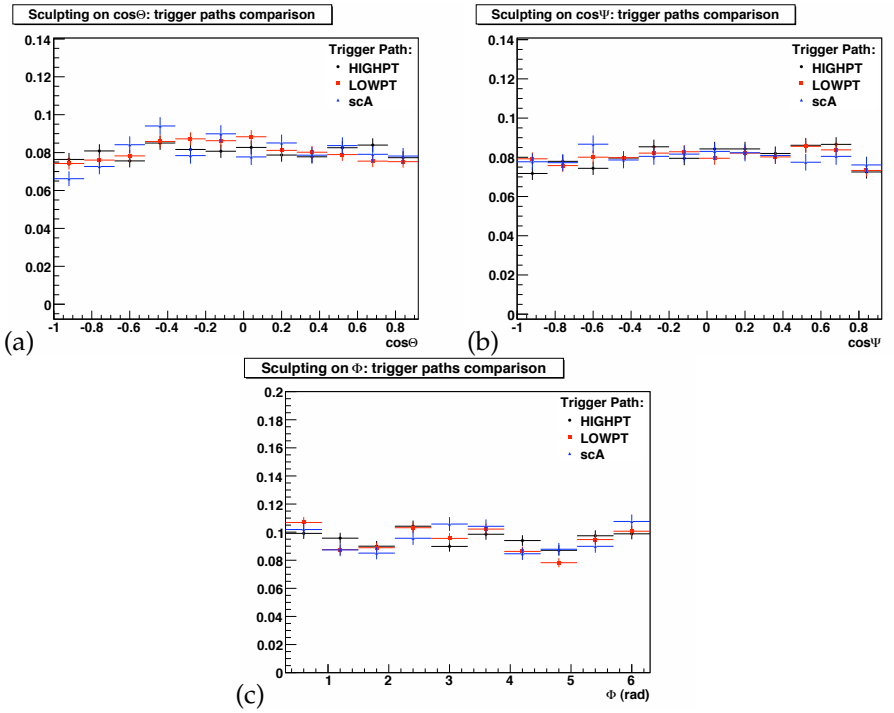

Figure B.4: Effect of different trigger path on angular detector angular acceptance: $\cos\Theta$ (a), $\cos\Psi$ (b) and Φ (c).

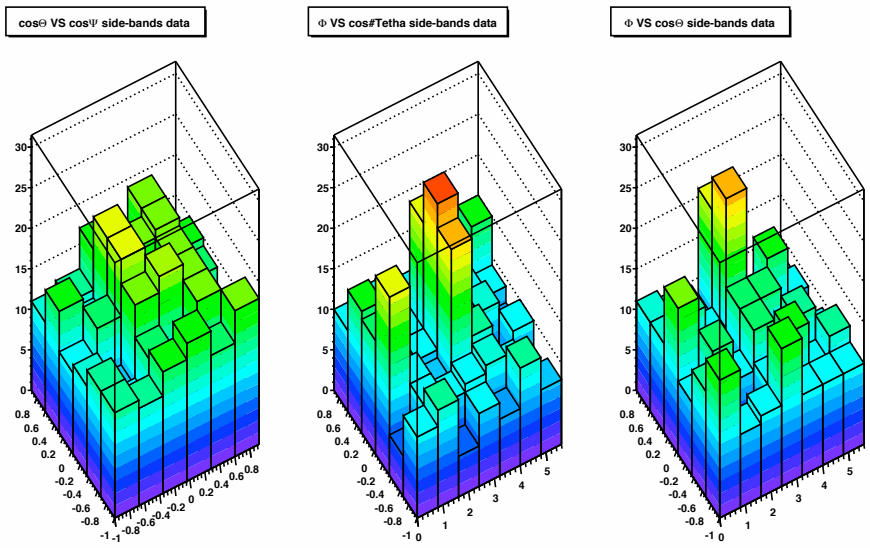

Figure B.5: Scatter plots to check for angular variables correlations in the side-band regions. On the right, $\cos\Theta$ versus $\cos\Psi$. In the middle, $\cos\Theta$ versus Φ. On the left, $\cos\Psi$ versus Φ.

The parameters $p_j^{(i)}$ then are determined form the fit (background parameters). Figure B.6 shows a binned fit to the sideband angular distributions using the above equations B.4.

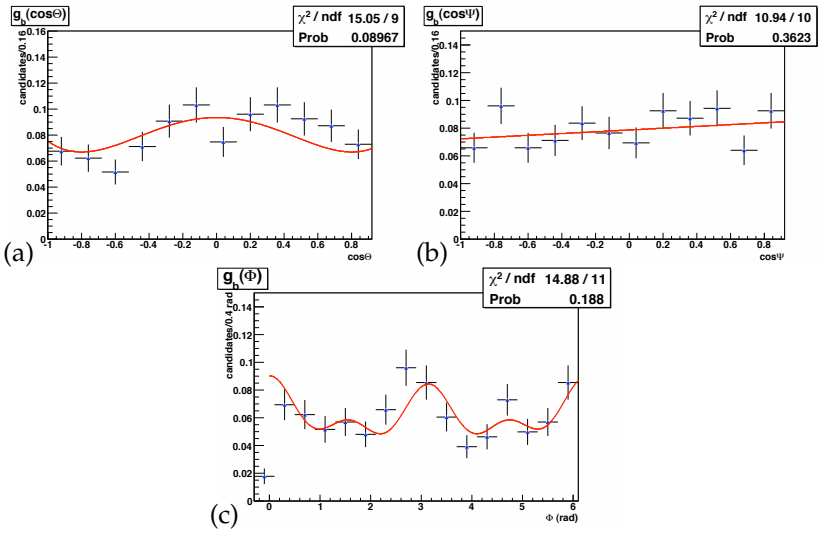

Figure B.6: Side-bands data angular fit for background parameterization for the $B_s \to J/\psi\phi$ decay: $\cos\Theta$ (a), $\cos\Psi$ (b) and Φ (c). Black points are side-bands data; red lines are the fitting functions described in the text.

B.3 PULLS DISTRIBUTIONS

We perform the complete fit on 5000 pseudo-experiments of 1000 events each, which is of the same order of the statistic that we have in 2.9 fb^{-1} of data. The results of this test are reported in tab. 34, and the pulls distributions are shown in fig. B.7.

Parameter	Mean	Variance	Prob(χ^2) [%]
M	0.00 ± 0.03	1.01 ± 0.02	15
σ	0.01 ± 0.03	1.01 ± 0.02	42
f_b	-0.02 ± 0.03	0.96 ± 0.02	73
b	-0.06 ± 0.03	0.98 ± 0.02	99
$\lvert A_0\rvert^2$	-0.02 ± 0.03	1.03 ± 0.02	17
$\lvert A_\parallel\rvert^2$	-0.02 ± 0.03	1.01 ± 0.02	34
δ	-0.58 ± 0.03	0.78 ± 0.02	0
$p_\Theta^{(1)}$	-0.02 ± 0.03	1.00 ± 0.02	27
$p_\Theta^{(2)}$	0.01 ± 0.03	1.01 ± 0.02	16
p_Ψ	0.06 ± 0.03	0.97 ± 0.02	33
$p_\Phi^{(1)}$	-0.01 ± 0.03	1.02 ± 0.02	2
$p_\Phi^{(2)}$	0.03 ± 0.03	0.98 ± 0.02	51
$p_\Phi^{(3)}$	0.00 ± 0.03	1.01 ± 0.02	61

Table 34: Pulls mean and variance for $B_s \to J/\psi\phi$ (5000 events per pseudo-experiment). The fourth column presents the χ^2 probability for a gaussian fit of the pulls distribution with mean and variance 0 and 1, respectively.

We find that the fitter returns unbiased estimates and consistent uncertainties for all parameters except for δ, which presents the same strange shape as in the case of the $B_s \to \phi\phi$ analysis.

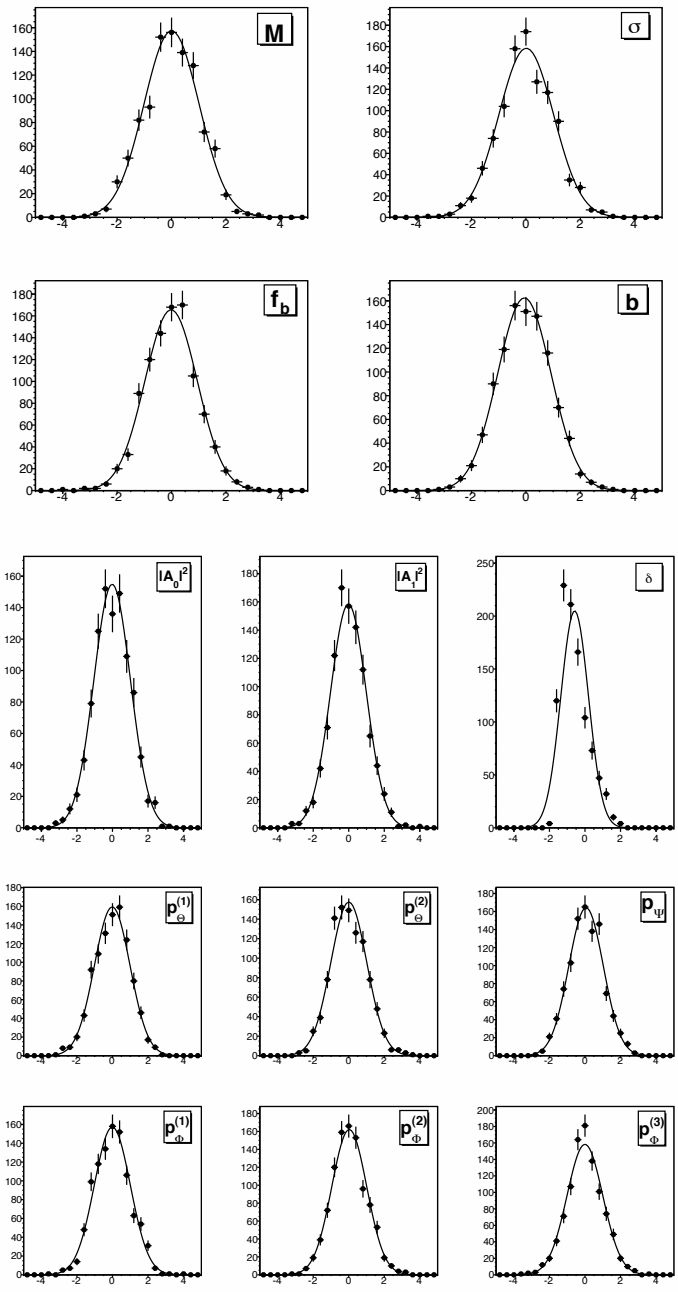

Figure B.7: Pulls distributions of the parameters for $B_s \to J/\psi\phi$ (5000 events per pseudo-experiment).

B.4 FIT TO THE REALISTIC MC

The fit to the realistic MC is the second test for the $B_s \to J/\psi\phi$ analysis. In order to check if the fit returns values consistent with the inputs given to our MC, we fit the phase space MC used for the calculation of the detector angular acceptance. The simulated events of the MC are passed through the full-fledged detector simulation. Then, they are selected with the same off-line requirements of the real data.

We expect to find no polarization, since the phase space MC has all the final state particles with averaged spins. This means that the polarization amplitudes are $|A_0|^2 \simeq |A_\parallel|^2 \simeq |A_\perp|^2 \simeq 0.33$ and that the strong phase is $\delta \simeq \pi/2$. The results of the fit are satisfactory, since they are very close to the expected values. They are listed in table 35. The fit projections on the three transversity angles distributions are reported in fig. B.8. The distributions are very well reproduced by the fitting functions.

Parameter	MC fit value
$\|A_0\|^2$	0.328 ± 0.006
$\|A_\parallel\|^2$	0.353 ± 0.009
δ [rad]	1.48 ± 0.03

Table 35: Parameters of realistic MC angular fit for $B_s \to J/\psi\phi$

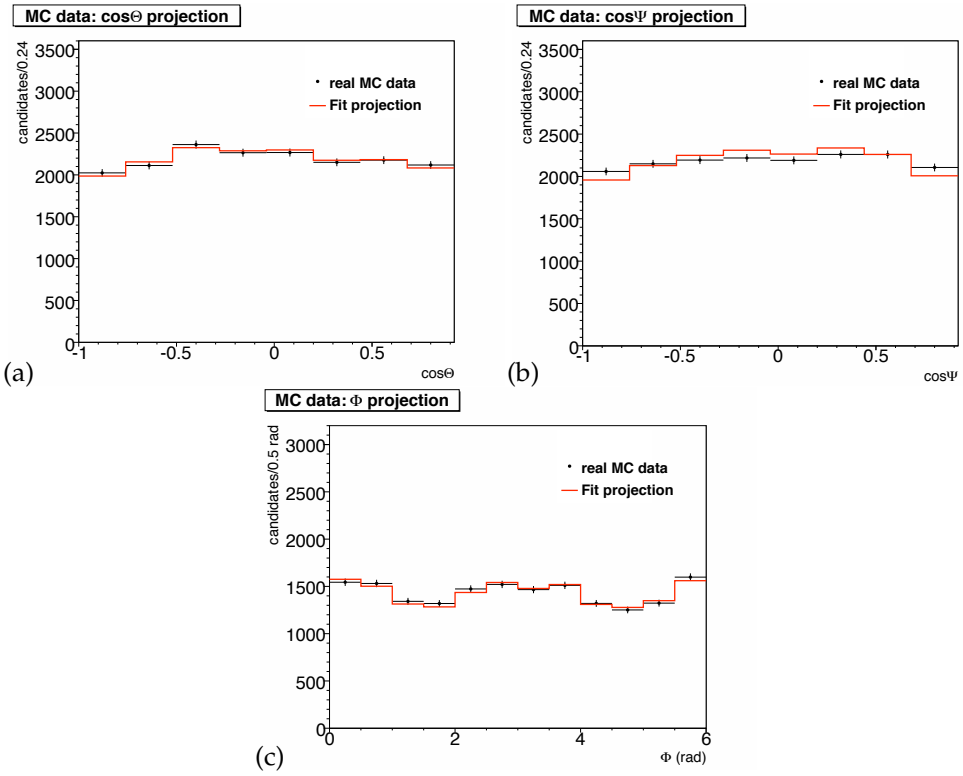

Figure B.8: Angular fit projections of realistic MC for $B_s \to J/\psi\phi$: $\cos\Theta$ (a), $\cos\Psi$ (b) and Φ (c). The χ^2 probabilities of the fit projections are 0.81, 0.006 and 0.86 respectively.

ACRONYMS

SM	Standard Model
LHC	Large Hadron Collider
CDF	Collider Detector at Fermilab
CDFII	CDF in Run II
QFT	Quantum Fields Theory
FNAL	Fermi National Accelerator Laboratory
CKM	Cabibbo-Kobayashi-Maskawa
SM	Standard Model
GIM	Glashow-Iliopoulos-Maiani
QED	Quantum ElectroDynamics
QCD	Quantum ChromoDynamics
OPE	Operator Product Expansion
pdf	probability density function
PDG	Particle Data Group
SLAC	Stanford Linear Accelerator Center
KEK	Ko Enerugi Kasokuki Kenkyu Kiko
SVXII	Silicon VerteX
ISL	Intermediate Silicon Layers
L00	Layer 00
COT	Central Outer Tracker
TOF	Time Of Flight detector
CEM	Central ElectroMagnetic Calorimeter
CES	CEntral Strip multi-wire proportional chambers
CPR	Central Pre-Radiator
CHA	Central HAdronic
WHA	Wall HAdronic
PEM	Plug ElectroMagnetic calorimeter
PHA	Plug HAdronic calorimeter
CMU	Central MUon detector

CMP	Central Muon uPgrade
CMX	Central Muon eXtension
IMU	Intermediate MUon detectors
CLC	Cherenkov Luminosity Counters
XFT	eXtremely Fast Tracker
SVT	Silicon Vertex Trigger
DAQ	Data AcQuisition
MC	Monte Carlo
TTT	Two Track Trigger
MVB	Minimum Variance Bound
ML	Maximum Likelihood

BIBLIOGRAPHY

[1] CDF Collaboration: T. Aaltonen. Measurement of Lifetime and Decay-Width Difference in $B_s^0 \to J/\psi\phi$ Decays. *Physical Review Letters*, 100:121803, 2008. (Cited on pages i, ii, vii, viii, 81, 90, 91, 93, 101, and 117.)

[2] Isard Dunietz, Robert Fleischer, and Ulrich Nierste. In Pursuit of New Physics with B_s Decays. *Physical Review D*, 63:114015, 2001. (Cited on page 1.)

[3] The Belle Collaboration: K. F. Chen. Time-Dependent CP-Violating Asymmetries in $b \to s\bar{q}q$ Transitions. *Physical Review D*, 72:012004, 2005. (Cited on page 1.)

[4] The BABAR Collaboration and B. Aubert. Measurement of the Branching Fraction and the CP-Violating Asymmetry for the Decay $B_0 \to K_S^0\pi^0$. *Physical Review D*, 71:111102, 2005. (Cited on page 1.)

[5] The BABAR Collaboration: B. Aubert. Measurement of CP Asymmetries in $B0 \to \phi K^0$ and $B_0 \to K^+K^-K_S^0$ Decays. *Physical Review D*, 71:091102, 2005. (Cited on page 1.)

[6] The BABAR Collaboration and B. Aubert. Measurements of Branching Fractions and Time-Dependent CP-Violating Asymmetries in $B \to \eta K$ Decays. *Physical Review Letters*, 94:191802, 2005. (Cited on page 1.)

[7] Alakabha Datta and David London. Triple-Product Correlations in $B \to V_1V_2$ Decays and New Physics. *International Journal of Modern Physics A*, 19:2505, 2004. (Cited on page 1.)

[8] The BABAR Collaboration and B. Aubert . Measurement of the $B \to \phi K^\star$ Decay Amplitudes. *Phys. Rev. Lett.*, 93(23):231804, Dec 2004. (Cited on pages 1 and 19.)

[9] Katsumi Senyo and for the Belle Collaboration. Search for new physics in $B \to VV$ decays and other hot topics from Belle, 2005. (Cited on page 1.)

[10] Y. Chao, P. Chang, and for the Belle Collaboration. Improved Measurements of Partial Rate Asymmetry in $B \to hh$ Decays. *Physical Review D*, 71:031502, 2005. (Cited on page 1.)

[11] K. Abe and for the Belle Collaboration. New Measurements of Time-Dependent CP-Violating Asymmetries in $b \to s$ Transitions at Belle, 2004. (Cited on page 1.)

[12] The BABAR Collaboration and B. Aubert. Measurements of the Branching Fraction and CP-Violating Asymmetries of $B_0 \to K_S^0\pi^0$ Decays, 2004. (Cited on page 1.)

[13] B. Aubert and BABAR Collaboration. Measurements of Branching Fractions and CP-Violating Asymmetries in B-Meson Decays to the Charmless Two-Body States $K^0\pi^+$, $\bar{K}^0K^+$, and $K^0\bar{K}^0$, 2004. (Cited on page 1.)

[14] The BABAR Collaboration and B. Aubert. Study of $B_0 \to \pi^0\pi^0$, $B^+ \to \pi^+\pi^0$ and $B^+ \to K^+\pi^0$ decays, 2004. (Cited on page 1.)

[15] Xiao-Gang He and Bruce McKellar. Hadron decay amplitudes from $B \to K\pi$ and $B \to \pi\pi$ decays, 2004. (Cited on page 1.)

[16] Baek, Seungwon and Hamel, Philippe and London, David and Datta, Alakabha and Suprun, Denis A. $B \to \pi K$ puzzle and new physics. *Phys. Rev. D*, 71(5):057502, Mar 2005. (Cited on page 1.)

[17] The BABAR Collaboration and B. Aubert. Vector-Tensor and Vector-Vector Decay Amplitude Analysis of $B^0 \to \phi K^\star$. *Physical Review Letters*, 98:051801, 2007. (Cited on pages 2, 26, and 118.)

[18] The BABAR Collaboration and B. Aubert. Measurements of Branching Fractions, Polarizations, and Direct CP-Violation Asymmetries in $B \to \rho K^\star$ and $B \to f^0(980)K^\star$ Decays. *Physical Review Letters*, 97(20):201801, 2006. (Cited on pages 2 and 26.)

[19] K. F. Chen and for the Belle Collaboration. Measurement of Polarization and Triple-Product Correlations in $B \to \phi K^\star$ Decays. *Physical Review Letters*, 94:221804, 2005. (Cited on page 2.)

[20] Ezequiel Alvarez, Luis N. Epele, Daniel Gomez Dumm, and Alejandro Szynkman. Right handed currents and FSI phases in $B^0 \to \phi K^{\star 0}$. *Physical Review D*, 70:115014, 2004. (Cited on page 2.)

[21] C. S. Kim and Ya-Dong Yang. Polarization Anomaly in $B \to \phi K^{\star 0}$ and Probe of Tensor Interactions, 2004. (Cited on page 2.)

[22] Martin Beneke and Johannes Rohrer and Deshan Yang. Branching fractions, polarisation and asymmetries of $B \to VV$ decays. *Nuclear Physics B*, 774(1-3):64 – 101, 2007. (Cited on pages 2, 26, 118, and 119.)

[23] A. Ali, G. Kramer, Y. Li, C.-D. Lü, Y.-L. Shen, W. Wang, and Y.-M. Wang. Charmless nonleptonic B_s decays to PP, PV, and VV final states in the perturbative QCD approach. , 76(7):074018–+, October 2007. (Cited on page 2.)

[24] CDF Collaboration: T. Aaltonen. First Flavor-Tagged Determination of Bounds on Mixing-Induced CP Violation in $B_s \to J/\psi\phi$ Decays. *Physical Review Letters*, 100:161802, 2008. (Cited on page 2.)

[25] V. M. Abazov et al. Measurement of B_s^0 mixing parameters from the flavor-tagged decay $B_s^0 \to J/\psi\phi$. *Phys. Rev. Lett.*, 101:241801, 2008. (Cited on page 2.)

[26] I.I. Bigi and A.I. Sanda. CP *violation*. Cambridge University Press, Cambridge, 2009. (Cited on page 2.)

[27] S Amato, J McCarron, F Muheim, B Souza de Paula, and Y Xie. LHCb's sensitivity to New CP-violating Phases in the Decay $B_s \to \phi\phi$. Technical Report LHCb-2007-047. CERN-LHCb-2007-047, CERN, Geneva, May 2007. (Cited on page 2.)

[28] CDF Collaboration and D. Acosta. First Evidence for $B_s^0 \to \phi\phi$ Decay and Measurements of Branching Ratio and A_{CP} for $B^+ \to \phi K^+$. *Physical Review Letters*, 95:031801, 2005. (Cited on pages 2 and 60.)

[29] Benedetto Di Ruzza, Lorenzo Ortolan, Giacomo Artoni, Mirco Dorigo, Marco Rescigno, and Anna Maria Zanetti. Study of the $B_s \to \phi\phi$ decay and measurement of its Branching Ratio. *CDF Internal Note*, 9743, 2009. unpublished. (Cited on pages vi, vii, viii, 2, 27, 55, 61, 62, 63, 65, 66, 67, 76, 77, 113, 117, 125, and 126.)

[30] K. Anikeev et al. *B* Physics at the Tevatron: Run II and Beyond, 2002. arXiv:hep-ph/0201071. (Cited on pages 5, 7, 8, 9, 11, and 14.)

[31] Donald H. Perkins. *Introduction to High Energy Physics*. Cambridge University Press, Cambridge, 2000. (Cited on page 7.)

[32] W. Beenakker, H. Kuijf, W. L. van Neerven, and J. Smith. QCD corrections to heavy-quark production in $p\bar{p}$ collisions. *Phys. Rev. D*, 40(1):54–82, Jul 1989. (Cited on page 8.)

[33] J. C. Collins, D. E. Soper, and G. Sterman. Perturbative QCD, 1989. (Cited on page 9.)

[34] Mario Greco and Simona Rolli. Light mesons production at the Tevatron to next-to-leading order. *Physical Review D*, 52:3853, 1995. (Cited on page 9.)

[35] S. Kretzer. Fragmentation Functions from Flavour-inclusive and Flavour-tagged e^+e^- Annihilations. *Physical Review D*, 62:054001, 2000. (Cited on page 9.)

[36] C. Amsler et al. Particle Data Group. *Physics Letters B*, 667, 2008 and 2009 partial update for the 2010 edition. (Cited on pages 10, 14, 15, 16, and 72.)

[37] Andrzej J. Buras, Sebastian Jaeger, and Jorg Urban. Master formulae for $\Delta F = 2$ NLO-QCD factors in the Standard Model and beyond. *Nuclear Physics B*, 605(1-3):600 – 624, 2001. (Cited on page 14.)

[38] CDF Collaboration. Observation of Bs-Bsbar Oscillations. *Physical Review Letters*, 97:242003, 2006. (Cited on page 14.)

[39] The DELPHI Collaboration. Search for B_s-$\bar{B}_s$ oscillations and a measurement of B_d-$\bar{B}_d$ oscillations using events with an inclusively reconstructed vertex. *Eur. Phys. J. C*, 28(2):155–173, may 2003. (Cited on page 15.)

[40] The BaBar Collaboration. Limits on the decay-rate difference of neutral B mesons and on CP, T, and CPT violation in $B^0 - \bar{B}^0$ oscillations. *Phys. Rev. D*, 70(1):012007, Jul 2004. (Cited on page 15.)

[41] Yosef Nir. Recent Developments in Theory of CP Violation, 1997. arXiv:hep-ph/9709301. (Cited on page 16.)

[42] Jean-Marc Gerard and Wei-Shu Hou. CP violation in inclusive and exclusive charmless B decays. *Phys. Rev. D*, 43(9):2909–2930, May 1991. (Cited on page 18.)

[43] Heavy Flavor Averaging Group, : E. Barberio, et al. Averages of b-hadron Properties at the End of 2005, 2006. arXiv:hep-ex/0603003. (Cited on page 19.)

[44] Xinqiang Li, Gongru Lu, and Yadong Yang. Charmless $\bar{B}_s \to VV$ Decays in QCD Factorization. *ERRATUM-IBID.D*, 71:019902, 2005. (Cited on pages 26 and 119.)

[45] D. Du and L. Guo. *J. Phys. G: Nucl. Part. Phys.*, 23:525, 1997. (Cited on pages 26 and 119.)

[46] Ahmed Ali, Gustav Kramer, Ying Li, Cai-Dian Lu, Yue long Shen, Wei Wang, and Yu-Ming Wang. Charmless non-leptonic B_s decays to PP, PV and VV final states in the pQCD approach. *Physical Review D*, 76:074018, 2007. (Cited on pages 26, 118, and 119.)

[47] Hai-Yang Cheng, Yong-Yeon Keum, and Kwei-Chou Yang. $B \to J/\psi K^\star$ decays in QCD factorization. *Phys. Rev. D*, 65(9):094023, May 2002. (Cited on page 26.)

[48] Mahiko Suzuki. Final-state interactions and s-quark helicity conservation in $B/^\star$. *Phys. Rev. D*, 64(11):117503, Nov 2001. (Cited on page 26.)

[49] Belle Collaboration. *Phys. Rev. Lett.*, 96:171801, 2006. (Cited on pages 26 and 119.)

[50] B. Aubert et al. A Study of $B^0 \to \rho^+\rho^-$ Decays and Constraints on the CKM Angle alpha. *Physical Review D*, 76:052007, 2007. (Cited on pages 26 and 119.)

[51] *BABAR* Collaboration. Measurements of Branching Fraction, Polarization, and Charge Asymmetry of $B^\pm \to \rho^\pm\rho^0$ and a Search for $B^\pm \to \rho^\pm f^0(980)$. *Physical Review Letters*, 97(26):261801, 2006. (Cited on pages 26 and 119.)

[52] *BABAR* Collaboration. b meson decays to $\omega k^\star$, $\omega\rho$, $\omega\omega$, $\omega\phi$, and ωf^0. *Physical Review D (Particles and Fields)*, 74(5):051102, 2006. (Cited on pages 26 and 119.)

[53] *BABAR* Collaboration. Evidence for $B^0 \to \rho^0\rho^0$ Decays and Implications for the Cabibbo-Kobayashi-Maskawa Angle α . *Physical Review Letters*, 98(11):111801, 2007. (Cited on page 26.)

[54] Belle Collaboration. Evidence for Neutral B Meson Decays to omega $K^{\star 0}$. *Physical Review Letters*, 101(23):231801, 2008. (Cited on pages 26 and 118.)

[55] *BABAR* Collaboration. Amplitude Analysis of the $B^\pm \to \phi K^{\star\pm}(892)$ Decay. *Physical Review Letters*, 99(20):201802, 2007. (Cited on pages 26 and 118.)

[56] Alakabha Datta, Andrei V. Gritsan, David London, Makiko Nagashima, and Alejandro Szynkman. Testing explanations of the $B \to \phi K^\star$ polarization puzzle. *Physical Review D (Particles and Fields)*, 76(3):034015, 2007. (Cited on page 26.)

[57] Prasanta Kumar Das and Kwei-Chou Yang. Data for polarization in charmless $B \to \phi K^\star$: A signal for new physics? *Phys. Rev. D*, 71(9):094002, May 2005. (Cited on page 26.)

[58] Amand Faessler, Thomas Gutsche, J. C. Helo, Sergey Kovalenko, and Valery E. Lyubovitskij. Possible resolution of the B-meson decay polarization anomaly in R-parity violating supersymmetry. *Physical Review D (Particles and Fields)*, 75(7):074029, 2007. (Cited on page 26.)

[59] *BABAR* Collaboration. Search for $B^0 \to \phi(K^+pi^-)$ decays with large K^+pi^- invariant mass. *Physical Review D (Particles and Fields)*, 76(5):051103, 2007. (Cited on page 26.)

[60] Belle Collaboration. Measurements of the Branching Fraction and Polarization in $B^+ \to \rho^+K^\star$ Decays. 95(14):141801, Sep 2005. (Cited on page 26.)

[61] The BABAR Collaboration: B. Aubert. Observation of $B^0 \to K^{\star 0}\bar{K}^{\star 0}$ and search for $B^0 \to K^{\star 0}K^{\star 0}$. *Physical Review Letters*, 100:081801, 2008. (Cited on page 26.)

[62] Gianluca De Lorenzo and Marco Rescigno. Polarization amplitudes in $B_d \to J/\psi K^\star$ and $B_d \to \phi K^\star$ using the Two Track Trigger. *CDF Internal Note*, 8501, 2006. (Cited on pages 27, 81, 101, and 102.)

[63] D. P. McGinnis. Fermilab Tevatron operational status. In C. Horak, editor, *proceedings of the Particle Accelerator Conference (PAC 05)*, 2005. in addition, detailed and updated information on the Tevatron is available in the following webpages: http://www-bd.fnal.gov/runII/index.html http://www-bdnew.fnal.gov/operations/rookiebooks/rbooks.html. (Cited on page 31.)

[64] D. Mohl et al. Physics and Technique of Stochastic Cooling. *Phys. Rept.*, 58, 1980. (Cited on page 32.)

[65] S. Nagaitsev et al. Experimental Demonstration of Relativistic Electron Cooling. *Phys. Rev. Lett.*, 96, 2006. (Cited on page 32.)

[66] Diego Tonelli. First observation of the $B_s^0 \to K^+K^-$ decay mode, and measurement of the B^0 and B_s^0 mesons decay-rates into two-body, charmless final states at CDF. Ph.d. thesis, Scuola Normale Superiore di Pisa, 2006. (Cited on page 33.)

[67] R. Blair and others (CDF II Collaboration). The CDF II Detector, Technical Design Report. *FERMILAB-Pub-96/390-E CDF*, 1996. (Cited on page 36.)

[68] A. Sill. CDF Run II silicon tracking projects. *Nucl. Instrum. Methods*, A447, 2000. (Cited on page 38.)

[69] A. Affolder et al. Status report of the intermediate silicon layers detector at CDF II. *Nucl. Instrum. Methods*, A485, 2002. (Cited on page 39.)

[70] A. Affolder et al. CDF Central Outer Tracker. *Nucl. Instrum. Methods*, A526, 2004. (Cited on page 40.)

[71] J. Marriner. Secondary vertex fit with mass and pointing constraints (CTVMFT). *CDF Internal Note*, 1996, 1993. unpublished. (Cited on page 41.)

[72] P. Gatto. Performance of the new tracking system at CDF II. Master's thesis, University of Padova, 2001. Ph.D. thesis, FERMILAB-THESIS-2001-23. (Cited on page 42.)

[73] S. Menzemer. TrackingCal - A tracking and alignment software package for the CDF II silicon detector. Master's thesis, University of Karlsruhe, 2002. CDF Internal Note 5968, unpublished. (Cited on page 42.)

[74] C. S. Hill et al. Operational experience and performance of the CDF II silicon detector. *Nucl. Instrum. Methods*, A530, 2004. (Cited on page 42.)

[75] D. Acosta et al. A Time-of-Flight detector in CDF-II. *Nucl. Instrum. Methods*, A518, 2004. (Cited on page 43.)

[76] L. Balka et al. The CDF central electromagnetic calorimeter. *Nucl. Instrum. Methods*, A267, 1988. (Cited on page 43.)

[77] S. R. Hahn et al. Calibration systems for the CDF central electromagnetic calorimeter. *Nucl. Instrum. Methods*, A267, 1988. (Cited on page 43.)

[78] M. Gallinaro. A New Scintillator Tile/Fiber Preshower Detector for the CDF Central Calorimeter. *IEEE Trans. Nucl. Sci.*, 52, 2005. (Cited on page 44.)

[79] S. Bertolucci et al. The CDF central and endwall hadron calorimeter. *Nucl. Instrum. Methods*, A267, 1988. (Cited on page 44.)

[80] M. Albrow et al. The CDF plug upgrade electromagnetic calorimeter: test beam results. *Nucl. Instrum. Methods*, A480, 2002. (Cited on page 44.)

[81] M. Albrow et al. A preshower detector for the CDF Plug Upgrade: test beam results. *Nucl. Instrum. Methods*, A431, 1999. (Cited on page 44.)

[82] G. Apollinari et al. Shower maximum detector for the CDF plug upgrade calorimeter. *Nucl. Instrum. Methods*, A412, 1998. (Cited on page 44.)

[83] G. Ascoli et al. CDF central muon detector. *Nucl. Instrum. Methods*, A268, 1988. (Cited on page 45.)

[84] C. M. Ginsburg et al. CDF Run 2 Muon System. *Eur. Phys. J.*, 33(S1002), 2004. (Cited on page 45.)

[85] C. Avila et al. A measurement of the proton-antiproton total cross-section at $\sqrt{s} = 1.8\,\text{TeV}$. *Phys. Lett.*, B445(419), 1999. (Cited on page 46.)

[86] D. Acosta et al. The performance of the CDF luminosity monitor. *Nucl. Instrum. Methods*, A494, 2002. (Cited on page 46.)

[87] E. J. Thomson et al. Online Track Processor for the CDF Upgrade. *IEEE Trans. Nucl. Sci.*, 49, 2002. (Cited on page 47.)

[88] B. Ashmanskas et al. The CDF Silicon Vertex Trigger. *Nucl. Instrum. Methods*, A518, 2004. (Cited on page 49.)

[89] M. Dell'Orso. The CDF Silicon Vertex Trigger. *Nucl. Phys. (Proc. Suppl.)*, B156, 2006. (Cited on page 49.)

[90] G. Gomez-Ceballos et al. Event Builder and Level 3 at the CDF experiment. *Nucl. Instrum. Methods*, A518, 2004. (Cited on page 51.)

[91] J. Antos et al. Data processing model for the CDF experiment. *Nucl. Instrum. Methods*, cerca, 2006. (Cited on page 52.)

[92] E. Gerchtein and M. Paulini. CDF detector simulation framework and performance. In *eConf. C0303241 TUMT005*, 2003. [physics/0306031]. (Cited on page 53.)

[93] R. Braun et al. *GEANT: Simulation Program For Particle Physics Experiments. User Guide And Reference Manual*, 1978. CERN-DD-78-2-REV. (Cited on page 53.)

[94] P. A. Movilla-Fernandez. Performance of the CDF Calorimeter Simulation in Tevatron Run II. In R. Yoshida S. Magill, editor, *Proceedings of the XII International Conference on Calorimetry in High Energy Physics (CALOR 06)*, 2006. [physics/0608081]. (Cited on page 53.)

[95] R. Veenhof. GARFIELD, recent developments. *Nucl. Instrum. Methods*, A419, 1998. (Cited on page 53.)

[96] M. Gold. Description of the Parameterized Charge Deposition Model. *CDF Internal Note*, 5871, 2002. unpublished. (Cited on page 53.)

[97] Ch. Paus et al. BottomMods. cdfcode-browser.fnal.gov/CdfCode/source/BottomMods/. (Cited on page 60.)

[98] P. Murat et al. Stntuple. cdfcodebrowser.fnal.gov/CdfCode/source/Stntuple/. (Cited on page 60.)

[99] C. R. Rao. Information and accuracy attainable in the estimation of statistical parameters. *Bull. Calcutta Math. Soc.*, 37(81), 1945. (Cited on page 61.)

[100] H. Cramer. *Mathematical Methods of Statistics*. Princeton University Press, 1946. (Cited on page 61.)

[101] K. Anikeev, P. Murat, and Ch. Paus. Description of BGenerator II, 1999. CDF Internal Note 5092. (Cited on page 65.)

[102] D. J. Lange. The EvtGen Particle Decay Simulation Package. *Nucl. Instrum. Meth.*, 2001. (Cited on page 65.)

[103] CDF Simulation Group. CDF Detector Simulation, 2000. www-cdf.fnal.gov/cdfsim/cdfsim main.html. (Cited on page 65.)

[104] R. Brun, F. Bruyant, M. Maire, A. C. McPherson, and P. Zanarini. GEANT3, 1987. CERN-DD/EE/84-1. (Cited on page 65.)

[105] F. James and Computing and Networks Division. Minuit, Function Minimization and Error Analysis. Technical report, CERN, Geneva, August 2007. Reference Manual Version 94.1. (Cited on page 73.)

[106] The CDF collaboration. Angular Analysis of $B_s \to J/\psi\phi$ and $B^0 \to J/\psi K^\star$ Decays and Measurements of $\Delta\Gamma_s$ and ϕ_s. *CDF Pubblic Note*, 8950, 2007. (Cited on pages 81 and 90.)

[107] A. C. Davison and D. V. Hinkley. *Bootstrap methods and their applications*. Cambridge University Press, Cambridge, 1997. (Cited on page 107.)

[108] Michael Joseph Morello. Measurements of CP Asymmetries and Branching Fractions of Two-Body Charmless Decays of B^0 and B_s^0 Mesons. Ph.d. thesis, Scuola Normale Superiore di Pisa, 2006.